

Structure and surface reactions of Iodine and Cadmium Iodide on fcc(111) metal surfaces

By Christopher John Fisher BSc

Thesis submitted to the University of Nottingham for the degree of
Doctor of Philosophy, August 1999

For my family

Abstract

Structural studies using the synchrotron based Normal Incidence X-Ray Standing Wave (NIXSW) technique of the copper(111)-($\sqrt{3}\times\sqrt{3}$)R30⁰-Iodine and copper(111)-($\sqrt{3}\times\sqrt{3}$)R30⁰- $\frac{1}{2}$ (CdI₂) surfaces are presented. For the copper-iodine system, the iodine was shown to adsorb in a mixture of fcc and hcp hollow sites at a distance of $2.16 \pm 0.05\text{\AA}$ from the copper surface, in a ($\sqrt{3}\times\sqrt{3}$)R30⁰ mesh. The hollow site ratio observed was $50 \pm 3\%$ in fcc sites and $50 \pm 3\%$ in hcp sites. For the copper-cadmium iodide system, the iodine was again shown to adsorb in a mixture of the three fold hollows, at a slightly smaller distance of $2.10 \pm 0.05\text{\AA}$ from the copper surface, again in a ($\sqrt{3}\times\sqrt{3}$)R30⁰ mesh. The ratio of occupation of the hollow sites was determined to be $37 \pm 3\%$ in fcc sites and $63 \pm 3\%$ in hcp sites. The copper(111)-($\sqrt{3}\times\sqrt{3}$)R30⁰-Iodine surface produced by annealing the copper(111)- $\frac{1}{2}$ (CdI₂) surface, was shown to have a different ratio again, at $80 \pm 3\%$ in fcc sites and $20 \pm 3\%$ in hcp sites. Possible explanations for the changing ratios are discussed including sample temperature during surface preparation, step density of the crystal, co-adsorption of adsorbate or contamination and surface coverage. The cadmium in the copper- $\frac{1}{2}$ (CdI₂) surface was shown to be adsorbed randomly in a mixture of the three fold hollow sites, at $2.25 \pm 0.05\text{\AA}$ from the copper surface. The ratio was found to be $48 \pm 3\%$ in fcc sites and $52 \pm 3\%$ in hcp sites.

Both studies were found to be affected by the presence of non-dipole effects in the angular distribution of the core level photoelectrons used to collect some of the data. This caused incorrect values for the standing wave structural parameters to be determined. A novel experiment was performed using two analyser geometries which enabled the importance of including the non-dipole terms in the standing wave equations to be confirmed. An updated version of

the standing wave equations is presented which allows quantification of and correction for the non-dipole terms.

The surface reactions of iodine and cadmium iodide on an aluminium(111) surface at room temperature are shown to result in etching of the surface and the production of aluminium iodide (AlI_3). For both systems, iodine forms a close-packed chemisorbed layer that has a $(\sqrt{7} \times \sqrt{7})R19.1^0$ symmetry, with an iodine coverage of $3/7$ of a monolayer. For the cadmium iodide surface, the cadmium is proposed as being located randomly above the chemisorbed iodine layer. With the sample liquid nitrogen cooled to low temperatures, iodine produced physisorbed multilayers, and cadmium iodide adsorbs intact, but with no ordered growth.

A novel technique, Line Of Sight Sticking Probability (LOSSP), which allows the measurement of sticking and reaction probabilities is presented and applied to the I/Al system. The initial sticking probability for iodine at 300 K was determined as 0.8 ± 0.1 . Under steady state etching conditions at 300 K the overall reaction probability for I_2 to form AlI_3 was, $R_{\text{SS}} = 0.36 \pm 0.07$. The surface consisted of a majority of chemisorbed iodine, with a minority of co-adsorbed AlI_3 , with a total iodine coverage of ~ 0.6 ML. The sticking probability of I_2 to solid iodine at 103 K was measured as $S_{\text{phys}} = 0.98 \pm 0.02$, while the sticking probability on the halogenated surface at 300 K was measured as $S_{\text{phys}} > 0.8 \pm 0.1$. Variable temperature measurements gave an activation energy for the desorption of AlI_3 of approximately 57 kJmol^{-1} .

Table of contents

Abstract	iii
Table of contents	v
Acknowledgements	ix
Declaration	x
Abbreviations	xi
Chapter 1 : Introduction	1
Chapter 2 : Theory	3
2.1 Adsorption site	4
2.2 Sticking and reaction probability	6
2.3 Auger electron spectroscopy	8
2.4 X-ray photoelectron spectroscopy	9
2.5 Low energy electron diffraction	10
2.6 Normal incidence X-ray standing wave	10
2.6.1 Introduction	10
2.6.2 General description of NIXSW	10
2.6.3 Mathematical description of NIXSW	12
2.6.4 Adsorption site	15
2.6.5 Coherent position and coherent fraction	17
2.6.6 Advantages of NIXSW	20

Chapter 3 : Experimental methods	21
3.1	Sample preparation and cleaning	21
	3.1.1 Aluminium(111)	21
	3.1.2 Copper(111)	23
3.2	Daresbury	23
	3.2.1 UHV chamber	25
3.3	Nottingham	26
	3.3.1 Sample holder	27
	3.3.2 Retarding field analyser	27
3.4	Adsorption sources	28
3.5	Data acquisition	29
	3.5.1 NIXSW	29
	3.5.2 Line of sight temperature programmed desorption	32
	3.5.3 Auger electron spectroscopy	34
Chapter 4 : Non-dipole photoemission and Normal Incidence X-ray		
Standing Wave experiments : Copper(111)-($\sqrt{3}\times\sqrt{3}$)R30⁰-Iodine.....		35
4.0	Introduction	35
Part 1 : Non-dipole photoemission and NIXSW	35
4.1	Introduction	35
	4.1.1 Copper(111)-($\sqrt{3}\times\sqrt{3}$)R30 ⁰ -Iodine	36
	4.1.2 Gallium Arsenide(001)-(2x1)-Tellurium	37
4.2	Dipole approximation and NIXSW	39
4.3	Experimental methods	40
4.4	Results.....	42
	4.4.1 40 ⁰ -geometry	43
	4.4.2 90 ⁰ -geometry	45
	4.4.3 Copper peaks	46
4.5	Discussion	48

Part 2 :Structure determination for Copper(111)-($\sqrt{3}\times\sqrt{3}$)R30⁰-Iodine using NIXSW	56
4.6.0 Introduction	56
4.6.1 Copper(111)-($\sqrt{3}\times\sqrt{3}$)R30 ⁰ -Iodine	56
4.6.2 Silver(111)-($\sqrt{3}\times\sqrt{3}$)R30 ⁰ -Iodine	57
4.6.3 Copper(111)-($\sqrt{3}\times\sqrt{3}$)R30 ⁰ -Chlorine & Bromine	58
4.7 Experimental results and discussion	59
4.8 Summary	65
Chapter 5 : A Normal Incidence X-ray Standing Wave study of Copper(111)-$\frac{1}{2}$(CdI₂)	66
5.0 Introduction	66
5.1 Experimental methods	67
5.2 Results	71
5.3 Discussion	75
5.4 Summary	85
Chapter 6 : Iodine etching of Aluminium(111)	86
6.0 Introduction	86
6.1 Review of halogen adsorption on aluminium	86
6.1.1 Chlorine adsorption on aluminium	87
6.1.2 Etching studies of aluminium	88
6.1.3 Other studies	90
6.2 Line of Sight Sticking Probability	91
6.3 Experimental methods	94
6.4 Results	97
6.5 Discussion	101
6.6 Summary	115

Chapter 7 : Growth and reaction of Cadmium Iodide on		
Aluminium(111)	116
7.0	Introduction	116
7.1	Relevant studies	117
	7.1.1 Indium Antimonide(001)-Cadmium Iodide	117
	7.1.2 Copper(111)-Cadmium Iodide	118
7.2	Experimental methods	120
7.3	Results	122
7.4	Discussion	125
7.5	Summary	132
References	133
Appendix	138
Publications	141

Acknowledgements

After many years in the making, it's finally here, my thesis. To start with I want to thank my supervisor Dr. Robert. G. Jones, for keeping me on the straight and narrow during my PhD, and kicking me when I needed it. Without his enthusiasm and encouragement, none of this work would exist. Thanks are also required to the people who had to work with me, either in the deepest, darkest corners of the Chemistry department, or the infamous Hotel Daresbury. These in no particular order of importance include, Roslinda, Sarah, Nicky, Ally, Frank, Steve and Gavin. Next up for congratulations, are the intrepid technicians who helped keep my rig running (well some of the time anyway), namely Neil, Ralph and Dave. None of the results from Daresbury would have been achieved without the help and support of the legendary Bruce Cowie (now departed to greener pastures at the ESRF), who managed to make beamline 6.3 an oasis, in an otherwise depressing place.

Thanks to Mum and Dad for always allowing me to make my own decisions in life, yet always being there to talk to. Dad deserves an even bigger thank you, because when I was young (many years ago!) he decided to do an Open University course. I still have fond memories of getting up at 6am to watch the T.V. programs from the science foundation course (some of which I understood), which sowed the seeds of my interest in science.

I also ought to acknowledge the EPSRC for paying the bills.

Finally, my biggest thanks must go to Sarah, who by the time you read this will be my wife. Sarah has shared my life for the past 7 ½ years, and we've been through a lot together, including our 1st degrees, buying a house, and all the nightmares of being a PhD student. Thanks for all the nagging! I hope it was worth it all in the end.

Declaration

I declare that the work contained in this thesis is my own original work,
except where due reference has been made to other authors.

The research was carried out at the University of Nottingham between
October 1994 and May 1998 and has not been previously submitted for a
degree at this or any other university.

C J Fisher

Christopher John Fisher

Dr. Robert. G. Jones

August 1999

Abbreviations

AES	Auger Electron Spectroscopy
AES-t	Auger signal as a function of time
CFS	Constant Final State
CHA	Concentric Hemispherical Analyser
CIS	Constant Initial State
D	Coherent position
EDC	Energy Distribution Curve
fcc	Face Centered Cubic
f_{co}	Coherent fraction
hcp	Hexagonal Close Packed
LEED	Low Energy Electron Diffraction
LOSSP	Line of Sight Sticking Probability
LOSTPD	Line of Sight Temperature Programmed Desorption
ML	Monolayer
NIXSW	Normal Incidence X-Ray Standing Wave
Q	Dipole correction parameter
R	Reaction probability
RFA	Retarding Field Analyser
S	Sticking probability
SEXAFS	Surface Extended X-Ray Absorption Fine Structure
SRS	Synchrotron Radiation Source
TOF	Time of Flight
TPD	Temperature Programmed Desorption
UHV	Ultra High Vacuum
XPS	X-Ray Photoelectron Spectroscopy

Chapter 1: Introduction

This thesis is concerned with studies of the structure and reaction of molecules adsorbed on the surface of single metal crystals. Before discussing the importance and relevance of surface studies, it is useful to define what is a surface is. This depends on the nature of the system being studied and the methods used to study it. For example, surface films can be up to 100 nm in thickness and the surface is often considered to be the whole of the film. For studies of metal crystals, it is customary to consider the surface as being the top few atomic layers whose arrangement is often different from the bulk. Alternatively, the atoms which are exposed to a non-metallic environment can be considered as constituting the surface.

The study of metal surfaces is of interest for a number of applications, these include heterogeneous catalysis, corrosion, semi-conductor devices, data storage materials, and thin film coatings. Investigations in this area to date, including those presented in this thesis, have generally been performed on model systems, using single crystal metal surfaces in a vacuum (operating at pressures of typically 1×10^{-10} mbar), since these can be relatively easily characterised. Although far removed from the complex conditions encountered in real industrial processes, it is hoped that the results from these findings can be utilised to provide a greater understanding of the processes occurring at surfaces. The ultimate aim is to enable new and improved catalysts, or corrosion resistant materials *etc.* to be designed.

The work presented concerns the interaction of iodine and cadmium iodide with copper and aluminium surfaces. Iodine and cadmium iodide, like all halogens and halogen containing molecules, play an important role in a large number of

industrial processes, including electrochemistry, etching, dry processing, surface preparation, and catalytic poisoners and promoters. It is feasible that any of these processes could involve either copper or aluminium surfaces, so an understanding of the structures formed and chemistry occurring during the interaction between them could be of value.

Chapters 2 and 3 of this thesis, describe the theory behind the experimental techniques, and detail how the experiments were performed. Chapters 4 and 5 concentrate on the structure of iodine and cadmium iodide overlayers on a copper(111) surface. Both these studies use the Normal Incidence X-ray Standing Wave (NIXSW) technique. In addition to the structural aspects of these two chapters, a more important phenomenon is discussed, which is the introduction of non-dipole terms into the photoemission process. As will be discussed in chapter 4, this has a significant effect on the NIXSW profiles obtained from some photoelectron peaks. It is also the first time that non-dipole behaviour has been observed experimentally for any element outside of the noble gases.

Chapters 6 and 7 also study iodine and cadmium iodide, but on the more highly reactive aluminium(111) surface. These studies concentrate on the surface reactions occurring on the aluminium, as a result of interactions with the adsorbates. Chapter 6 also presents a new technique, termed Line of Sight Sticking Probability (LOSSP), which allows the measurement of sticking probabilities, an important surface property, with relatively simple equipment.

Chapter 2 : Theory

The aim of this chapter is to provide the theory necessary to understand the results and techniques used in this thesis. Some topics are covered in greater detail than others. The interested reader is directed towards the standard surface science textbooks for broader discussion [2.1,2.2,2.3].

2.1 Adsorption site

An adsorbed molecule or atom does not just locate anywhere on the surface. It usually has a preferred position, termed the adsorption site. This will be the place on the surface where it is most strongly bound to the surface. If a two-dimensional map of the surface is formed in terms of the adsorbate binding energy, then if the map is planar, *i.e.* the binding energy is the same all over the surface, then the adsorbate is said to form a two-dimensional gas and has complete translational freedom. However, if the binding energy map is corrugated, then the minima will correspond to the adsorption sites. Saddle points and maxima provide barriers to surface diffusion. Perhaps unsurprisingly, adsorption sites often correspond with the high symmetry sites found on a metal crystal surface. The commonly observed locations are atop sites (suggesting a bond to a single surface atom) and hollow sites (multiple bonding to surface atoms for chemisorbed species). For an fcc crystal with a (111) surface, there are two types of hollow site, which depend on which layer of the substrate the hollow is above. Fcc sites are above a 3rd layer substrate atom and hcp sites are above a 2nd layer substrate atom.

These are all illustrated in Figure 2.1. Other commonly observed adsorption sites are the bridge sites, where the adsorbate forms simultaneous bonds to only two surface atoms, resulting in a lower symmetry. All the adsorption sites are discussed further, with reference to NIXSW, in section 2.6.4.

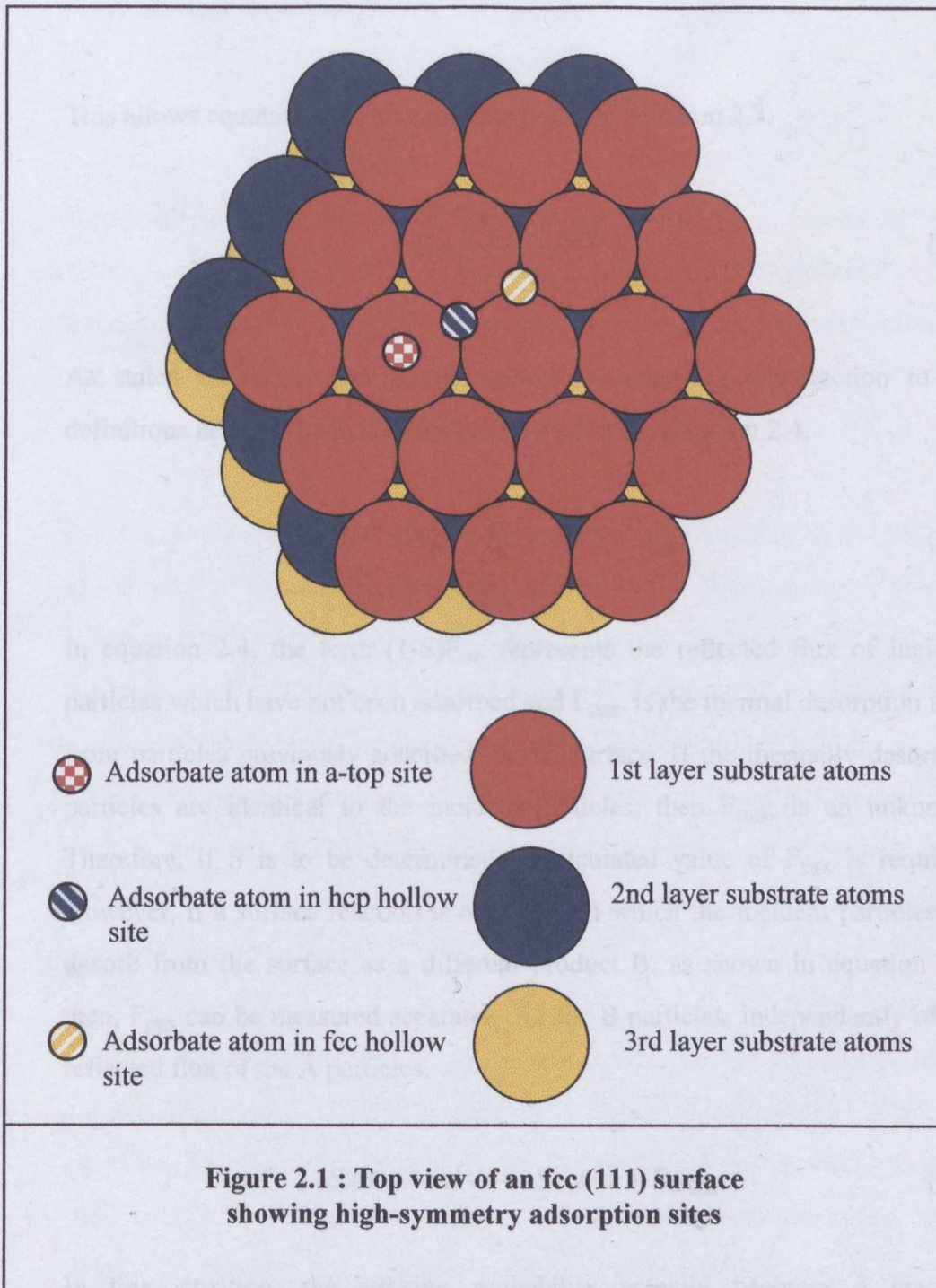
Many surface science techniques can be used to determine the adsorption site (*e.g.* SEXAFS, NEXAFS, NIXSW, PED, RAIRS *etc.* [2.1,2.2,2.3]). Section 2.6 describes the Normal Incidence X-ray Standing Wave (NIXSW) technique that has been used in this thesis.

2.2 Sticking and reaction probability

The sticking probability of a species is defined here as the probability that an identifiable incident particle will stick on impact with the sample surface and remain adsorbed. However, if the surface has a finite surface coverage and the temperature is sufficiently high then there is the possibility of thermal desorption. For this to be correctly accounted for in the sticking probability measurement, it is necessary to define the sticking probability in terms of measurable quantities. Assuming that thermal desorption is not occurring on the time-scale of the experiment, then the sticking probability (S), of a species incident on a surface, is defined as the ratio of the rate of adsorption, r_a (particles $\text{m}^{-2} \text{s}^{-1}$), to the rate of impingement, F_{IN} (particles $\text{m}^{-2} \text{s}^{-1}$), as shown equation 2.1.

$$S = \frac{r_a}{F_{IN}} \quad (2.1)$$

In chapter 6, a new experiment for determining sticking probabilities will be presented, which relies on measuring the reflected flux from the sample. Therefore, it is necessary to rewrite equation 2.1, in terms of the reflected flux, F_{OUT} .



The rate of adsorption (r_a) is related to the reflected flux (F_{OUT}), by equation 2.2.

$$r_a = (F_{IN} - F_{OUT}) \quad (2.2)$$

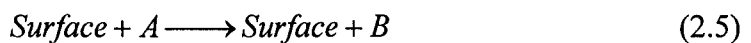
This allows equation 2.1, to be rewritten, giving equation 2.3.

$$S = \frac{(F_{IN} - F_{OUT})}{F_{IN}} \quad (2.3)$$

As stated earlier, if thermal desorption is occurring, a correction to the definitions needs to be made, this is achieved using equation 2.4.

$$F_{OUT} = (1-S)F_{IN} + F_{DES} \quad (2.4)$$

In equation 2.4, the term $(1-S)F_{IN}$, represents the reflected flux of incident particles which have not been adsorbed and F_{DES} , is the thermal desorption flux, from particles previously adsorbed on the surface. If the thermally desorbing particles are identical to the incident particles, then F_{DES} , is an unknown. Therefore, if S is to be determined, a calculated value of F_{DES} is required, However, if a surface reaction is occurring in which the incident particles, A, desorb from the surface as a different product B, as shown in equation 2.5, then, F_{DES} can be measured separately for the B particles, independently of the reflected flux of the A particles.



In this situation, the sticking probability actually becomes a reaction probability R, where R is defined by equation 2.6.

$$S = R = \frac{(F_{A,IN} - F_{A,OUT})}{F_{A,IN}} \quad (2.6)$$

A value of $R = 0$ implies that no reaction is occurring, whilst $R = 1$, means that every incident particle reacts.

2.3 Auger Electron Spectroscopy

Auger electron spectroscopy (AES) is one of the most commonly used techniques in surface science. It provides a non-destructive method to enable the determination of chemical species present on a surface. If used correctly it can allow quantification of surface contaminations as low as 1 % of a monolayer, or even less.

An Auger electron, named after its discoverer Pierre Auger [2.4], is produced as the result of the de-excitation of an ionised atom in a non-radiative process. When an atom is ionised (either by X-rays, or an electron beam of 10^3 - 10^5 eV), the atom is left in a high-energy state due to the formation of a core-state hole. The atom relaxes by filling the newly created core-state hole with an electron from a less tightly bound orbital. The energy resulting from this can manifest itself in two ways, either as the radiative emission of an X-ray photon, or as the non-radiative emission of an Auger electron. The energy diagram for the Auger process is shown in Figure 2.2.

Auger electron spectroscopy is an important tool, because the energy of the emitted Auger electron is independent of the energy of the ionising radiation or electrons. Therefore, any ionising source will produce Auger electrons with the same energy. In addition, the energy is only dependent upon the energy levels within the emitting atom, therefore every element produces Auger electrons with distinct energies. Notation for Auger electrons uses the X-ray level notation for energy levels, so that the Auger transition shown in Figure 2.5,

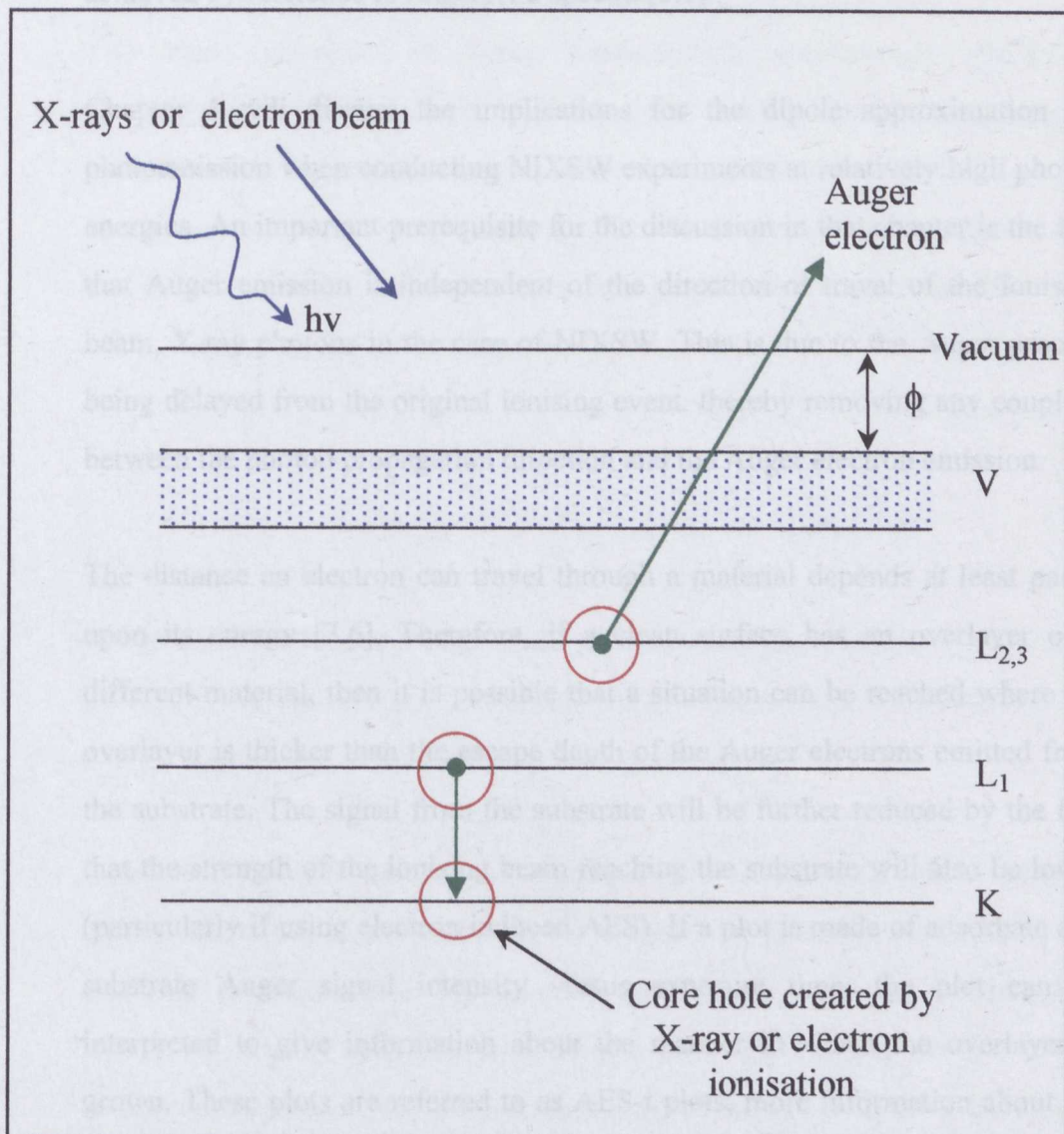


Figure 2.2 : Energy diagram for AES

Schematic diagram for Auger electron emission. Diagram shows ionisation of atom represented by circle in the K level by either electrons or X-rays. This is followed by relaxation of an electron from the L₁ level and emission of an Auger electron from L_{2,3}. V is the valence band and ϕ is the work function of the sample.

would be termed a $KL_1L_{2,3}$ Auger. Identification of Auger transitions is achieved by reference to fingerprint spectra [2.5].

Chapter 4 will discuss the implications for the dipole approximation for photoemission when conducting NIXSW experiments at relatively high photon energies. An important prerequisite for the discussion in that chapter is the fact that Auger emission is independent of the direction of travel of the ionising beam, X-ray photons in the case of NIXSW. This is due to the Auger process being delayed from the original ionising event, thereby removing any coupling between the photon propagation direction and the Auger electron emission.

The distance an electron can travel through a material depends at least partly upon its energy [2.6]. Therefore, if a clean surface has an overlayer of a different material, then it is possible that a situation can be reached where the overlayer is thicker than the escape depth of the Auger electrons emitted from the substrate. The signal from the substrate will be further reduced by the fact that the strength of the ionising beam reaching the substrate will also be lower (particularly if using electron induced AES). If a plot is made of adsorbate and substrate Auger signal intensity versus exposure time, the plot can be interpreted to give information about the manner in which the overlayer is grown. These plots are referred to as AES-t plots, more information about the nature of these plots can be found in a published review [2.7].

2.4 X-ray Photoelectron Spectroscopy

The basic principle of X-ray photoelectron spectroscopy (XPS) is straightforward, it is simply the excitation of electrons within an atom/molecule with X-rays of sufficient energy to ionise a core level electronic shell, so that an electron is ejected into the vacuum. The distribution of photoelectrons with energy, is commonly referred to as an energy distribution curve or EDC. The relevant equation for the process developed by Einstein, is shown in equation 2.7.

$$KE = E_p - E_B + \phi \quad (2.7)$$

where KE is the kinetic energy of the photoelectron produced, E_p is the photon energy, E_B is the core level binding energy, and ϕ the work function. The energy diagram for XPS is illustrated in Figure 2.3.

Because of the differences in the binding energy of electrons within different atoms, the detected photoelectrons are unique to a particular element. E_B can easily be calculated from experimental spectra and compared with tables of core level binding energies to determine both the emitting atom and the electronic shell involved. Surface sensitivity is achieved in XPS by careful choice of the photon energy such that the photoelectrons of interest are produced with kinetic energies in the range 100 – 1000 eV.

Equation 2.7 does not provide an exact description of a photoelectrons energy. Further factors include relaxation effects within the emitting atom and on surrounding atoms following ionisation and work function differences between the spectrometer and the sample.

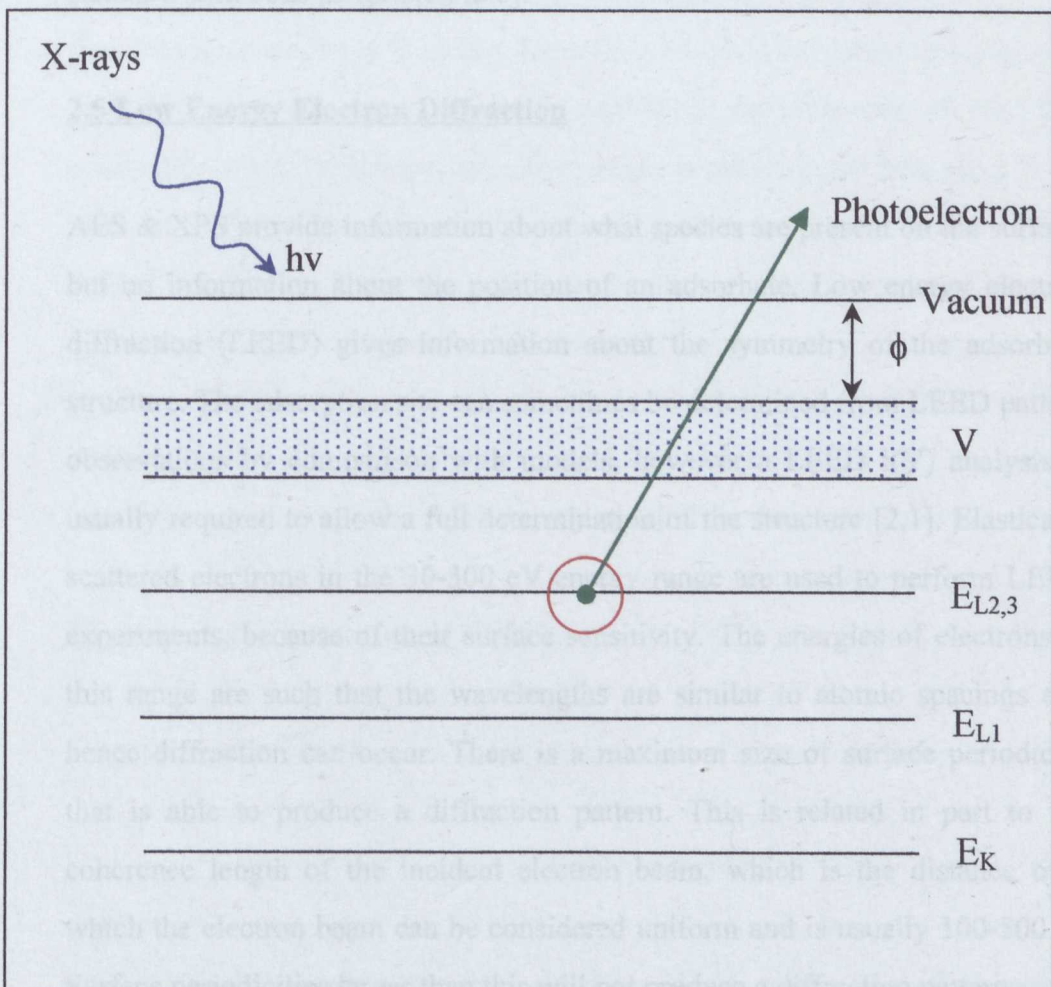


Figure 2.3 : Energy diagram for XPS

Schematic diagram for photoelectron emission. Diagram shows ionisation of atom represented by circle in the $E_{L2,3}$ level, followed by emission of photoelectron. V is the valance band and ϕ is the work function of the sample.

Photoelectrons are produced with a characteristic angular distribution. Further details of this can be found in chapter 4 where the effect of photon energy on angular distributions and hence on NIXSW experiments is discussed, and in standard textbooks [2.1,2.2,2.3,2.6].

2.5 Low Energy Electron Diffraction

AES & XPS provide information about what species are present on the surface, but no information about the position of an adsorbate. Low energy electron diffraction (LEED) gives information about the symmetry of the adsorbate structure. The adsorption site can sometimes be determined from LEED pattern observations by comparison with models, however a LEED I(V) analysis is usually required to allow a full determination of the structure [2.1]. Elastically scattered electrons in the 30-300 eV energy range are used to perform LEED experiments, because of their surface sensitivity. The energies of electrons in this range are such that the wavelengths are similar to atomic spacings and hence diffraction can occur. There is a maximum size of surface periodicity that is able to produce a diffraction pattern. This is related in part to the coherence length of the incident electron beam, which is the distance over which the electron beam can be considered uniform and is usually 100-500 Å. Surface periodicities larger than this will not produce a diffraction pattern.

2.6 Normal Incidence X-ray Standing Wave

2.6.1 Introduction

Normal Incidence X-ray Standing Wave (NIXSW) is a technique that combines both diffraction and spectroscopy, to enable the determination of adsorbate position on single crystal surfaces. The sample is placed in the path of an X-ray beam such that a standing wave is created within the crystal (due to Bragg reflection). The photon energy is scanned through the Bragg peak, during which the adsorbate experiences a changing intensity of X-rays, due to the standing wave moving by one half of the bulk layer spacing. Monitoring the photoabsorption for the adsorbate allows the determination of its position relative to the planes of the single crystal causing the Bragg reflection.

2.6.2 General Description of NIXSW

The Bragg equation is,

$$n\lambda = 2d \sin \theta \quad (2.8)$$

where, λ is the wavelength of the radiation, d is the separation of the atomic planes within the crystal, θ is the angle of the radiation to the atomic planes and n is an integral number (1,2,3 ...). If equation 2.8 is satisfied for a single crystal, then an intense diffracted beam of X-rays is produced. In this situation, a coherent wave is going into the crystal and a coherent wave is also being reflected. These two waves interact and form a standing wave within the crystal, often referred to as the standing wavefield [2.8,2.9]. As the waves are coherent, their amplitudes can be added together, before squaring to get the intensity. Assuming that the crystal is perfect and that no x-ray absorption occurs, then the relationship between the incident and reflected beams is such that at some point the amplitudes are at a maximum together and produce 4

times the intensity ($(1 + 1)^2 = 4$), whilst at other points the amplitudes cancel out giving zero intensity. The periodicity of the standing wavefield is such that the maxima and minima lie in planes parallel to the Bragg scattering planes. It should also be noted that as the incident and reflected beams also overlap outside the crystal, the standing wavefield therefore extends far beyond the crystals surface. This means that there are apparently planes above the actual surface as far as the standing wavefield is concerned. Figure 2.4 illustrates how the standing wavefield intensity varies through the crystal and beyond the surface.

In order to fully understand how the standing wavefield is created and how it behaves, it is necessary to use the dynamical theory of X-ray diffraction [2.10]. This shows that under conditions which fully satisfy the Bragg condition (for a non-absorbing crystal), there is a limit to the penetration depth of the X-rays into the crystal. Hence, there is a finite width to the range of energies & angles which will generate a reflected beam. This is shown by the Darwin-Prins rocking curve, in Figure 2.5a. The term η measures the distance in energy from the midpoint of the curve; it will be used in the mathematical description of NIXSW given in section 2.6.3. Within the range of total reflectivity given by Figure 2.5a, the phase of the reflected beam changes in a regular manner and as the phase of the incoming wave remains constant, then the waves will have to travel a different distance before the standing wave is created. This results in changed positions of the nodes and anti-nodes of the standing wavefield. Figure 2.5b shows how the phase of the wavefield changes as a function of η . Again, it is the dynamical theory of X-ray diffraction that calculates this phase change behaviour. The maximum change of phase is a quarter wavelength of the incident X-rays and therefore, the nodes/anti-nodes will move a maximum of one half of the layer spacing of the Bragg scattering planes. Figure 2.6 illustrates how the position of the nodes and antinodes of the standing wavefield relative to the substrate planes depends upon the photon energy relative to the Bragg energy.

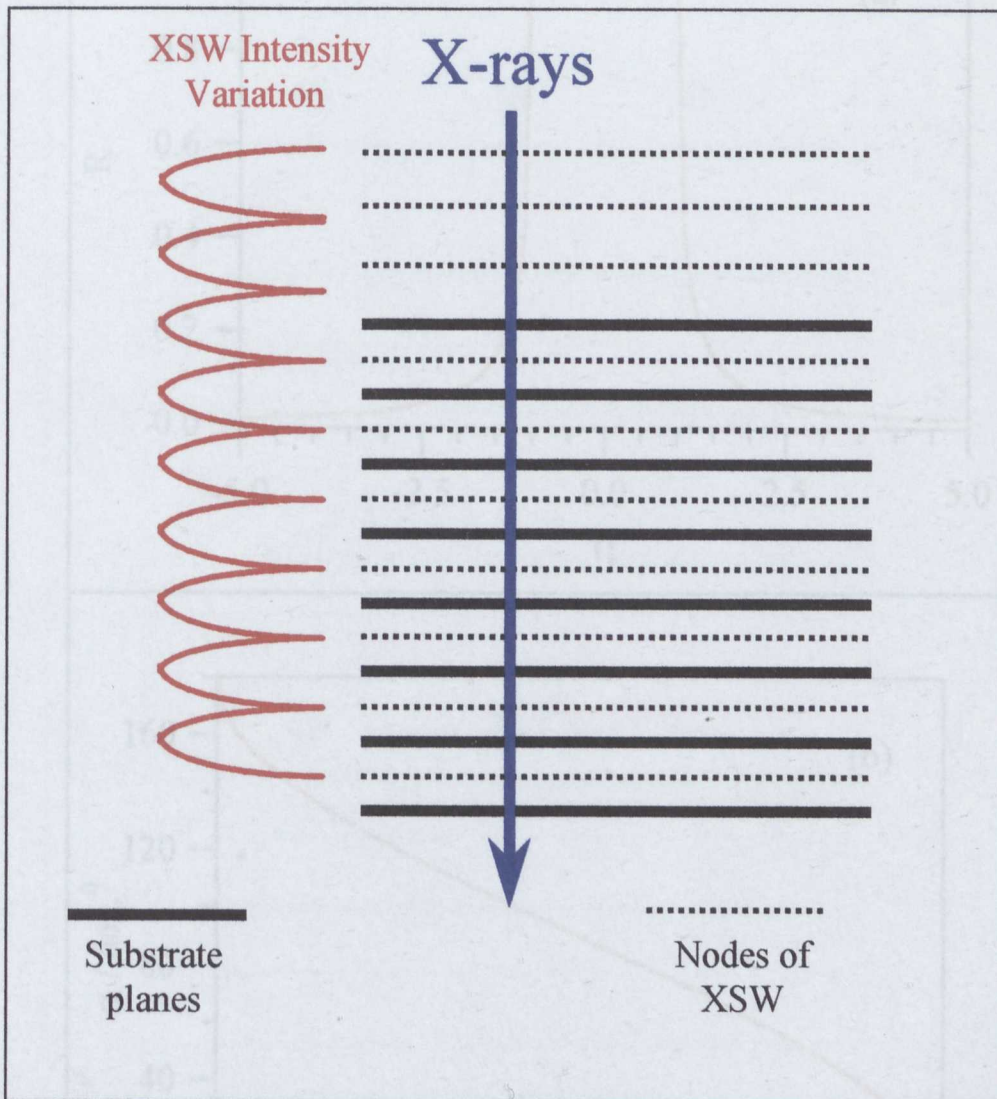


Figure 2.4 : Intensity variation of X-ray standing wavefield

Figure 2.7 : Darwin-Fresnel rocking curve and phase angle plot
 (a) X-ray intensity (Darwin curve) as a function of the scattering angle 2θ for a perfect crystal
 (b) Phase angle for the Darwin-Fresnel wave intensity profile as a function of 2θ

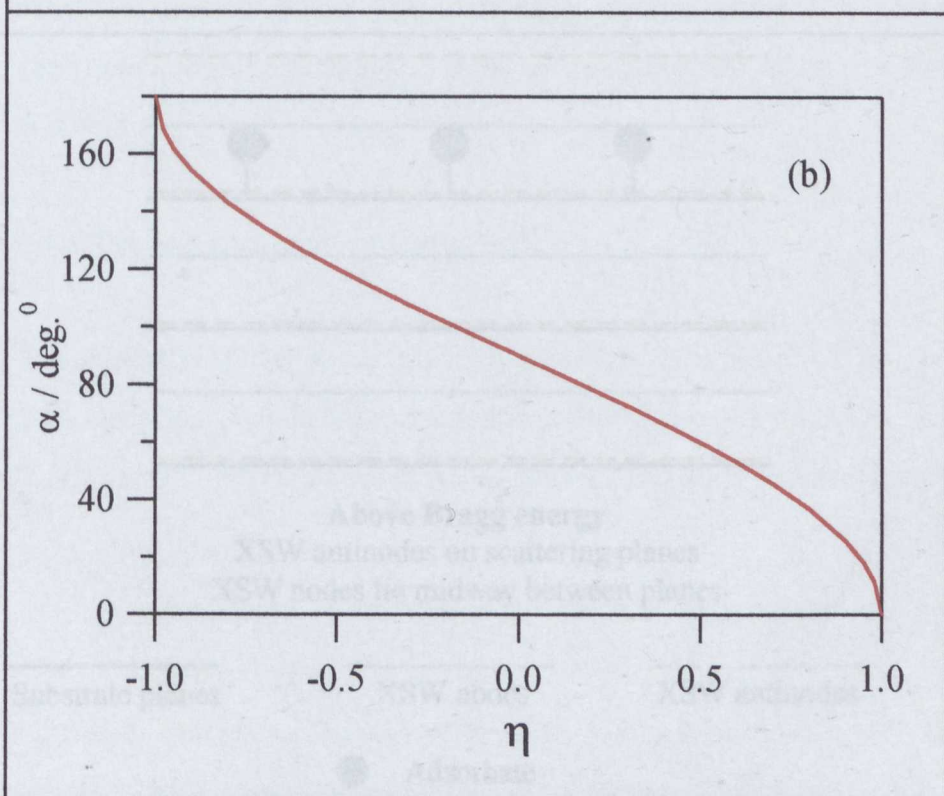
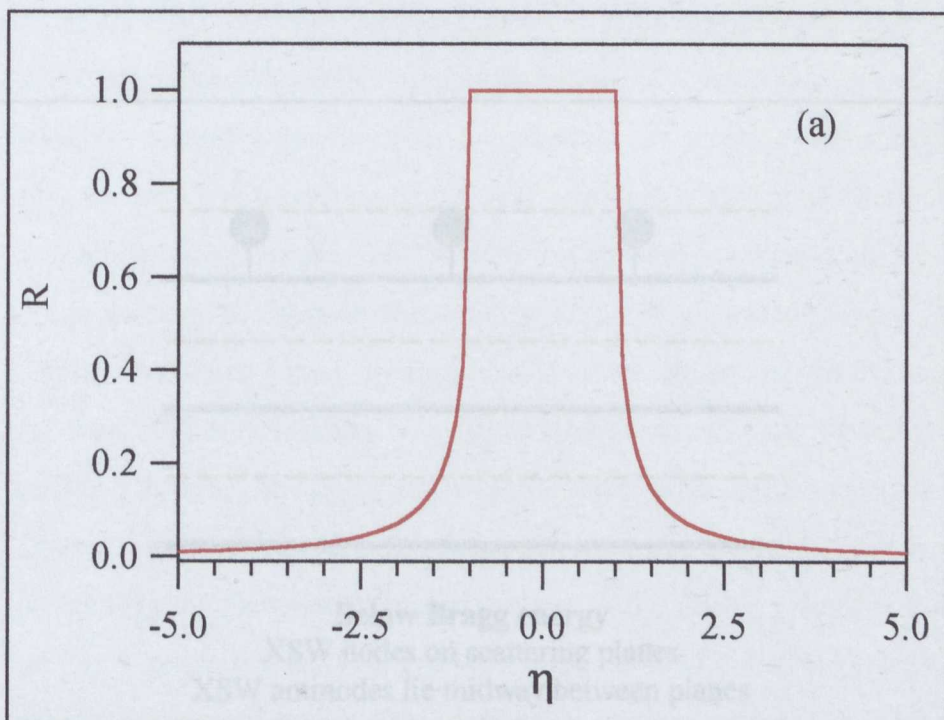
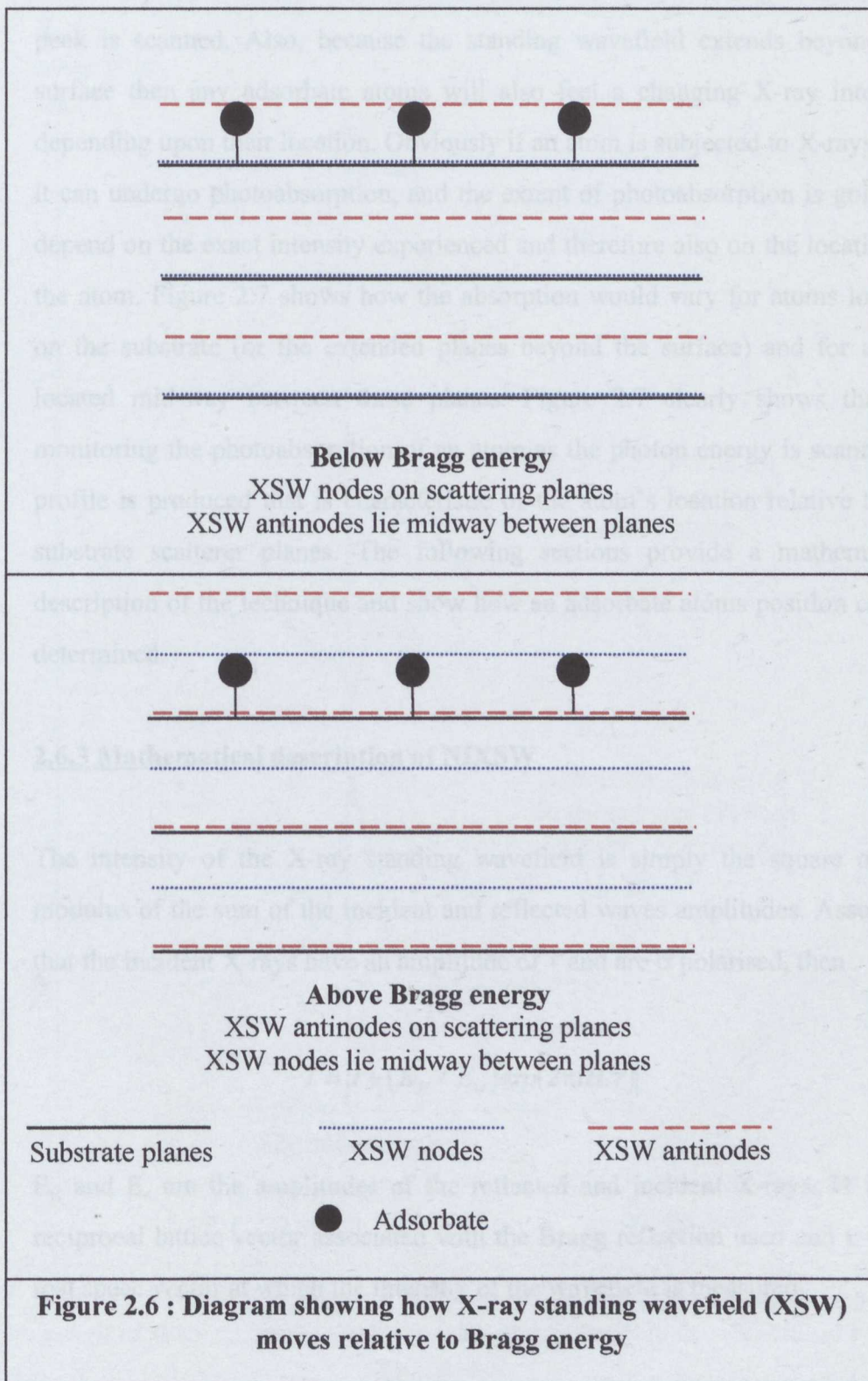


Figure 2.5 : Darwin-Prins rocking curve and phase angle plot

(a) X-ray reflectivity (Darwin curve) as a function of the parameter η , for a non-absorbing crystal.

(b) Phase angle for the standing wave intensity profile as a function of η .



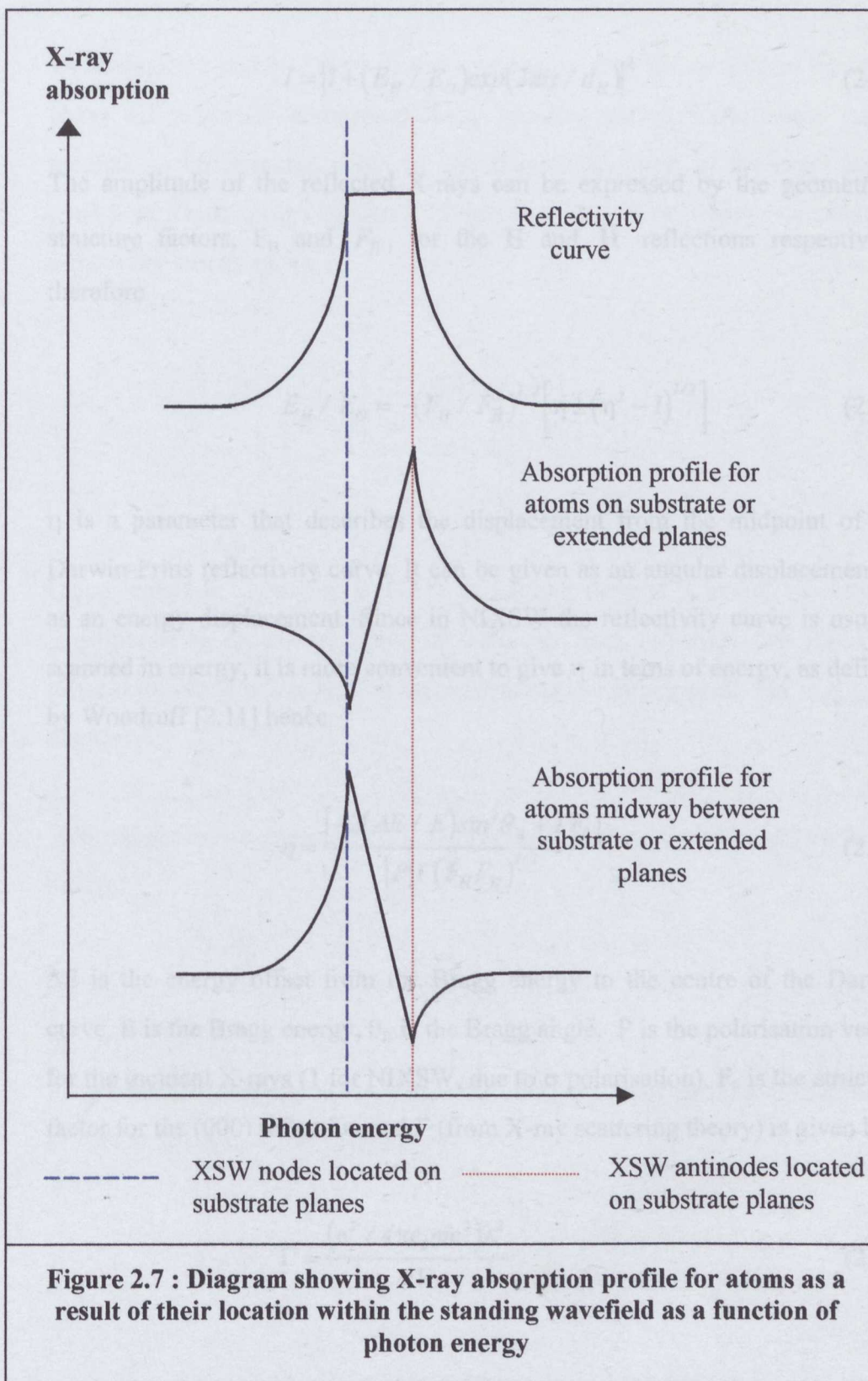
Because of the phase change behaviour discussed above and because of the existence of nodes and antinodes of X-ray intensity within the crystal when a standing wave is created, atoms located at different positions relative to the substrate planes will receive a different pattern of X-ray intensity as the Bragg peak is scanned. Also, because the standing wavefield extends beyond the surface then any adsorbate atoms will also feel a changing X-ray intensity depending upon their location. Obviously if an atom is subjected to X-rays then it can undergo photoabsorption, and the extent of photoabsorption is going to depend on the exact intensity experienced and therefore also on the location of the atom. Figure 2.7 shows how the absorption would vary for atoms located on the substrate (or the extended planes beyond the surface) and for atoms located mid-way between these planes. Figure 2.7 clearly shows that by monitoring the photoabsorption of an atom as the photon energy is scanned, a profile is produced that is characteristic of the atom's location relative to the substrate scatterer planes. The following sections provide a mathematical description of the technique and show how an adsorbate atoms position can be determined.

2.6.3 Mathematical description of NIXSW

The intensity of the X-ray standing wavefield is simply the square of the modulus of the sum of the incident and reflected waves amplitudes. Assuming that the incident X-rays have an amplitude of 1 and are σ polarised, then

$$I = \left| 1 + (E_H / E_O) \exp(2\pi i \mathbf{H} \cdot \mathbf{r}) \right|^2 \quad (2.9)$$

E_H and E_O are the amplitudes of the reflected and incident X-rays, \mathbf{H} is the reciprocal lattice vector associated with the Bragg reflection used and \mathbf{r} is the real space vector at which the intensity of the wavefield is measured.



In equation 2.9, the $\mathbf{H}\cdot\mathbf{r}$ term can be rewritten in terms of the distance, z , of the absorber above the atomic scattering planes generating the Bragg reflection, which are separated by a distance d_H , thus

$$I = \left| 1 + (E_H / E_O) \exp(2\pi iz / d_H) \right|^2 \quad (2.10)$$

The amplitude of the reflected X-rays can be expressed by the geometrical structure factors, F_H and $F_{\bar{H}}$, for the \mathbf{H} and $\bar{\mathbf{H}}$ reflections respectively, therefore

$$E_H / E_O = -(F_H / F_{\bar{H}})^{1/2} \left[\eta \pm (\eta^2 - 1)^{1/2} \right] \quad (2.11)$$

η is a parameter that describes the displacement from the midpoint of the Darwin-Prins reflectivity curve. It can be given as an angular displacement or as an energy displacement. Since in NIXSW the reflectivity curve is usually scanned in energy, it is more convenient to give η in terms of energy, as defined by Woodruff [2.11] hence

$$\eta = \frac{[-2(\Delta E / E) \sin^2 \theta_B + \Gamma F_0]}{|P| \Gamma (F_H F_{\bar{H}})^{1/2}} \quad (2.12)$$

ΔE is the energy offset from the Bragg energy to the centre of the Darwin curve, E is the Bragg energy, θ_B is the Bragg angle, P is the polarisation vector for the incident X-rays (1 for NIXSW, due to σ polarisation), F_0 is the structure factor for the (000) reflection and Γ (from X-ray scattering theory) is given by

$$\Gamma = \frac{(e^2 / 4\pi\epsilon_0 mc^2) \lambda^2}{\pi V} \quad (2.13)$$

e and m are the charge and mass of an electron, ϵ_0 is the permittivity of free space, c the speed of light, λ the wavelength of the X-rays and V the volume of the unit cell.

Equations 2.12 and 2.13 show the importance of using the dynamical theory of X-ray diffraction to understand X-ray standing waves. Kinematical theory predicts an infinitesimal width for the reflectivity curve, at the exact Bragg condition. Rearranging equation 2.12, gives equation 2.14, which calculates the reflectivity energy range.

$$\Delta E = \pm \left(\frac{\left(E |P| \Gamma (F_H F_{\bar{H}})^{\frac{1}{2}} \right)}{2 \sin^2 \theta_B} \right) \quad (2.14)$$

Using equation 2.14 for a (111) reflection from a copper(111) crystal corresponds to an energy range of 0.87 eV. Note however, that this total reflectivity range is not centred on the kinematical Bragg peak, but is slightly displaced.

With reference to equation 2.11, E_H/E_0 is related to the reflectivity (R) as shown below :

$$E_H / E_0 = \sqrt{R} \exp(i\Phi) \quad (2.15)$$

$i\Phi$ is a phase factor which represents the changing phase of the reflected wave as the Bragg condition is scanned.

Using this equation, equation 2.10, can be rewritten as

$$I = \left| 1 + \sqrt{R} \exp(\Phi - 2\pi iz / d_H) \right|^2 \quad (2.16)$$

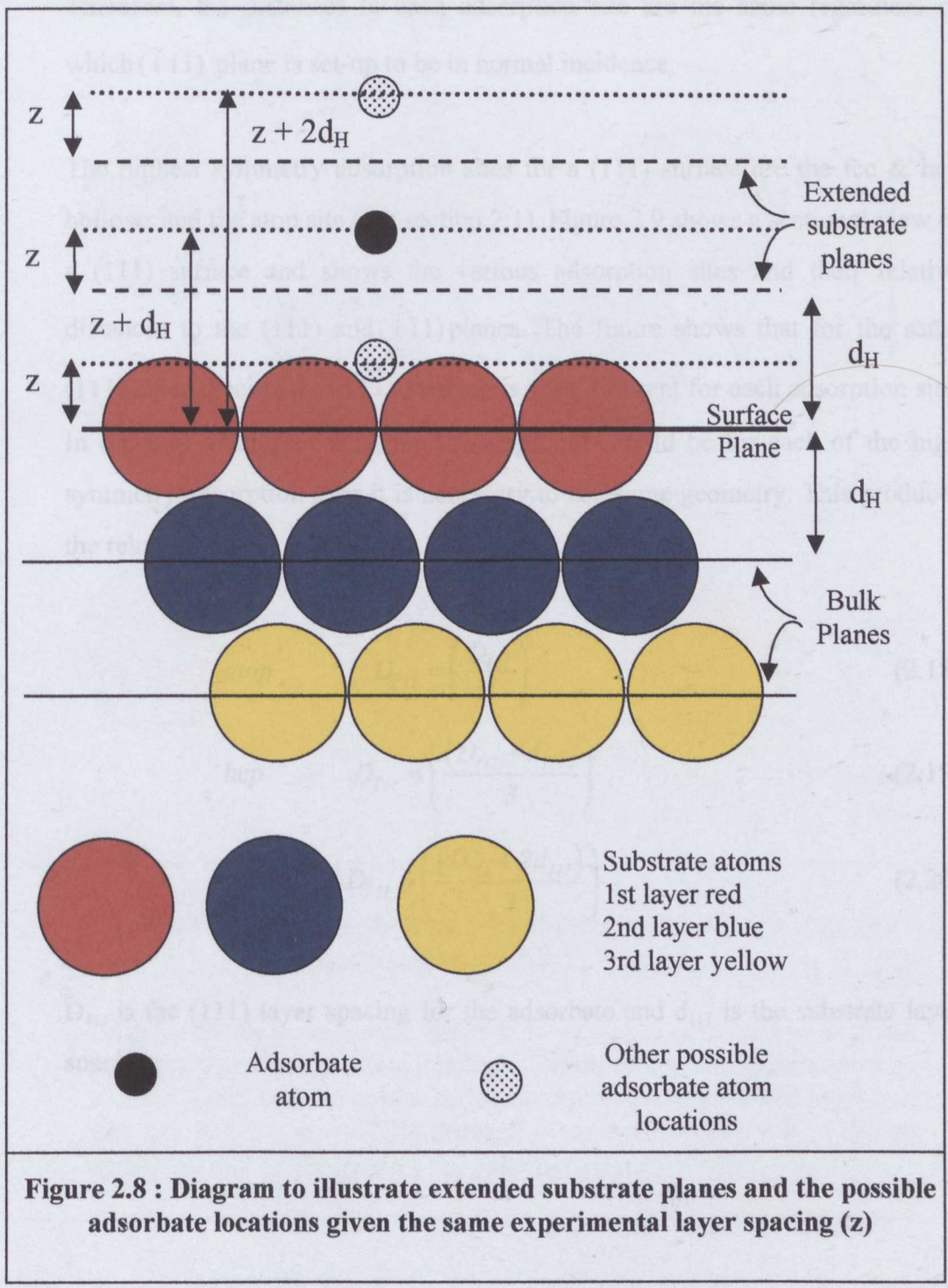
which leads to, as shown by Woodruff [2.11]

$$I = 1 + R + 2\sqrt{R} \cos(\Phi - 2\pi z / d_H) \quad (2.17)$$

2.6.4 Adsorption site

Equation 2.17 allows an adsorbate's height above the scatterer planes to be determined from the experimental profile. However, because of the extended scatterer planes generated by the standing wavefield extending outside the crystal, it should be remembered that the actual distance could be $z + nd_H$ (where n is an integer and d_H is the substrate layer separation). Figure 2.8 shows three possible adsorbate atom locations for the same layer spacing (z) which would have been determined experimentally. The black atom represents the "true" location of the adsorbate, the other two possible adsorbate locations shown (small shaded circles) all share the same layer spacing relative to either the substrate or extended planes but are not the "true" location for this example. In order to decide what is the correct distance, it is often necessary to use some chemical judgement by calculating what bond lengths would be for a given adsorbate height and deciding if the bond length seems physically realistic.

The next consideration is that if only one set of scatterer planes has been used, then only a distance perpendicular to those planes will be found. In order to overcome this it is necessary to perform NIXSW with two or more sets of planes. The NIXSW studies presented in this thesis (see chapters 4 and 5) all used a (111) crystal, therefore, it was most convenient to use the (111) planes parallel to the surface and the $(\bar{1}\bar{1}1)$ planes at 70.5° to the surface, thus



providing two distances, which allows a full structural determination. Two planes are sufficient because there are three symmetrically equivalent ($\bar{1}11$) planes and the main high symmetry adsorption sites have three fold symmetry. Therefore, the distances to each adsorption site are the same regardless of which ($\bar{1}11$) plane is set-up to be in normal incidence.

The highest symmetry adsorption sites for a (111) surface are the fcc & hcp hollows and the atop site (see section 2.1). Figure 2.9 shows a sectional view of a (111) surface and shows the various adsorption sites and their relative distances to the (111) and ($\bar{1}11$) planes. The figure shows that for the same (111) layer spacing the ($\bar{1}11$) spacing is very different for each adsorption site. In order to determine what the layer spacing should be for each of the high symmetry adsorption sites it is necessary to use some geometry. This produces the relationships in equations 2.18-2.20.

$$\text{atop} \quad D_{\bar{1}11} = \left(\frac{D_{111}}{3} \right) \quad (2.18)$$

$$\text{hcp} \quad D_{\bar{1}11} = \left(\frac{(D_{111} + d_{111})}{3} \right) \quad (2.19)$$

$$\text{fcc} \quad D_{\bar{1}11} = \left(\frac{(D_{111} + 2d_{111})}{3} \right) \quad (2.20)$$

D_{111} is the (111) layer spacing for the adsorbate and d_{111} is the substrate layer spacing.

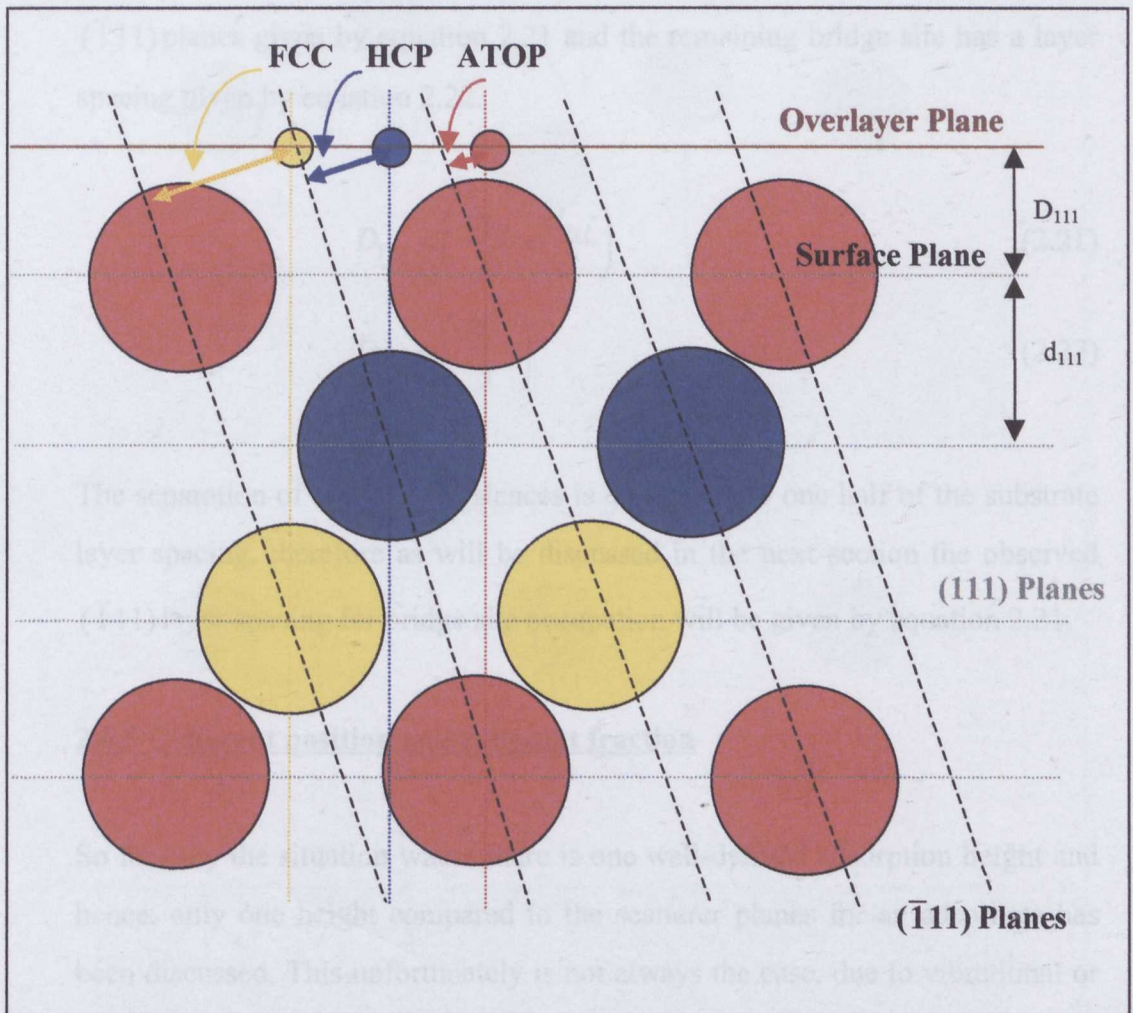


Figure 2.9 : Diagram showing high-symmetry adsorption sites and their distances to the $(\bar{1}11)$ planes.

Diagram shows the substrate atoms as large circles with each layer in the substrate shown by a different colour. The adsorbate atoms are shown as smaller circles and are colour coded according to the substrate layer that they are directly above. The distance of each adsorption site is shown relative to the $(\bar{1}11)$ planes by the coloured arrows.

The other main adsorption site to be considered are the bridge sites. These sites only have two-fold symmetry therefore leading to three symmetrically inequivalent bridge sites. Two of the bridge sites have a distance relative to the $(\bar{1}11)$ planes given by equation 2.21 and the remaining bridge site has a layer spacing given by equation 2.22.

$$D_{\bar{1}11} = \left(\frac{D_{III}}{3} + \frac{d_{III}}{2} \right) \quad (2.21)$$

$$D_{\bar{1}11} = \left(\frac{D_{III}}{3} \right) \quad (2.22)$$

The separation of these two distances is equivalent to one half of the substrate layer spacing, therefore as will be discussed in the next section the observed $(\bar{1}11)$ layer spacing for bridge site occupation will be given by equation 2.21.

2.6.5 Coherent position and coherent fraction

So far only the situation where there is one well-defined adsorption height and hence, only one height compared to the scatterer planes for an adsorbate has been discussed. This unfortunately is not always the case, due to vibrational or static disorder (see Figure 2.10), which will cause a distribution of possible z values. If a distribution of z values is incorporated with a probability for a given z value of $f(z).dz$ within a range dz about the value of z , then equation 2.17 becomes

$$I = I + R + 2\sqrt{R} \int_0^{d_H} f(z) \cos(\Phi - (2\pi z / d_H)) dz \quad (2.23)$$

This can be written as [2.11],

$$I = I + R + 2f_{co} \sqrt{R} \cos(\Phi - (2\pi D / d_H)) \quad (2.24)$$

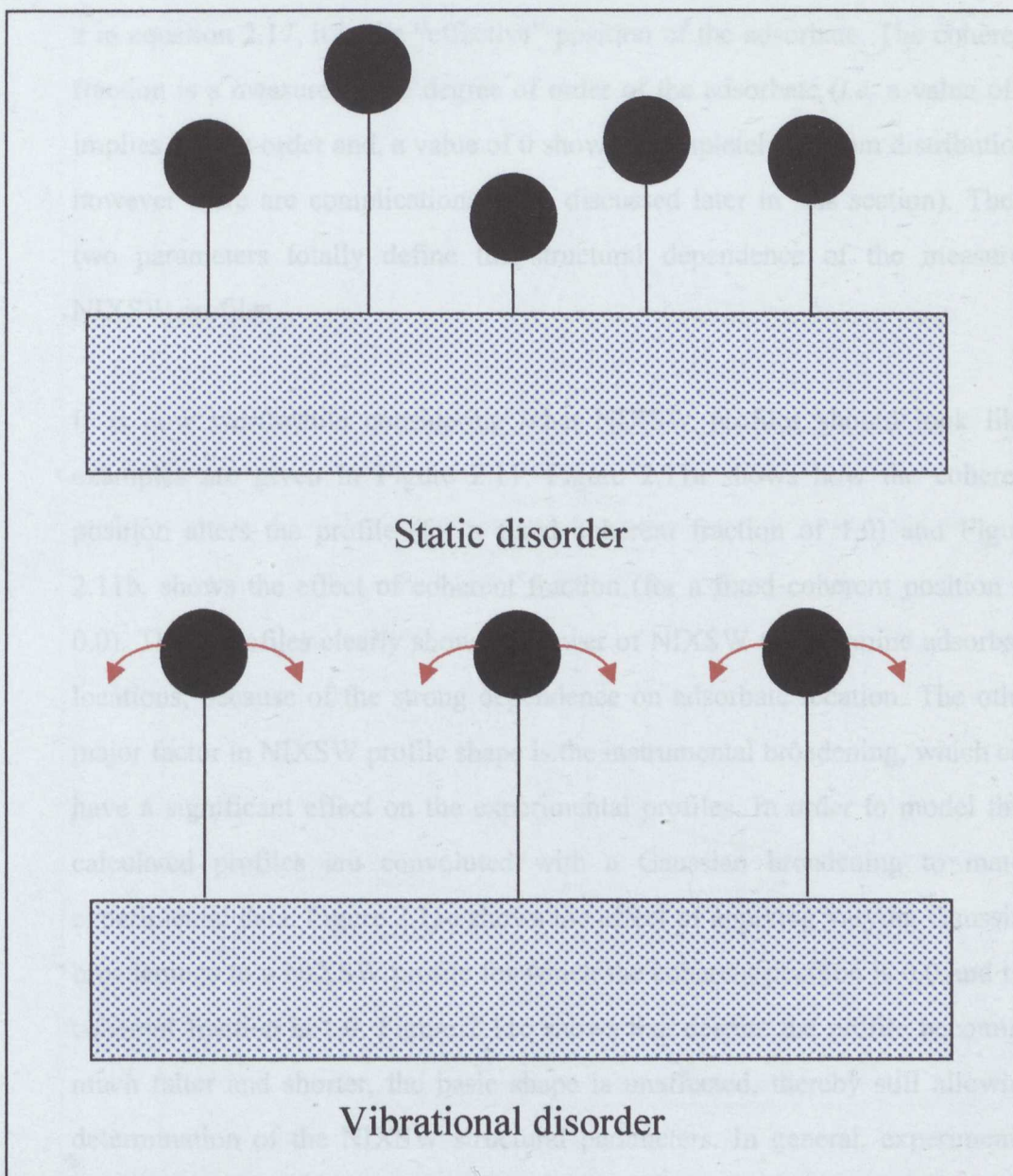


Figure 2.10 : Representation of static and vibrational disorder

The substrate is represented by the shaded rectangle, with adsorbate atoms as circles bonded to the surface. The vibrational motion of the atoms is suggested by the arrows.

The two new parameters introduced into equation 2.24 are the coherent position, D and the coherent fraction f_{co} . Coherent position, is the equivalent of z in equation 2.17, it is the “effective” position of the adsorbate. The coherent fraction is a measure of the degree of order of the adsorbate (*i.e.* a value of 1 implies perfect order and, a value of 0 shows a completely random distribution, however there are complications to be discussed later in this section). These two parameters totally define the structural dependence of the measured NIXSW profiles.

It is now worthwhile considering what NIXSW profiles should look like, examples are given in Figure 2.11. Figure 2.11a shows how the coherent position alters the profile (for a fixed coherent fraction of 1.0) and Figure 2.11b, shows the effect of coherent fraction (for a fixed coherent position of 0.0). These profiles clearly show the power of NIXSW to determine adsorbate locations, because of the strong dependence on adsorbate location. The other major factor in NIXSW profile shape is the instrumental broadening, which can have a significant effect on the experimental profiles. In order to model this, calculated profiles are convoluted with a Gaussian broadening to match experimental data. Figure 2.11c shows the effect of applying varying Gaussian broadenings to a NIXSW profile for which the coherent position is 0.0 and the coherent fraction is 1.0. Figure 2.11c shows that despite the profile becoming much fatter and shorter, the basic shape is unaffected, thereby still allowing determination of the NIXSW structural parameters. In general, experimental instrumental broadening is approximately 0.5 eV.

Returning to equation 2.24, the simplest way of relating the coherent position and coherent fraction to the actual position distribution is achieved using equation 2.25 [2.12].

$$f_{co} \exp(2\pi i D / d_H) = \int_0^{d_H} f(z) \exp(2\pi i z / d_H) dz \quad (2.25)$$

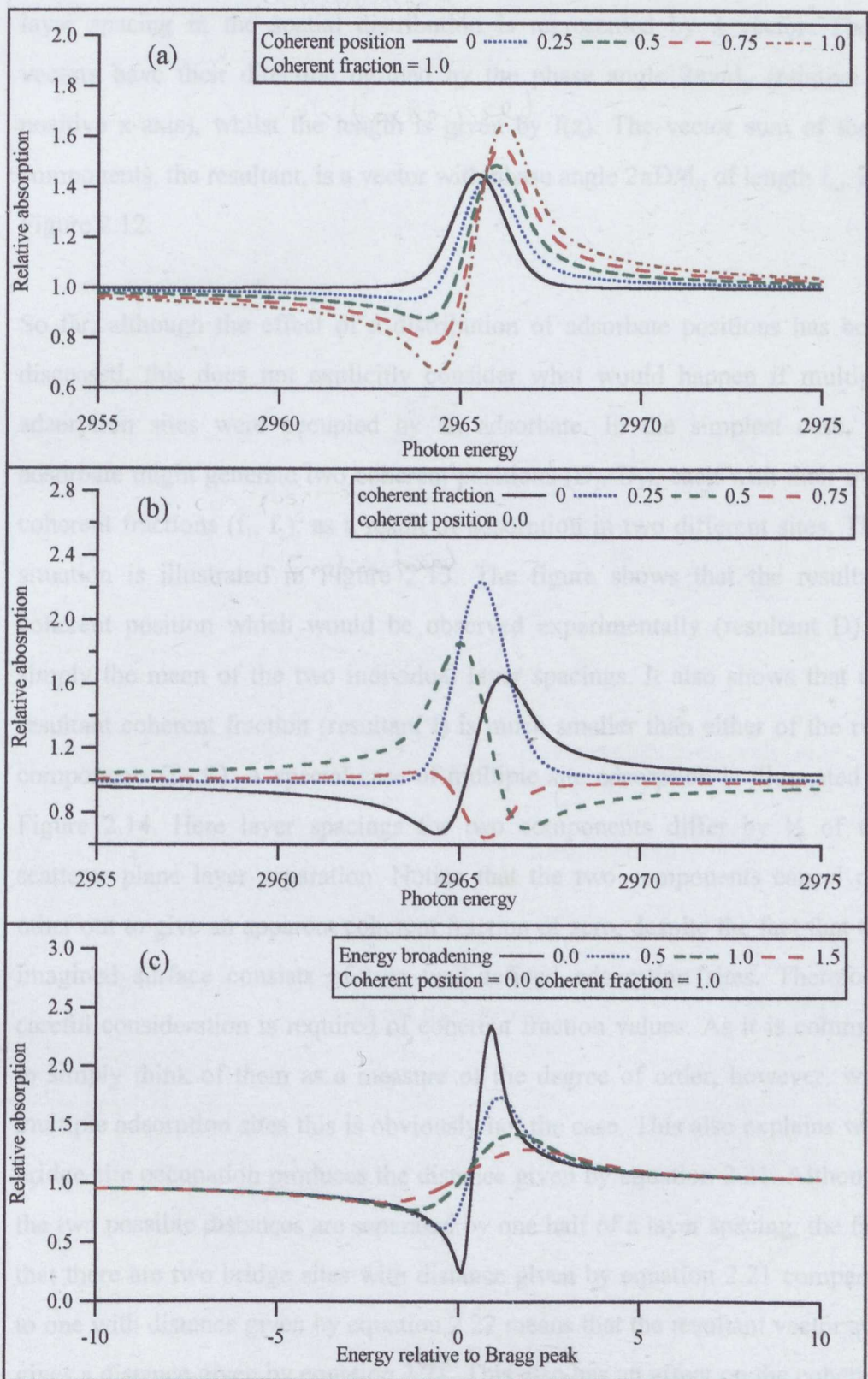
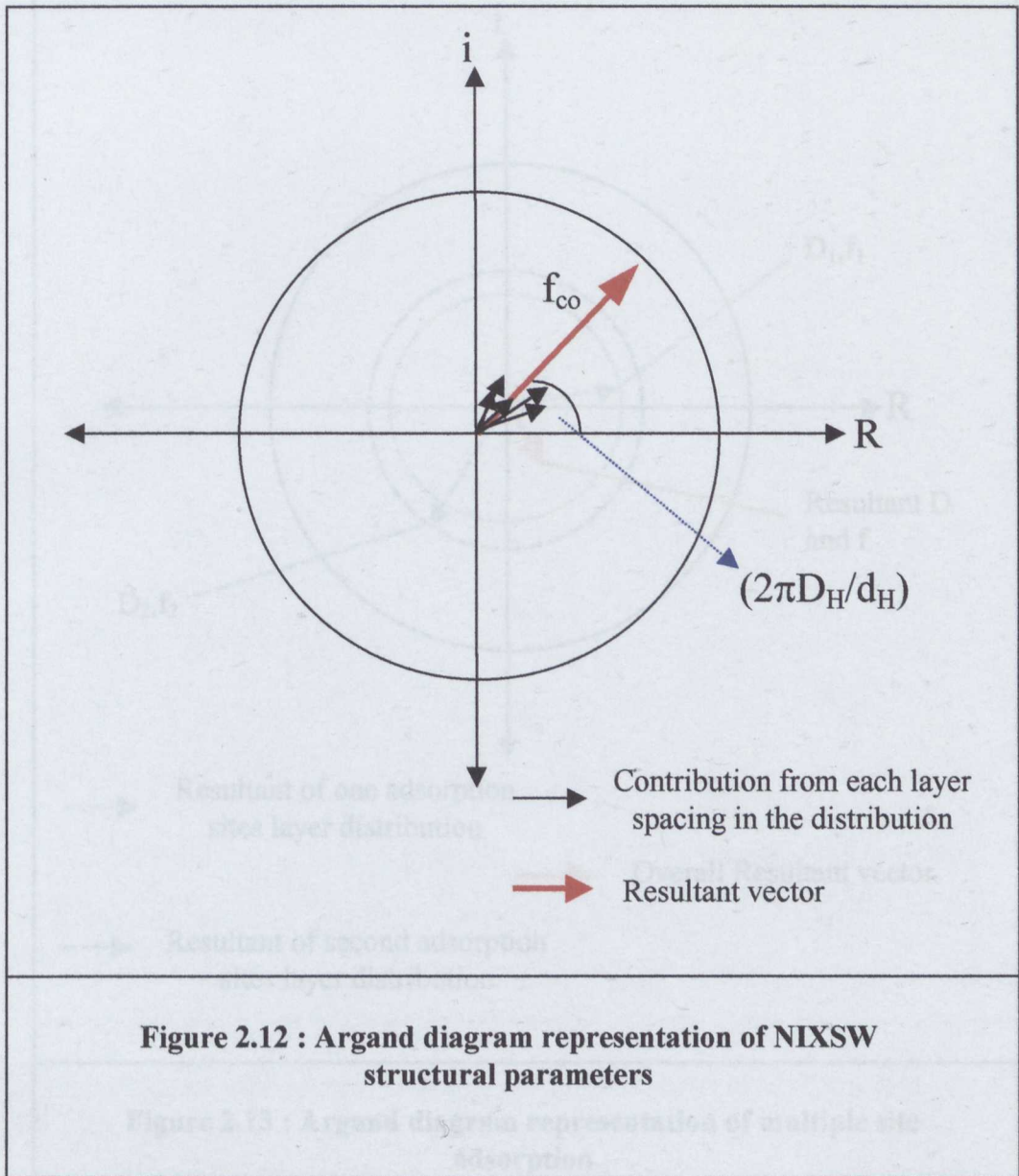


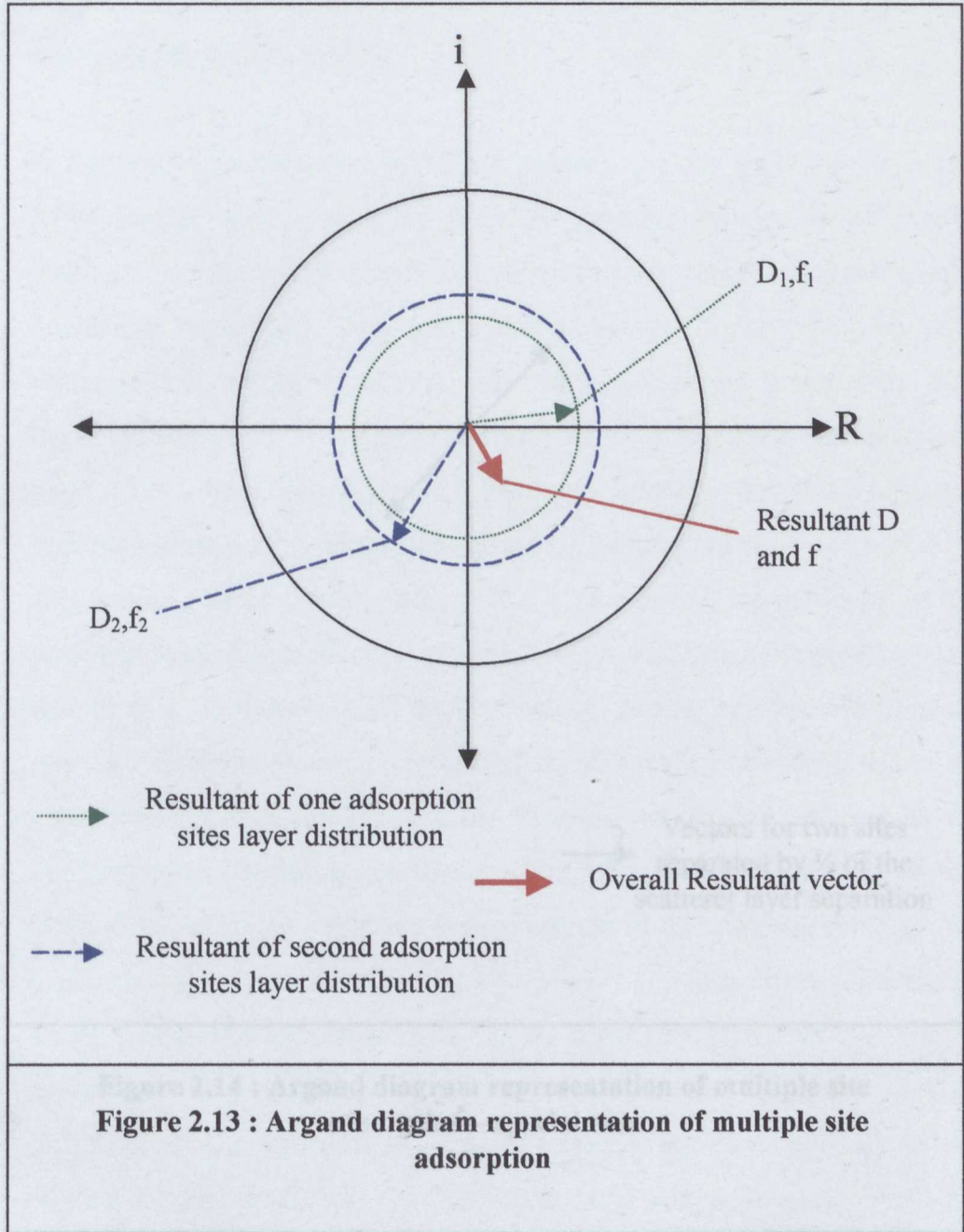
Figure 2.11 : Example NIXSW profiles

- a) Shows effect of coherent position
- b) Shows effect of coherent fraction
- c) Shows effect of energy broadening

This allows a simple graphical representation of the NIXSW parameters. The method involves using an Argand diagram [2.12] within which each adsorbate layer spacing in the spatial distribution is represented by a vector. These vectors have their direction defined by the phase angle $2\pi z/d_H$ (relative to positive x-axis), whilst the length is given by $f(z)$. The vector sum of these components, the resultant, is a vector with phase angle $2\pi D/d_H$ of length f_{co} , see Figure 2.12.

So far, although the effect of a distribution of adsorbate positions has been discussed, this does not explicitly consider what would happen if multiple adsorption sites were occupied by an adsorbate. In the simplest case, an adsorbate might generate two coherent positions (D_1, D_2), each with their own coherent fractions (f_1, f_2), as a result of adsorption in two different sites. This situation is illustrated in Figure 2.13. The figure shows that the resultant coherent position which would be observed experimentally (resultant D) is simply the mean of the two individual layer spacings. It also shows that the resultant coherent fraction (resultant f) is much smaller than either of the two components (f_1, f_2). A special case of multiple site adsorption is illustrated in Figure 2.14. Here layer spacings for two components differ by $\frac{1}{2}$ of the scatterer plane layer separation. Notice that the two components cancel out other out to give an apparent coherent fraction of zero, despite the fact that the imagined surface consists of two well-defined adsorption sites. Therefore, careful consideration is required of coherent fraction values. As it is common to simply think of them as a measure of the degree of order, however, with multiple adsorption sites this is obviously not the case. This also explains why bridge site occupation produces the distance given by equation 2.21. Although the two possible distances are separated by one half of a layer spacing, the fact that there are two bridge sites with distance given by equation 2.21 compared to one with distance given by equation 2.22 means that the resultant vector still gives a distance given by equation 2.21. This also has an affect on the coherent fraction, because the resultant vector can only have a maximum length of $1/3$,





therefore the maximum coherent fraction observable for bridge site occupation is $1/2$.

2.6.4 Advantages of NIXSW

So far most of the discussion of NIXSW would be equally applicable to grazing XSW studies where the primary beam is normally brought in at grazing incidence to the crystal planes and the reflection curve is assumed as a function of angle θ . There are several advantages in performing an XSW experiment at normal incidence. They are:

- 1. The incident X-ray beam is normally incident on the surface of the sample. This requires not only a highly collimated and monochromatic X-ray beam, but also a non-perfect crystal surface. This is because if the irregularity of the sample is large compared to the wavelength, the standing wave will be lost. Therefore, XSW experiments at grazing incidence are usually restricted to semi-conductor surfaces which have the required degree of perfection. However, by bringing the X-ray to normal incidence, the sample, because the Bragg condition has a unique solution, can be tilted to the exact incidence angle and is thus oriented in a unique direction. This allows the use of less perfect samples, i.e. mixed single crystals. Additionally,

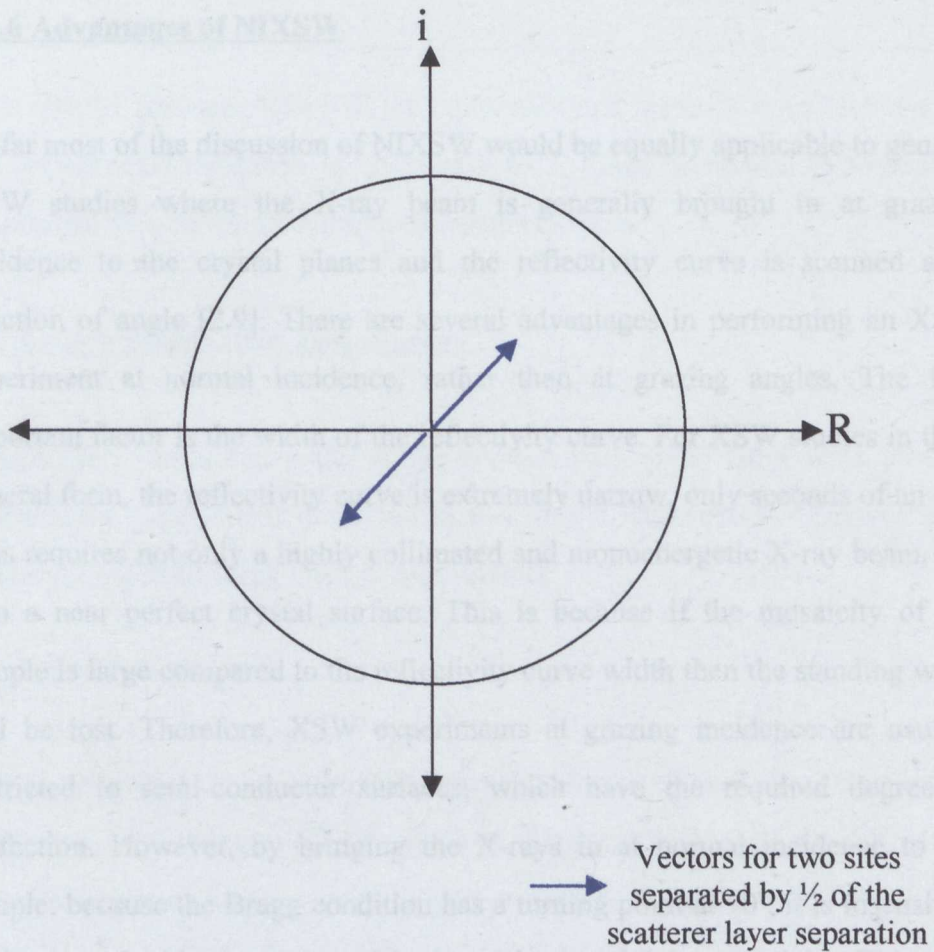


Figure 2.14 : Argand diagram representation of multiple site adsorption – special case

therefore the maximum coherent fraction observable for bridge site occupation is 1/3.

2.6.6 Advantages of NIXSW

So far most of the discussion of NIXSW would be equally applicable to general XSW studies where the X-ray beam is generally brought in at grazing incidence to the crystal planes and the reflectivity curve is scanned as a function of angle [2.9]. There are several advantages in performing an XSW experiment at normal incidence, rather than at grazing angles. The first important factor is the width of the reflectivity curve. For XSW studies in their general form, the reflectivity curve is extremely narrow, only seconds of an arc. This requires not only a highly collimated and monoenergetic X-ray beam, but also a near perfect crystal surface. This is because if the mosaicity of the sample is large compared to the reflectivity curve width then the standing wave will be lost. Therefore, XSW experiments at grazing incidence are usually restricted to semi-conductor surfaces, which have the required degree of perfection. However, by bringing the X-rays in at normal incidence to the sample, because the Bragg condition has a turning point at 90° , it is insensitive to the exact incidence angle and is thus tolerant of finite mosaicity. This then allows the use of less perfect samples, *i.e.* metal single crystals. Additionally, it means that an NIXSW experiment can be easily carried out on synchrotron experimental stations designed for other surface science techniques such as SEXAFS, because the beam convergence required for SEXAFS, which in turn implies angular spread, will not affect the experiments as it would for grazing incidence. Scanning the Bragg condition in energy instead of angle also simplifies the experimental apparatus, as it allows a standard UHV manipulator to be used, instead of a high precision goniometer.

For more information on NIXSW and a review of a number of applications, the reader is directed towards the review by Woodruff [2.13].

Chapter 3 : Experimental methods

This chapter presents details of the equipment and methods used to carry out the experiments described in chapters 4 to 7. Some additional experimental details can also be found within each results chapter.

3.1 Sample preparation and cleaning

Copper and aluminium metal single crystals with (111) faces were used to perform the experiments described in this thesis. This section describes their preparation and cleaning prior to experiments.

3.1.1 Aluminium(111)

The aluminium(111) crystal used in these studies was prepared from a single crystal rod of aluminium. The methods of alignment by X-ray Laue diffraction and spark erosion were used to prepare a slice of the rod, with a (111) face front and back. The slice was then further processed by spark planing and polished by hand to a mirror finish using a series of decreasing sized diamond pastes (Hyprez) down to one micron grit size. The crystal was 15 mm in diameter and 2 mm thick.

The initial cleaning procedure in vacuum was carried out using argon ion bombardment, The chamber was filled to a pressure of $\sim 6 \times 10^{-5}$ Torr with argon (99.999 % pure, checked regularly by mass spectrometry), the ion-sputter gun was then operated (20 mA emission). The resultant argon ions were accelerated to 2 keV and directed normal to the surface, producing a drain current of between 3 and 8 μA for a period of one hour.

After bombardment the sample was heated to 493 K for annealing (the calculated anneal temperature, from one half of the melting point in Kelvin), After this initial cleaning cycle, AES showed that there was still large amounts of carbon and oxygen present on the surface and more importantly that the aluminium Auger was undetectable. Further cleaning cycles consisting of one hour argon ion bombardments, followed by annealing at 493 K, eventually reduced the carbon and oxygen contamination (but did not completely remove it) to allow the observation of the aluminium Auger peak. However, as shown in Figure 3.1a, the aluminium Auger peak was at a shifted energy of ~ 55 eV compared to the literature value for clean aluminium of 67 eV [3.1]. Further cleaning cycles caused the appearance of a second aluminium peak, this time at the expected energy of 67 eV, as shown in Figure 3.1b, with the initial peak moving to a slightly lower energy of ~ 54 eV. Many repeated cleaning cycles gradually reduced the height of the 54 eV peak, whilst the 67 eV peak continued to grow. Eventually, further cleaning produced no more changes in the spectrum, this is shown in Figure 3.1c. Once this aluminium Auger spectrum was produced, the oxygen and carbon contamination on the surface was also observed to have fallen. The oxygen peak was undetectable and a small carbon peak remained, approximately 0.1 % of the aluminium peak to peak height.

The 55 eV peak is the result of the interaction of oxygen with aluminium producing an Auger peak more characteristic of bulk aluminium oxide [3.2]. However, Figure 3.1c shows that even for the “clean” aluminium Auger spectrum there was still a lower energy peak. This is believed to be a plasmon loss peak, as the energy difference between the aluminium Auger and the low energy peak exactly matches one of the plasmon energies of aluminium [3.2].

Once the sample was adjudged clean by AES, the sample was not producing a LEED pattern. It was assumed that the anneal temperature of 493 K was therefore too low. The anneal temperature was gradually increased, until a

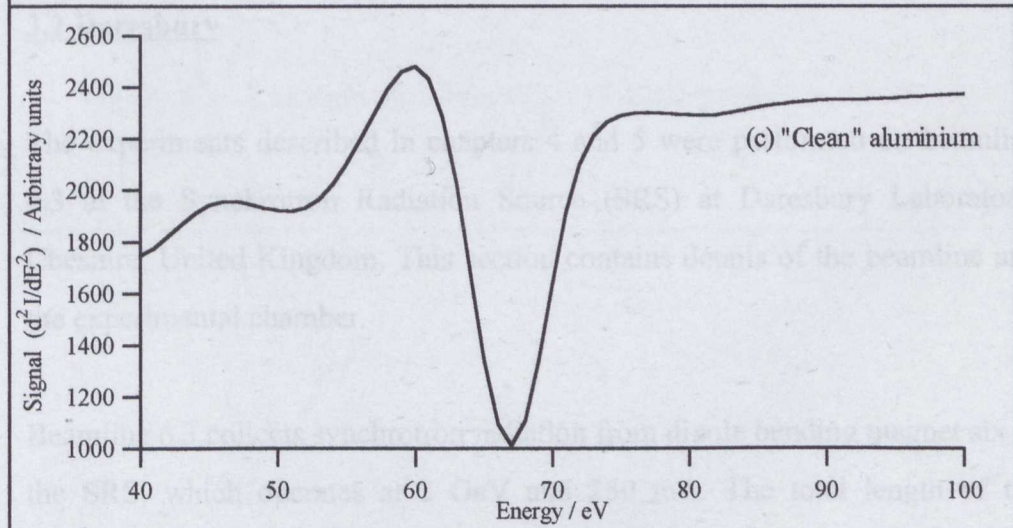
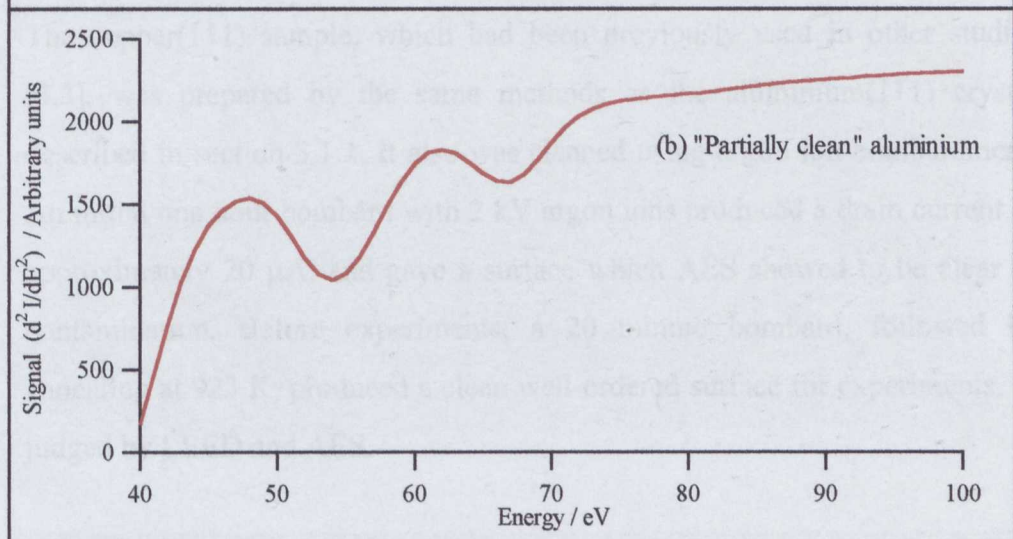
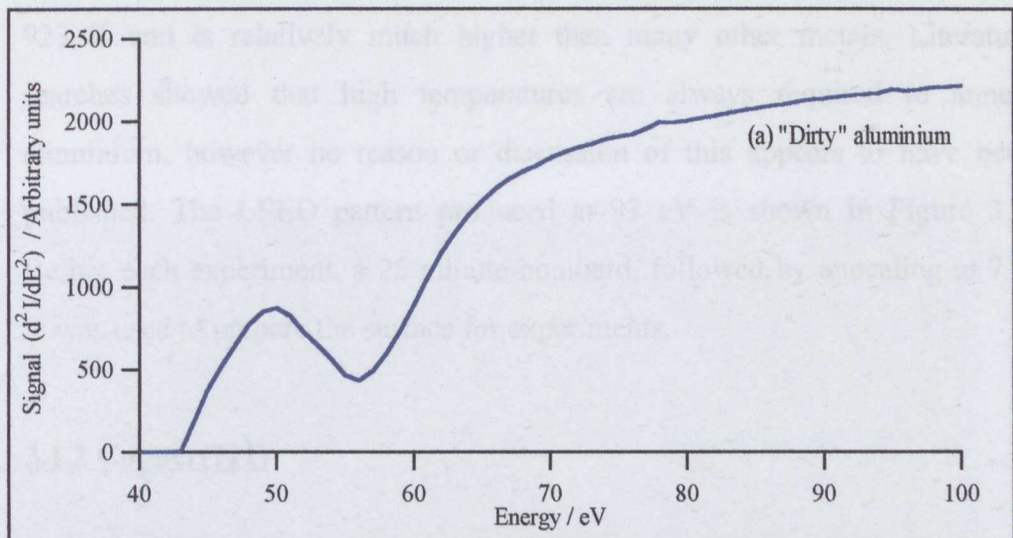


Figure 3.1 : Graphs showing Auger spectra for the aluminium(111) sample at various stages of cleaning

(1x1) LEED pattern was obtained. It was found that the optimum anneal temperature was 773 K. This is very close to the melting point of aluminium at 923 K and is relatively much higher than many other metals. Literature searches showed that high temperatures are always required to anneal aluminium, however no reason or discussion of this appears to have been published. The LEED pattern produced at 93 eV is shown in Figure 3.2. Before each experiment, a 25 minute bombard, followed by annealing at 773 K was used to prepare the surface for experiments.

3.1.2 Copper(111)

The copper(111) sample, which had been previously used in other studies [3.3], was prepared by the same methods as the aluminium(111) crystal described in section 3.1.1. It also was cleaned using argon ion bombardment. An initial one hour bombard with 2 kV argon ions produced a drain current of approximately 20 μ A, and gave a surface which AES showed to be clear of contamination. Before experiments, a 20 minute bombard, followed by annealing at 923 K, produced a clean well-ordered surface for experiments, as judged by LEED and AES.

3.2 Daresbury

The experiments described in chapters 4 and 5 were performed on beamline 6.3 at the Synchrotron Radiation Source (SRS) at Daresbury Laboratory, Cheshire, United Kingdom. This section contains details of the beamline and the experimental chamber.

Beamline 6.3 collects synchrotron radiation from dipole bending magnet six of the SRS, which operates at 2 GeV and 250 mA. The total length of the beamline is 16.5 m from source to sample. Figure 3.3 shows a schematic diagram of the beamline. Radiation passing along the beamline first enters the

filter rack, where two 2000 Å thick carbon filters remove the ultra-violet component of the beam. A set of horizontal and vertical beams defining the slit is situated before the toroidal pre-mirror. The mirror is made of fused quartz and is coated with gold. It reflects radiation from 5 mrad in the horizontal plane and



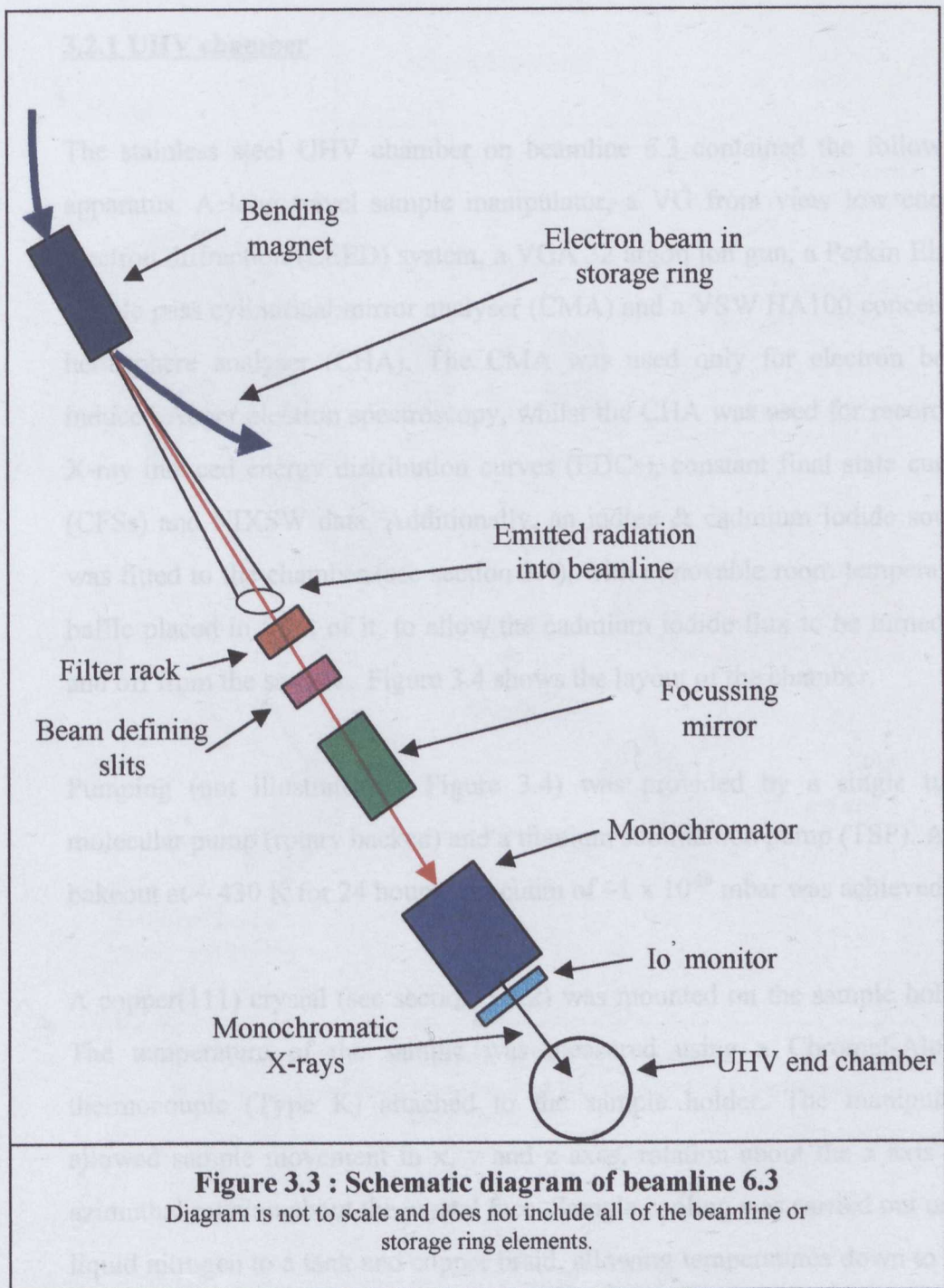
Figure 3.2 : Example aluminium(111) LEED pattern at 93 eV

The final section of the beamline before the UHV chamber is the beam monitoring section. Two parallel beam monitors could be used, either a thin aluminium foil (A) or an 80% transmission copper mesh (B). These experiments used the copper mesh. X-rays hitting the mesh caused electrons to be emitted, which were recorded directly as a dark signal using a photomultiplier. The output from the PMT amplifier was used as part of a feedback loop to control the monochromator. The readings from the beam current monitor was also used as part of the data monitoring procedure for NIXS.

filter rack, where ten 2000 Å thick carbon filters remove the ultra-violet component of the beam. A set of horizontal and vertical beam defining slits is situated before the toroidal pre-mirror. The mirror is made of fused quartz coated with gold, it accepts radiation from 5 mrad in the horizontal plane and 0.6 mrad in the vertical plane. Radiation is accepted at a grazing incidence of 0.5° , giving a high-energy cut-off of 11.1 keV. Focusing occurs in both horizontal and vertical planes, with a demagnification of the beam at the sample by two to one [3.4].

A double crystal monochromator is fitted on the beamline, which has been described in more detail previously [3.4,3.5]. It contains three pairs of crystals, InSb(111), Ge(220) and Ge(111), which could be exchanged in UHV using a linear motor drive. The maximum range of photon energies available was 1745 to 11000 eV. The experiments to be described used the Ge(111) crystal pair, providing a tuneable photon energy range of 2000 to 8430 eV. Both crystals could be rotated about their front faces, with the bottom crystal also having a translation motion, to provide a constant beam exit height from the monochromator into the experimental chamber. Water cooling of the top crystal was used, since the thermal load produced by the synchrotron beam would otherwise have compromised the performance of the monochromator [3.5]. All movements of the monochromator were controlled by the beamline PC.

The final section of the beamline before the UHV chamber is the beam monitoring section. Two possible beam monitors could be used, either a thin aluminium foil (I_0) or an 86% transmittance copper mesh (I_0'). These experiments used the copper mesh. X-rays hitting the mesh caused electrons to be emitted, which were recorded directly as a drain current using a picoammeter. The output from the I_0' monitor was used as part of a feed back loop to control the monochromator. The readings from the beam current monitor were also used as part of the data normalising procedure for NIXSW.



The beam defining apertures were set to ensure that the beam size was sufficiently small, so that only the sample was hit by the beam and not the surrounding sample holder.

3.2.1 UHV chamber

The stainless steel UHV chamber on beamline 6.3 contained the following apparatus. A long travel sample manipulator, a VG front view low energy electron diffraction (LEED) system, a VGA 32 argon ion gun, a Perkin Elmer double pass cylindrical mirror analyser (CMA) and a VSW HA100 concentric hemisphere analyser (CHA). The CMA was used only for electron beam induced Auger electron spectroscopy, whilst the CHA was used for recording X-ray induced energy distribution curves (EDCs), constant final state curves (CFSs) and NIXSW data. Additionally, an iodine & cadmium iodide source was fitted to the chamber (see section 3.4), with a movable room temperature baffle placed in front of it, to allow the cadmium iodide flux to be turned on and off from the sample. Figure 3.4 shows the layout of the chamber.

Pumping (not illustrated in Figure 3.4) was provided by a single turbo molecular pump (rotary backed) and a titanium sublimation pump (TSP). After bakeout at ~ 430 K for 24 hours, a vacuum of $\sim 1 \times 10^{-10}$ mbar was achieved.

A copper(111) crystal (see section 3.1.2) was mounted on the sample holder. The temperature of the sample was measured using a Chromel-Alumel thermocouple (Type K) attached to the sample holder. The manipulator allowed sample movement in x, y and z axes, rotation about the z axis and azimuthal rotation about the crystal face. Sample cooling was carried out using liquid nitrogen to a tank and copper braid, allowing temperatures down to 103 K to be reached. Sample heating was carried out using electron bombardment. The filaments mounted behind the sample plate were operated at 3 A and a high voltage bias of 300 V was applied to the sample.

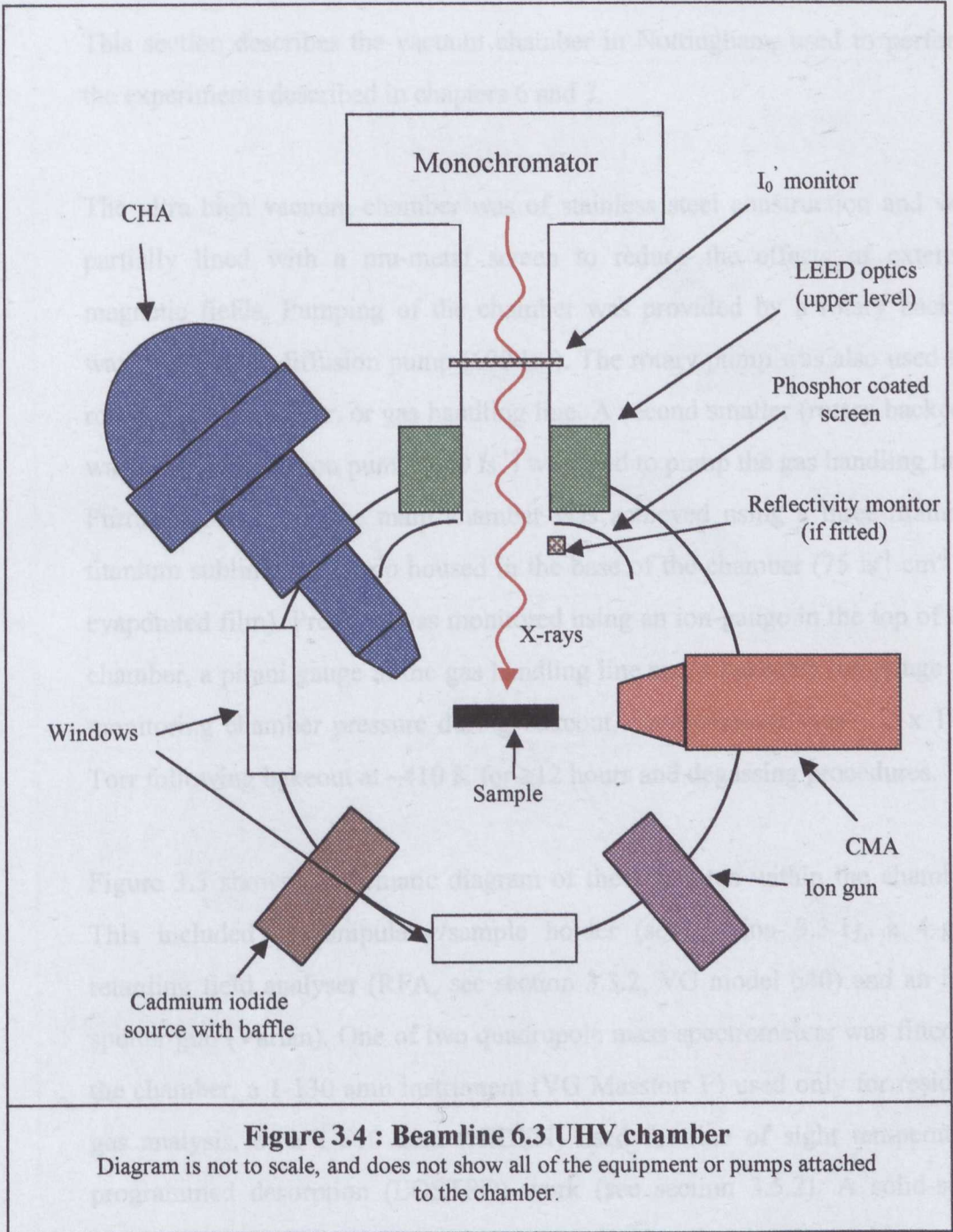


Figure 3.4 : Beamline 6.3 UHV chamber

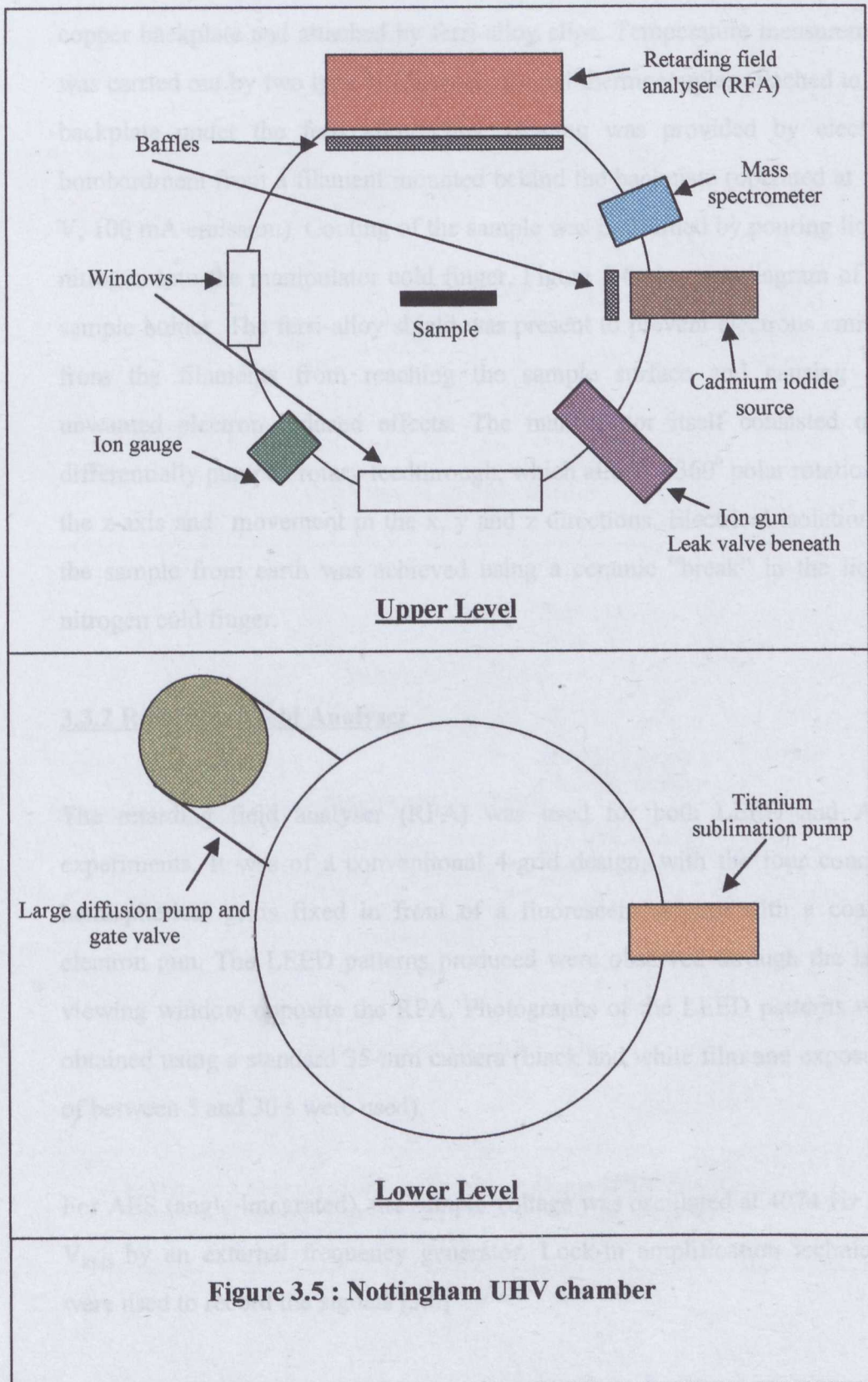
Diagram is not to scale, and does not show all of the equipment or pumps attached to the chamber.

3.3 Nottingham

This section describes the vacuum chamber in Nottingham, used to perform the experiments described in chapters 6 and 7.

The ultra high vacuum chamber was of stainless steel construction and was partially lined with a mu-metal screen to reduce the effects of external magnetic fields. Pumping of the chamber was provided by a rotary backed water cooled oil diffusion pump (600 ls^{-1}). The rotary pump was also used for roughing the chamber, or gas handling line. A second smaller (rotary backed), water cooled diffusion pump (150 ls^{-1}) was used to pump the gas handling line. Further pumping of the main chamber was achieved using a three-filament titanium sublimation pump housed in the base of the chamber ($75 \text{ ls}^{-1} \text{ cm}^{-2}$ of evaporated film). Pressure was monitored using an ion-gauge in the top of the chamber, a pirani gauge in the gas handling line and a bakeable ion-gauge for monitoring chamber pressure during bakeout. Base pressure was $\sim 2 \times 10^{-10}$ Torr following bakeout at $\sim 410 \text{ K}$ for ≥ 12 hours and degassing procedures.

Figure 3.5 shows a schematic diagram of the apparatus within the chamber. This included a manipulator/sample holder (see section 3.3.1), a 4-grid retarding field analyser (RFA, see section 3.3.2, VG model 640) and an ion-sputter gun (Varian). One of two quadrupole mass spectrometers was fitted to the chamber, a 1-130 amu instrument (VG Masstorr F) used only for residual gas analysis, or a 1-510 amu (HIDEN) used for line of sight temperature programmed desorption (LOSTPD) work (see section 3.5.2). A solid-state iodine source (see section 3.4) was also attached to the chamber, with a room temperature baffle placed in front of it. A baffle could also be positioned in front of the RFA.



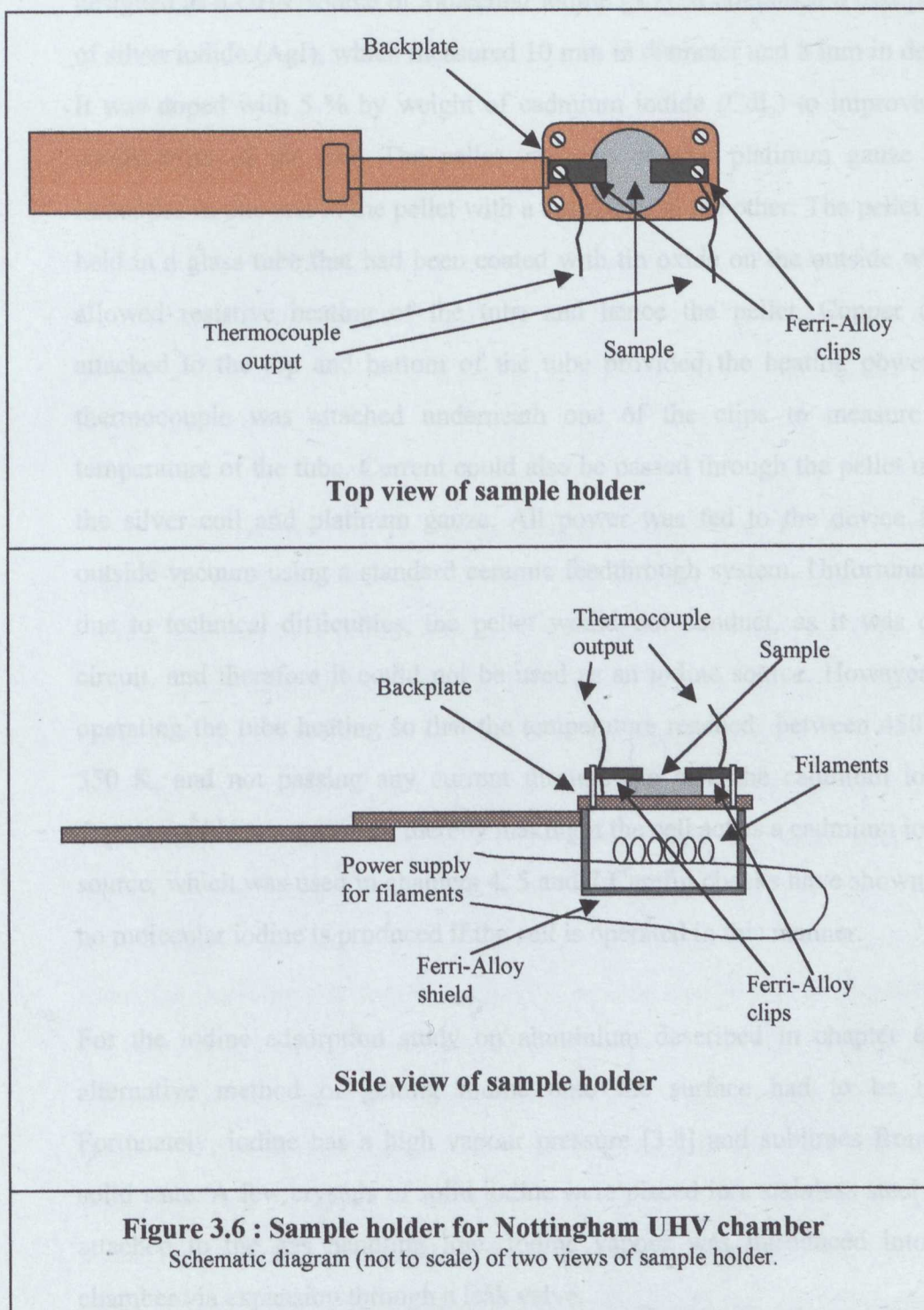
3.3.1 Sample holder

The sample, an aluminium(111) crystal (see section 3.1.1) was mounted on a copper backplate and attached by ferri-alloy clips. Temperature measurement was carried out by two type K Chromel-Alumel thermocouples attached to the backplate under the ferri alloy clips. Heating was provided by electron bombardment from a filament mounted behind the backplate (operated at 500 V, 100 mA emission). Cooling of the sample was performed by pouring liquid nitrogen into the manipulator cold finger. Figure 3.6 shows a diagram of the sample holder. The ferri-alloy shield was present to prevent electrons emitted from the filaments from reaching the sample surface and causing any unwanted electron induced effects. The manipulator itself consisted of a differentially pumped rotary feedthrough, which allowed 360° polar rotation in the z-axis and movement in the x, y and z directions. Electrical isolation of the sample from earth was achieved using a ceramic “break” in the liquid nitrogen cold finger.

3.3.2 Retarding Field Analyser

The retarding field analyser (RFA) was used for both LEED and AES experiments. It was of a conventional 4-grid design, with the four concave hemispherical grids fixed in front of a fluorescent screen, with a coaxial electron gun. The LEED patterns produced were observed through the large viewing window opposite the RFA. Photographs of the LEED patterns were obtained using a standard 35-mm camera (black and white film and exposures of between 5 and 30 s were used).

For AES (angle-integrated), the sample voltage was oscillated at 4074 Hz at 3 V_{RMS} by an external frequency generator. Lock-in amplification techniques were used to record the signals [3.6]



3.4 Adsorption sources

The main adsorption source used was a solid-state electrolysis device, designed as a UHV source of molecular iodine [3.7]. It contained a cast pellet of silver iodide (AgI), which measured 10 mm in diameter and 8 mm in depth. It was doped with 5 % by weight of cadmium iodide (CdI_2) to improve the conductivity of the cell. The pellet was cast so that platinum gauze was imbedded in one end of the pellet with a silver coil at the other. The pellet was held in a glass tube that had been coated with tin oxide on the outside which allowed resistive heating of the tube and hence the pellet. Copper clips attached to the top and bottom of the tube provided the heating power. A thermocouple was attached underneath one of the clips to measure the temperature of the tube. Current could also be passed through the pellet using the silver coil and platinum gauze. All power was fed to the device from outside vacuum using a standard ceramic feedthrough system. Unfortunately, due to technical difficulties, the pellet would not conduct, as it was open circuit, and therefore it could not be used as an iodine source. However, by operating the tube heating so that the temperature reached between 450 and 550 K, and not passing any current through the cell, the cadmium iodide dopant could be evaporated, thereby making it the cell act as a cadmium iodide source, which was used in chapters 4, 5 and 7. Careful checks have shown that no molecular iodine is produced if the cell is operated in this manner.

For the iodine adsorption study on aluminium described in chapter 6, an alternative method of getting iodine onto the surface had to be used. Fortunately, iodine has a high vapour pressure [3.8] and sublimes from the solid state. A few crystals of solid iodine were placed in a stainless steel tube attached to the gas handling line. Iodine vapour was introduced into the chamber via expansion through a leak valve.

3.5 Data acquisition

The aim of this section is to present an explanation of how some of the data presented in chapters 4 to 9 was collected and the methods by which it was processed. Some results chapters contain further details.

3.5.1 NIXSW

As described in section 2.6, it is necessary to record NIXSW data with respect to two sets of planes. With a (111) crystal the obvious choices are the (111) planes parallel to the surface and the ($\bar{1}11$) planes at 70.5° to the surface in the correct azimuth.

In order to set-up for NIXSW experiments, the sample was first positioned so that it was approximately normal to the X-ray beam (*i.e.* approximately in the correct place for (111) NIXSW). The photon energy was then set to be about 10 eV higher than that required for the Bragg condition. This meant that the reflected beam from the sample was directed back towards the beamline, but deflected ideally to the right of the beam entrance port, producing a spot on the phosphorescent screen mounted around the beam port. The exact position of the spot depends upon the azimuthal angle of the sample. The shape of the reflected spot should match that of the incident beam (see Figure 3.7) assuming the sample is well ordered. The photon energy was deliberately set above the Bragg energy to make sure that the spot appeared on this side, as the other side of the screen was blocked by the CHA. This set-up is illustrated in Figure 3.7. The sample position was altered carefully so that the reflected spot was maximised as close to the beam port as possible. To aid the sample positioning, the drain current from the screen was recorded and displayed on a meter, since maximising this signal generally produced the best reflected spot. The photon energy was gradually lowered and the sample position altered, until the reflected beam went straight back through the beam entrance port. In

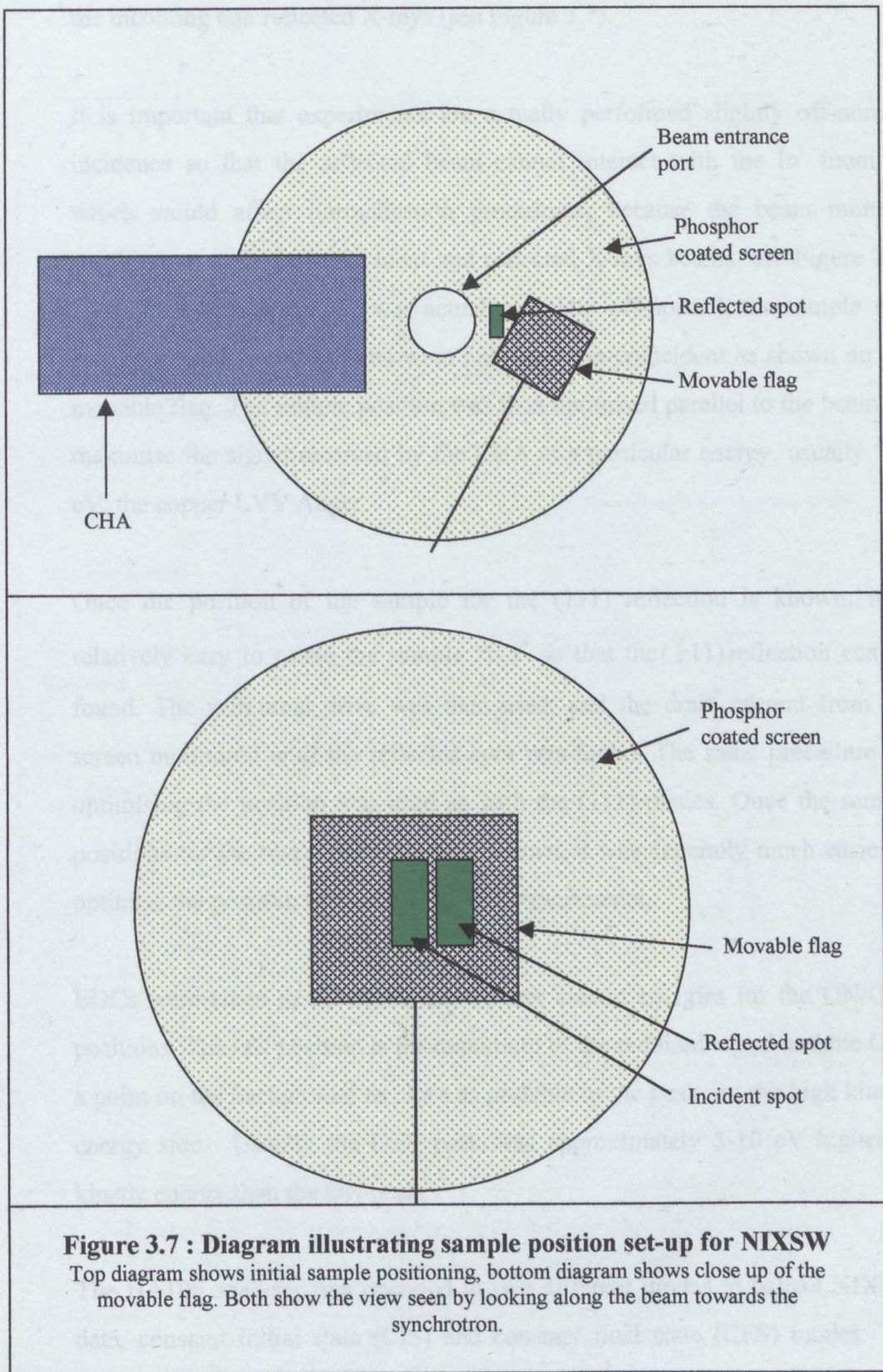


Figure 3.7 : Diagram illustrating sample position set-up for NIXSW

Top diagram shows initial sample positioning, bottom diagram shows close up of the movable flag. Both show the view seen by looking along the beam towards the synchrotron.

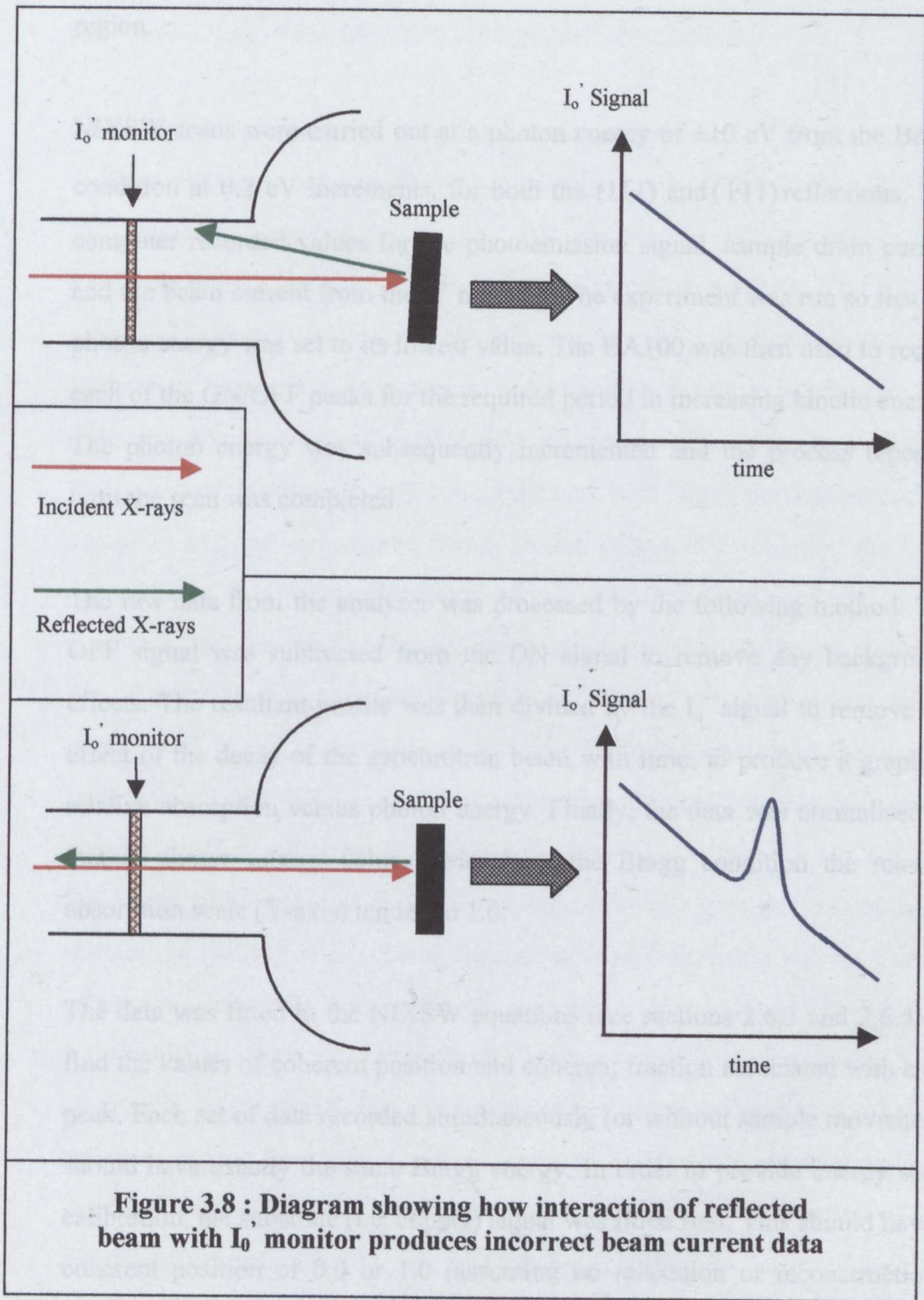
order to check that this was the case, a flag, made of nickel mesh coated in phosphor could be positioned in front of the beam to show the position of both the incoming and reflected X-rays (see Figure 3.7).

It is important that experiments are actually performed slightly off-normal incidence so that the reflected beam cannot interact with the Io' monitor, which would affect normalisation procedures, because the beam monitor would measure both the incident and reflected X-rays beams, see Figure 3.8. To ensure that the sample was actually slightly off-normal, the sample was rotated so that the two beams were only just non-coincident as shown on the movable flag. The sample position was then optimised parallel to the beam, to maximise the signal received by the CHA at a particular energy, usually 909 eV, the copper LVV Auger.

Once the position of the sample for the (111) reflection is known, it is relatively easy to rotate the sample 70.5° so that the $(\bar{1}11)$ reflection can be found. The azimuthal drive was then used, and the drain current from the screen monitored until the reflected spot was found. The same procedure for optimising the position was used as with the (111) planes. Once the sample positions for the two reflections were known, it was generally much easier to optimise the position for further NIXSW experiments.

EDCs were taken to determine the correct kinetic energies for the ON/OFF positions. The ON position is the maximum of the required signal and the OFF a point on the background as close as possible to the peak, on the high kinetic energy side. Usually the OFF peak was approximately 5-10 eV higher in kinetic energy than the ON peak.

The HA100 analyser was operated in two different modes to collect NIXSW data, constant initial state (CIS) and constant final state (CFS) modes. The CFS mode was used to record Auger signals, at a constant kinetic energy,



independent of the photon energy. CIS mode was used to record photoelectron NIXSW profiles, which have a constant binding energy. The binding energy of the peak was calculated from an EDC and the necessary kinetic energy tracked by the computer as the photon energy was scanned through the standing wave region.

NIXSW scans were carried out at a photon energy of ± 10 eV from the Bragg condition at 0.2 eV increments, for both the (111) and ($\bar{1}11$) reflections. The computer recorded values for the photoemission signal, sample drain current and the beam current from the I_0 ' monitor. The experiment was run so that the photon energy was set to its lowest value. The HA100 was then used to record each of the ON/OFF peaks for the required period in increasing kinetic energy. The photon energy was subsequently incremented and the process repeated until the scan was completed.

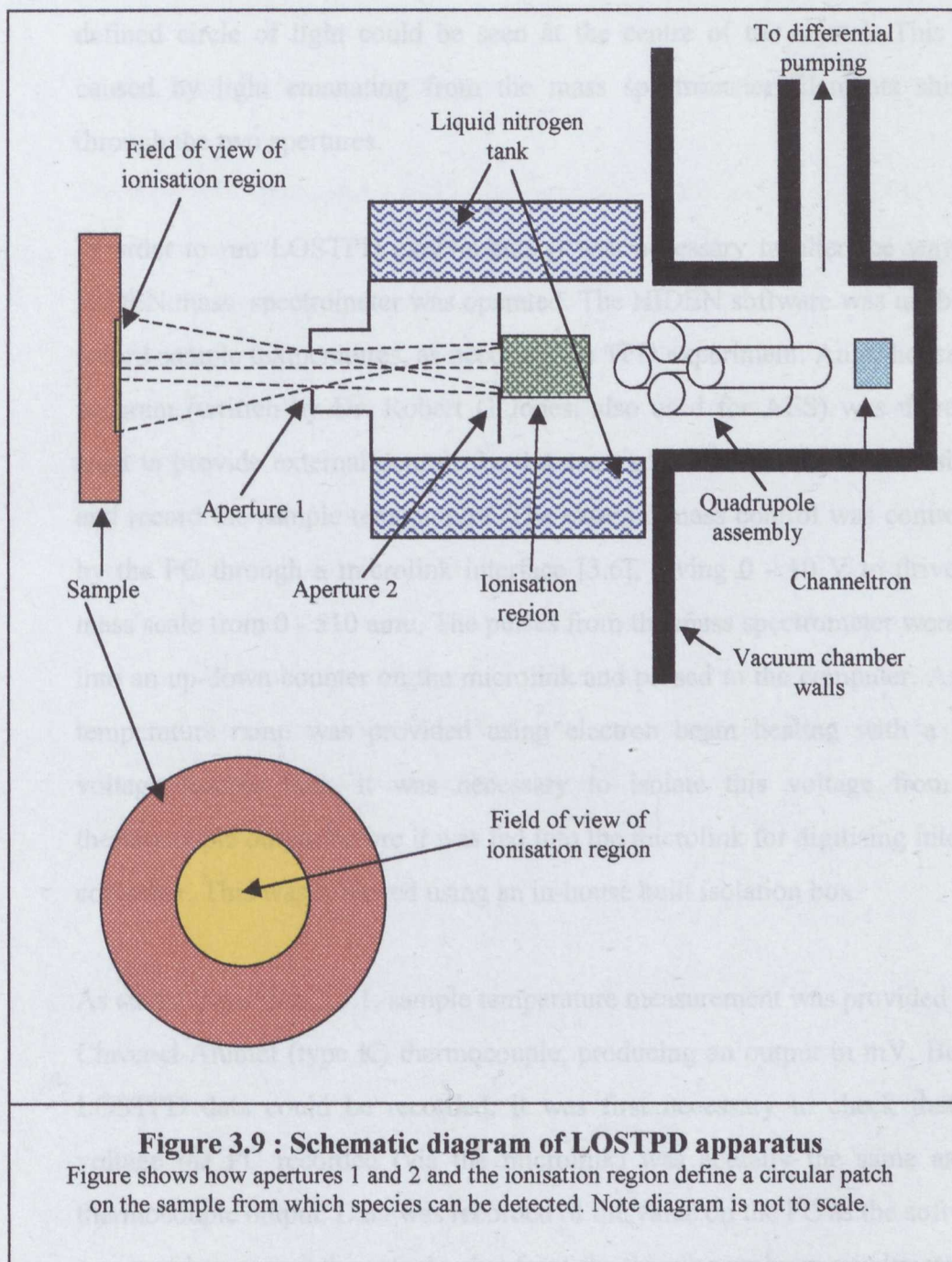
The raw data from the analyser was processed by the following method. The OFF signal was subtracted from the ON signal to remove any background effects. The resultant profile was then divided by the I_0 ' signal to remove the effect of the decay of the synchrotron beam with time, to produce a graph of relative absorption versus photon energy. Finally, the data was normalised so that at photon energy values away from the Bragg condition the relative absorption scale (Y-axis) tended to 1.0.

The data was fitted to the NIXSW equations (see sections 2.6.3 and 2.6.5) to find the values of coherent position and coherent fraction associated with each peak. Each set of data recorded simultaneously (or without sample movement) should have exactly the same Bragg energy. In order to provide energy scale calibration, the substrate (i.e. copper) signal was fitted first. This should have a coherent position of 0.0 or 1.0 (assuming no relaxation or reconstruction), thus, giving values of E_{Bragg} , σ (the instrumental energy broadening) and the coherent fraction for the copper. The values of E_{Bragg} and σ , were then used to

fit the adsorbate experimental data. All data fitting procedures were carried out using an Apple Macintosh running IGOR 3 and in-house procedures written by Dr. Robert G. Jones.

3.5.2 Line of sight temperature programmed desorption

Line of sight temperature programmed desorption (LOSTPD) experiments were carried out using a quadrupole mass spectrometer (HIDEN HAL RC 511 PIC, capable of measuring $1 < m/z < 510$, operated in pulse counting mode, with a detection limit of $\sim 10^{-14}$ Torr), situated at 90° to the RFA. The HIDEN mass spectrometer was added to the chamber later than the diagram shown in Figure 3.5, it replaced the cadmium iodide source shown in the Figure. The mass spectrometer was surrounded with a copper nozzle, which was attached to a large tank (see Figure 3.9). Filling the tank with liquid nitrogen caused the nozzle to become a cryogenic pump, so that only species entering the mass spectrometer from a circular patch of the sample surface (defined by the geometry, and the sizes of the apertures) could reach the ionisation region of the mass spectrometer and be detected (see Figure 3.9). Apertures 1 and 2 were 3 and 6 mm in diameter respectively with distances from the sample surface of 57 and 167 mm. A species emanating from anywhere outside the circular patch would either fail to enter the mass spectrometer or it would hit the nitrogen cooled copper tank and effectively be pumped, assuming a sticking probability of 1.0. Some species, such as hydrogen, methane, carbon monoxide and noble gases are not effectively pumped by this method, however they were not of experimental interest so this is not important. If the alignment was correct, this set-up provided excellent spatial resolution, because only species desorbing from an area $\sim 1/10$ of the sample could be detected. Any species desorbing from the backplate or other areas of the sample holder would not be able to reach the detector. To determine that the sample manipulator was lined up correctly with the nozzle and the mass spectrometer, the following procedure was used. The mass spectrometer was



set to degas mode, thus producing brightly glowing filaments. The ion-gauge was turned off. Then using an image intensifier through an appropriate window, the sample was viewed. When it was in the correct position, a clearly defined circle of light could be seen at the centre of the crystal. This was caused by light emanating from the mass spectrometer filaments shining through the two apertures.

In order to run LOSTPD experiments it was necessary to alter the way the HIDEN mass spectrometer was operated. The HIDEN software was unable to record sample temperatures, as needed for a TPD experiment. An in house PC program (written by Dr. Robert G Jones, also used for AES) was therefore used to provide external control for the mass spectrometer, collect the signal and record the sample temperature. The external mass control was controlled by the PC through a microlink interface [3.6], giving 0 - 10 V to drive the mass scale from 0 - 510 amu. The pulses from the mass spectrometer were fed into an up-down counter on the microlink and passed to the computer. As the temperature ramp was provided using electron beam heating with a high voltage sample bias, it was necessary to isolate this voltage from the thermocouple output before it was fed into the microlink for digitising into the computer. This was achieved using an in-house built isolation box.

As stated in section 3.3.1, sample temperature measurement was provided by a Chromel-Alumel (type K) thermocouple, producing an output in mV. Before LOSTPD data could be recorded, it was first necessary to check that the voltage the PC recorded (via the microlink) was actually the same as the thermocouple output. Data was recorded of the value on the PC as the software was running, versus the actual value from the thermocouple on a voltmeter, as the sample was cooled or heated. The data was used to alter the analogue to digital conversion equation within the PC software to make the sure that the values for the thermocouple output were correct.

The LOSTPD apparatus was also used to perform a new experiment for determining sticking probabilities which has been termed Line Of Sight Sticking Probability (LOSSP), this will be explained in detail in chapter 6.

3.5.3 Auger electron spectroscopy

For the results in chapter 6 and 7, the sensitivity of the lock-in-amplifier had to be altered according to the Auger transition being followed. This was set at 10 μV for the cadmium and iodine Augers, but this had to be reduced to 500 μV for the aluminium peak, because of the size of the peak and the sloping background. This implies that the values for the aluminium peak-to-peak heights quoted and plotted on the figures are actually a factor of 50 lower than reality. The aluminium peak-to-peak heights were calculated from the height at 60 eV minus the height at 67 eV and then corrected for the sloping baseline, which was taken from a saturated surface from which no aluminium Auger peak was detectable (see Figure 3.10). The cadmium and iodine peak-to-peak heights were simply calculated from the maximum and minimum heights, because the background was flat for these peaks.

Normal Incidence X-ray Standing Wave experiments :

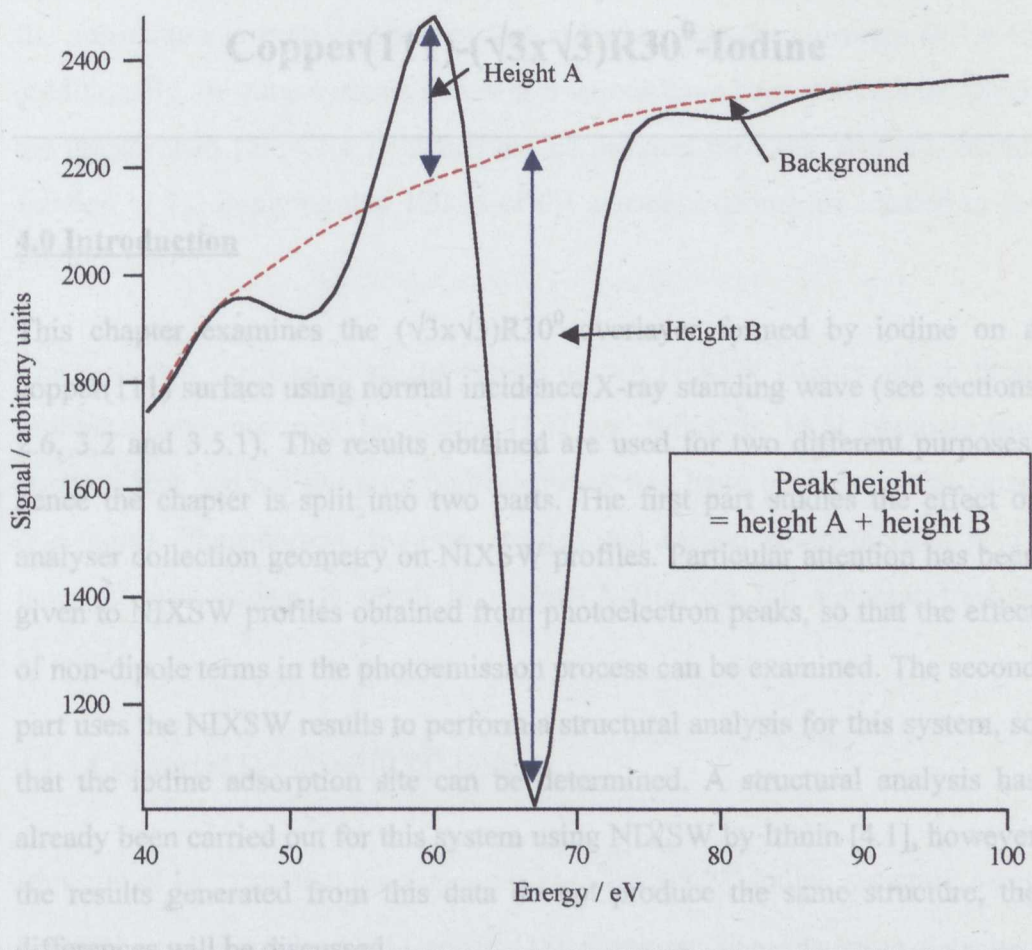


Figure 3.10 : Diagram illustrating calculation of aluminium Auger peak-to-peak height

Part 1 : Non-dipole photoemission and NLXSW

4.1 Introduction

This part of the chapter presents a NLXSW study of the $(\sqrt{3} \times \sqrt{3})R30^\circ$ structure formed by iodine on the copper(111) surface, focussing on a problem experienced with fitting the NLXSW data obtained from photoelectron peaks. The fitting of NLXSW data is generally regarded as straightforward, with the structural parameters generated, the coherent position and coherent fraction

Chapter 4 : Non-dipole photoemission and Normal Incidence X-ray Standing Wave experiments : Copper(111)-($\sqrt{3}\times\sqrt{3}$)R30⁰-Iodine

4.0 Introduction

This chapter examines the ($\sqrt{3}\times\sqrt{3}$)R30⁰ overlayer formed by iodine on a copper(111) surface using normal incidence X-ray standing wave (see sections 2.6, 3.2 and 3.5.1). The results obtained are used for two different purposes, hence the chapter is split into two parts. The first part studies the effect of analyser collection geometry on NIXSW profiles. Particular attention has been given to NIXSW profiles obtained from photoelectron peaks, so that the effect of non-dipole terms in the photoemission process can be examined. The second part uses the NIXSW results to perform a structural analysis for this system, so that the iodine adsorption site can be determined. A structural analysis has already been carried out for this system using NIXSW by Ithnin [4.1], however the results generated from this data do not produce the same structure, the differences will be discussed.

Part 1 : Non-dipole photoemission and NIXSW

4.1 Introduction

This part of the chapter presents a NIXSW study of the ($\sqrt{3}\times\sqrt{3}$)R30⁰ structure formed by iodine on the copper(111) surface, focussing on a problem experienced with fitting the NIXSW data obtained from photoelectron peaks. The fitting of NIXSW data is generally regarded as straightforward, with the structural parameters generated, the coherent position and coherent fraction

(see section 2.6.5), being treated as absolute. However, there have been a number of systems reported where the data does not appear to fit correctly [4.1-4.5]. The most serious problems have occurred when trying to fit NIXSW profiles obtained from photoelectrons. In some systems a coherent fraction for the adsorbate has been determined that is higher than the substrate [4.1,4.4]. Additionally, in some systems coherent fractions have been determined which are greater than 1.0 [4.1,4.3], which has no physical meaning, with a coherent fraction of 1.2 implying that 120 % of the adsorbate atoms are located in the same place!

The next two sections detail the results of two NIXSW studies where these problems have occurred for iodine [4.1] and tellurium [4.5] photoelectron peaks. These are not the only photoelectrons that have been shown to cause difficulties. Phosphorous, fluorine, oxygen and carbon photoemission peaks have all been shown to result in unusual values for the coherent fraction [4.2,4.3].

4.1.1 Copper(111)-($\sqrt{3}\times\sqrt{3}$)R30⁰-Iodine

Ithnin et al [4.1] studied the copper(111)-($\sqrt{3}\times\sqrt{3}$)R30⁰-Iodine structure using NIXSW, recording the (111) and ($\bar{1}11$) reflections. The adsorbate data was collected using the iodine MNN Auger, 3p_{3/2} and 3d_{5/2} photoelectrons. However, fitting of the iodine data produced very different values for the NIXSW structural parameters depending upon which iodine peak was used. Ithnins (111) data is shown in Table 4.1. It shows that the coherent position obtained for the iodine from each of the peaks was essentially the same. However, the coherent fractions differ, with the iodine 3d_{5/2} coherent fraction being greater than 1.0. Ithnins ($\bar{1}11$) results are also shown in Table 4.1. The iodine 3d_{5/2} peak again has a coherent fraction that does not agree with that obtained from the iodine MNN Auger. Table 4.1, shows that the value is approximately half that of the Auger peak. Also there is a greater spread in the values obtained for the coherent position.

Peak	(111)		$(\bar{1}11)$	
	Coherent position (± 0.05)	Coherent fraction (± 0.05)	Coherent position (± 0.05)	Coherent fraction (± 0.05)
Iodine Auger	1.048	0.762	0.795	0.457
Iodine 3p _{3/2}	1.070	0.611	0.836	0.400
Iodine 3d _{5/2}	1.071	1.064	0.778	0.214

Table 4.1: Summary of NIXSW results by Ithnin [4.1], from Copper(111)-($\sqrt{3}\times\sqrt{3}$)R30⁰-Iodine, for the (111), and $(\bar{1}11)$ reflections

4.1.2 Gallium Arsenide(001)-(2x1)-Tellurium

Sugiyama and Maeyama [4.5] studied the adsorption of tellurium on a gallium arsenide (001) surface using chemical state resolved NIXSW [4.2]. A GaAs(001) wafer was placed in a molecular beam epitaxy chamber, where it was annealed under an arsenic flux to remove impurities. Gallium arsenide was grown homo-epitaxially on the arsenic stabilised surface. Several monolayers of tellurium were then deposited, which after annealing produced a (2x1) reconstructed GaAs(001)-Tellurium surface. NIXSW data was recorded for the $(\bar{1}11)$ and (111) normal incidence Bragg reflection conditions at ~ 1.9 keV. The tellurium standing wave was monitored using the 3d_{5/2} photoelectron peak. As this was a chemical state resolved study, instead of simply recording the ON/OFF positions as described in section 3.5.1, an EDC was taken across the tellurium 3d_{5/2} photoemission peak for each photon energy in the NIXSW scan [4.2]. Each EDC was then fitted to generate two separate peaks, which were considered to be the result of tellurium atoms adsorbed in different sites. Each separate EDC was fitted to generate the NIXSW parameters for each of the chemically shifted Te atoms (peaks A and B). Table 4.2 shows a summary of these results.

NIXSW Signal	(111)		(-111)	
	Coherent position	Coherent fraction	Coherent position	Coherent fraction
Total Te 3d _{5/2} Signal	0.950 ± 0.002	0.813 ± 0.009	0.221 ± 0.002	0.80 ± 0.02
Te Peak A	0.923 ± 0.002	0.872 ± 0.008	0.175 ± 0.006	0.92 ± 0.04
Te Peak B	0.002 ± 0.007	0.780 ± 0.002	0.309 ± 0.009	0.78 ± 0.06

Table 4.2 Summary of Gallium Arsenide(001)-(2x1)-Tellurium results of Sugiyama et al [4.5]

It is immediately clear from Table 4.2, that the total ($\bar{1}11$) tellurium 3d_{5/2} photoelectron profile gives a coherent fraction that is fairly high and would be consistent with single site occupation (see section 2.6.5). However, it was stated that there were two types of tellurium atoms, because the Te 3d_{5/2} photoelectron peak could be separated into two chemically shifted peaks. These tellurium atoms are probably bound in different locations, with different interactions with the gallium arsenide substrate, hence producing the chemically shifted tellurium photoelectron peaks. It was shown in section 2.6.5, that multiple site adsorption should lead to a reduction in coherent fraction in at least one plane, depending upon the sites involved. The coherent positions quoted in Table 4.2, show that the atoms are not located in similar places, therefore the ($\bar{1}11$) coherent fractions should be much lower. The reason that the values are too high, is probably the same reason as for the iodine 3d_{5/2} peak in section 4.1.1. Tellurium is in the same row of the periodic table and adjacent to iodine, therefore suggesting that NIXSW profile shapes are sensitive to some atomic property.

4.2 Dipole approximation and NIXSW

NIXSW profiles are often recorded by following the emission of photoelectrons from the surface to be studied, usually because the relevant Auger electrons are either unavailable (because of overlap with other peaks), or are too weak. The experimental set-up used (see section 3.2) was such that the analyser was angle resolving. This meant that any physical effects which altered the angular distribution of the emitted electrons from the sample would affect the NIXSW profile. Angle resolved photoemission has been used for many years to provide tests of basic physical processes, in both gas phase and solid-state interactions with radiation [4.6]. In order to understand and simulate the data collected by these experiments, a theory was developed called the dipole approximation for photoemission [4.7]. This allowed easy characterisation and quantification of behaviour, as a function of electron ejection angle. The electromagnetic field of the incident radiation, is typically expressed as $\exp(i\mathbf{k}\cdot\mathbf{r})$ (\mathbf{k} is the photon wavevector and \mathbf{r} the electron position vector). In the dipole approximation, this is expanded as, $1 + i\mathbf{k}\cdot\mathbf{r} + \dots$ etc and then truncated so that $\exp(i\mathbf{k}\cdot\mathbf{r}) = 1$. In physical terms this means that higher order terms, such as those due to electric-quadrupole and magnetic-dipole interactions are neglected.

The dipole approximation was first applied to angle resolved experiments when relatively low photon energies were used, typically ultra-violet radiation from a helium lamp. In this situation the dipole approximation is based on two physical assumptions. The first is that the photoelectron velocities following ultra-violet excitation are small compared to the speed of light, therefore removing any relativistic effects. The second is that the wavelength of the ionising radiation is much larger than the size of the orbitals from which the electrons are ejected, thus removing any higher order effects from the photoemission. In recent years the photon energies available for experiments have greatly increased with the wider availability of second and third generation synchrotron sources, providing anything from 1 eV to 100 keV photon beams [4.8]. However, as the photon energy is increased past the ultra-

violet level, there is a point where these assumptions fail. This means that the dipole approximation is no longer valid, because the higher order terms start to affect photoemission behaviour. (Note that relativistic effects are not important for the experiments described in this thesis at photon energies of 3 keV.)

In order to test whether non-dipole effects are the cause of the problems associated with photoelectron detection of NIXSW profiles, a novel experiment was performed. Data was collected for the (111) and ($\bar{1}11$) reflections from the copper(111)-($\sqrt{3}\times\sqrt{3}$)R30⁰-Iodine surface, in two analyser geometries. The first had the analyser in its usual position of 40⁰ to the X-ray beam, the second had it at 90⁰ to the X-ray beam. Comparison of the two data sets allowed any possible non-dipole effects to be studied.

4.3 Experimental methods

These experiments were performed on beamline 6.3 of the SRS at Daresbury laboratory, the experimental set-up is explained in section 3.2.

In order to form the required ($\sqrt{3}\times\sqrt{3}$)R30⁰ iodine surface structure, a cadmium iodide multilayer was formed and then annealed to crack it into the iodine monolayer surface structure, as shown in a previous study [4.1,4.9]. After sample annealing, when the sample temperature had fallen below ~ 333 K, the baffle was opened to the cadmium iodide source, which had been previously heated to 523 K. Cadmium iodide was deposited onto the clean copper(111) surface for ~ 45 minutes, thus producing the required multilayer. Annealing this surface to 200⁰C for ~ 2 minutes caused the cadmium iodide multilayer to decompose and both cadmium metal and excess cadmium iodide to desorb, leaving a monolayer of iodine in a ($\sqrt{3}\times\sqrt{3}$)-R30⁰ structure, as confirmed by LEED. Electron induced AES gave an I:Cu peak-to-peak height ratio of ~ 0.33:1, as expected for the monolayer iodine structure [4.1,4.9].

A wide range EDC (Figure 4.1) using a photon energy of 3000 eV shows the species present on the surface. Higher resolution EDCs over each peak (see

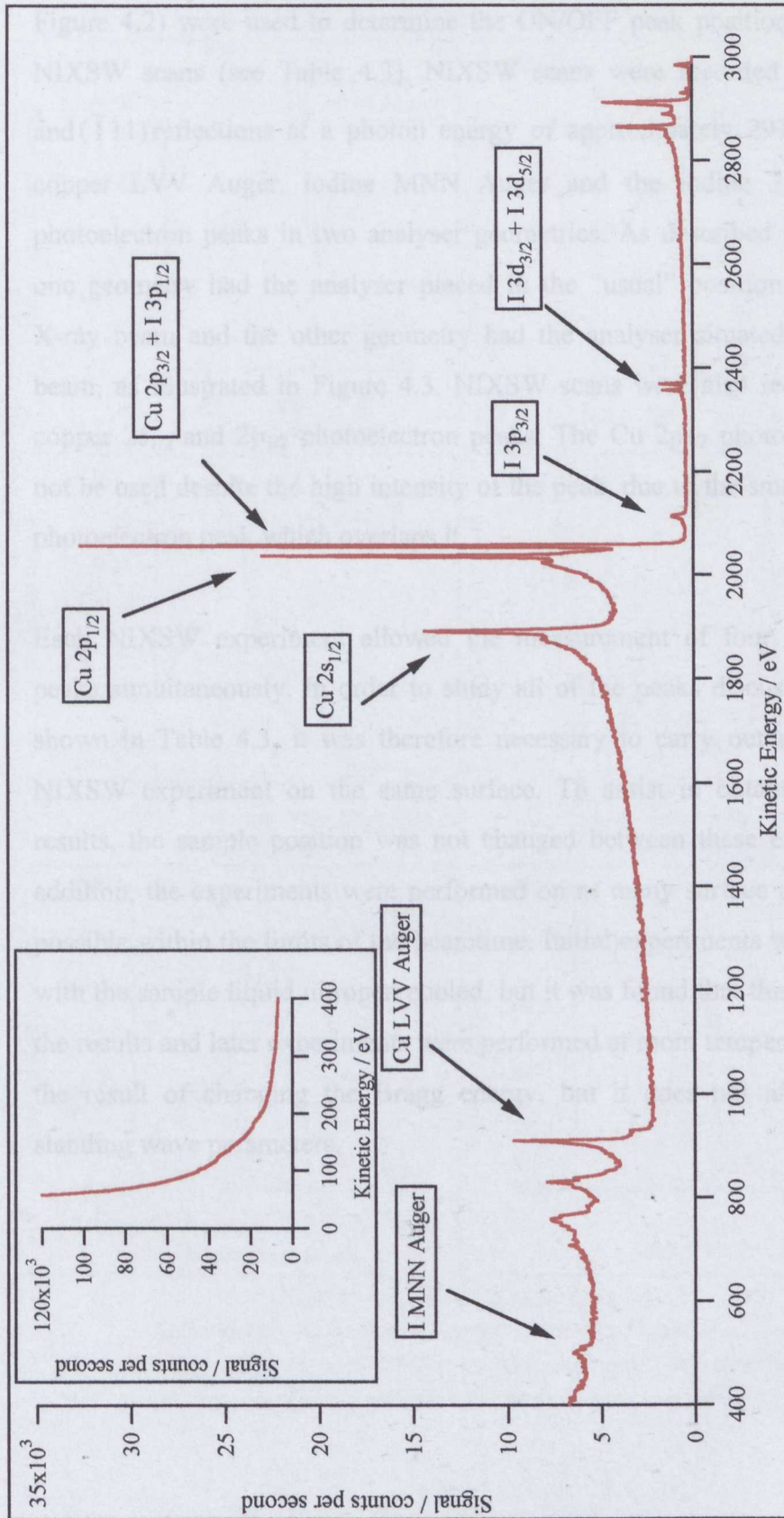


Figure 4.1 : Wide range EDC

EDC at a photon energy of 3000 eV. Scan at 2 eV increments, with 1 second counting time. Inset shows 55-400 eV range. Relevant peaks are labelled.

Figure 4.2) were used to determine the ON/OFF peak positions required for NIXSW scans (see Table 4.3). NIXSW scans were recorded for the (111) and $(\bar{1}11)$ reflections at a photon energy of approximately 2976 eV, for the copper LVV Auger, iodine MNN Auger and the iodine $3p_{3/2}$ and $3d_{5/2}$ photoelectron peaks in two analyser geometries. As described in section 4.2, one geometry had the analyser placed in the “usual” position of 40° to the X-ray beam and the other geometry had the analyser situated at 90° to the beam, as illustrated in Figure 4.3. NIXSW scans were also recorded for the copper $2s_{1/2}$ and $2p_{1/2}$ photoelectron peaks. The Cu $2p_{3/2}$ photoelectron could not be used despite the high intensity of the peak, due to the small iodine $3p_{1/2}$ photoelectron peak which overlaps it.

Each NIXSW experiment allowed the measurement of four photoemission peaks simultaneously. In order to study all of the peaks discussed above and shown in Table 4.3, it was therefore necessary to carry out more than one NIXSW experiment on the same surface. To assist in obtaining consistent results, the sample position was not changed between these experiments. In addition, the experiments were performed on as many surface preparations as possible within the limits of the beamtime. Initial experiments were performed with the sample liquid nitrogen cooled, but it was found that this did not affect the results and later experiments were performed at room temperature. This has the result of changing the Bragg energy, but it does not affect the other standing wave parameters.

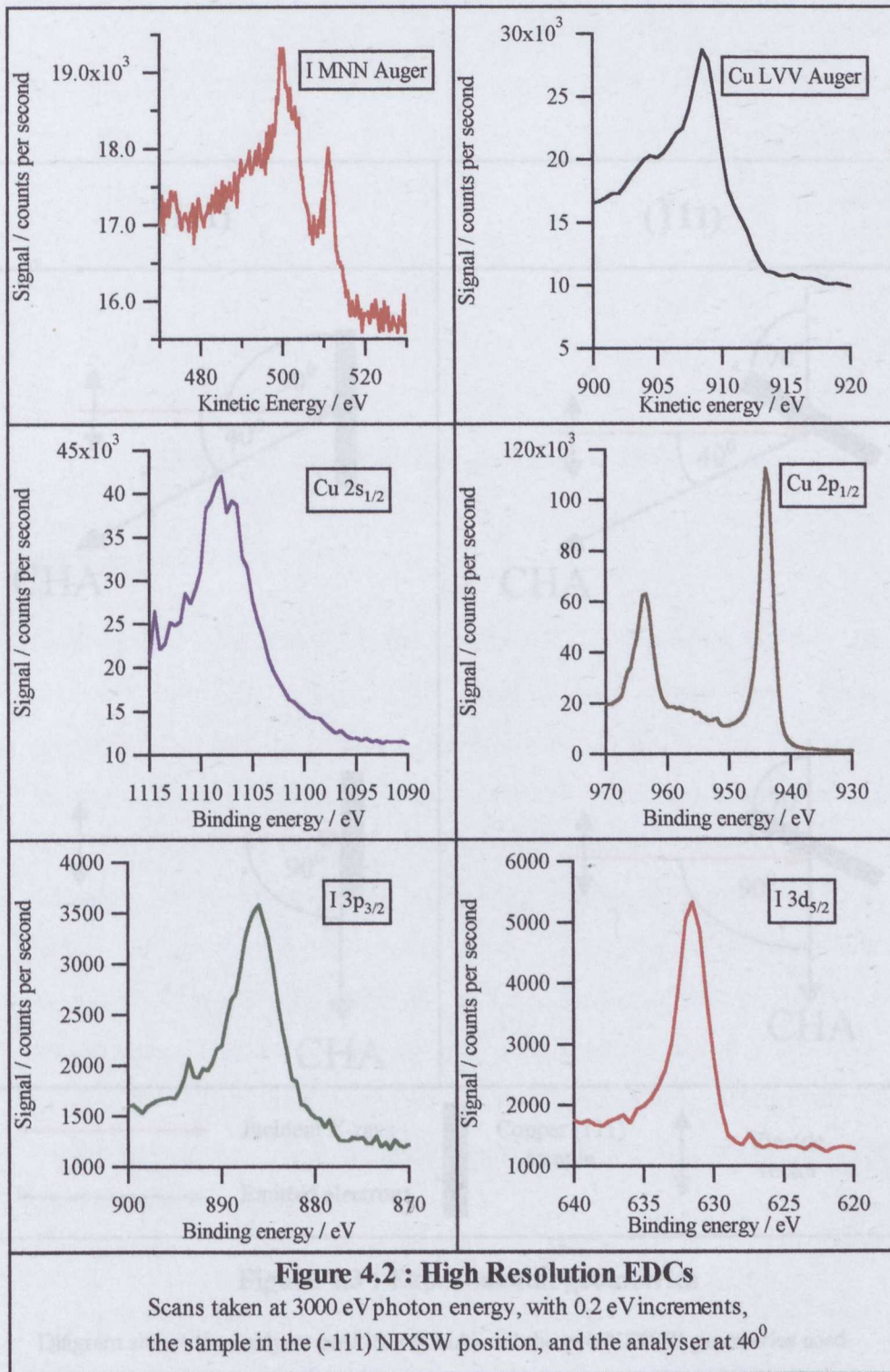
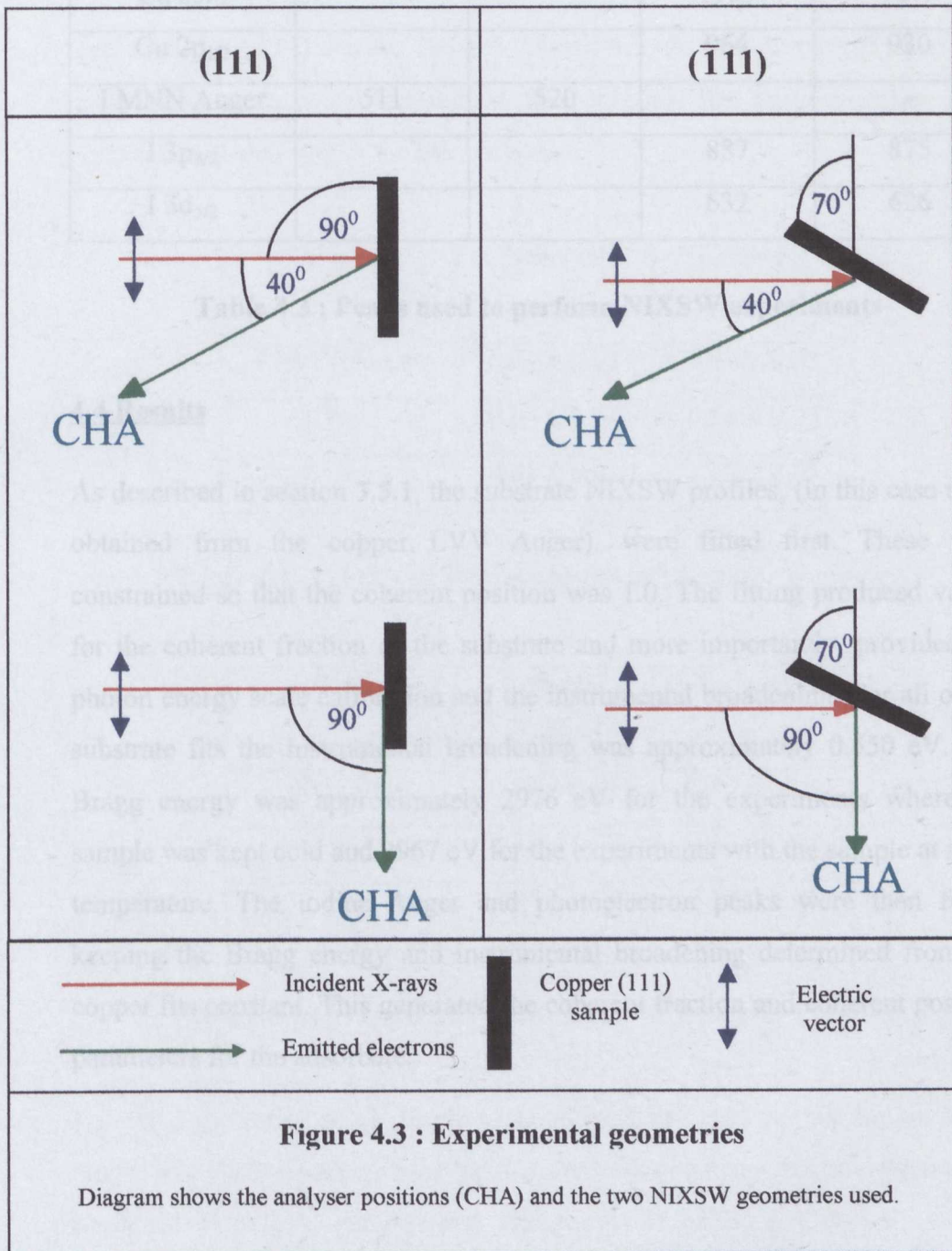


Figure 4.2 : High Resolution EDCs

Scans taken at 3000 eV photon energy, with 0.2 eV increments, the sample in the (-111) NIXSW position, and the analyser at 40°



Peak	Auger energy / eV		Binding energy / eV	
	ON	OFF	ON	OFF
Cu LVV Auger	909	919	-	-
Cu 2s _{1/2}	-	-	1108	1075
Cu 2p _{1/2}	-	-	964	930
I MNN Auger	511	520	-	-
I 3p _{3/2}	-	-	887	875
I 3d _{5/2}	-	-	632	626

Table 4.3 : Peaks used to perform NIXSW experiments

4.4 Results

As described in section 3.5.1, the substrate NIXSW profiles, (in this case those obtained from the copper LVV Auger), were fitted first. These were constrained so that the coherent position was 1.0. The fitting produced values for the coherent fraction of the substrate and more importantly, provided the photon energy scale calibration and the instrumental broadening. For all of the substrate fits the instrumental broadening was approximately 0.550 eV. The Bragg energy was approximately 2976 eV for the experiments where the sample was kept cold and 2967 eV for the experiments with the sample at room temperature. The iodine Auger and photoelectron peaks were then fitted, keeping the Bragg energy and instrumental broadening determined from the copper fits constant. This generated the coherent fraction and coherent position parameters for the adsorbate.

4.4.1 40⁰-geometry

The results with the analyser in its “usual” 40⁰ position for the iodine peaks are shown in Tables 4.4 and 4.5. Table 4.4 contains the (111) reflection results and Table 4.5 the ($\bar{1}11$) results. Figures 4.4 and 4.5, show examples of the iodine experimental data, superimposed on the theoretical fits. Sample copper LVV Auger data is also shown for comparison.

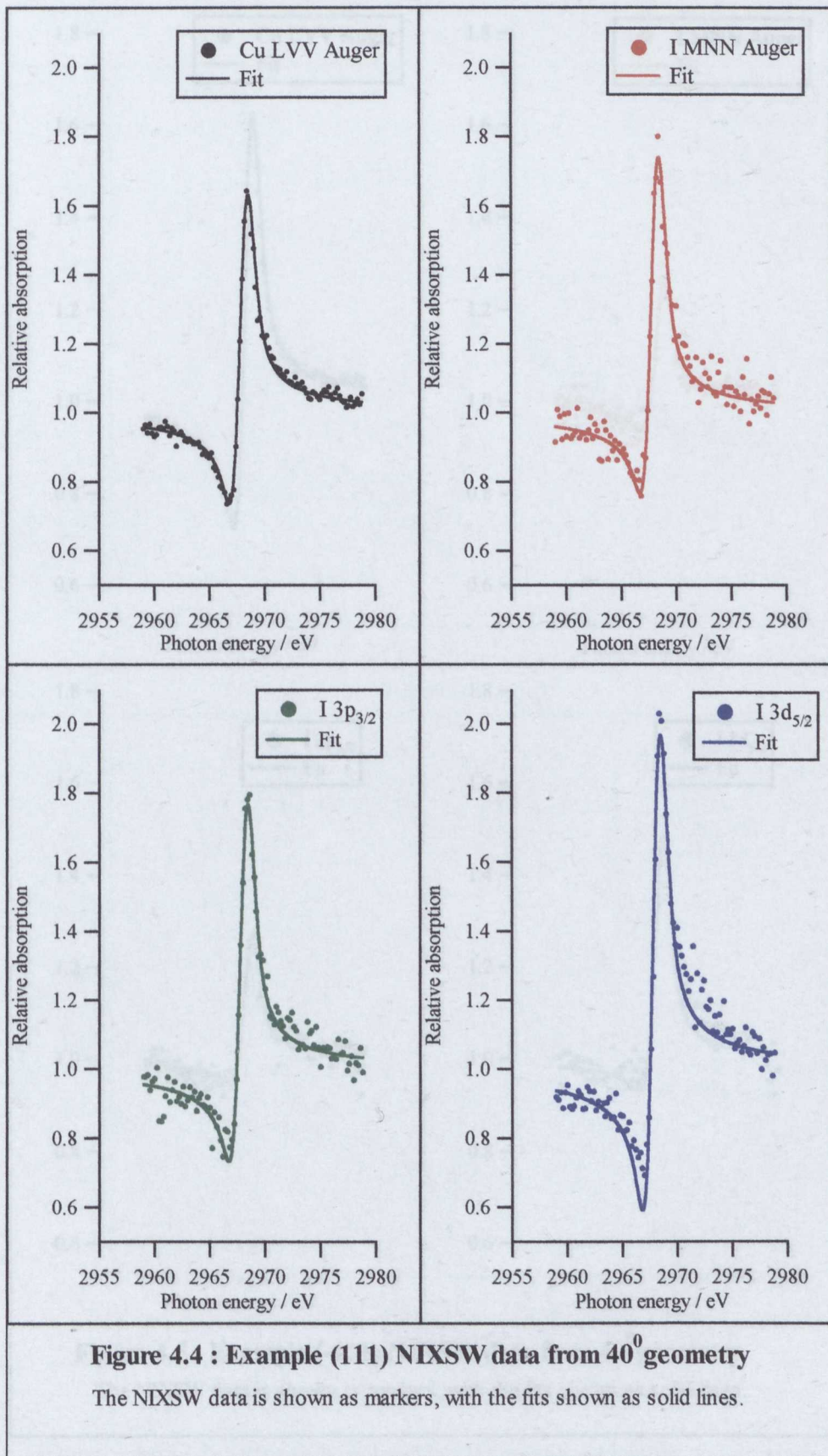
Peak	Coherent position	Coherent Fraction
I MNN Auger	0.04 ± 0.02	0.77 ± 0.05
I 3p _{3/2}	0.04 ± 0.02	0.89 ± 0.05
I 3d _{5/2}	0.05 ± 0.02	1.25 ± 0.05

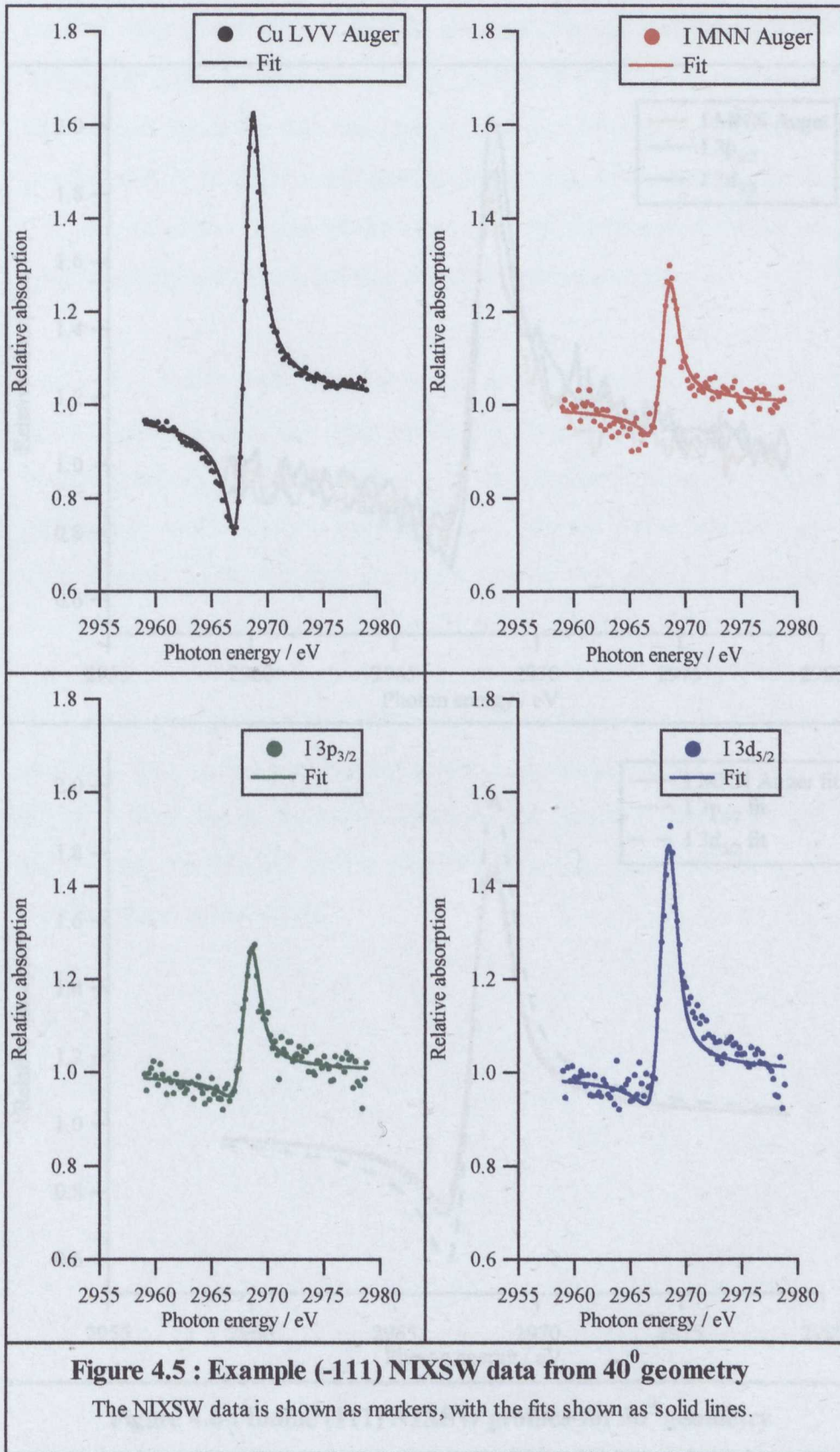
Table 4.4 : (111) NIXSW results for 40⁰ analyser geometry

Peak	Coherent position	Coherent Fraction
I MNN Auger	0.89 ± 0.02	0.43 ± 0.05
I 3p _{3/2}	0.88 ± 0.02	0.40 ± 0.05
I 3d _{5/2}	1.01 ± 0.02	0.38 ± 0.05

Table 4.5 : ($\bar{1}11$) NIXSW results for 40⁰ analyser geometry

As stated in section 4.1.1, Ithnin [4.1] showed that data for the iodine MNN Auger and photoelectron peaks for this analyser geometry did not produce the same values of coherent fraction. The results in Tables 4.4, and 4.5 clearly support this conclusion. Figure 4.6 shows the (111) iodine NIXSW data and fits. It is apparent that the profiles are not identical and hence will produce different values for the standing wave parameters. Interestingly, the profiles appear to have the same basic shape, but the peak-to-peak heights differ. The iodine 3d_{5/2} profile, is larger than the iodine 3p_{3/2}, which in turn is larger than





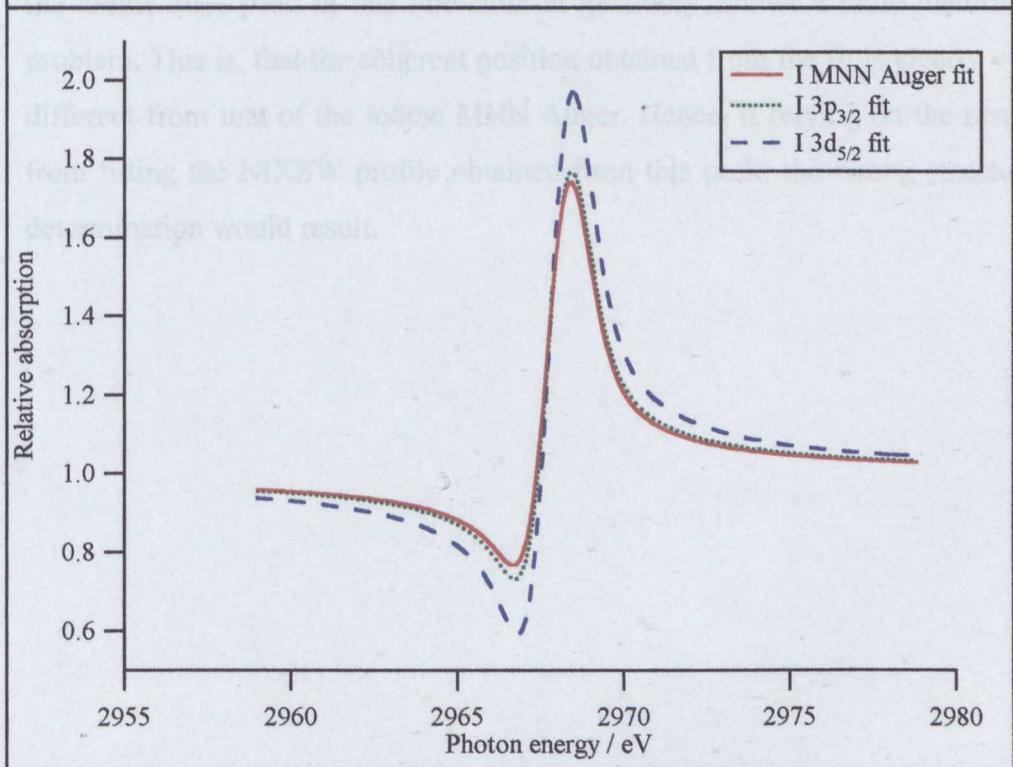
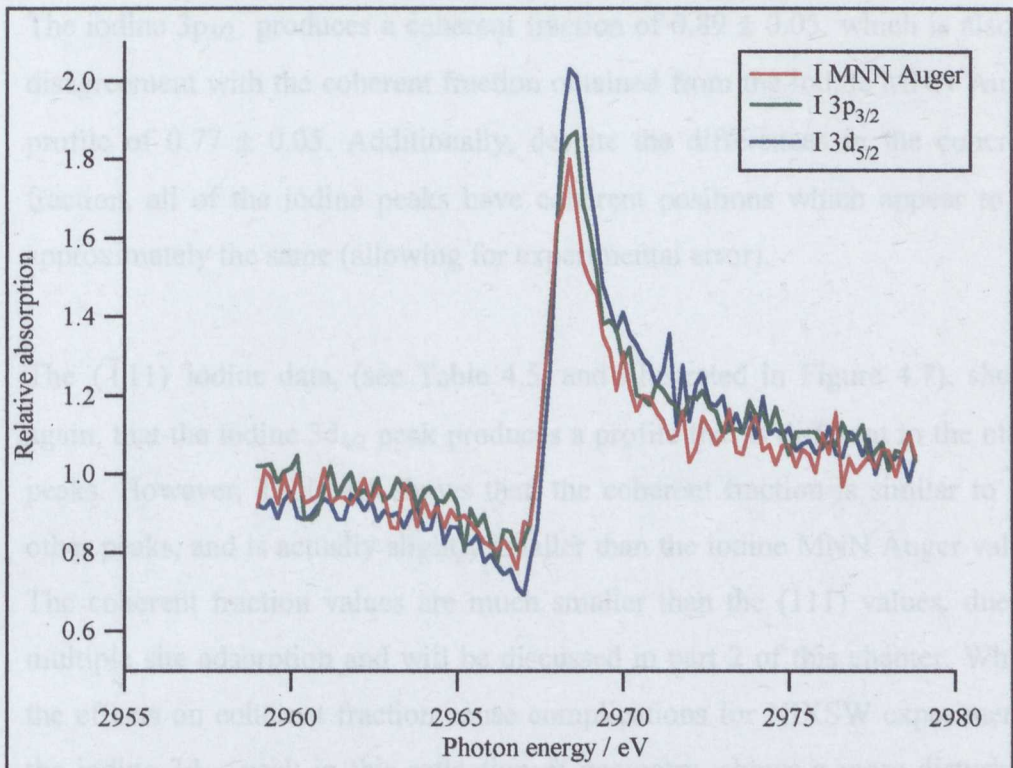
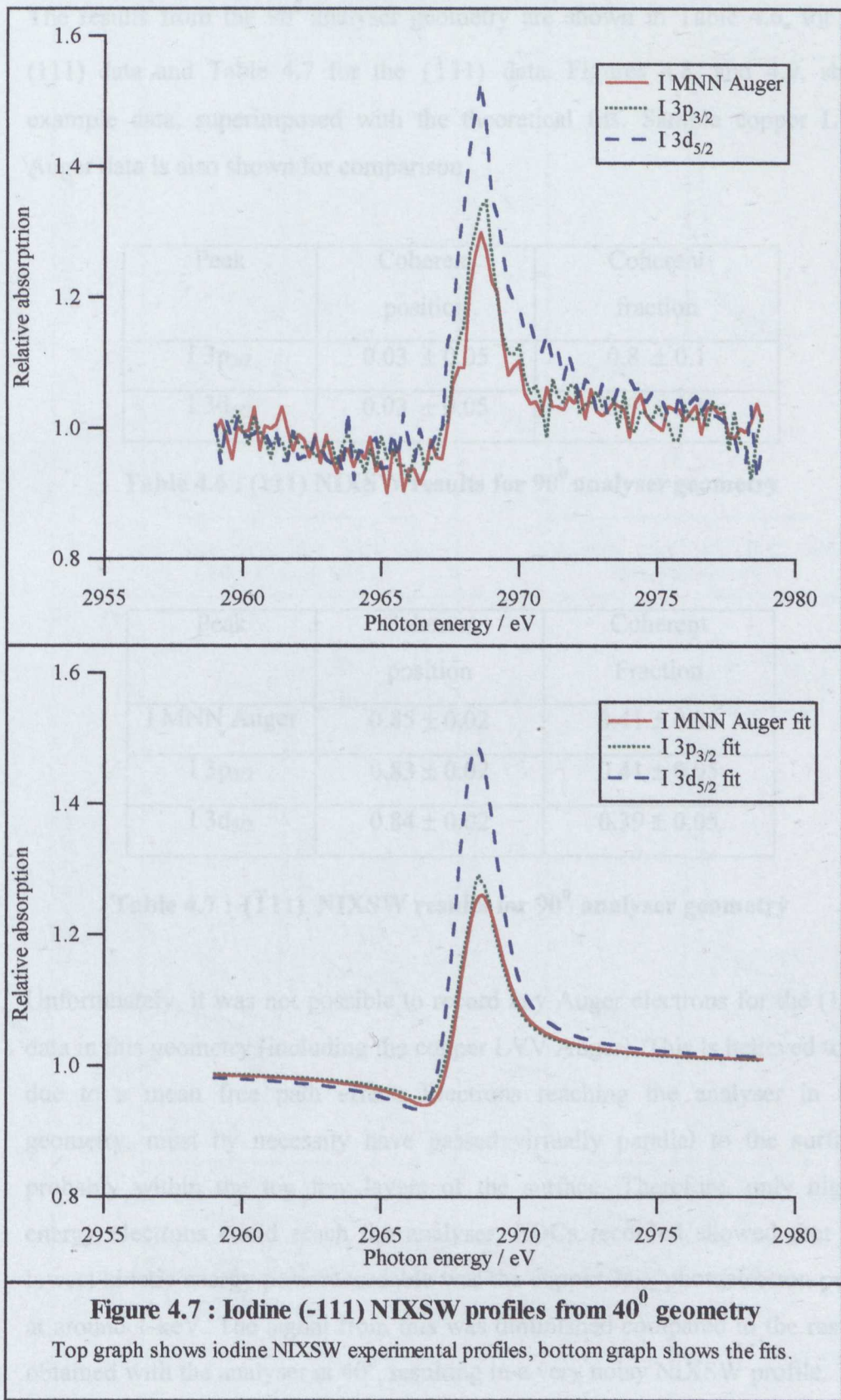


Figure 4.6 : Iodine (111) NIXSW profiles for 40⁰ geometry

Top graph shows the iodine NIXSW experimental profiles, bottom graph shows the fits.

the iodine MNN Auger profile. This agrees with the pattern in the coherent fraction values, with the iodine $3d_{5/2}$ giving a coherent fraction of 1.25 ± 0.05 . The iodine $3p_{3/2}$ produces a coherent fraction of 0.89 ± 0.05 , which is also in disagreement with the coherent fraction obtained from the iodine MNN Auger profile of 0.77 ± 0.05 . Additionally, despite the differences in the coherent fraction, all of the iodine peaks have coherent positions which appear to be approximately the same (allowing for experimental error).

The $(\bar{1}11)$ iodine data, (see Table 4.5, and illustrated in Figure 4.7), shows again, that the iodine $3d_{5/2}$ peak produces a profile that is different to the other peaks. However, Table 4.5 shows that, the coherent fraction is similar to the other peaks, and is actually slightly smaller than the iodine MNN Auger value. The coherent fraction values are much smaller than the (111) values, due to multiple site adsorption and will be discussed in part 2 of this chapter. Whilst the effects on coherent fraction cause complications for NIXSW experiments, the iodine $3d_{5/2}$ peak in this reflection & geometry, shows a more disturbing problem. This is, that the coherent position obtained from the fit is clearly very different from that of the iodine MNN Auger. Hence, if relying on the results from fitting the NIXSW profile obtained from this peak, the wrong structural determination would result.



4.4.2 90⁰-geometry

The results from the 90⁰ analyser geometry are shown in Table 4.6, for the (111) data and Table 4.7 for the ($\bar{1}11$) data. Figures 4.8, and 4.9, show example data, superimposed with the theoretical fits. Sample copper LVV Auger data is also shown for comparison

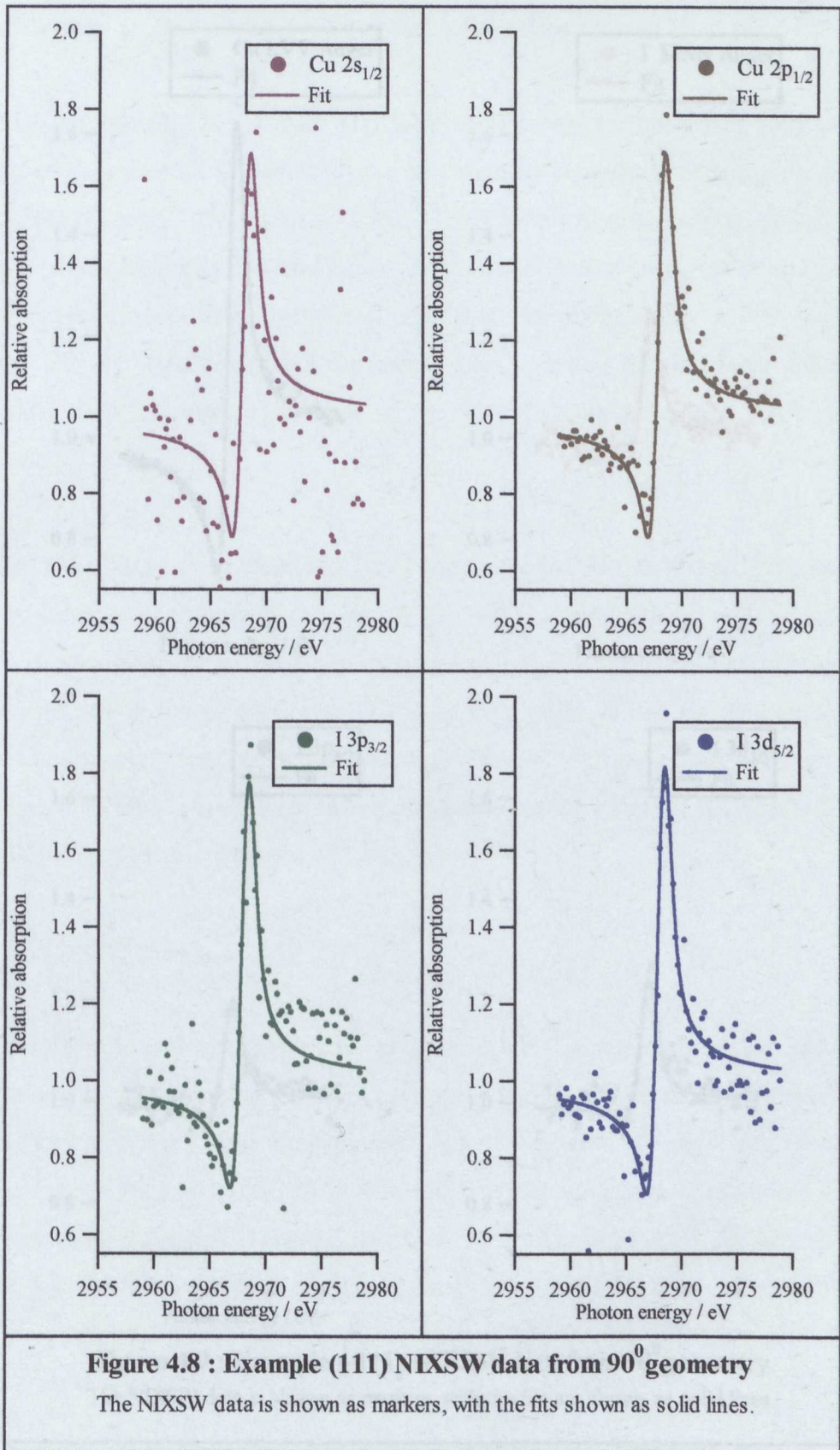
Peak	Coherent position	Coherent fraction
I 3p _{3/2}	0.03 ± 0.05	0.8 ± 0.1
I 3d _{5/2}	0.03 ± 0.05	0.9 ± 0.1

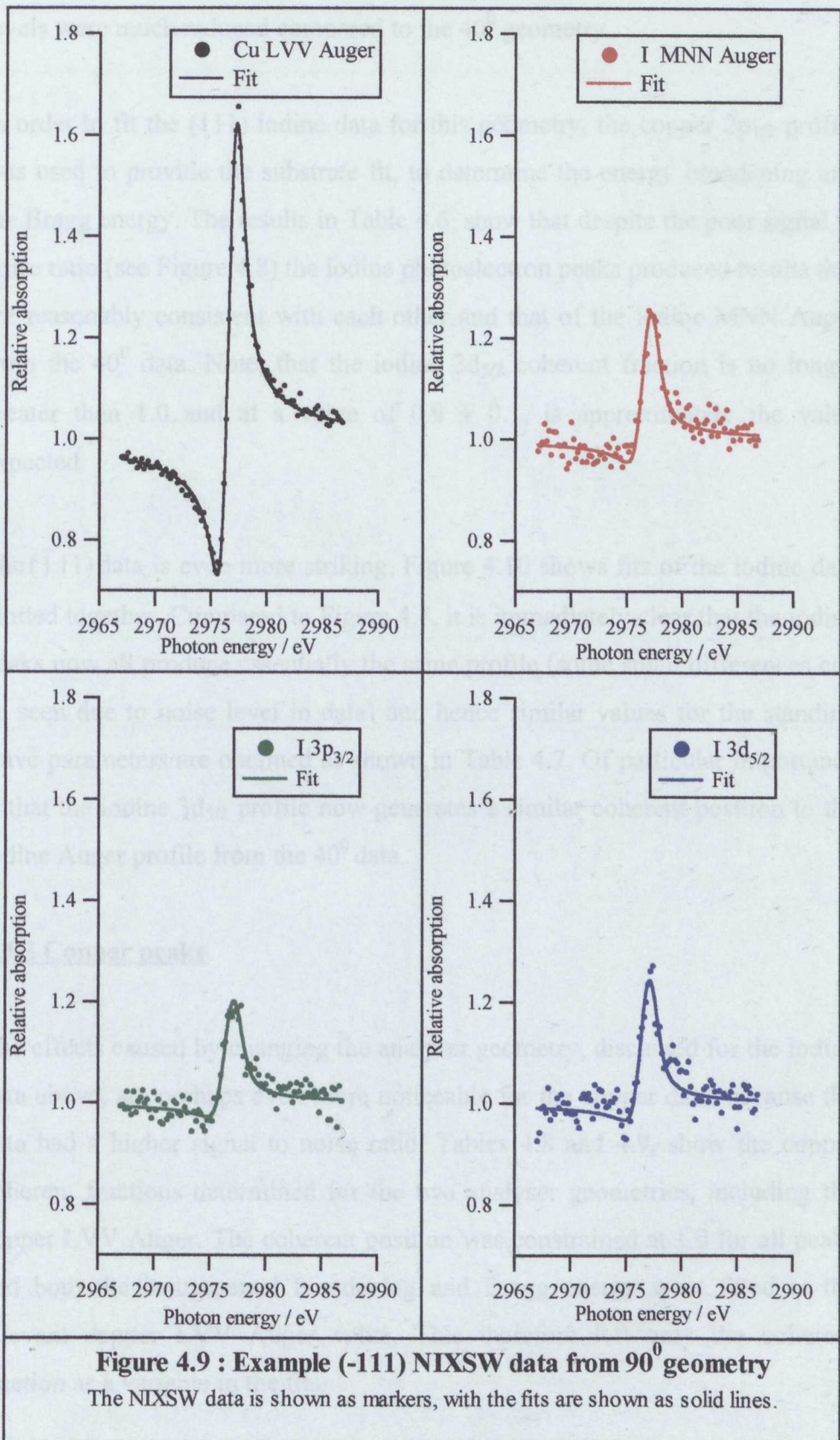
Table 4.6 : (111) NIXSW results for 90⁰ analyser geometry

Peak	Coherent position	Coherent Fraction
I MNN Auger	0.85 ± 0.02	0.41 ± 0.05
I 3p _{3/2}	0.83 ± 0.02	0.41 ± 0.05
I 3d _{5/2}	0.84 ± 0.02	0.39 ± 0.05

Table 4.7 : ($\bar{1}11$) NIXSW results for 90⁰ analyser geometry

Unfortunately, it was not possible to record any Auger electrons for the (111) data in this geometry (including the copper LVV Auger). This is believed to be due to a mean free path effect. Electrons reaching the analyser in this geometry, must by necessity have passed virtually parallel to the surface, probably within the top few layers of the surface. Therefore, only higher energy electrons could reach the analyser. EDCs recorded showed that the lowest kinetic energy peak recordable was the copper 2s_{1/2} photoelectron peak, at around 1 keV. The signal from this was diminished compared to the results obtained with the analyser at 40⁰, resulting in a very noisy NIXSW profile. The





remaining higher energy peaks were all recordable, but in all cases signal levels were much reduced compared to the 40^0 geometry.

In order to fit the (111) iodine data for this geometry, the copper $2p_{1/2}$ profile was used to provide the substrate fit, to determine the energy broadening and the Bragg energy. The results in Table 4.6, show that despite the poor signal to noise ratio (see Figure 4.8) the iodine photoelectron peaks produced results that are reasonably consistent with each other and that of the iodine MNN Auger from the 40^0 data. Note, that the iodine $3d_{5/2}$ coherent fraction is no longer greater than 1.0 and at a value of 0.9 ± 0.1 , is approximately the value expected.

The $(\bar{1}11)$ data is even more striking, Figure 4.10 shows fits of the iodine data plotted together. Compared to Figure 4.7, it is immediately clear that the iodine peaks now all produce essentially the same profile (some small differences can be seen due to noise level in data) and hence similar values for the standing wave parameters are obtained as shown in Table 4.7. Of particular importance is that the iodine $3d_{5/2}$ profile now generates a similar coherent position to the iodine Auger profile from the 40^0 data.

4.4.3 Copper peaks

The effects caused by changing the analyser geometry, discussed for the iodine data above, are perhaps even more noticeable for the copper data, because the data had a higher signal to noise ratio. Tables 4.8 and 4.9, show the copper coherent fractions determined for the two analyser geometries, including the copper LVV Auger. The coherent position was constrained at 1.0 for all peaks and both the instrumental broadening and Bragg energy were fixed at the relevant copper LVV Auger value. This therefore left only the coherent fraction as a variable in the fits.

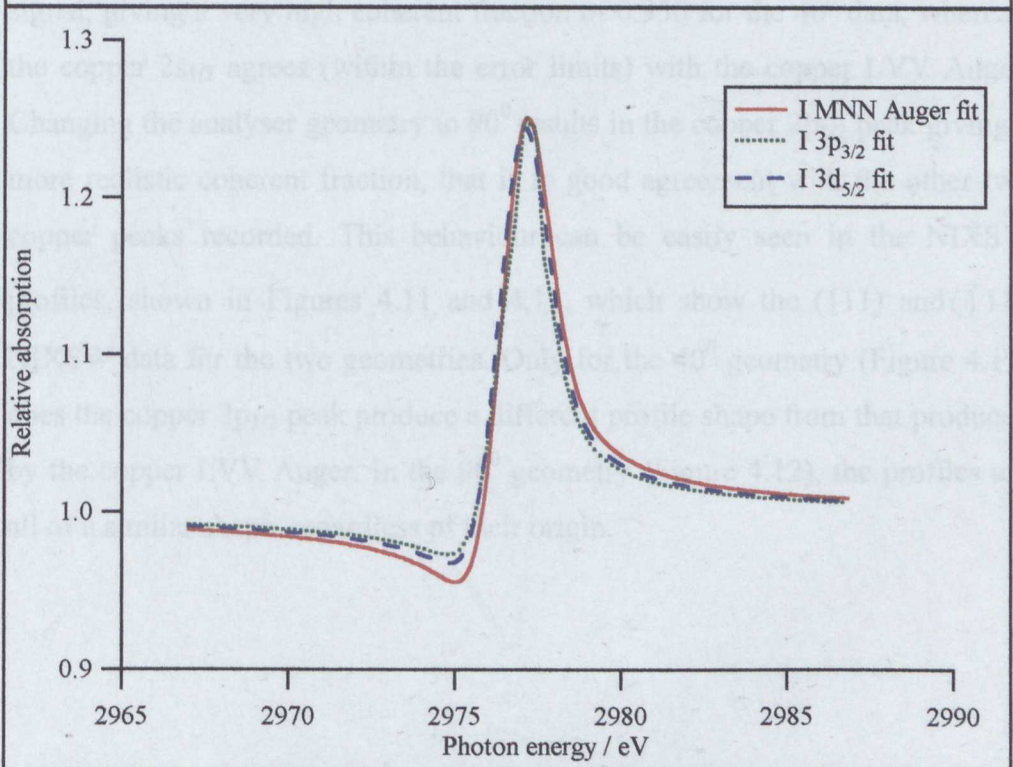
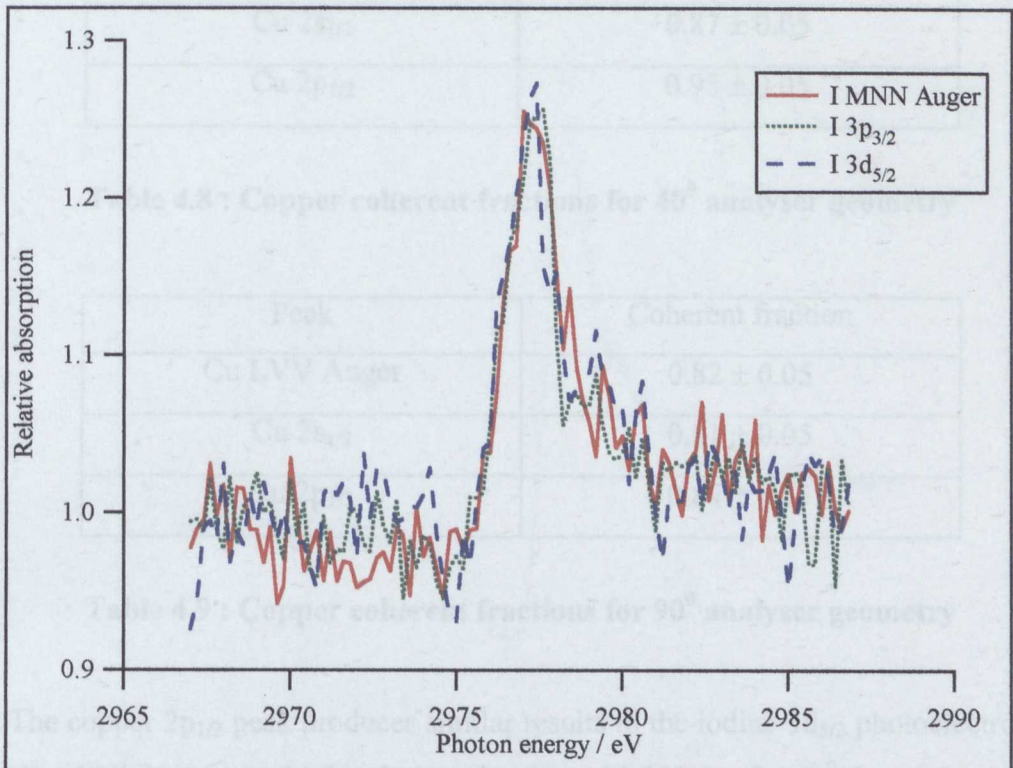


Figure 4.10 : Iodine (-111) NIXSW profiles from 90° geometry

Top graph shows the iodine NIXSW experimental profiles, bottom graph shows the fits.

Peak	Coherent fraction
Cu LVV Auger	0.83 ± 0.05
Cu $2s_{1/2}$	0.87 ± 0.05
Cu $2p_{1/2}$	0.95 ± 0.05

Table 4.8 : Copper coherent fractions for 40° analyser geometry

Peak	Coherent fraction
Cu LVV Auger	0.82 ± 0.05
Cu $2s_{1/2}$	0.81 ± 0.05
Cu $2p_{1/2}$	0.84 ± 0.05

Table 4.9 : Copper coherent fractions for 90° analyser geometry

The copper $2p_{1/2}$ peak produces similar results to the iodine $3d_{5/2}$ photoelectron signal, giving a very high coherent fraction of 0.950 for the 40° data, whereas, the copper $2s_{1/2}$ agrees (within the error limits) with the copper LVV Auger. Changing the analyser geometry to 90° results in the copper $2p_{1/2}$ peak giving a more realistic coherent fraction, that is in good agreement with the other two copper peaks recorded. This behaviour can be easily seen in the NIXSW profiles, shown in Figures 4.11 and 4.12, which show the (111) and $(\bar{1}11)$ NIXSW data for the two geometries. Only for the 40° geometry (Figure 4.11) does the copper $2p_{1/2}$ peak produce a different profile shape from that produced by the copper LVV Auger. In the 90° geometry (Figure 4.12), the profiles are all of a similar shape, regardless of their origin.

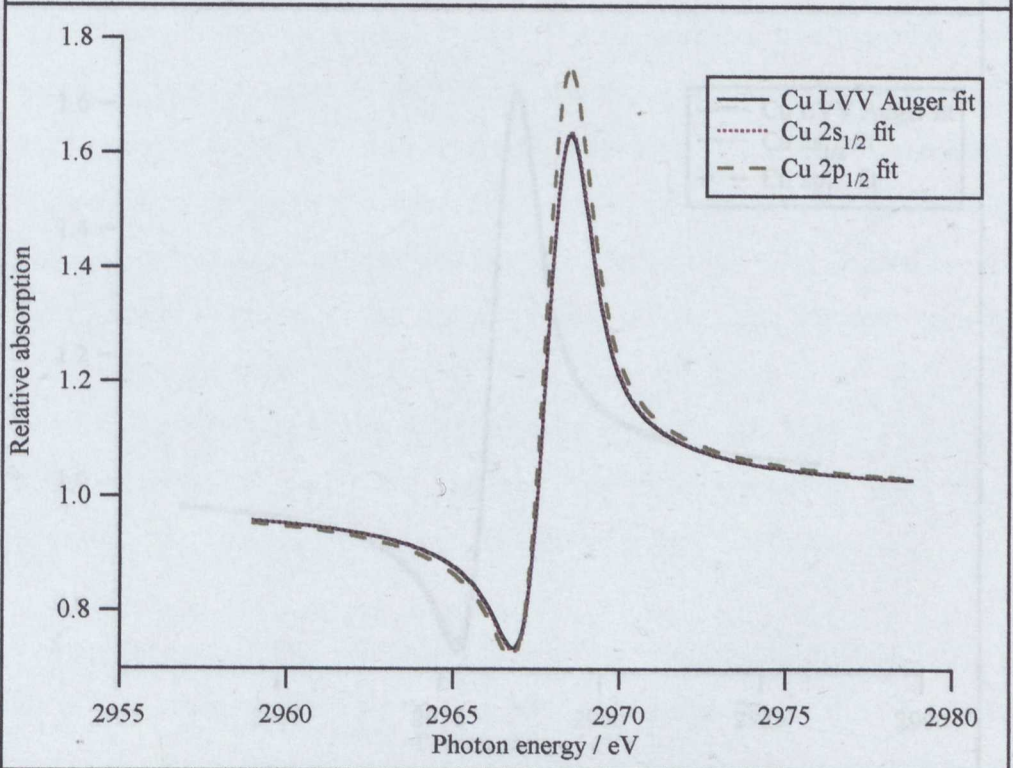
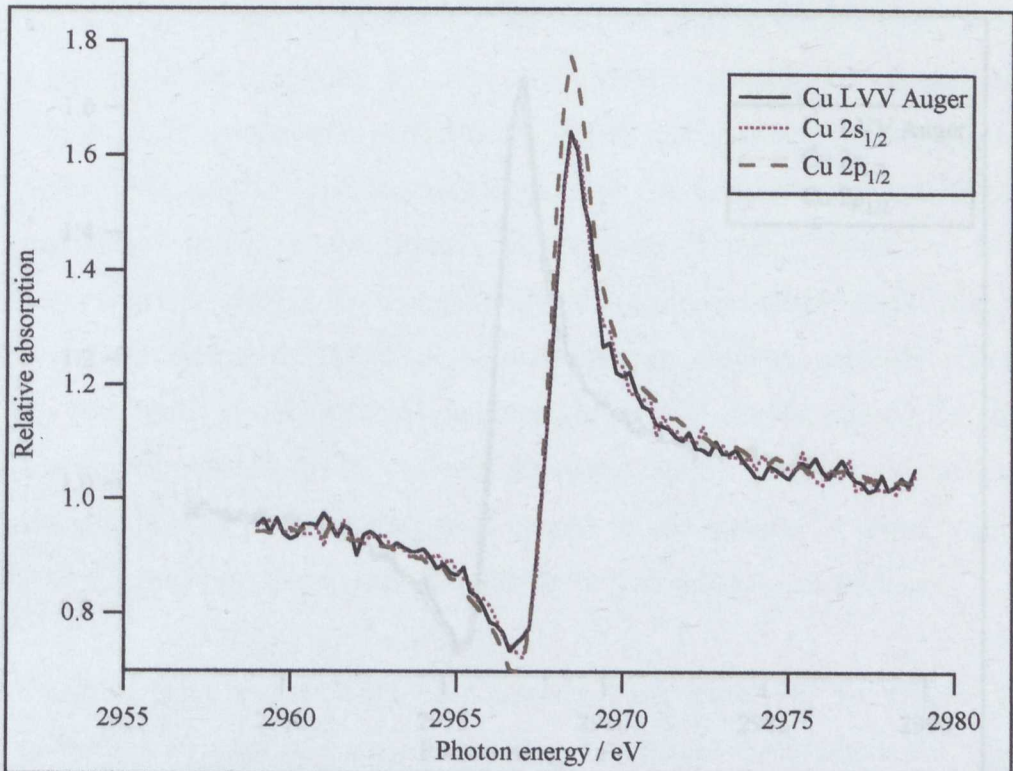


Figure 4.11 : Copper NIXSW profiles from 40⁰ geometry

Data recorded from (-111) reflection.

Top graph shows experimental NIXSW profiles, bottom graph shows the fits.

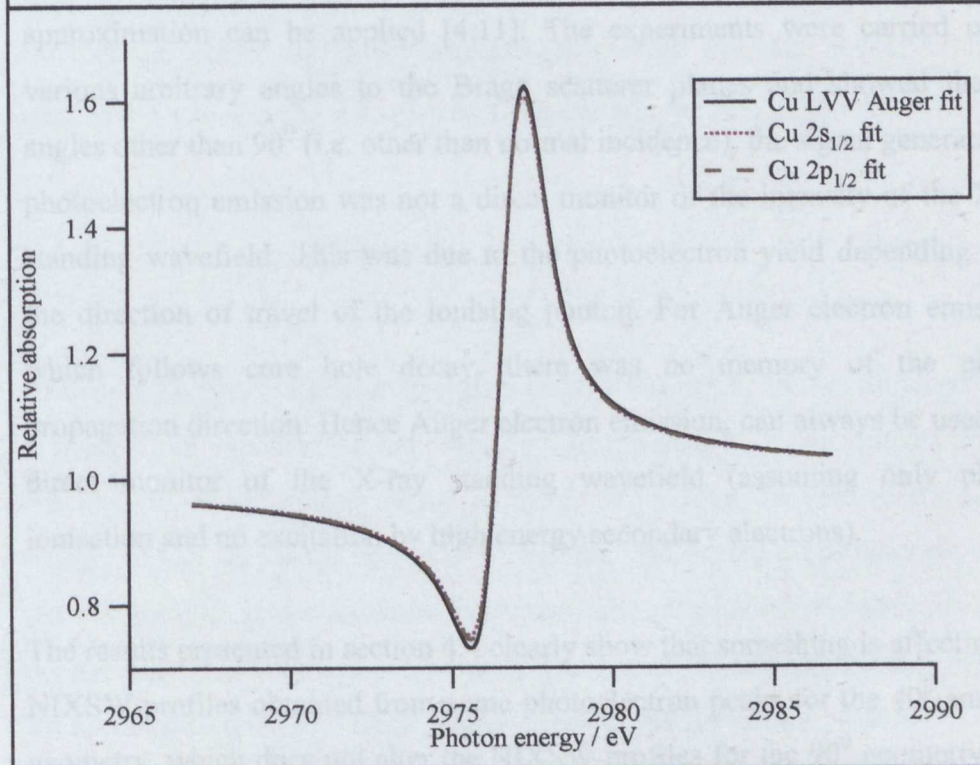
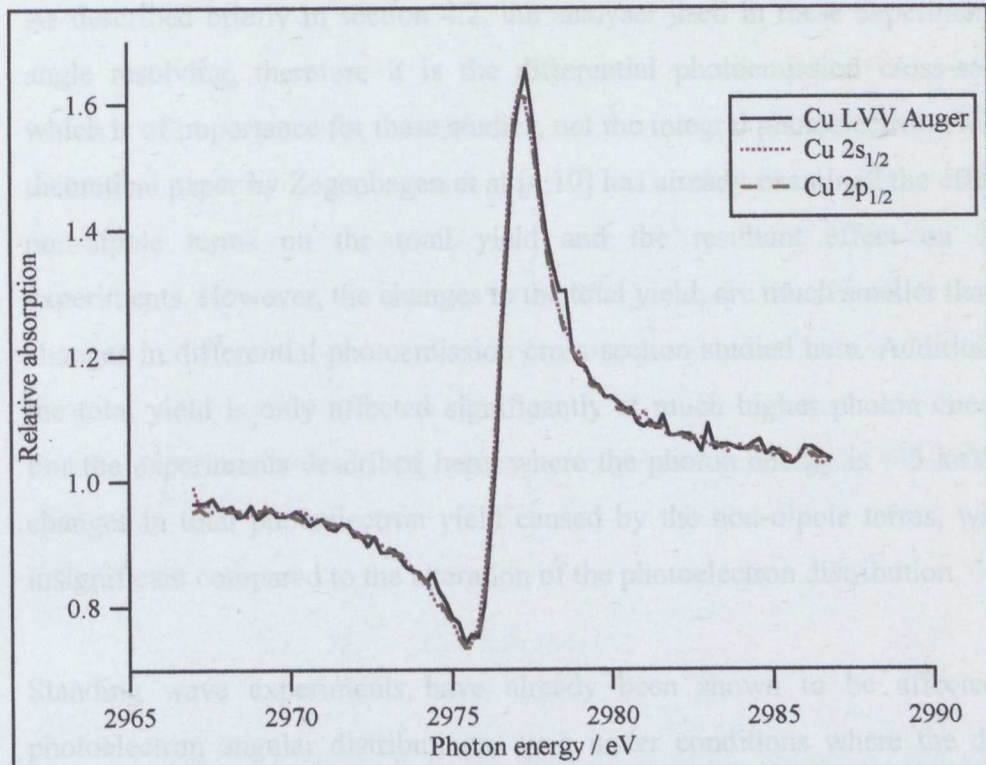


Figure 4.12 : Copper NIXSW profiles from 90^0 geometry

Data recorded from (-111) reflection.

Top graph shows experimental NIXSW profiles, bottom graph shows the fits.

4.5 Discussion

As described briefly in section 4.2, the analyser used in these experiments is angle resolving, therefore it is the differential photoemission cross-section which is of importance for these studies, not the integral photoelectron yield. A theoretical paper by Zegenhagen et al [4.10] has already examined the effect of non-dipole terms on the total yield and the resultant effect on XSW experiments. However, the changes to the total yield, are much smaller than the changes in differential photoemission cross-section studied here. Additionally, the total yield is only affected significantly at much higher photon energies. For the experiments described here, where the photon energy is ~ 3 keV, the changes in total photoelectron yield caused by the non-dipole terms, will be insignificant compared to the alteration of the photoelectron distribution.

Standing wave experiments have already been shown to be affected by photoelectron angular distributions, even under conditions where the dipole approximation can be applied [4.11]. The experiments were carried out at various arbitrary angles to the Bragg scatterer planes and showed that for angles other than 90° (i.e. other than normal incidence), the signal generated by photoelectron emission was not a direct monitor of the intensity of the X-ray standing wavefield. This was due to the photoelectron yield depending upon the direction of travel of the ionising photon. For Auger electron emission, which follows core hole decay, there was no memory of the photon propagation direction. Hence Auger electron emission, can always be used as a direct monitor of the X-ray standing wavefield (assuming only photon ionisation and no excitation by high energy secondary electrons).

The results presented in section 4.4 clearly show that something is affecting the NIXSW profiles obtained from some photoelectron peaks for the 40° analyser geometry, which does not alter the NIXSW profiles for the 90° geometry. It is concluded that this is due to the photoelectron angular distributions being changed, so that the photoelectron yield is no longer proportional to the intensity of the X-ray standing wavefield, even for normal incidence. It is the

introduction of non-dipole terms into the photoemission process, which alters the photoelectron angular distributions, resulting in the changes to the NIXSW profiles.

It is now necessary to adopt a theoretical approach so that it is possible for the NIXSW equations to be compensated for the non-dipole effects and to understand why the non-dipole terms do not modify the NIXSW profiles for the 90° geometry, and yet do effect the 40° geometry data recorded in these experiments. The important atomic physics for the photon interaction processes involved here, is contained within the matrix element that describes the probability of an electron being excited by a photon beam (M_{if}). This is given by equation 4.1.

$$M_{if} = \langle f | \exp(i\mathbf{k} \cdot \mathbf{r}) \mathbf{A} \cdot \mathbf{p} | i \rangle \quad (4.1)$$

\mathbf{k} is the photon wavevector; \mathbf{r} , the electron position vector; \mathbf{A} , the photon polarisation vector and \mathbf{p} the electron momentum operator. As described in section 4.2, the term $\exp(i\mathbf{k} \cdot \mathbf{r})$ is expanded as shown in equation 4.2.

$$\exp(i\mathbf{k} \cdot \mathbf{r}) \approx 1 + i\mathbf{k} \cdot \mathbf{r} - \frac{1}{2}(\mathbf{k} \cdot \mathbf{r})^2 + \dots \quad (4.2)$$

In the dipole approximation it is assumed that $\mathbf{k} \cdot \mathbf{r} \ll 1$, so that all terms apart from unity in equation 4.2 are discarded. In physical terms this means that the wavelength of the photon beam, is much larger than the size of the orbital being excited. As photon energies increase beyond that of ultra-violet radiation, the wavelength of the radiation decreases, and eventually becomes similar to orbital size. This situation is obviously going to occur at lower photon energies for atoms with relatively large orbitals, such as the iodine $3d_{5/2}$ levels.

Assuming that the dipole approximation is valid, the differential photoemission cross-section ($d\sigma/d\Omega$) (for a linearly polarised beam) is given by equation 4.3.

$$\frac{d\sigma}{d\Omega} = \left(\frac{\sigma}{4\pi} \right) \left[\frac{1 + \beta(\cos^2\theta - 1)}{2} \right] \quad (4.3)$$

θ is the angle between the photoelectron emission direction and \mathbf{A} (the photon polarisation vector – see equation 4.1) and β , is an asymmetry parameter [4.12]. The significant point about this equation is that it generates a symmetrical photoelectron angular distribution, which is independent of the photon propagation direction (as shown schematically in Figure 4.13). It is the independence to the photon propagation direction which is important to NIXSW studies. For the 40° analyser geometry, (as illustrated in Figure 4.14), the analyser collects electrons in a “backward” sense relative to the incident photon propagation direction, i.e. the velocity component of the photoelectron is in the opposite sense to that of the incident photon. However, the analyser collects electrons in a “forward” sense relative to the reflected X-rays (i.e. photons which have suffered 180° scattering by the copper lattice). If the dipole approximation is applicable, then the signal the analyser receives will be independent of the direction of travel of the photons (assuming the same photon intensity), because the angular distribution is symmetrical.

If the case is now considered where the dipole approximation is not valid, and the non-dipole terms become important, it is necessary to include terms beyond unity in the expansion shown in equation 4.2. This results in a changed expression for the differential photoemission cross-section shown in equation 4.4 [4.13].

$$\frac{d\sigma}{d\Omega} = \left(\frac{\sigma}{4\pi} \right) \left[\frac{1 + \beta(3\cos^2\theta - 1)}{2} + (\delta + \gamma\cos^2\theta)\sin\theta\cos\phi \right] \quad (4.4)$$

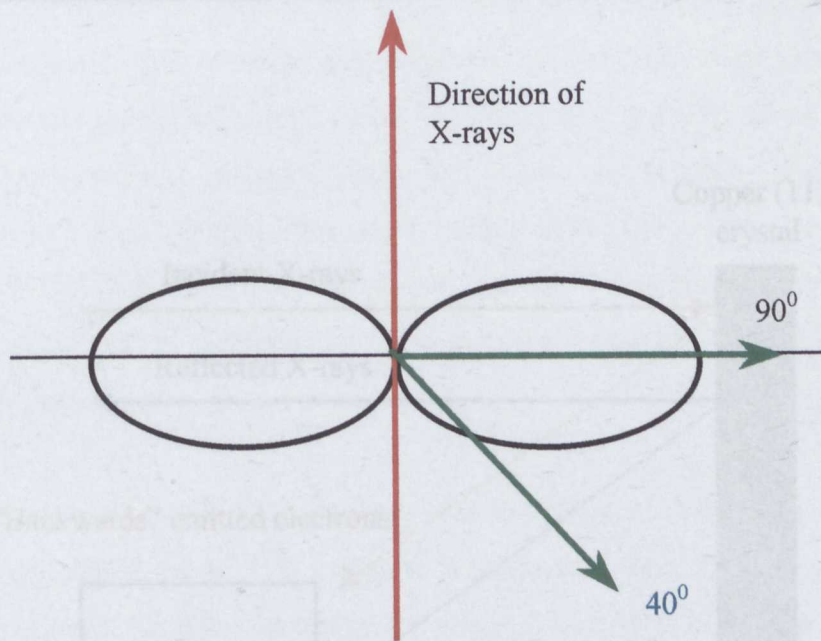


Figure 4.13 : Schematic representation of symmetrical angular distribution

Black line represents angular distribution generated by equation 4.3.
Green lines show the direction of emitted electrons towards the CHA for each geometry.

Notice that in equation 4.4 two more asymmetry parameters are now required (δ , the magnetic-dipole interference and γ , the electric-quadrupole interference [4.13,4.16]). δ is the angle between the photon propagation direction and the projection of the electron wavevector in the plane perpendicular to \mathbf{k} . The

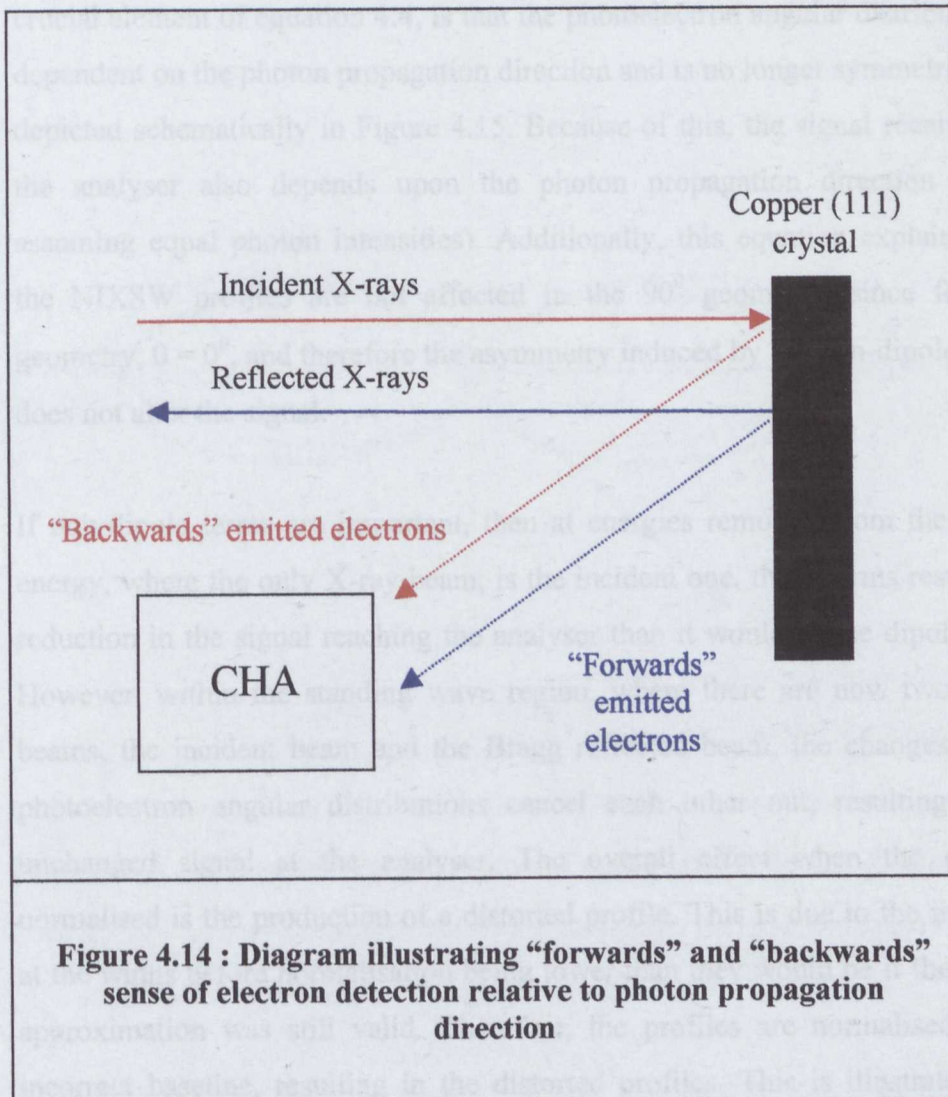
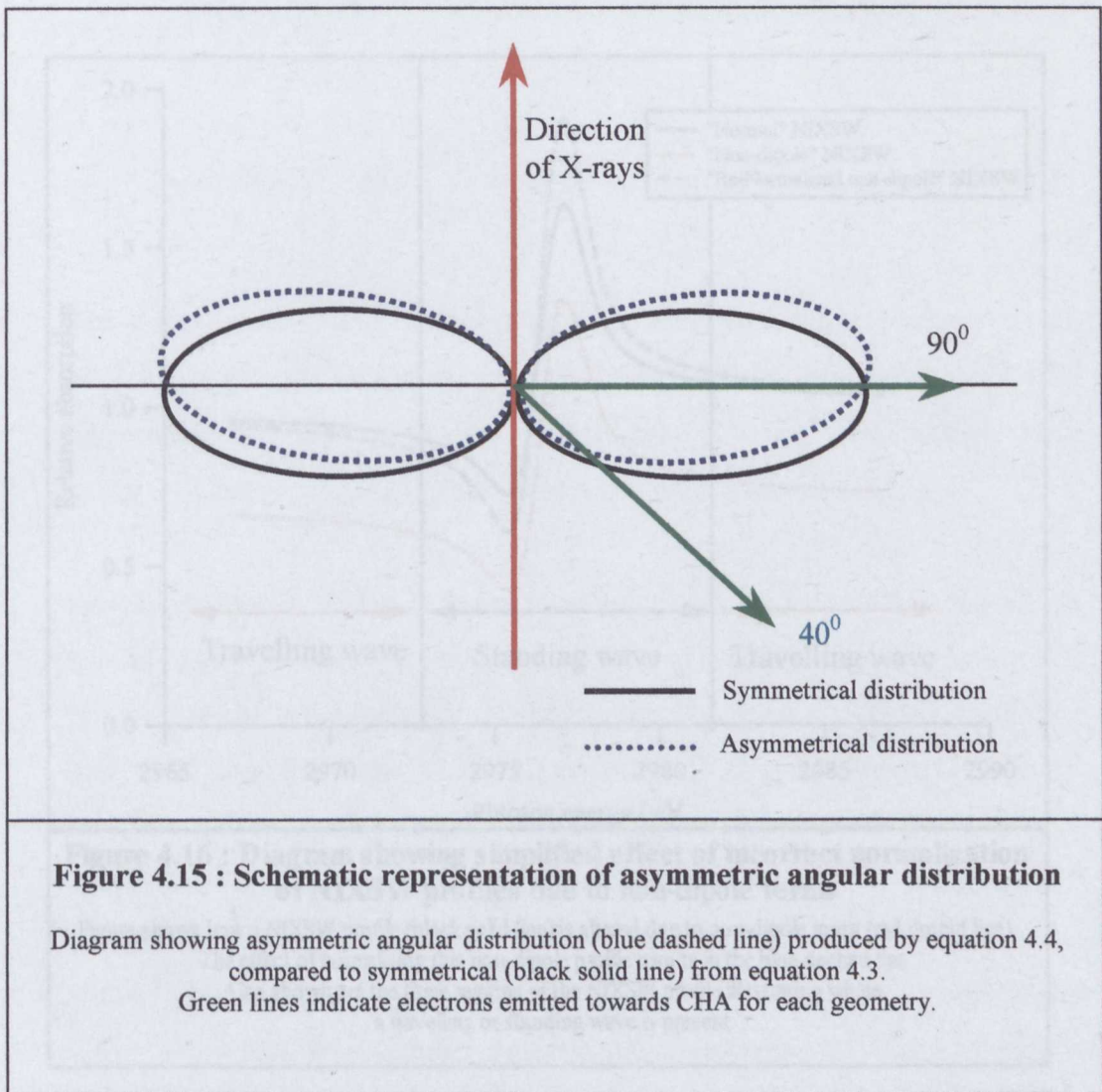


Figure 4.14 : Diagram illustrating "forwards" and "backwards" sense of electron detection relative to photon propagation direction

simplified form in Figure 4.16, because the amount the profile is altered depends exactly upon how much the non-dipole terms influence the photoemission from the orbital concerned. Finding the normalized profile with the current version of the NIXSW software does not produce the correct result, because the changes in the NIXSW profile induced by the non-dipole terms are not accounted for.

Notice that in equation 4.4 two more asymmetry parameters are now required (δ , the magnetic-dipole interactions and γ , the electric-quadrupole interactions [4.13,4.16]), ϕ is the angle between the photon propagation direction and the projection of the electron wavevector in the plane perpendicular to \mathbf{A} . The crucial element of equation 4.4, is that the photoelectron angular distribution is dependent on the photon propagation direction and is no longer symmetrical, as depicted schematically in Figure 4.15. Because of this, the signal received by the analyser also depends upon the photon propagation direction (again assuming equal photon intensities). Additionally, this equation explains why the NIXSW profiles are not affected in the 90° geometry, since for that geometry, $\theta = 0^\circ$, and therefore the asymmetry induced by the non-dipole terms does not alter the signal.

If non-dipole terms are important, then at energies removed from the Bragg energy, where the only X-ray beam, is the incident one, these terms result in a reduction in the signal reaching the analyser than it would in the dipole case. However, within the standing wave region, where there are now two X-ray beams, the incident beam and the Bragg reflected beam, the changes in the photoelectron angular distributions cancel each other out, resulting in an unchanged signal at the analyser. The overall effect when the data is normalised is the production of a distorted profile. This is due to the intensity at the wings before normalisation being lower than they would be if the dipole approximation was still valid. Therefore, the profiles are normalised to an incorrect baseline, resulting in the distorted profiles. This is illustrated in a simplified form in Figure 4.16, of course the amount the profile is altered depends exactly upon how much the non-dipole terms influence the photoemission from the orbital concerned. Fitting the normalised profile with the current version of the NIXSW equations does not produce the correct results, because the changes in the NIXSW profile induced by the non-dipole terms are not accounted for.



It is possible to reverse the standing wave equations to compensate for the non-dipole terms, to allow the "correct" values for the coherent position and coherent fraction to be determined. Assuming photoemission detection of the standing wave, an expression for the signal obtained at a specific glancing angle θ is given as [4.13]:

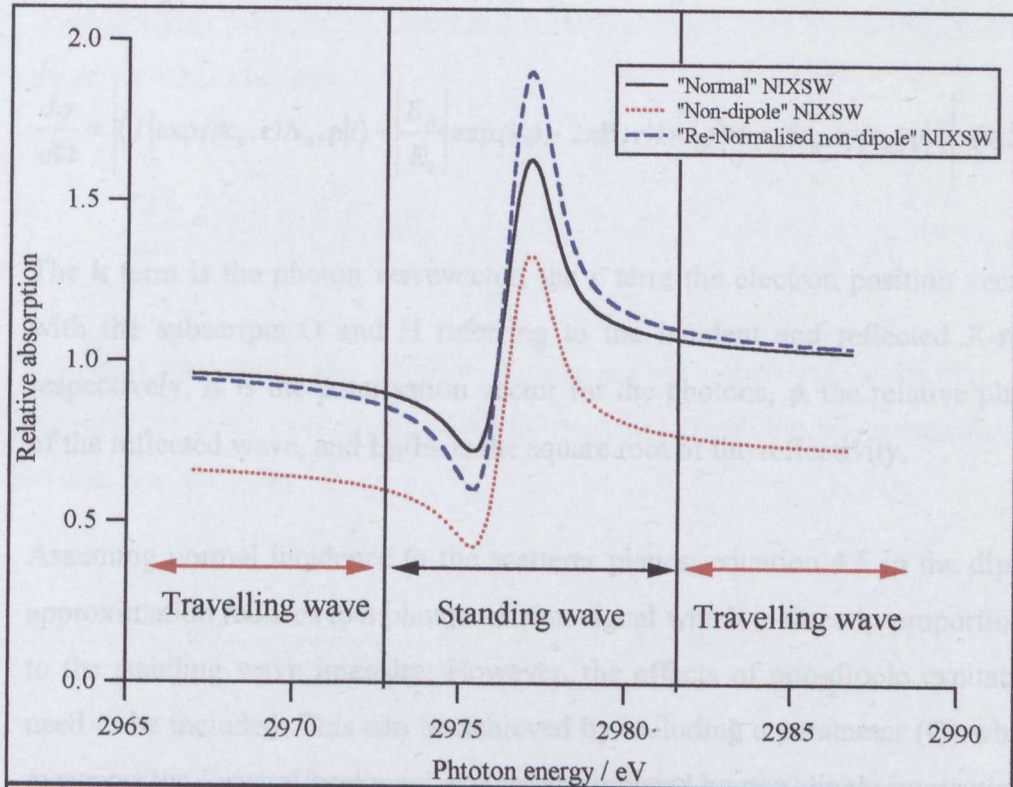


Figure 4.16 : Diagram showing simplified effect of incorrect normalisation of NIXSW profiles due to non-dipole terms

Figure shows how a NIXSW profile (black solid line) is altered due to non-dipole terms (red dotted line). The effect of normalising this non-dipole profile results in the blue dashed line. Also shown are the three regions of the NIXSW profile illustrating where a travelling or standing wave is present.

It is possible to rewrite the standing wave equations to compensate for the non-dipole terms, to allow the “correct” values for the coherent position and coherent fraction to be determined. Assuming photoemission detection of the standing wave, an expression for the signal detected at a specific direction can be written as [4.13]:

$$\frac{d\sigma}{d\Omega} \propto \left| \langle f | \exp(i\mathbf{k}_0 \cdot \mathbf{r}) \mathbf{A}_0 \cdot \mathbf{p} | i \rangle + \frac{E_H}{E_0} \exp(i(\phi - 2\pi\mathbf{H} \cdot \mathbf{r})) \times \langle f | \exp(i\mathbf{k}_H \cdot \mathbf{r}) \mathbf{A}_H \cdot \mathbf{p} | i \rangle \right|^2 \quad (4.5)$$

The \mathbf{k} term is the photon wavevector, the \mathbf{r} term the electron position vector, with the subscripts O and H referring to the incident and reflected X-rays respectively, \mathbf{A} is the polarisation vector for the photons, ϕ , the relative phase of the reflected wave, and E_H/E_0 is the square root of the reflectivity.

Assuming normal incidence to the scatterer planes, equation 4.5 in the dipole approximation reduces to a photoemission signal which is directly proportional to the standing wave intensity. However, the effects of non-dipole excitation need to be included. This can be achieved by including a parameter (Q) which measures the forward/backward asymmetry induced by non-dipole interactions. Q is defined so that the ratio of the photoemission intensity for ϕ values of 0° and 180° is given by $(1+Q)/(1-Q)$. Q lies within the range -1 to +1, and in the case of pure dipole interactions it is 0. Using this formalism it is possible to separate out the key angular dependence components of the two matrix elements in equation 4.5 to produce equation 4.6.

$$\frac{d\sigma}{d\Omega} \propto \left| M(1-Q)^{1/2} \sqrt{R} \exp(i(\phi - 2\pi\mathbf{H} \cdot \mathbf{r})) M(1+Q)^{1/2} \right|^2 \quad (4.6)$$

Where M contains all other aspects including the angular dependence relative to the polarisation vector (\mathbf{A}), which as it lies in the same direction for both the incident and reflected waves in the NIXSW experiment, it is identical for both components. Expanding this gives

$$\frac{d\sigma}{d\Omega} \propto (1-Q) + R(1+Q) + 2\sqrt{R}(1-Q^2)^{1/2} \cos(\phi - 2\pi\mathbf{H}\cdot\mathbf{r}) \quad (4.7)$$

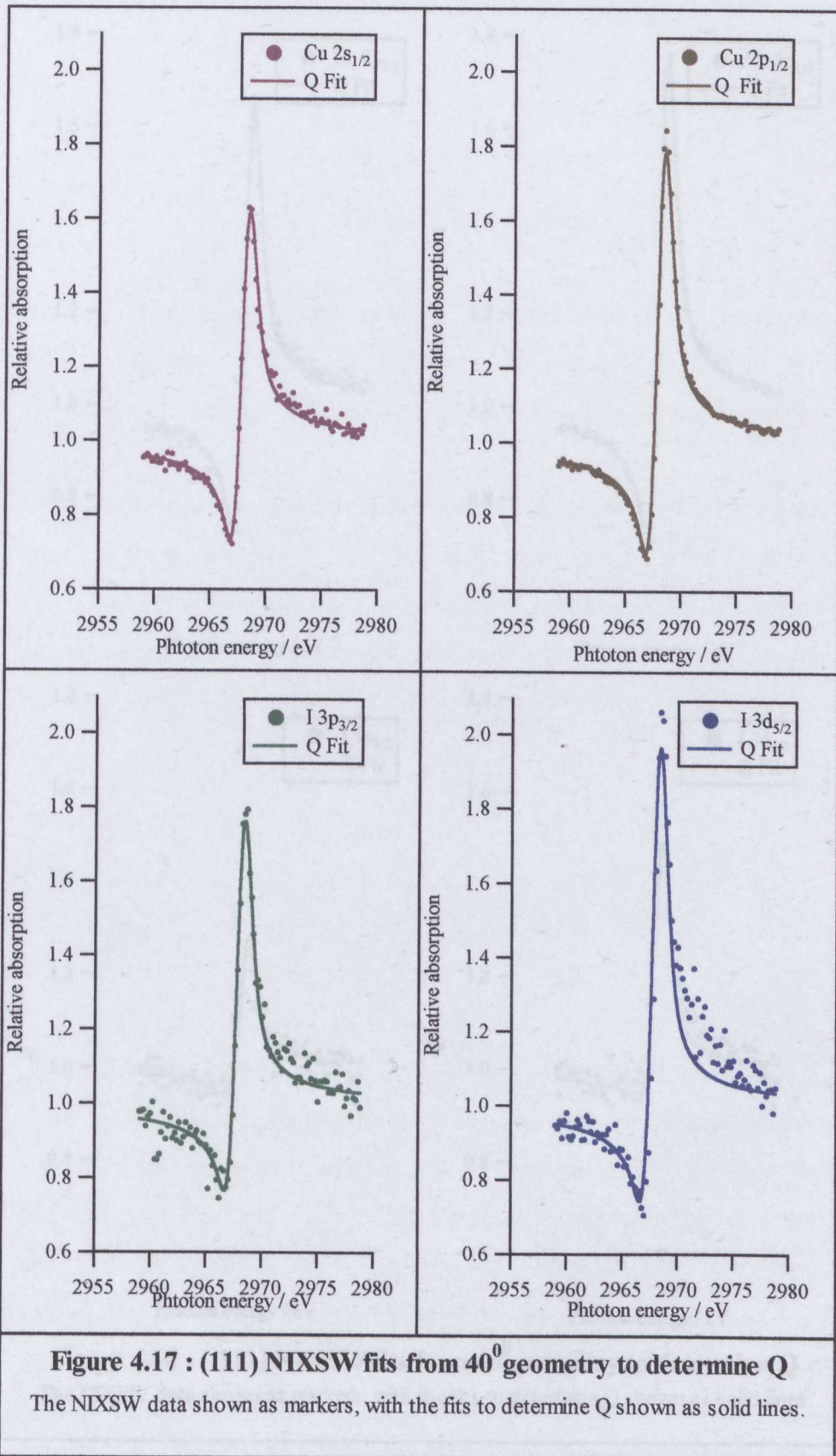
For Q equals zero, equation 4.7 reduces to the normal expression for the standing wave intensity given in section 2.6.3. If a distribution of adsorber layer spacings (as shown in section 2.6.5) is included, then a modified form of equation 4.7 is obtained.

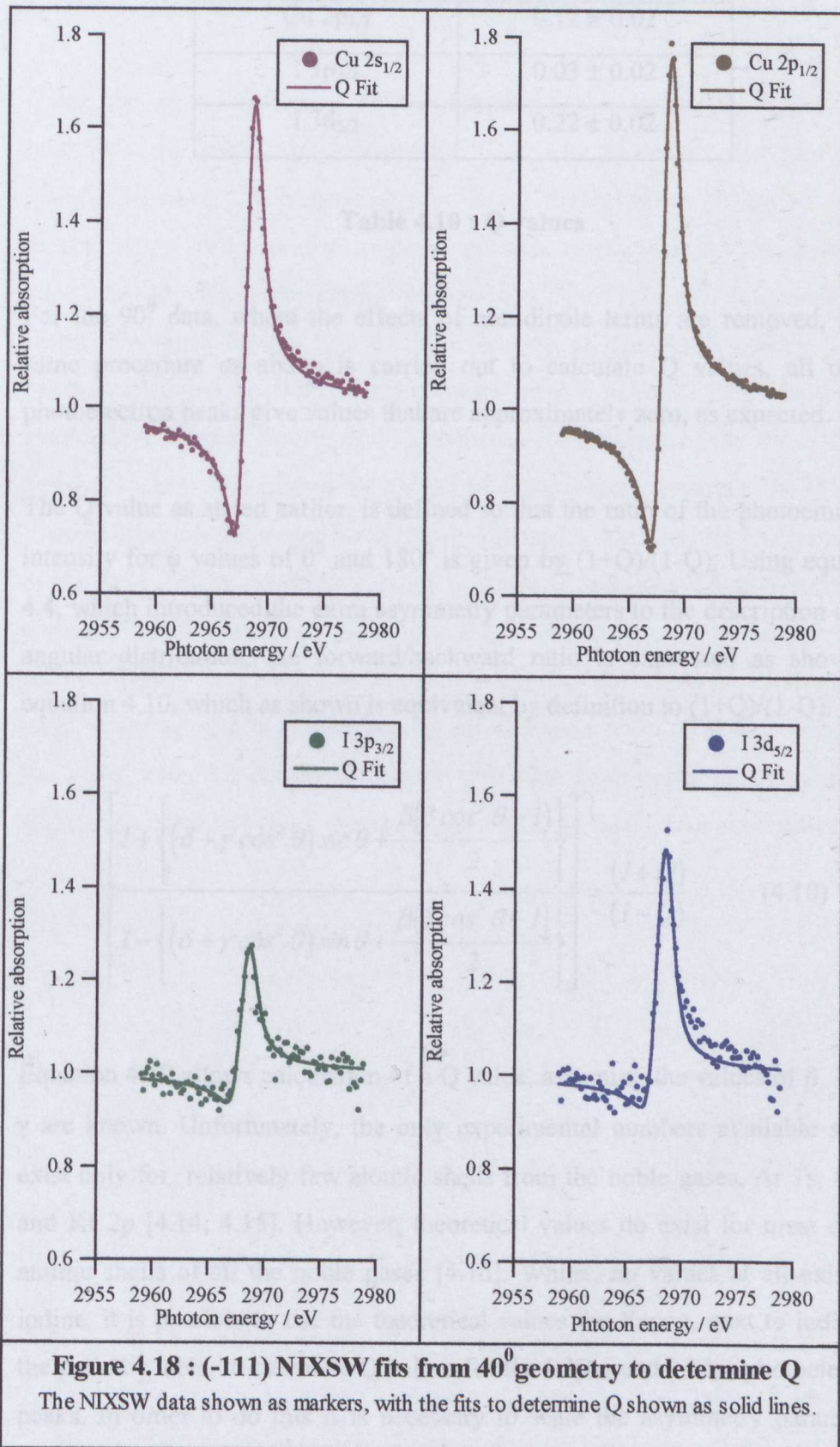
$$\frac{d\sigma}{d\Omega} \propto (1-Q) + R(1+Q) + 2\sqrt{R}f_{co}(1-Q^2)^{1/2} \cos\left(\phi - 2\pi\frac{D}{d_H}\right) \quad (4.8)$$

Earlier it was shown that NIXSW profiles are normalised to values of 1.0 at energies far away from Bragg (see section 3.5.1). Applying this normalisation to equation 4.8 gives

$$\frac{d\sigma}{d\Omega} \propto 1 + \frac{R(1+Q)}{(1-Q)} + 2\sqrt{R}f_{co}\left(\frac{1+Q}{1-Q}\right)^{1/2} \cos\left(\phi - 2\pi\frac{D}{d_H}\right) \quad (4.9)$$

The 40⁰ NIXSW data has been reanalysed using this modified expression. The process was essentially similar to that discussed in sections 3.5.1 and 4.3. Firstly, the copper LVV Auger NIXSW profile was fitted for an experiment (using Q=0, as it is an Auger electron), then the iodine MNN Auger profile was fitted using the values of the Bragg energy and instrumental broadening determined from the copper fit (again using Q=0). For the fitting of the photoelectron peaks the NIXSW parameters constrained at those of the appropriate Auger peak, with only the new Q parameter varied to optimise the fit. Examples of the fits obtained are shown in Figures 4.17 and 4.18, with the resultant Q values given in Table 4.10.





Photoelectron Peak	Q
Cu 2s _{1/2}	0.00 ± 0.02
Cu 2p _{1/2}	0.12 ± 0.02
I 3p _{3/2}	0.03 ± 0.02
I 3d _{5/2}	0.22 ± 0.02

Table 4.10 : Q values

For the 90° data, where the effects of non-dipole terms are removed, if the same procedure as above is carried out to calculate Q values, all of the photoelectron peaks give values that are approximately zero, as expected.

The Q value as stated earlier, is defined so that the ratio of the photoemission intensity for ϕ values of 0° and 180° is given by (1+Q)/(1-Q). Using equation 4.4, which introduced the extra asymmetry parameters to the description of the angular distribution, the forward/backward ratio is expressed as shown in equation 4.10, which as shown is equivalent by definition to (1+Q)/(1-Q).

$$\frac{\left[1 + \left\{ (\delta + \gamma \cos^2 \theta) \sin \theta + \frac{\beta(3 \cos^2 \theta - 1)}{2} \right\} \right]}{\left[1 - \left\{ (\delta + \gamma \cos^2 \theta) \sin \theta + \frac{\beta(3 \cos^2 \theta - 1)}{2} \right\} \right]} = \frac{(1+Q)}{(1-Q)} \quad (4.10)$$

Equation 4.10 allows calculation of a Q value, assuming the values of β , δ and γ are known. Unfortunately, the only experimental numbers available so far exist only for relatively few atomic shells from the noble gases, Ar 1s, Kr 2s and Kr 2p [4.14, 4.15]. However, theoretical values do exist for most of the atomic shells of all the noble gases [4.16]. Whilst, no values at all exist for iodine, it is possible to use the theoretical values for Xenon, next to iodine in the periodic table, to calculate Q values for the I 3p_{3/2} and I 3d_{5/2} photoelectron peaks. In order to do this it is necessary to scale the asymmetry parameters from Xenon to match the energies used in these experiments, as the parameters

are energy dependent. This process has been discussed elsewhere [4.2]. The Q values calculated were 0.03 for the I $3p_{3/2}$ and 0.22 for the I $3d_{5/2}$. These are in excellent agreement with the values found experimentally in Table 4.10.

Using the new formulation of the standing wave equations, it should be possible to fit NIXSW profiles obtained from any photoelectron peaks at any energy. However, it is necessary to know the Q value, which is energy dependent. In some cases it might be possible to calculate a value from first principles as discussed above. However, if the relevant Auger peak is recordable, then the Q value for that element, at that Bragg energy can be easily determined, as with the experiments here. If neither of these options are available, a further option is to produce an overlayer where the coherent fraction is zero. This allows the data to be fitted directly to obtain the Q value. This method relies on producing a truly incoherent surface and has been used in chapter 5, which describes a NIXSW study of cadmium iodide adsorbed on copper(111). Zegenhagen [4.10] proposed another method by which you could record NIXSW profiles at two energies, one where the dipole approximation is valid, and one at a higher energy where it breaks down. These experiments show that even for the lowest energy reflection from copper(111) the dipole approximation is not valid, therefore Zegenhagen's method would not work.

Part 2 : Structure determination for Copper(111)-($\sqrt{3}\times\sqrt{3}$)R30⁰-Iodine using NIXSW

4.6.0 Introduction

This part of the chapter uses the NIXSW data described in part 1, to perform a structure determination for the copper(111)-($\sqrt{3}\times\sqrt{3}$)R30⁰-Iodine surface. Before examining the experimental results, it is worth considering the literature on similar systems. Halogen adsorption commonly produces a ($\sqrt{3}\times\sqrt{3}$)R30⁰ overlayer structure on fcc(111) metal surfaces, for coverages of 1/3 of a monolayer. This section will concentrate on the studies of iodine ($\sqrt{3}\times\sqrt{3}$)R30⁰ adsorption structures on Cu(111) and Ag(111). Ag(111) is included since the structures observed on the two metals are very closely related. A review by Jones [4.17] contains details of these, and many of the structures observed for halogen adsorption on metal surfaces.

4.6.1 Copper(111)-($\sqrt{3}\times\sqrt{3}$)R30⁰-Iodine

Citrin et al [4.18] used surface extended X-ray adsorption fine structure (SEXAFS) measurements to examine the copper(111)-($\sqrt{3}\times\sqrt{3}$)R30⁰-Iodine structure, formed by room temperature adsorption of iodine vapour. SEXAFS data was recorded for the iodine overlayer and for bulk copper iodide (which was used as a reference). The SEXAFS data was recorded at two sample geometries, one with the synchrotron polarisation direction parallel to the surface and the other nearly perpendicular. The ratio of the two polarisation dependent SEXAFS data was compared with theoretical calculations to enable the adsorption site to be determined. The three-fold co-ordinated hollow sites were found to be the preferred site. However, it was not possible to distinguish between the fcc or hcp sites.

NIXSW has also been used to study this system. Ithnin et al [4.1] (see section 4.1.1) formed the copper(111)-($\sqrt{3}\times\sqrt{3}$)R30⁰-Iodine structure by thermal decomposition of a cadmium iodide multilayer [4.9]. NIXSW data was recorded for the (111) and ($\bar{1}11$) reflections using the copper Auger, iodine Auger and iodine 3p_{3/2} & 3d_{5/2} photoelectrons. The (111) data was used to show that the iodine adsorbs in the three-fold hollows, again agreeing with Citrin. The ($\bar{1}11$) data was used to perform a triangulation to determine which of the hollow sites was involved. However, the ($\bar{1}11$) data gave very low coherent fractions indicating probable multiple site adsorption (see section 2.4.5). Analysis of the data using the Argand diagram construction for NIXSW (see section 2.4.5) showed that the iodine actually adsorbs in a mixture of the two three-fold hollows. The hcp sites were slightly preferred over the fcc sites, with the ratio calculated at 60:40 %.

4.6.2 Silver(111)-($\sqrt{3}\times\sqrt{3}$)R30⁰-Iodine

Citrin [4.19] also studied the silver(111)-($\sqrt{3}\times\sqrt{3}$)R30⁰-Iodine structure formed using adsorption of iodine vapour at room temperature. SEXAFS data showed similar results to iodine adsorption on copper(111), with the adsorption site determined to be the three-fold hollows. Again it was not possible to determine which of the hcp or fcc hollows was involved.

Forstman et al [4.20] studied this system in an early demonstration of the LEED I(V) technique. The ($\sqrt{3}\times\sqrt{3}$)R30⁰-iodine structure was again prepared by room temperature adsorption from iodine vapour. The model of the overlayer chosen consisted of one iodine atom to every three silver atoms. Comparisons between the experimental and theoretical profiles showed that the fcc hollows were the preferred adsorption site.

Maglietta et al [4.21] performed a repeat LEED I(V) analysis for the silver(111)-($\sqrt{3}\times\sqrt{3}$)R30⁰-Iodine structure. They had difficulty preparing a suitable structure using room temperature adsorption as employed by the

previous studies. Although room temperature adsorption produced the required $(\sqrt{3}\times\sqrt{3})R30^0$ LEED pattern, it was adjudged not to be sharp enough to perform a reliable LEED I(V) analysis. Iodine vapour was consequently adsorbed onto the surface at elevated sample temperatures of between 100 - 150 °C to surface coverages above 1/3 monolayer. The sample was then heated for short periods to higher temperatures until LEED/AES showed that the $(\sqrt{3}\times\sqrt{3})R30^0$ -Iodine 0.33ML structure had formed. The LEED I(V) analysis was more sophisticated than that of Forstman. The initial model tested was that proposed by Forstman, with the iodine atoms distributed over a $(\sqrt{3}\times\sqrt{3})R30^0$ net on an undisturbed silver (111) surface, and the iodine adsorbed in the fcc hollow sites. The theoretical fits however, did not produce a satisfactory match to the experimental data. The best model involved occupation of both the fcc and hcp three-fold hollows, in different regions of the surface. The model produced results indicating that between 55-70 % of the iodine is adsorbed in the fcc hollow sites, with the balance in hcp sites. It was stated that although these results appear to be in contradiction to other studies of this system, it was probably the result of the different sample preparation method, which resulted in a different $(\sqrt{3}\times\sqrt{3})R30^0$ -I structure than had been studied previously.

4.6.3 Copper(111)- $(\sqrt{3}\times\sqrt{3})R30^0$ -Chlorine & Bromine

A system which shows similar behaviour to the iodine adsorption systems described above, is the co-adsorption of chlorine and bromine on copper(111) [4.22]. Each species is capable of forming a $(\sqrt{3}\times\sqrt{3})R30^0$ structure on copper(111) at coverages of 1/3 of a monolayer [4.17]. For the pure copper(111)- $(\sqrt{3}\times\sqrt{3})R30^0$ -Chlorine structure, the chlorine is known to be located in the fcc hollows from NIXSW and photoelectron diffraction data [4.17]. For this study the mixed halogen surface structure was prepared by the dissociation of 1-bromo-2-chloroethane on a copper(111) surface [4.22]. The total halogen concentration was believed to be 0.33ML with equal amounts of chlorine and bromine, which were assumed to be randomly distributed on a regular $(\sqrt{3}\times\sqrt{3})R30^0$ mesh with one halogen atom per unit mesh. NIXSW data

was recorded using the (111) and ($\bar{1}11$) reflections at 2976 eV. The fitting of the data showed that mixed site adsorption was occurring. The data was fitted to allow mixtures of the fcc and hcp hollows. The results showed a preference for the fcc hollows for both halogens. Chlorine had a fcc:hcp ratio of 75:25, with bromine giving 80:20.

4.7 Experimental results and discussion

The structure determination was carried out using the average coherent positions and coherent fractions for a selection of the data only, to remove any profiles considered to unreliable. For the (111) data, only NIXSW profiles collected from Auger peaks with the analyser in the 40^0 geometry were used, due to the Q factor affecting the photoelectron peaks. No data was used from the 90^0 analyser geometry due to the poor signal to noise ratio. For the ($\bar{1}11$) data, the data from the Auger peaks from the 40^0 data was averaged with all the data from the 90^0 geometry. This maximised the amount of data available, whilst removing any effects caused by Q or poor signal. The resultant averages are shown in Table 4.11.

Atom	(111)		(-111)	
	Coherent position	Coherent fraction	Coherent position	Coherent fraction
Copper	1.0*	0.83 ± 0.05	1.0*	0.82 ± 0.05
Iodine	0.04 ± 0.02	0.77 ± 0.05	0.85 ± 0.02	0.42 ± 0.05

Table 4.11 : NIXSW results used for structure determination

(* = value fixed)

Table 4.11 shows the copper substrate produced an average coherent fraction of 0.83 ± 0.05 which is consistent with a well-ordered surface. The iodine Auger results for the (111) data give a coherent fraction of 0.77 ± 0.05 , which is comparable to that of the copper substrate, thereby indicating that the iodine

atoms in the overlayer are not randomly located. However, for the $(\bar{1}11)$ data, the iodine coherent fraction reduces to 0.42 ± 0.05 . One possible explanation is that the disorder in the $(\bar{1}11)$ planes is higher than that of the (111) planes. However, the most likely possibility is mixed site adsorption as discussed in section 2.4.5.

Using the copper(111) layer spacing of 2.08 \AA and the iodine coherent position for the (111) data of 0.04 ± 0.02 , the (111) Cu-I layer spacing is calculated as $0.08 \pm 0.05 \text{ \AA}$ (0.04×2.08). This value is too small to be the “true” layer spacing and would produce an unrealistic nearest neighbour distance. The reason is, as described in section 2.4.5, because NIXSW only allows the determination of adsorbate layer spacings relative to the extended bulk planes of the copper. Therefore, the actual layer spacing can be 0.08 \AA or $(0.08 + 2.08) \text{ \AA}$ or $(0.08 + 2 \times 2.08) \text{ \AA}$ etc. However, only a distance of $0.08 + 2.08$ or 2.16 \AA , gives sensible values for the Cu-I distances.

Using the iodine (111) layer spacing of 2.16 \AA the Cu-I distance for various adsorption sites was calculated, assuming no reconstruction or relaxation of the copper surface. These are shown in Table 4.12.

Site	Cu-I distance / \AA
Atop	2.16
Bridge	2.51
3-fold hollow	2.61

Table 4.12 : Cu-I distances

The SEXAFS data by Citrin [4.18] gave a Cu-I distance of 2.66 \AA , Ithins [4.1] data, which concluded that the three-fold hollows were the adsorption site gave a Cu-I distance of 2.63 \AA . This suggests adsorption is at the three-fold hollows as expected, although the bridge sites are still probably within the range of experimental error.

Using the equations described in section 2.4.5 and the experimental (111) layer spacing, the expected layer spacings for the various adsorption sites relative to the ($\bar{1}11$) planes were calculated. This produced the distances listed in Table 4.13. (Note that the distance for the bridge sites is the resultant distance that would be observed by NIXSW, see section 2.4.5.)

Site	Calculated ($\bar{1}11$) distance / Å
Atop	0.72
Bridge	1.76
Fcc 3-fold hollow	2.11
Hcp 3-fold hollow	1.41

Table 4.13 : Calculated ($\bar{1}11$) layer spacings

The experimental ($\bar{1}11$) coherent position as listed in Table 4.11, was 0.85 ± 0.02 , giving an experimental ($\bar{1}11$) layer spacing of 1.77 ± 0.05 Å (2.08×0.85). At first glance Table 4.13 would therefore appear to imply that the iodine atoms occupy the bridge sites. However, as described in detail in section 2.4.5, because of the symmetry of bridge sites, the maximum possible coherent fraction for an adsorbate in bridge sites is only 0.33. The experimental coherent fraction was 0.42 ± 0.05 (see Table 4.11), significantly higher than this, thus ruling out the bridge sites.

The atop site is definitely ruled out, as its calculated ($\bar{1}11$) layer spacing is obviously too far from the experimental data. None of the remaining sites immediately appears to fit the data, however if an Argand diagram is constructed (see section 2.4.6 and Figure 4.19) plotting the ($\bar{1}11$) vectors for fcc and hcp hollow adsorption sites together with the experimental data, it becomes clear that as with Ithnins results [4.1], a mixture of iodine adsorption in the fcc and hcp hollows is the only possible model for the NIXSW data.

Instead of drawing out Argand diagrams by hand to determine the percentage occupation of each adsorption site, a new approach has been used. A simple Fortran 77 program (see Appendix) was written to model the Argand diagram construction. It calculates the resultant vector produced by combining all combinations (in steps of 1 %) of fcc and hcp hollows using simple trigonometry. A sample of the results generated by the program is shown in Table 4.14.

% fcc	% hcp	Coherent position	Coherent fraction
80	20	0.97	0.72
60	40	0.89	0.53
50	50	0.85	0.50
40	60	0.89	0.53
20	80	0.72	0.72

Table 4.14 : Adsorption site calculation results

As shown in Table 4.11 the $(\bar{1}11)$ coherent position was 0.85 ± 0.02 , the nearest match from the computer program results, as shown in Table 4.14, was a mixture consisting of 50 ± 3 % fcc sites and 50 ± 3 % hcp sites. However, the coherent fraction determined from the program is 0.50, this is higher than the experimental value of 0.42 ± 0.05 . This is due to the fact that the vectors for the individual sites in the program assumed perfect order. If these are first reduced by a factor of 0.8, which is an approximation of the possible coherent fraction for the components (from the (111) coherent fraction of 0.77 ± 0.05), then the calculated coherent fraction becomes 0.40, much closer to the experimental value. Obviously the coherent position calculated and hence the percentage occupations remain unchanged as the length of vectors are reduced by the same amount and hence the direction of the resultant vector is unchanged.

These results show that iodine is forming a mixed-site overlayer, however for an ideal $(\sqrt{3}\times\sqrt{3})R30^0$ overlayer there is only one adsorbate atom per unit cell and therefore all adsorbate atoms would have to occupy the same site. The various possibilities for domains etc. were discussed by Ithnin [4.1].

As shown in section 4.6.1, Ithnin [4.1] calculated a different percentage occupation, with a mixture of 40 % fcc and 60 % hcp. In order to compare two studies, the results from Ithnins work were processed using the new Fortran program. The computer produced a result indicating a mixture of 40 ± 3 % fcc and 60 ± 3 % hcp, confirming Ithnins conclusions, but this produces an obvious disagreement with the structure derived here. The first possibility is that the different answers are simply the result of experimental error. Ithnins $(\bar{1}11)$ coherent position was 0.795 ± 0.05 , the data here produced 0.85 ± 0.03 . If experimental errors were the cause then it is possible that the two studies produced results from identical surfaces. However, if a graph is drawn (Figure 4.20) with Ithnins data (cp 0.795, f_{co} 0.457) compared to the data here (cp 0.85, f_{co} 0.42), it is clear that the two sets of parameters actually originate from very different looking NIXSW profiles. This suggests that the actual structures studied in each case were different. The study by Maglietta [4.21] on silver used elevated surface temperatures, and the overlayer was found to consist of a mixture of fcc and hcp hollows. Maglietta suggested that the mixed overlayer was the result of the different surface preparation method used. Therefore, it is possible that a different structure has been produced here due to a different surface preparation. In theory the same method as Ithnin was used to generate the surface, but the most likely variable is the surface temperature. In conjunction with Maglietta's results this suggests that the preferred adsorption site for iodine is the fcc hollow as shown by Forstman [4.20]. But, that as the surface temperature is raised there must be some exchange with the hcp hollows. When the sample is cooled the exchange must be stopped due to an energetic barrier which freezes out the ratio attained at the higher temperature. This means that not only the maximum surface temperature reached, but the cooling rate as well could influence the surface structure produced. Another possibility for the variation in results is the state of the sample crystal.

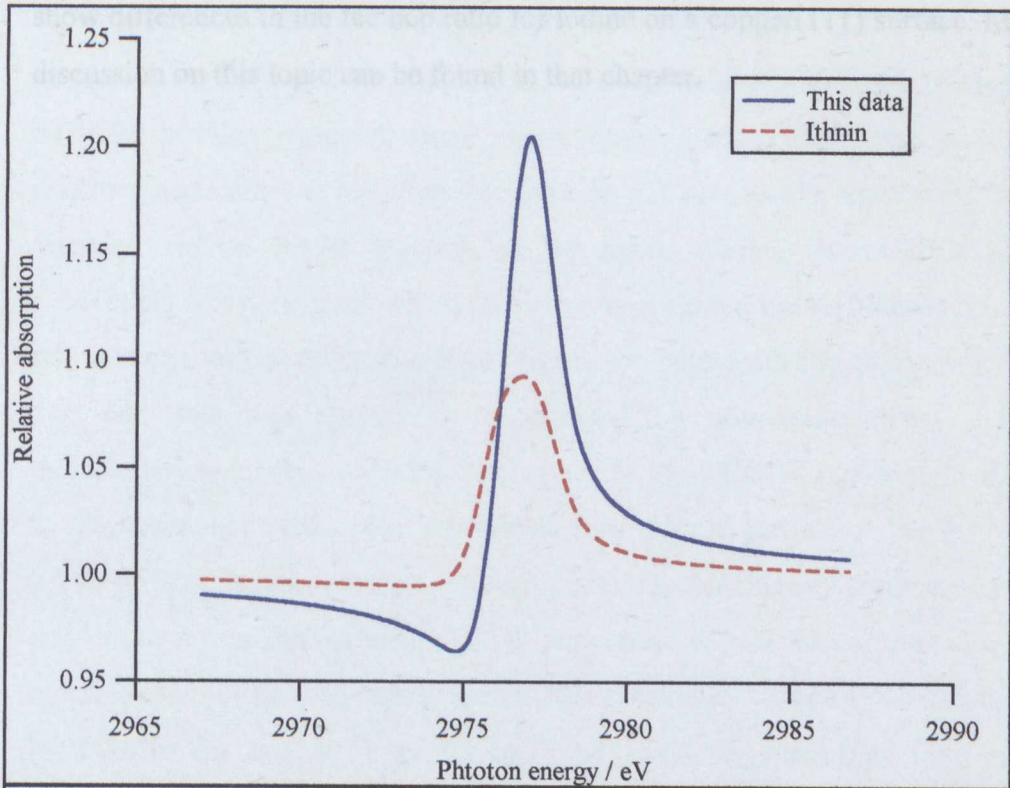


Figure 4.20 : Comparison of (-111) NIXSW fits between this work and Ithnin [4.1]

Differences in step density might lead to differences in ratios due to changes in the domain structure of the overlayer. The results presented in chapter 5, also show differences in the fcc:hcp ratio for iodine on a copper(111) surface. More discussion on this topic can be found in that chapter.

4.8 Summary

This chapter presented a NIXSW study of the copper(111)-($\sqrt{3}\times\sqrt{3}$)R30⁰-Iodine structure. Part one of the chapter examined difficulties with the fitting of NIXSW profiles obtained from photoelectron peaks where the coherent fractions and coherent positions obtained do not necessarily agree with those obtained via an Auger electron of the same species. A novel NIXSW experiment was performed where the data was collected in two geometries, one with the analyser at 40⁰ to the X-ray beam, the other with the analyser at 90⁰. The 40⁰ data was shown to be affected by non-dipole terms in the photoemission process resulting in changes to the NIXSW profiles generated by photoelectron peaks. The non-dipole terms could not affect the 90⁰ data because the collection geometry was insensitive to the changes produced by the non-dipole terms. An updated NIXSW expression was developed that allowed quantification of the non-dipole terms. This parameter, termed Q was found to be 0.00 for Cu 2s_{1/2}, 0.12 for Cu 2p_{3/2}, 0.03 for I 3p_{3/2} and 0.22 for I 3d_{5/2}. Comparisons were made with calculated values of Q, using extrapolated asymmetry parameters from Xenon orbitals.

Part two used the NIXSW data to perform a structural analysis for this surface. The data was used to show that the iodine was adsorbed in essentially equal amounts in the fcc and hcp hollows, the calculated mixture was 50 ± 3 % fcc and 50 ± 3% hcp, at a height of 2.16 Å above the copper surface. This structure was observed to be different from that determined from previous studies. No definite conclusion could be drawn as to the reason for the change in ratio, although temperature during surface preparation and the state of the crystal surface were considered.

Chapter 5: A Normal Incidence X-ray Standing Wave study of Copper(111)-($\sqrt{3}\times\sqrt{3}$)-R30⁰- $\frac{1}{2}$ (CdI₂)

5.0 Introduction

This chapter presents a NIXSW study of the structure produced by the adsorption of a cadmium iodide (CdI₂) monolayer on a copper(111) surface. The only relevant study was performed by Ithnin [5.1]. LEED and AES were used to follow the adsorption and desorption of cadmium iodide on a copper(111) surface. An important conclusion drawn from the study was that during the initial stages of adsorption there was a surface phase of $\frac{1}{2}$ (CdI₂), compared to multilayer adsorption where epitaxial growth of cadmium iodide occurred. The structure of the $\frac{1}{2}$ (CdI₂) phase formed during initial adsorption was considered to consist of a single layer of iodine atoms (0.33 ML) in a ($\sqrt{3}\times\sqrt{3}$)-R30⁰ arrangement, with 0.16 ML of cadmium. The cadmium was assumed to be randomly located or the unit mesh would have been larger than the observed ($\sqrt{3}\times\sqrt{3}$)-R30⁰. It was postulated that the iodine was located in the three-fold hollow sites, with the cadmium atoms located randomly in three-fold hollows below the iodine.

The aim of this study was twofold, first of all it was to determine the structure of the $\frac{1}{2}$ (CdI₂) surface phase using NIXSW. The second aim was to find Q values (see chapter 4) for some of the cadmium photoelectron peaks. As it was expected that they would be of similar magnitude to the I 3d Q value (0.22) as discussed in the last chapter, due to their shallow binding energies.

5.1 Experimental methods

As with chapter 4 all experiments were carried out on beamline 6.3 of the SRS at Daresbury Laboratory. Details of the beamline and the experimental UHV chamber can be found in sections 3.2 and 3.2.1.

Before NIXSW experiments could be performed, it was necessary to determine the correct exposure of cadmium iodide needed to form the $\frac{1}{2}(\text{CdI}_2)$ monolayer structure. The previous study [5.1] had shown that the $\frac{1}{2}(\text{CdI}_2)$ surface contains exactly the same iodine coverage as the $(\sqrt{3}\times\sqrt{3})\text{-R}30^\circ$ -Iodine structure. The iodine surface was prepared by the same method used in chapter 4, by adsorption of a cadmium iodide multilayer followed by annealing to 473 K. A different cadmium iodide source & pellet was used, which meant the operating temperature of the source was 473 K, lower than that in chapter 4. A higher source temperature would have been preferential to allow shorter adsorption times, however the pellet was producing gaseous contaminants (H_2O , CO_2 , CO etc) and even at 473 K the pressure in the chamber rose to 2×10^{-9} mbar, any higher source temperature would have produced too many contaminants.

Following annealing to 473 K, LEED showed the expected $(\sqrt{3}\times\sqrt{3})\text{-R}30^\circ$ LEED pattern. Electron induced AES of this surface showed only copper and iodine peaks, no carbon, oxygen or sulphur contamination was observed. Photon stimulated EDCs ($h\nu = 3000$ eV) were then recorded of the iodine Auger and copper Auger with the sample in the $(\bar{1}11)$ position, to provide accurate ratios for calibration. This determined an I:Cu peak-to-peak height ratio of 0.29:1. All photon stimulated EDCs were recorded with the sample in the same geometry to ensure reproducibility.

The copper(111) crystal was then cleaned and annealed again. Cadmium iodide was adsorbed onto the surface for ~300 seconds at a time. In between

adsorption cycles, photon stimulated EDCs at a photon energy of 3000 eV were recorded of the copper and iodine Auger peaks, until the I:Cu ratio was 0.28 at an adsorption time of 2100 seconds. This value for the I:Cu ratio is slightly lower than that for the pure iodine monolayer. This value was selected since adsorbing beyond the monolayer structure would result in more than one cadmium and iodine height above the scatterer planes which would have complicated the NIXSW data. LEED of this surface produced a good $(\sqrt{3}\times\sqrt{3})\text{-R}30^\circ$ pattern as expected. Photon induced Auger measurements showed that the Cd:I ratio was 0.75:1, this value indicates that the stoichiometry is the same as multilayer growth, i.e. CdI_2 , thereby showing that the surface formed is indeed the $\frac{1}{2}(\text{CdI}_2)$ phase.

The sample was set-up for NIXSW as described in section 3.5.1. However, an additional piece of apparatus had been fitted to the chamber, this was a photodiode to measure the intensity of the reflected beam. The purpose of this was to allow the determination of the non-structural parameters, i.e. the energy broadening and the Bragg energy, instead of using the substrate NIXSW profile. Due to experimental difficulties this was not used, however the sample position was set so that the reflected X-ray beam from the crystal intersected with the photodiode to produce a maximum signal for all experiments to ensure a consistent geometry. The diode itself was placed as close as possible to the beam entrance position, to make the scatterer planes as normal as possible to the X-ray beam. In order to prevent the diode obstructing the X-ray beam and reducing the X-ray flux at the sample, its side was coated with fluorescent paint. Therefore, if a glow from it was observed then the sample and diode positioning was repeated until no glow was observed.

As with the experiments described in chapter 4, both the (111) and $(\bar{1}\bar{1}\bar{1})$ reflections from the copper(111) surface at a photon energy of ~ 2963 eV were used to record NIXSW profiles. EDCs taken of the $\frac{1}{2}(\text{CdI}_2)$ structure were

used to determine the binding energies of the photoelectron peaks and the kinetic energies of the relevant Auger peaks, see Table 5.1 and Figure 5.1.

Peak	Auger Electron Kinetic Energy / eV		Photoelectron Binding energy / eV	
	ON	OFF	ON	OFF
Cu LVV Auger	909	922	-	-
Cu 2p _{1/2}	-	-	958	920
I MNN Auger	501	525	-	-
Cd Auger	370	395	-	-
Cd 3p _{1/2}	-	-	659	600
Cd 3d _{5/2}	-	-	413	397

Table 5.1 : Table of peaks and ON/OFF positions used

Note that the I 3d_{5/2} and the Cd 3p_{3/2} photoelectron peaks overlapped, hence neither could be used. The I 3d_{3/2} photoelectron peak could have been used instead, but its Q value was unknown, therefore it also was not used. The Cu 2p_{1/2} photoelectron peak was recorded to provide a test of the Q value determined in chapter 4.

As noted in chapters 3 and 4 only four ON/OFF peak combinations could be recorded within an individual NIXSW experiment. Since more than four peaks were required, the experiment was repeated using a different set of peaks on the same surface preparation with no sample movement, to ensure consistency. At least three NIXSW scans were recorded for each peak for different surface preparations to provide data averaging.

As stated in section 5.0, the cadmium 3d_{5/2} and 3p_{1/2} photoelectrons were predicted to have a non-zero Q value. It was expected that the Q values would be obtained by using the NIXSW parameters from the cadmium Auger profile

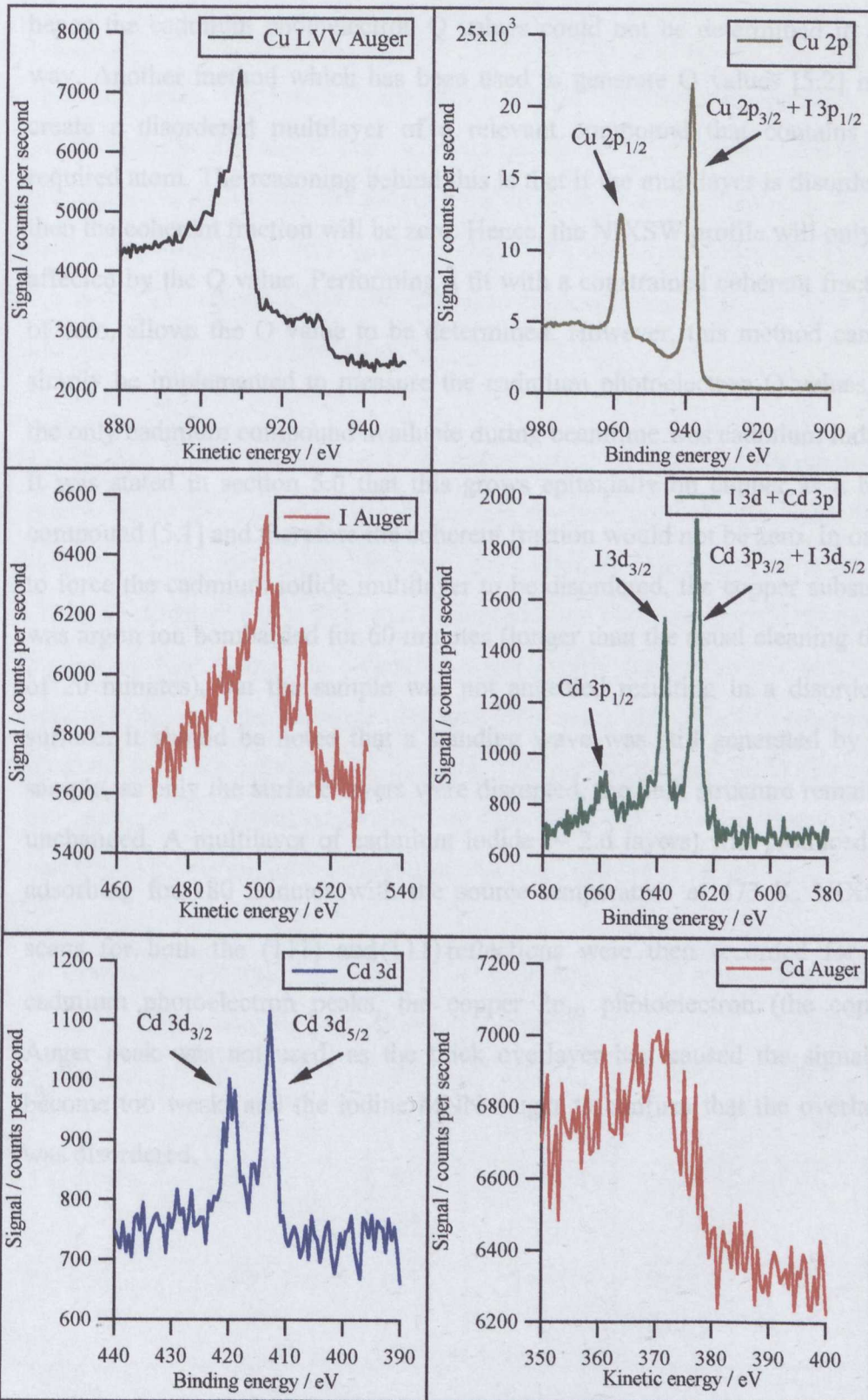


Figure 5.1 : High resolution EDCs

All EDCs recorded at a photon energy of 3000 eV, with 0.2 eV increments.
Counting times were between 2 and 5 seconds depending upon the peak.

to fit the cadmium photoelectron peaks, as described in chapter 4. However, as will be discussed later, the cadmium Auger NIXSW data was unreliable and hence the cadmium photoelectron Q values could not be determined in this way. Another method which has been used to generate Q values [5.2] is to create a disordered multilayer of a relevant compound that contains the required atom. The reasoning behind this is that if the multilayer is disordered then the coherent fraction will be zero. Hence, the NIXSW profile will only be affected by the Q value. Performing a fit with a constrained coherent fraction of zero, allows the Q value to be determined. However, this method cannot simply be implemented to measure the cadmium photoelectron Q values, as the only cadmium compound available during beamtime was cadmium iodide. It was stated in section 5.0 that this grows epitaxially on copper as a bulk compound [5.1] and therefore the coherent fraction would not be zero. In order to force the cadmium iodide multilayer to be disordered, the copper substrate was argon ion bombarded for 60 minutes (longer than the usual cleaning time of 20 minutes), but the sample was not annealed resulting in a disordered surface. It should be noted that a standing wave was still generated by the sample, as only the surface layers were disrupted, the bulk structure remained unchanged. A multilayer of cadmium iodide (~ 2.6 layers) was produced by adsorbing for 180 minutes with the source temperature at 473 K. NIXSW scans for both the (111) and $(\bar{1}\bar{1}\bar{1})$ reflections were then recorded for the cadmium photoelectron peaks, the copper $2p_{1/2}$ photoelectron (the copper Auger peak was not used, as the thick overlayer had caused the signal to become too weak) and the iodine MNN Auger to confirm that the overlayer was disordered.

5.2 Results

Figure 5.2 shows the (111) NIXSW experimental profiles for the various cadmium peaks. The figure clearly shows that the three cadmium peaks do not produce identical profiles. The cadmium photoelectron peaks are affected by non-dipole terms as with the iodine photoelectron peaks in chapter 4. All the cadmium profiles look very similar to that of the copper substrate (see Figures 5.6 and 5.7) indicating that the cadmium layer spacing must be close to a multiple of the copper layer spacing.

Figure 5.3 shows the $(\bar{1}11)$ NIXSW experimental profiles for the cadmium peaks. Again the cadmium photoelectrons produce profiles that differ from that of the cadmium Auger. However, the cadmium Auger appears to have a distinctly different shape from that of the cadmium photoelectrons. This can be proved by first fitting the cadmium Auger profile (using the non-structural parameters from the substrate fit) and then using the NIXSW parameters obtained to fit the cadmium $3d_{5/2}$ profile. This has been done and is illustrated in Figure 5.4. The fitting parameters are shown in Table 5.2. Note that the only variable in the fitting for the cadmium $3d_{5/2}$ peak was the Q value.

Peak	Energy broadening	Coherent position	Coherent fraction	Q	Bragg energy / eV
Cu Auger	0.63 ±0.03	1.00*	0.85 ± 0.05	0.00*	2972.2 ± 0.1
Cd Auger	0.63*	0.96 ± 0.02	0.54 ± 0.05	0.00*	2972.2*
Cd $3d_{5/2}$	0.63*	0.96*	0.54*	0.25 ± 0.02	2972.2*

Table 5.2 : Fitting parameters for Cd Auger and Cd $3d_{5/2}$ from Figure 5.4

*** denotes constrained parameter in fit**

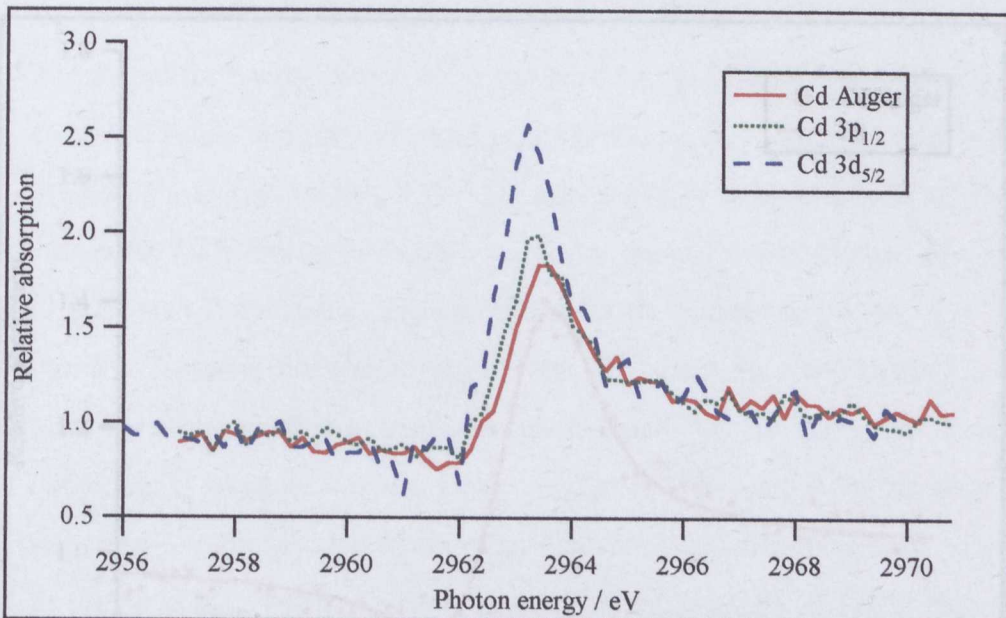


Figure 5.2 : Cadmium (111) NIXSW data

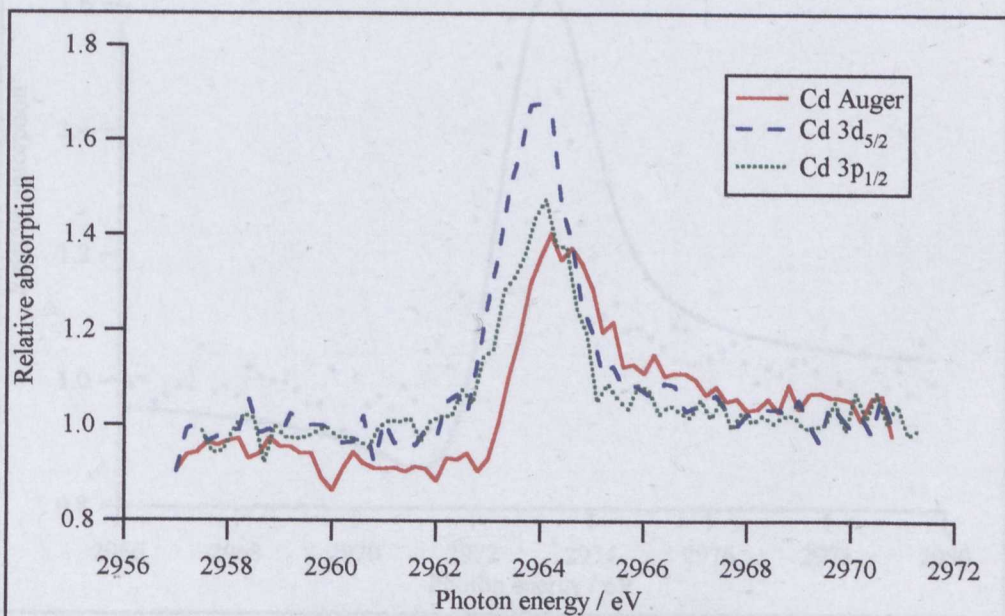


Figure 5.3 : Cadmium (-111) NIXSW data

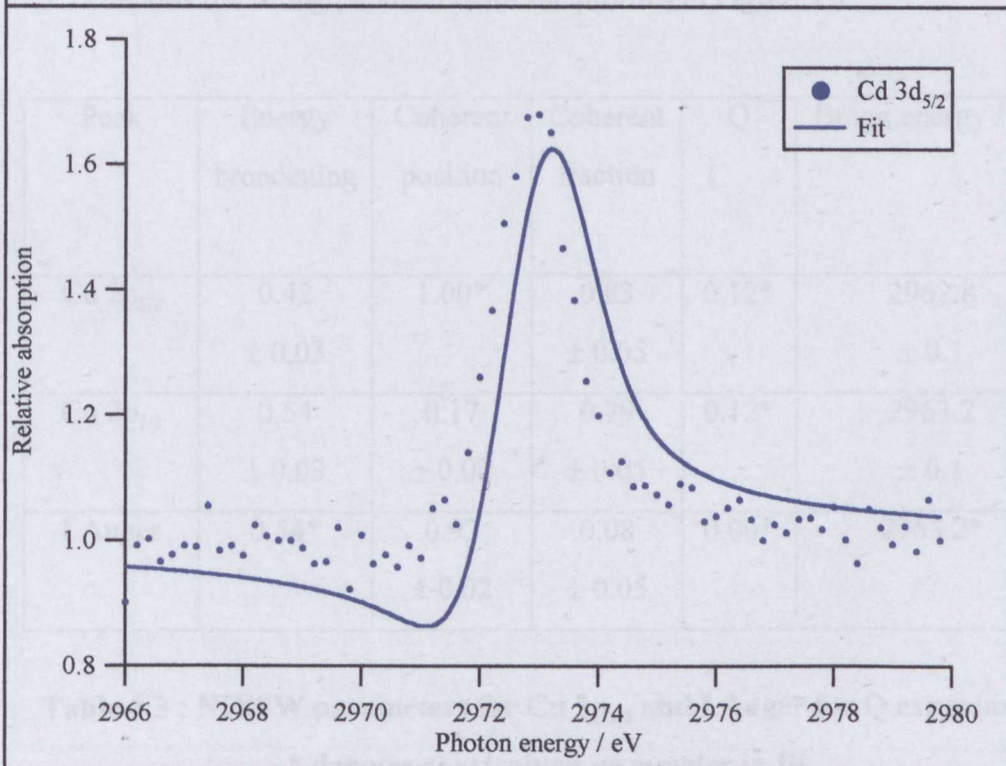
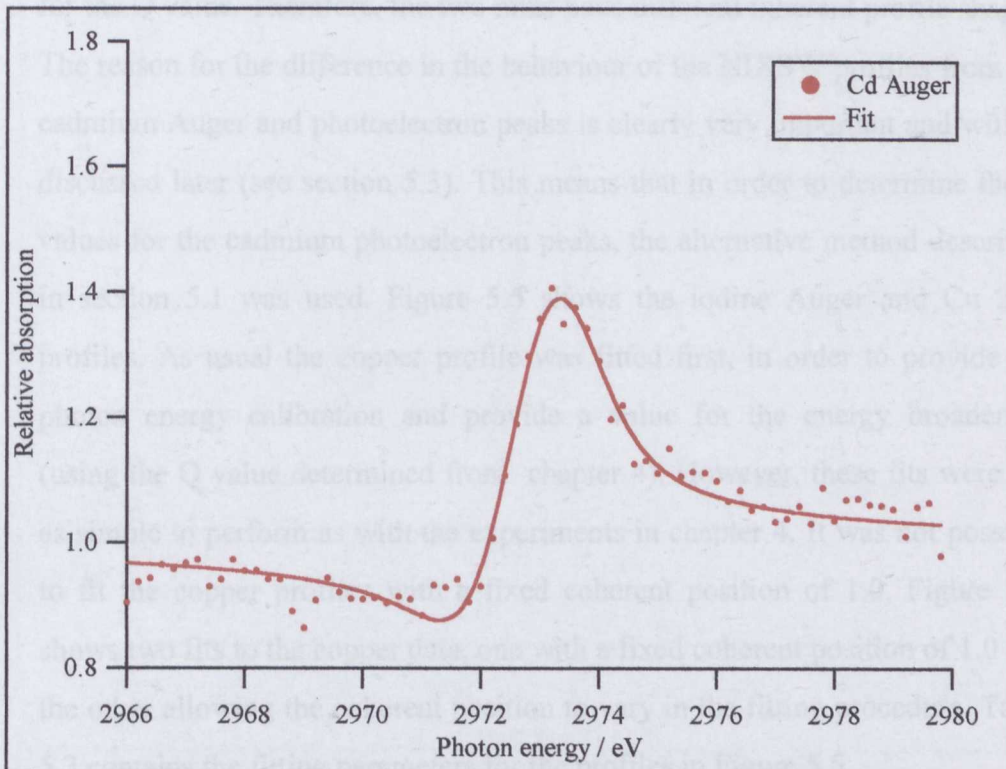


Figure 5.4 : Cadmium Auger and $3d_{5/2}$ profiles from (-111) reflection

Top graph shows cadmium Auger profile and fit. Bottom graph shows the cadmium 3d profile fitted with all parameters except Q fixed at those from the cadmium Auger profile.

This shows that the cadmium Auger is a different shape from the photoelectron peak.

Figure 5.4 clearly shows that the cadmium $3d_{5/2}$ profile will not fit to the NIXSW parameters obtained from the cadmium Auger profile, even allowing for the Q value. Therefore, the two must have different inherent profile shapes. The reason for the difference in the behaviour of the NIXSW profiles from the cadmium Auger and photoelectron peaks is clearly very important and will be discussed later (see section 5.3). This means that in order to determine the Q values for the cadmium photoelectron peaks, the alternative method described in section 5.1 was used. Figure 5.5 shows the iodine Auger and Cu $2p_{1/2}$ profiles. As usual the copper profile was fitted first, in order to provide the photon energy calibration and provide a value for the energy broadening (using the Q value determined from chapter 4). However, these fits were not as simple to perform as with the experiments in chapter 4. It was not possible to fit the copper profiles with a fixed coherent position of 1.0. Figure 5.5, shows two fits to the copper data, one with a fixed coherent position of 1.0 and the other allowing the coherent position to vary in the fitting procedure. Table 5.3 contains the fitting parameters for the profiles in Figure 5.5.

Peak	Energy broadening	Coherent position	Coherent fraction	Q	Bragg energy / eV
Cu $2p_{1/2}$	0.42 ± 0.03	1.00*	0.83 ± 0.05	0.12*	2962.8 ± 0.1
Cu $2p_{1/2}$	0.54 ± 0.03	0.17 ± 0.02	0.79 ± 0.05	0.12*	2963.2 ± 0.1
I Auger	0.54*	0.92 ± 0.02	0.08 ± 0.05	0.00*	2963.2*

Table 5.3 : NIXSW parameters for Cu $2p_{1/2}$ and I Auger for Q experiment

*** denotes constrained parameter in fit**

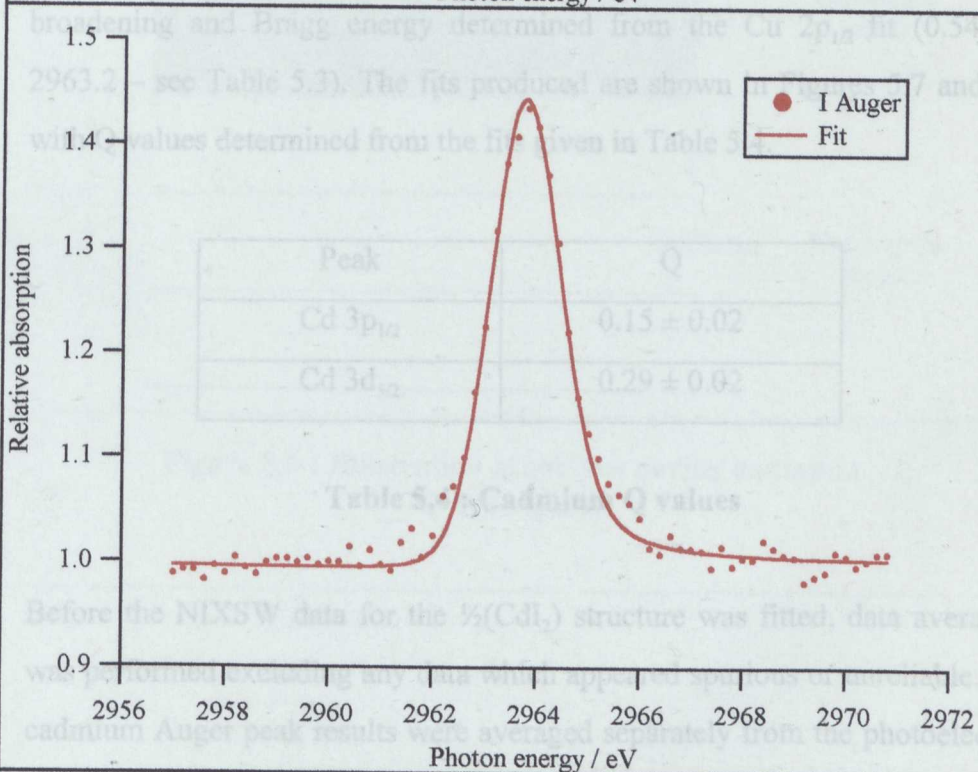
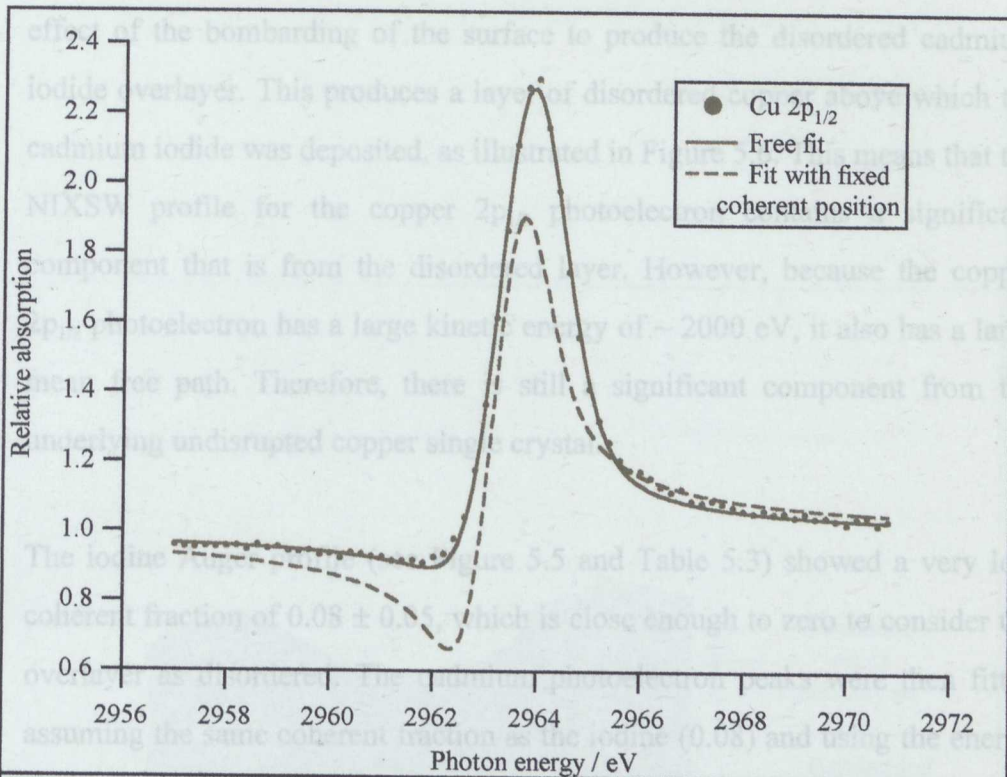


Figure 5.5 : Copper & Iodine NIXSW data for Q experiment

NIXSW data is shown as markers with the fits as lines.

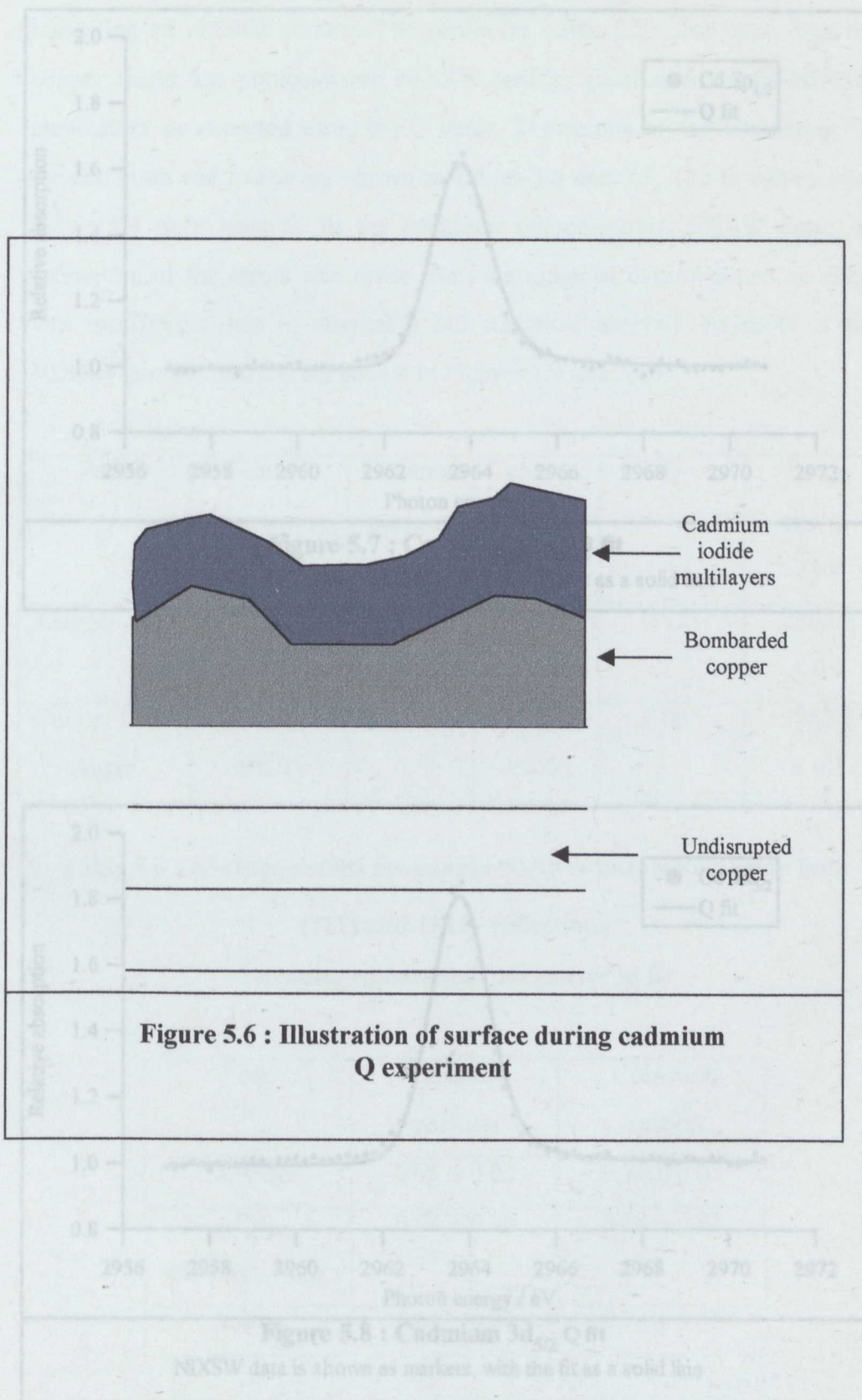
It is immediately apparent that the variable coherent position (0.17 ± 0.02) produces a better fit to the copper $2p_{1/2}$ experimental data. This is due to the effect of the bombarding of the surface to produce the disordered cadmium iodide overlayer. This produces a layer of disordered copper above which the cadmium iodide was deposited, as illustrated in Figure 5.6. This means that the NIXSW profile for the copper $2p_{1/2}$ photoelectron contains a significant component that is from the disordered layer. However, because the copper $2p_{1/2}$ photoelectron has a large kinetic energy of ~ 2000 eV, it also has a large mean free path. Therefore, there is still a significant component from the underlying undisrupted copper single crystal.

The iodine Auger profile (see Figure 5.5 and Table 5.3) showed a very low coherent fraction of 0.08 ± 0.05 , which is close enough to zero to consider the overlayer as disordered. The cadmium photoelectron peaks were then fitted assuming the same coherent fraction as the iodine (0.08) and using the energy broadening and Bragg energy determined from the Cu $2p_{1/2}$ fit (0.54 and 2963.2 – see Table 5.3). The fits produced are shown in Figures 5.7 and 5.8, with Q values determined from the fits given in Table 5.4.

Peak	Q
Cd $3p_{1/2}$	0.15 ± 0.02
Cd $3d_{5/2}$	0.29 ± 0.02

Table 5.4 : Cadmium Q values

Before the NIXSW data for the $\frac{1}{2}(\text{CdI}_2)$ structure was fitted, data averaging was performed excluding any data which appeared spurious or unreliable. The cadmium Auger peak results were averaged separately from the photoelectron peaks to confirm that different results are obtained compared to the cadmium photoelectrons. Again, the copper data was used to provide the energy broadening and the Bragg energy, see Table 5.5. For the Cu $2p_{1/2}$ photoelectron



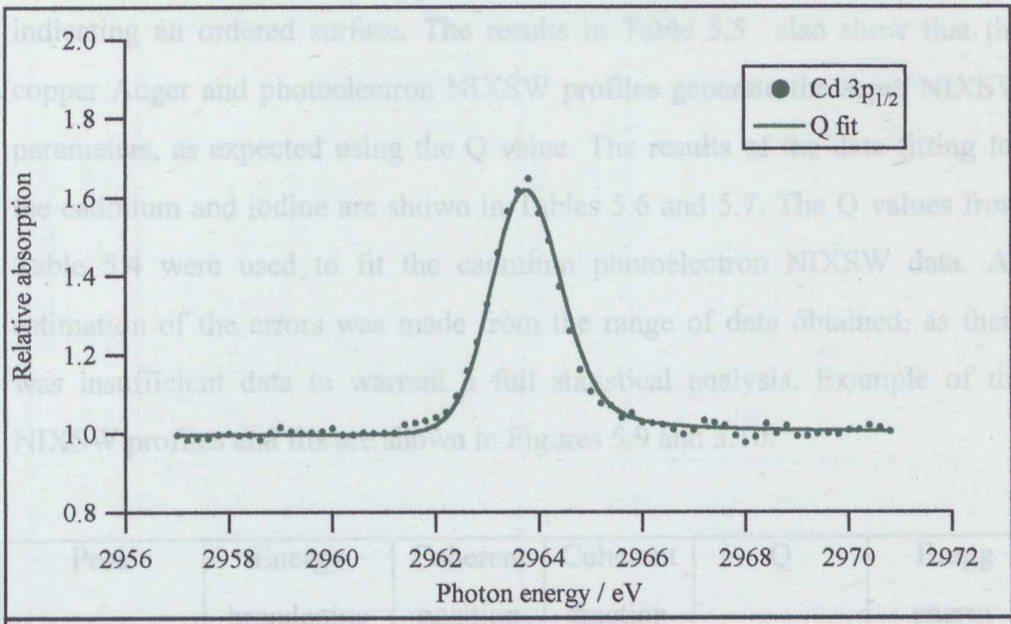


Figure 5.7 : Cadmium 3p_{1/2} Q fit
 NIXSW data is shown as markers, with the fit as a solid line

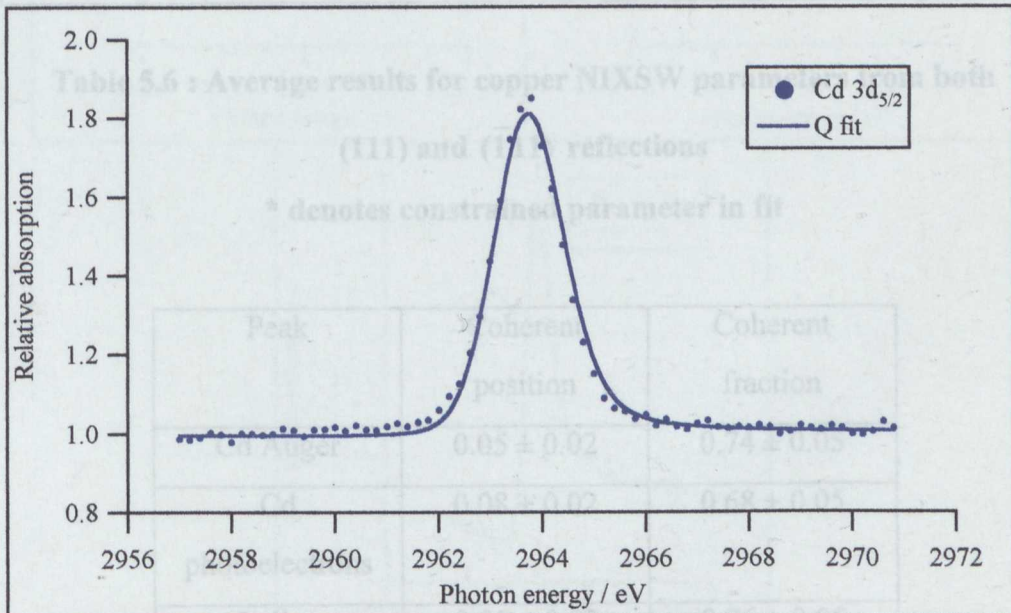


Figure 5.8 : Cadmium 3d_{5/2} Q fit
 NIXSW data is shown as markers, with the fit as a solid line

Peak	Coherent position	Coherent fraction	Q value	Peak position / eV
Copper 3p _{1/2}	0.48 ± 0.03	1.00*	0.85 ± 0.05	2962.8 ± 0.1
Copper LVV	0.52 ± 0.03	1.00*	0.82 ± 0.05	2962.8 ± 0.1
Auger	0.05 ± 0.02	0.74 ± 0.02	0.88 ± 0.02	2963.5 ± 0.1

data, the Q value determined in chapter 4 was used (0.12). The average coherent fraction for the copper substrate was found to be 0.84 ± 0.01 , indicating an ordered surface. The results in Table 5.5 also show that the copper Auger and photoelectron NIXSW profiles generate the same NIXSW parameters, as expected using the Q value. The results of the data fitting for the cadmium and iodine are shown in Tables 5.6 and 5.7. The Q values from Table 5.4 were used to fit the cadmium photoelectron NIXSW data. An estimation of the errors was made from the range of data obtained, as there was insufficient data to warrant a full statistical analysis. Example of the NIXSW profiles and fits are shown in Figures 5.9 and 5.10.

Peak	Energy broadening / eV	Coherent position	Coherent fraction	Q	Bragg energy / eV
Copper $2p_{1/2}$	0.48 ± 0.03	1.00*	0.86 ± 0.05	0.12*	2962.8 ± 0.1
Copper LVV Auger	0.52 ± 0.03	1.00*	0.82 ± 0.05	0.00*	2962.8 ± 0.1

Table 5.6 : Average results for copper NIXSW parameters from both (111) and $\bar{1}\bar{1}\bar{1}$ reflections

*** denotes constrained parameter in fit**

Peak	Coherent position	Coherent fraction
Cd Auger	0.05 ± 0.02	0.74 ± 0.05
Cd photoelectrons	0.08 ± 0.02	0.68 ± 0.05
Iodine	0.01 ± 0.02	0.76 ± 0.05

Tables 5.6 : (111) NIXSW results

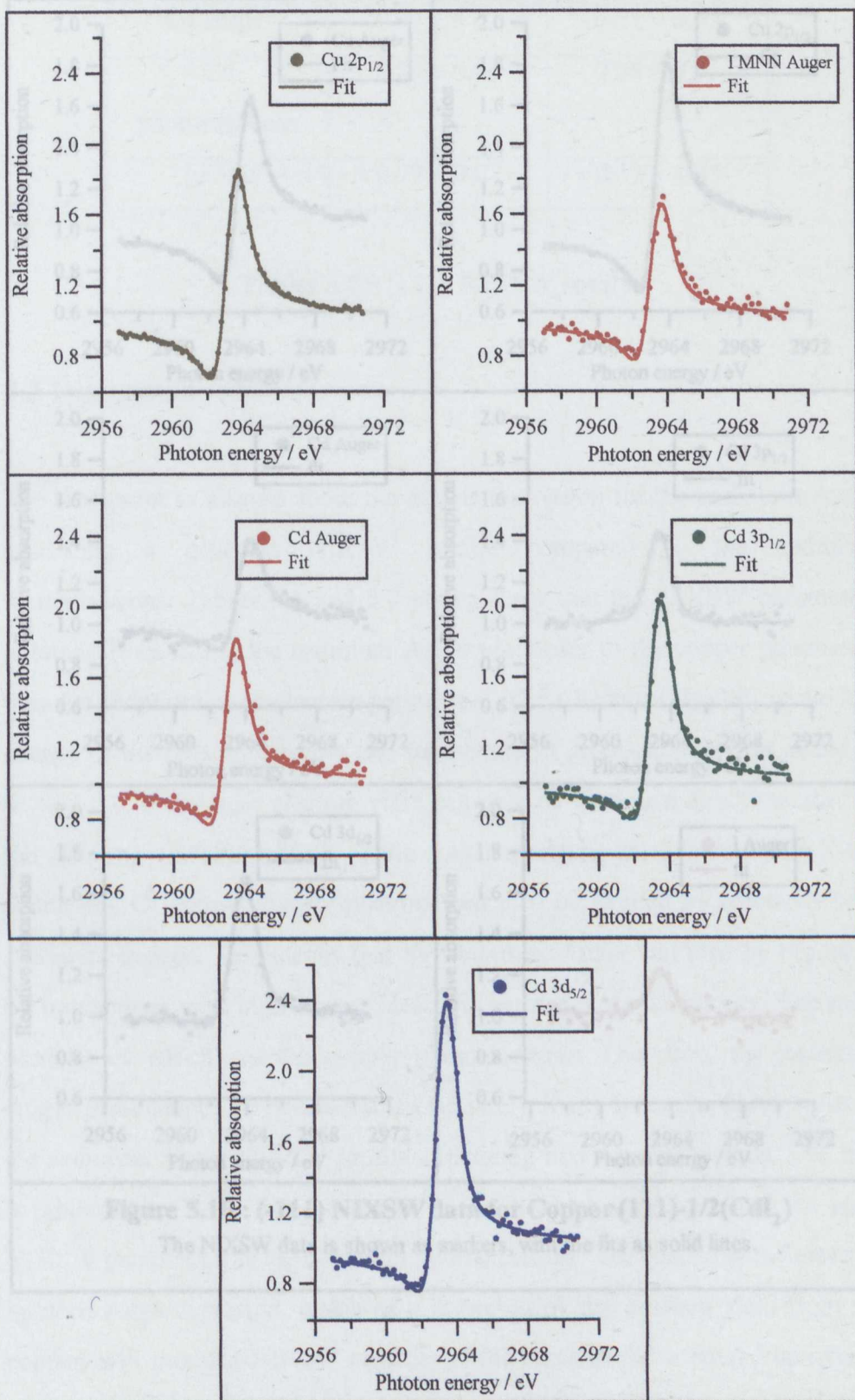


Figure 5.9 : (111) NIXSW data for Copper (111)-1/2(CdI₂)
 The NIXSW data is shown as markers with the fits as solid lines.

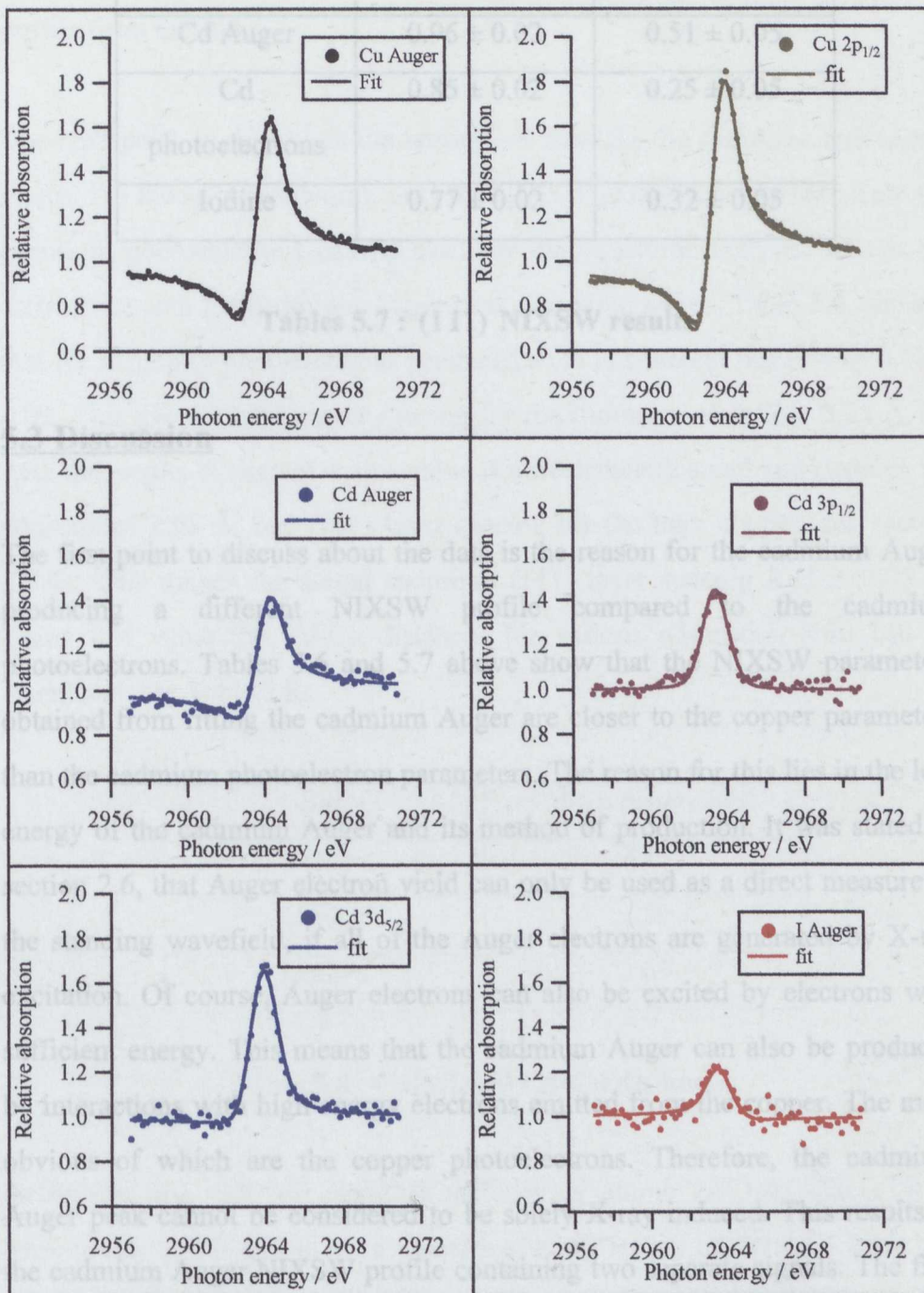


Figure 5.10 : (-111) NIXSW data for Copper (111)-1/2(CdI₂)

The NIXSW data is shown as markers, with the fits as solid lines.

Peak	Coherent Position	Coherent Fraction
Cd Auger	0.96 ± 0.02	0.51 ± 0.05
Cd photoelectrons	0.85 ± 0.02	0.25 ± 0.05
Iodine	0.77 ± 0.02	0.32 ± 0.05

Tables 5.7 : (111) NIXSW results

5.3 Discussion

The first point to discuss about the data is the reason for the cadmium Auger producing a different NIXSW profile compared to the cadmium photoelectrons. Tables 5.6 and 5.7 above show that the NIXSW parameters obtained from fitting the cadmium Auger are closer to the copper parameters than the cadmium photoelectron parameters. The reason for this lies in the low energy of the cadmium Auger and its method of production. It was stated in section 2.6, that Auger electron yield can only be used as a direct measure of the standing wavefield, if all of the Auger electrons are generated by X-ray excitation. Of course, Auger electrons can also be excited by electrons with sufficient energy. This means that the cadmium Auger can also be produced by interactions with high energy electrons emitted from the copper. The most obvious of which are the copper photoelectrons. Therefore, the cadmium Auger peak cannot be considered to be solely X-ray induced. This results in the cadmium Auger NIXSW profile containing two separate signals. The first is produced by X-ray induced Auger emission which would produce the same NIXSW parameters as the cadmium photoelectrons. The second is the electron induced Auger emission, which as it is caused by the electron yield from the copper, will produce NIXSW parameters the same as the copper. The overall profile produced therefore results from a mixture of these two separate elements, producing NIXSW parameters that are also a mixture. If the actual

portion of the cadmium Auger electrons generated by the secondary electrons was known, it might be possible to extract the “real” cadmium Auger NIXSW profile from the data.

The next point to discuss is the adsorption sites for the cadmium and iodine atoms. For the cadmium atoms, only the NIXSW parameters obtained from the cadmium photoelectrons can be used for the structural analysis, due to the difficulties with the cadmium Auger peak discussed above. Table 5.6, showed that the cadmium photoelectrons produced a (111) coherent position of 0.08 ± 0.02 . This gives a (111) layer spacing for the cadmium of 0.17 ± 0.05 Å. As with the results in chapter 4, this value is unrealistically small and requires the addition of 2.08 Å, one (111) layer spacing for the bulk copper (see section 2.6.4). This makes the actual cadmium (111) layer spacing 2.25 ± 0.05 Å. Using this value the Cd-Cu distances for various adsorption sites can be calculated, see Table 5.8.

Site	Cd-Cu distance /Å
Atop	2.25
Bridge	2.59
Hollow	2.69

Table 5.8 : Calculated Cd-Cu distances

Given that the radii of cadmium and copper atoms are 1.48 and 1.28 Å respectively [5.3], this gives a theoretical bond length of 2.76 Å. Table 5.8 shows that the closest match is the hollow sites. In order to test this, and to determine which of the hollow sites is involved, it is necessary to use the $(\bar{1}11)$ NIXSW data. The experimental (111) layer spacing of 2.25 ± 0.05 Å was used to calculate the expected distances relative to the $(\bar{1}11)$ planes. This produced the values in Table 5.9. Note that the value shown for the bridge

sites is the resultant distance which would be observed by the NIXSW experiment (see section 2.6.5).

Adsorption Site	Calculated (-111) Distance / Å
Atop	0.75
Bridge	1.79
hcp hollow	1.44
fcc hollow	2.14

Table 5.9 : Calculated ($\bar{1}11$) distances for various adsorption sites

The ($\bar{1}11$) coherent fraction for the cadmium was 0.85 ± 0.02 , giving a ($\bar{1}11$) layer spacing of 1.77 ± 0.05 Å. Table 5.9 shows that the closest match is for the bridge sites. Section 2.6.5 showed that for bridge site occupation the maximum coherent fraction observable was 0.33. Table 5.7 shows that the experimental ($\bar{1}11$) coherent fraction is indeed lower than this (0.25 ± 0.05). However, the (111) data discussed above showed that the hollow sites were the probable location, as was suggested in the initial study of this system [5.1]. The only way for hollow sites to be involved is that multiple site adsorption is occurring, as with the results in chapter 4, with a mixture of both the fcc and hcp hollow sites involved. Using the Fortran computer program described in chapter 4 (see Appendix) to model the Argand diagram construction, a theoretical set of NIXSW parameters was calculated assuming perfect order of each component, for each combination of the hcp and fcc hollows from 0-100 % in 1 % steps. Table 5.10 shows the a selection of results from the calculation.

% fcc	% hcp	Coherent position	Coherent fraction
80	20	0.99	0.72
60	40	0.91	0.53
50	50	0.86	0.50
48	52	0.85	0.50
40	60	0.81	0.53
20	80	0.73	0.72

Table 5.10 : Calculated coherent position and coherent fraction for various percentage occupations of fcc and hcp hollows

The closest match from Table 5.10 to the experimental $(\bar{1}11)$ coherent position gives a ratio that consists of 48 ± 3 % fcc and 52 ± 3 % hcp. However, the calculation gives a coherent fraction of 0.5, which compares to the experimental value of 0.25 ± 0.05 . The reason is the assumption of perfect order in each of the hollow sites contributions to the resultant vector in the Argand diagram. The (111) coherent fraction from the cadmium NIXSW profiles was only 0.68 ± 0.05 , much less than 1.0. Reducing the individual components in the program produces a calculated coherent fraction of 0.34. This is still higher than the experimental value, although it does lie within the extremes of experimental error. The most probable explanation for the difference is that the NIXSW data was all collected at room temperature. This means that there could be considerable vibration & movement of the cadmium atoms resulting in a lowering of the coherent fraction. Another possibility is that there is more disorder relative to the $(\bar{1}11)$ planes than there is relative to the (111) planes [5.4].

For the iodine atoms, the (111) coherent position was 0.01 ± 0.02 , giving a layer spacing of 0.02 ± 0.05 Å. Therefore, as with the cadmium atoms, it is necessary to add 2.08 Å, the bulk (111) copper layer spacing, to give a realistic

(111) layer spacing for the iodine of $2.10 \pm 0.05 \text{ \AA}$. The I-Cu distances were calculated using this layer spacing and are shown in Table 5.11.

Site	Calculated I-Cu distance / \AA
Atop	2.10
Bridge	2.45
Hollow	2.56

Table 5.11 : Calculated I-Cu distances

Given that the radii of iodine and copper atoms are 1.34 \AA and 1.28 \AA [5.4], this gives a theoretical I-Cu distance of 2.61 \AA . As with the cadmium atoms, the closest match is for the hollow sites. Note, however that the estimation of the iodine atom size is sufficiently poor, that the bridge sites cannot be ruled out on this basis. Therefore, as usual it is necessary to use the $(\bar{1}\bar{1}1)$ NIXSW data to completely define the adsorption site for the iodine atoms.

Using the (111) layer spacing of $2.10 \pm 0.05 \text{ \AA}$ for the iodine atoms, the expected distance relative to the $(\bar{1}\bar{1}1)$ planes was calculated using the equations given in section 2.6.4. The distances produced are shown in Table 5.12.

Adsorption Site	Calculated $(\bar{1}\bar{1}1)$ Distance / \AA
Atop	0.70
Bridge	1.74
hcp hollow	1.39
fcc hollow	2.09

Table 5.12 : Calculated $(\bar{1}\bar{1}1)$ layer spacings

Table 5.7 gave the $(\bar{1}11)$ coherent position for the iodine as 0.77 ± 0.02 , which makes the $(\bar{1}11)$ layer spacing 1.60 ± 0.05 Å. Table 5.12 shows that the atop site can immediately be ruled out as its layer spacing is clearly too small. The closest match is for the bridge sites, however they can also be ruled out because the experimental coherent fraction for the iodine is too large for bridge site occupation. Note, that although the $(\bar{1}11)$ iodine coherent fraction of 0.32 ± 0.05 is less than the maximum observable for bridge site occupation (see section 2.6.5). The effective coherent fraction for the iodine would be 0.97 ($0.32/0.33$). This is much higher than the observed (111) coherent fraction of 0.76 ± 0.05 , thereby ruling out the bridge sites.

The only remaining solution is again a combination of the fcc and hcp hollows, as for the cadmium atoms discussed earlier, and for the results described in chapter 4. The Fortran program (see Appendix) was again used to model the Argand diagram construction to determine the ratio between the two hollow sites. As with the cadmium atoms, the initial calculation assumed perfect order in the components before calculating the resultant vector. The results generated are shown in Table 5.13.

% fcc	% hcp	Coherent position	Coherent fraction
80	20	0.96	0.72
60	40	0.89	0.53
50	50	0.84	0.50
40	60	0.78	0.53
37	63	0.77	0.55
20	80	0.71	0.72

Table 5.13 : Site occupation calculation for I in $\frac{1}{2}(\text{CdI}_2)$

Table 5.13 indicates that the closest match to the experimental data is a ratio that consists of 37 ± 3 % occupation of the fcc hollows and 63 ± 3 % occupation of the hcp hollows. Reducing the coherent fraction of the components before calculating the resultant by the (111) coherent fraction of 0.76, produces a calculated coherent fraction of 0.41. Again, this is higher than the experimental value of 0.32, but as with the cadmium data was taken at room temperature so some vibration and movement would be expected. Although as stated earlier it is quite common for there to be more disorder relative to the $(\bar{1}11)$ planes [5.4].

It was stated earlier that the $\frac{1}{2}(\text{CdI}_2)$ surface consists of 0.33 ML of iodine, with 0.16 ML of cadmium. The LEED pattern was shown to be $(\sqrt{3} \times \sqrt{3})\text{-R}30^\circ$. Chapter 4 showed that iodine adsorption on copper forms a $(\sqrt{3} \times \sqrt{3})\text{-R}30^\circ$ structure with the iodine atoms located in a mixture of the fcc and hcp hollows, also with an associated iodine coverage of 0.33 ML. The structure formed by the $\frac{1}{2}(\text{CdI}_2)$ layer, is therefore assumed to have iodine in a $(\sqrt{3} \times \sqrt{3})\text{-R}30^\circ$ arrangement. The NIXSW results presented show this adsorbs in mixed hollow sites, consisting of 37 ± 3 % in the fcc hollows with the remainder of 63 ± 3 % in the hcp hollows. The cadmium atoms as shown earlier also adsorb in a mixture of the three-fold hollow sites (48 ± 3 % fcc and 52 ± 3 % hcp), however the cadmium must be randomly located, because of its lower surface coverage. If the cadmium had formed an ordered structure then the unit mesh for the structure would have been larger, which would have changed the observed $(\sqrt{3} \times \sqrt{3})\text{-R}30^\circ$ pattern. Figure 5.11 shows a schematic diagram of the structure proposed for this system (produced using a freeware ray-tracing program [5.5]). As discussed by Ithnin [5.6], a perfect $(\sqrt{3} \times \sqrt{3})\text{R}30^\circ$ structure should consist of one domain, with the adsorbate in one adsorption site. The data for the iodine clearly shows that this is not the case, as with the results in chapter 4. Ithnin [5.6] also discussed the need for further experiments to determine the cause of the mixed site adsorption.

A further NIXSW experiment was performed after annealing the $\frac{1}{2}(\text{CdI}_2)$ layer to 473 K. The purpose of this was to force the formation of the copper (111)- $(\sqrt{3}\times\sqrt{3})\text{R}30^\circ$ -iodine surface, to allow comparison of the fcc:hcp ratio for the iodine. Following annealing the surface produced the expected $(\sqrt{3}\times\sqrt{3})\text{R}30^\circ$ LEED pattern. Photon stimulated EDCs (at a photon energy of 3000 eV) showed only iodine and copper peaks. No cadmium signal remained, and no contamination was observed. However, the I:Cu Auger peak-to-peak height ratio had fallen from 0.28:1 to 0.17:1. The drop in ratio is approximately 50 %, suggesting the cadmium desorbed from the surface in the form of CdI_2 , taking 0.16 ML of iodine with it. NIXSW data was recorded for this new surface using the iodine MNN Auger and copper $2p_{1/2}$ peaks for the $(\bar{1}11)$ reflection only. This was because the (111) NIXSW profiles recorded for both the Cu-I and Cu- $\frac{1}{2}(\text{CdI}_2)$ surfaces gave approximately identical (111) layer spacings. The NIXSW data recorded and fits are shown in Figure 5.12. The results from the fitting process are shown in Table 5.14.

Peak	Energy Broadening / eV	Coherent position	Coherent fraction	Q	Bragg energy / eV
Cu $2p_{1/2}$	0.53 ± 0.03	1.00*	0.84 ± 0.05	0.12*	2962.9 ± 0.1
I Auger	0.53*	0.96 ± 0.02	0.62 ± 0.05	0.00*	2962.9*

Table 5.14 : Results for annealed $\frac{1}{2}(\text{CdI}_2)$ layer

*** denotes value constrained in fit**

The experimental $(\bar{1}11)$ coherent position of 0.96 ± 0.02 gives a $(\bar{1}11)$ layer spacing of 2.00 ± 0.05 Å. This is significantly different to the 1.60 ± 0.05 Å found for the $\frac{1}{2}(\text{CdI}_2)$ structure and for the Cu-I results from chapter 4 which gave 1.77 ± 0.05 Å and from Ithnins results for the Cu-I system which gave 1.65 ± 0.05 Å. Of course, with such a large difference in the $(\bar{1}11)$ layer spacing a large change would be expected in the adsorption site. As

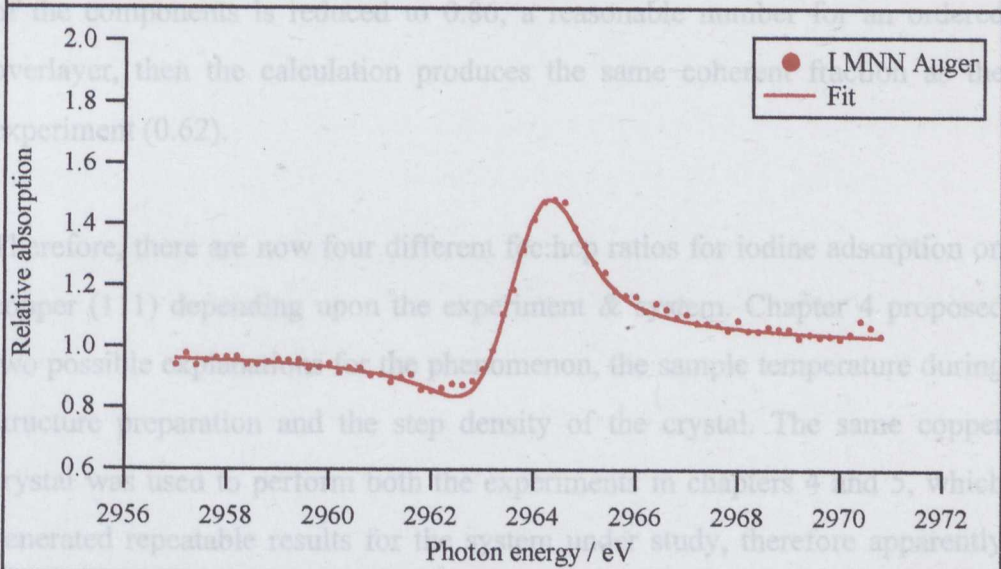
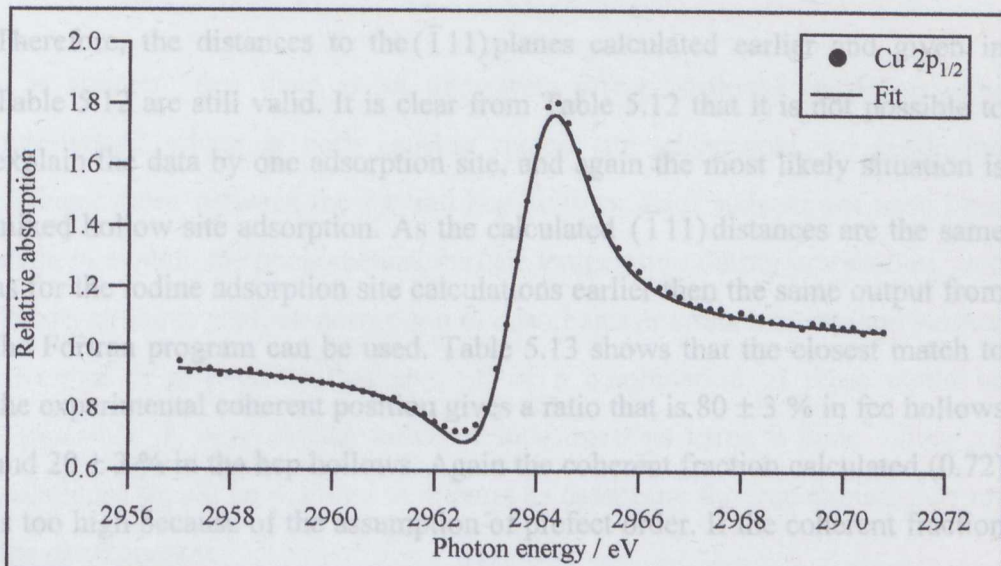


Figure 5.12 : (-111) NIXSW data for Copper (111)-Iodine

Surface was produced by annealing the 1/2(CdI₂) layer to 473 K.

NIXSW data is shown as markers, with the fits shown as solid lines.

only ($\bar{1}11$) NIXSW data was recorded, it is assumed that (111) layer spacing for the iodine remained the same as for the $\frac{1}{2}(\text{CdI}_2)$ layer at $2.10 \pm 0.05 \text{ \AA}$. Therefore, the distances to the ($\bar{1}11$) planes calculated earlier and given in Table 5.12 are still valid. It is clear from Table 5.12 that it is not possible to explain the data by one adsorption site, and again the most likely situation is mixed hollow site adsorption. As the calculated ($\bar{1}11$) distances are the same as for the iodine adsorption site calculations earlier then the same output from the Fortran program can be used. Table 5.13 shows that the closest match to the experimental coherent position gives a ratio that is $80 \pm 3 \%$ in fcc hollows and $20 \pm 3 \%$ in the hcp hollows. Again the coherent fraction calculated (0.72) is too high because of the assumption of perfect order. If the coherent fraction of the components is reduced to 0.86, a reasonable number for an ordered overlayer, then the calculation produces the same coherent fraction as the experiment (0.62).

Therefore, there are now four different fcc:hcp ratios for iodine adsorption on copper (111) depending upon the experiment & system. Chapter 4 proposed two possible explanations for the phenomenon, the sample temperature during structure preparation and the step density of the crystal. The same copper crystal was used to perform both the experiments in chapters 4 and 5, which generated repeatable results for the system under study, therefore apparently ruling out step density as a possibility. An additional factor is present for the $\frac{1}{2}(\text{CdI}_2)$ data, which is the presence of the cadmium atoms. It must be assumed that there is some interaction between the cadmium and iodine atoms, which might influence the observed fcc:hcp ratio. Another possibility is the interaction with any co-adsorbed contaminants. For the Cu-I surface produced by annealing the $\frac{1}{2}(\text{CdI}_2)$ structure, the most obvious factor is the reduction on surface coverage compared to the saturated iodine monolayer. The preference for the fcc hollows sites for this surface would appear to suggest that the fcc hollows are the preferred site for low coverage. However, this does not explain why the saturated iodine monolayer contains a mixture of fcc and hcp hollow

site adsorption, as it would be possible to construct the surface using only one type of hollow site.

It is apparent that there is an interesting effect occurring in the systems investigated which is both causing mixed site adsorption and producing different ratios between the fcc and hcp hollows. Four suggestions have been made to explain the phenomenon, surface temperature during preparation, step density of the crystal, co-adsorption of adsorbates or contaminants, and surface coverage. It is possible that any, all or a combination of these could be responsible. A very careful series of investigations using a wide variety of techniques would be required to attempt to determine the true explanation for this phenomenon.

5.4 Summary

The structure of the $\frac{1}{2}(\text{CdI}_2)$ phase on copper(111) has been determined using NIXSW. In order to fit the experimental data Q values for the cadmium photoelectrons used had to be determined, these were found to be 0.15 ± 0.02 for the Cd $3p_{1/2}$ and 0.29 ± 0.02 for the Cd $3d_{5/2}$. The cadmium Auger was shown to be unusable, due to its low energy resulting in it being partially excited by secondary electron emission from the Cu surface, resulting in NIXSW parameters that were more indicative of the copper NIXSW parameters than the cadmium. The structure was shown to consist of a $(\sqrt{3} \times \sqrt{3})R30^\circ$ overlayer of iodine at 0.33 ML, which contained $37 \pm 3 \%$ in fcc sites and $63 \pm 3 \%$ in hcp sites, with the iodine located $2.10 \pm 0.05 \text{ \AA}$ above the copper surface. The cadmium was shown to be randomly located in a mixture of hollow sites, with a slightly larger height above the surface of $2.25 \pm 0.05 \text{ \AA}$, and a ratio of $48 \pm 3 \%$ in fcc sites and $52 \pm 3 \%$ in hcp sites.

The structure of the iodine monolayer produced by annealing the $\frac{1}{2}(\text{CdI}_2)$ surface was shown to have a radically different ratio, with $80 \pm 3 \%$ of the iodine adsorbed in the fcc hollows, with the remaining $20 \pm 3 \%$ in the hcp hollows.

It was suggested that further experiments are required in order to investigate the phenomenon of the changing ratios for the iodine adsorption site.

Chapter 6 : Iodine Etching of Aluminium(111)

6.0 Introduction

The experimental results presented in this chapter are for the aluminium(111)-iodine system. The next few sections present a review of the relevant literature on the behaviour of halogens interacting with aluminium surfaces. The experimental results presented include LEED, AES and LOSTPD experiments, together with a new method for determining sticking and reaction probabilities termed line of sight sticking probability or LOSSP.

6.1 Review of halogen adsorption on aluminium.

The interaction of halogens with metal surfaces has generally been well investigated, for a review of halogen adsorption studies the reader is directed towards the review by Jones [6.1]. Few studies however, have examined halogens on aluminium surfaces. Most of the early studies concentrated on polycrystalline aluminium and generally the surfaces were not clean, due to difficulties in removing any oxygen contamination. Other studies have concentrated on the etching of aluminium by halogens, by either thermal or plasma etching, because of aluminium's importance to the microprocessor industry (see section 6.1.2). The following sections will describe the previous studies that are relevant to the experimental results presented later in this chapter.

6.1.1 Chlorine adsorption on aluminium

Anderson and Gani [6.2] were the first to examine the interaction of chlorine with a polycrystalline aluminium surface. They exposed an aluminium film to chlorine vapour at 5×10^{-5} Torr with the sample at room temperature. The results showed that chlorine was rapidly adsorbed by the surface.

The next study was carried out by Smith [6.3], again using a polycrystalline aluminium sample. Attempts to clean the surface in vacuum proved impossible, therefore clean aluminium surfaces were prepared by aluminium vapour deposition. The freshly grown polycrystalline aluminium surface was exposed to chlorine vapour at various pressures from 5×10^{-8} to 2×10^{-6} Torr and at varying sample temperatures from room temperature to 803 K. Removing the chlorine flux was shown to give a rapid increase in the aluminium Auger peak-to-peak height, possibly due to AlCl_3 desorption, although this was not recognised at the time. The initial sticking probability for the chlorine was calculated to be 0.01, which seems a very low value. Smith postulated that chlorine interacts with aluminium in two states, either as a physisorbed molecule $(\text{Cl}_2)_{\text{ads}}$, or after dissociation as a Cl-Al complex. No attempt was made to give a structure for this complex.

An ultra-high vacuum single crystal study of chlorine on aluminium was performed by Bermudez et al, on a (111) surface [6.4]. A combination of techniques was used, including AES, LEED, TPD and work function measurements. Chlorine was exposed to the surface from the vapour phase at a pressure of 5×10^{-8} Torr. No significant difference was observed between chlorine uptake on a bombarded and annealed, or bombarded only surface, indicating that surface disorder is not an important factor. A 20 L exposure gave a calculated coverage of 0.61 monolayers. The initial sticking probability was estimated at 0.12, higher than the 0.01 calculated by Smith for polycrystalline aluminium. Work function measurements showed that for the initial stages of adsorption the work function increased, indicating that negatively charged species (*e.g.* Cl^- or Cl_2^-) were formed above the surface.

However, the work function then remained constant, despite continued uptake of chlorine. This was assigned to be the result of adsorption at sub-surface sites, possibly accompanied by rearrangement of the surface aluminium atoms to accommodate the large halogen species. TPD measurements showed only atomic chlorine (Cl^+) detected as a desorption product, neither Cl_2^+ nor AlCl_3^+ were detected. The absence of molecular chlorine indicated that adsorption was predominantly dissociative. Atomic chlorine desorbed in a single broad peak at 473 K, with AES showing a 90 % reduction in the chlorine peak to peak height. No desorption peak could be assigned to the loss of chlorine from sub-surface sites. It was not known whether the sub-surface chlorine desorbs over a very broad temperature range, or in a peak above 623 K (where desorption from the sample holder made data collection difficult), or if chlorine diffuses into the bulk. A quadrupole mass spectrometer (QMS) placed in front of the sample was unable to detect any etch products even for chlorine exposures at pressures of 2×10^{-7} Torr. LEED showed a gradual degradation in the clean (1x1) pattern, with 80 L removing the pattern altogether. After 40 L, which gave an estimated coverage of greater than one monolayer, the (1x1) surface LEED pattern was still clearly visible, suggesting that three-dimensional patches had formed rather than a uniform film. No indication of any ordered overlayer was seen. A two stage model was proposed for Cl_2 adsorption. For low exposures chlorine was rapidly adsorbed at surface sites. After 20-30 L, uptake occurred more slowly at sub-surface sites, possibly accompanied by rearrangement of the surface aluminium atoms.

6.1.2 Etching studies of aluminium

As mentioned earlier, a number of studies have concentrated on the interaction of chlorine with aluminium employing thermal or plasma etching. The interest in this comes from the electronics industry, because aluminium is an ideal material to make integrated circuit connections, because of its low resistance and ease of deposition. Whilst the fundamentals of silicon dry etching are reasonably understood, the basic physical and chemical mechanisms for the dry etching of aluminium have not been as well established [6.5]. Recently

IBM and several other computer chip manufacturers have announced that they plan to be engineering new chips with aluminium interconnections early in the 21st century.

Danner and Hess [6.6] used a plasma reactor, with gas phase flow titration techniques to study the plasma etching of aluminium. The results showed surprisingly that the rate of etching for chlorine molecules was four times greater than that for chlorine atoms. The higher rate was believed to be the result of an enhanced sticking coefficient on the chlorinated surface for the chlorine molecules compared to that for chlorine atoms. Dipole interactions between the incoming chlorine molecules and chlorine bound to the surface were believed to be the cause. Below 298 K, the etching was quenched due to the energy barrier being too great for product desorption to occur.

Janssen et al [6.7] used a time of flight technique, TOF (pseudo-random cross-correlation TOF) to study the thermal etching of aluminium. A molecular beam of chlorine (7×10^{16} molecules $\text{cm}^{-2}\text{s}^{-1}$) was used, giving a background pressure of 1×10^{-6} mbar. TOF distributions were measured for the AlCl^+ , AlCl_2^+ and AlCl_3^+ ion signals, for three surface temperatures, 440, 720 and 800 K. The TOF distributions were then fitted with Maxwell-Boltzmann (MB) distributions. The results showed that the major part (90-95 %) of the MB distributions were at the measured temperature of the surface. This indicates that chlorine easily physisorbs on the aluminium or chlorine covered surface and has a sufficiently long residence time to acquire the temperature of the surface. The results showed that Al_2Cl_6 was the major product below 450 K, between 500-650 K AlCl_3 became the major product, and at sample temperatures greater than 700 K, AlCl was the only product. In each case a decrease in the yield of one component (*e.g.* Al_2Cl_6) was matched by a corresponding increase in the next major product (*e.g.* AlCl_3).

6.1.3 Other studies

So far no studies to the authors knowledge have been presented that examine the interaction of molecular iodine or bromine with any aluminium surface.

However, there has been some work on the interaction of alkyl halides with aluminium surfaces. An example of this is the work performed by Hara et al who studied the surface reaction of CH_2I_2 on an Al(111) surface [6.8]. They used AES and TPD measurements to study the system. The results showed that CH_2I_2 reacts with the aluminium surface at temperatures as low as 108 K. Some of the carbon species generated are located beneath the surface. For coverages of less than 1 ML, no CH_2I_2 was seen desorbing from the surface. The main reaction was the formation of a surface aluminium compound involving a $\text{CH}_3\text{-Al}$ bond. When the sample temperature was increased, organo-aluminium compounds like $\text{CH}_3\text{Al(H)I}$ desorb through the decomposition of the surface compound. For coverages greater than one monolayer, the main reaction was the formation of C_2H_4 and AlI_3 . The amount of aluminium surface compound was not significantly increased compared to coverages of less than one monolayer. The reactions were considered to proceed on the surface by a similar mechanism to the Simmons-Smith reaction [6.9], involving carbenes.

6.2 Line of Sight Sticking Probability

Some of the results presented in this chapter were obtained using a novel method we have developed, which with relatively minor modifications to a standard UHV chamber allows the measurement of sticking probability. The advantage of this method is that it does not require the use of a molecular beam system, or accurate calibration of surface coverage and gas pressure.

Previous measurements of sticking probability have been carried out either by monitoring the surface coverage as a function of exposure, or by monitoring the reflected fluxes using the King and Wells method [6.10]. The former of these enables a wide range of sticking probabilities (S) to be determined, $10^{-9} < S < 1$, however, the accuracy is entirely dependent upon the precise calibration of the surface coverage and pressure measurements. The latter method, only allows a smaller range to be measured, $0.01 < S < 1.0$, and requires the use of a molecular beam system. However, this produces values for the sticking probability which are independent of the coverage and pressure calibrations, resulting in a very high accuracy (± 0.01).

Our method, can be considered as a “reverse” King and Wells experiment, so it is useful to briefly discuss how their method works. A molecular beam is used as the source of adsorbate particles, with either an ionisation gauge, or mass spectrometer to measure the particle fluxes. The molecular beam is initially directed onto an inert surface, for which the sticking probability of the particles is zero. The pressure in the apparatus is then measured, P_{in} . The surface of interest is then positioned so that the molecular beam hits it and a new pressure recorded, P_{out} . If the incident beam intensity and pumping speed remain unaltered and the gas emanating from the surface is randomised and thermalised by scattering within the apparatus, then the pressures recorded are proportional to the fluxes of the particles. It was shown in section 2.2, that sticking probability is defined as follows.

$$S = \frac{(F_{in} - F_{out})}{F_{in}} \quad (6.1)$$

As the fluxes in the King and Wells methods are proportional to the measured pressures, (assuming that the gas is randomised and thermalised) then the sticking probability can be written in terms of the measured pressure, as shown in equation 6.2

$$S = \frac{(P_{in} - P_{out})}{P_{in}} \quad (6.2)$$

As stated earlier, the sticking probability measurement obtained by this method is independent of both surface coverage and pressure gauge calibrations, removing large potential sources of error and resulting in a high degree of accuracy ($S \pm 0.01$).

The new experiment described here, uses the apparatus devised to perform a LOSTPD experiment [6.11], which was described in section 3.5.2. Instead of carrying out a thermal desorption experiment, here a new methodology is presented, so that sticking probabilities can be determined. This new technique has been termed, Line of Sight Sticking Probability or LOSSP. The measurement is made using a randomised adsorbate input flux and the detection of a reflected beam of adsorbate or reaction products, hence a “reverse King and Wells” method.

The LOSSP experiment is carried out by backfilling the chamber with the adsorbate gas to the required pressure. The flux at the sample surface is therefore random and can be defined using a cosine distribution [6.12]. The detector in these experiments is a quadrupole mass spectrometer which is placed inside a liquid nitrogen cooled shroud (see section 3.5.2 and Figure 3.9), so that the only species reaching the detector have followed a line of sight trajectory from the sample surface. Species emanating from any other part of the chamber are unable to reach the detector because they impact on

the shroud and are condensed. Some gases such as H₂, N₂, CO, He etc. are not condensable at liquid nitrogen temperatures. These gases are therefore able to reach the detector from any trajectory. As the experiments described here did not require the measurement of any species for which this is the case, it was not a problem. Initially the sample is moved out of the line of sight position and the signal, C_{in} for a given m/z is recorded for a chosen adsorbate gas pressure. This signal originates from species emanating from the chamber wall directly opposite the mass spectrometer. This surface is the equivalent of the inert surface in the King & Wells method. If the chamber is conditioned correctly to the adsorbate gas, so that the sticking probability on the wall can be assumed to be zero, then the chamber wall can be considered inert. The value of C_{in} is directly proportional to the total gas flux at the sample surface from the 2π steradians above it. After cleaning, the sample is positioned back in the line of sight position and gas admitted to the chamber, at the same pressure as previously. The signal, C_{out} for the given m/z is recorded, which is proportional to the flux emitted at azimuthal angle φ, and polar angle θ. The signals recorded are related to the sticking probability as given by equation 6.3.

$$S = \frac{(C_{in} - C_{out})}{C_{in}} \quad (6.3)$$

A correction must be made to equation 6.3 if the temperatures of the incident and desorbed gas or gases are different, because otherwise the signals recorded by the detector will no longer be in direct proportion to the fluxes, F_{in} and F_{out}. Iodine adsorption on aluminium was the first system we applied LOSSP to.

6.3 Experimental methods

The vacuum chamber used to perform this experiment is described in section 3.3. The LOSTPD apparatus and the method of sample alignment is discussed in section 3.5.2.

The preparation method and cleaning is described in section 3.1.1. The clean aluminium sample gave a very sharp (1x1) LEED pattern, as shown in Figures 3.2 and 6.7. Iodine vapour was introduced into the chamber through a leak valve as described in section 3.4.

LOSSP experiments used the Pyrex window opposite the mass spectrometer as the inert surface for measuring C_{in} , which was considered to be unreactive towards the iodine. In order to follow both the sticking probability and the surface reaction of the iodine, two masses were followed simultaneously, the I_2^+ peak at $m/z = 254$, and the AlI^+ peak at $m/z = 154$. The AlI^+ peak was used as it was more intense than the AlI_3^+ peak at $m/z = 408$. Unfortunately, it was not possible to record the $Al_2I_6^+$ peak at $m/z = 816$, as this was outside the range of the mass spectrometer, thus removing the possibility of studying aluminium iodide dimer formation. Iodine was allowed to fill the chamber to a pressure of 4×10^{-7} Torr. The LOSSP technique was used to record the sticking probability for the adsorption of iodine at two sample temperatures, 103 and 300 K. Additionally, an experiment was performed where the sample was being cooled whilst following the I_2^+ and AlI^+ peaks.

The liquid nitrogen shroud used to provide the line of sight capability, actually created a small problem. For the sample surface, in its line of sight position the shroud subtended a solid angle of 7.6 % of the full 2π steradians above the surface. However, the shroud only subtended 1 % of the space above the inert surface (*i.e.* the Pyrex window). The shroud acts to reduce the flux at the sample and the inert surface, as the iodine is unable to bounce off the shroud, because it becomes cryogenically pumped. Because of the difference in the solid angle subtended by the shroud for each surface, the affect on the flux is

different for each case. The difference although small needs to be corrected for in the data analysis. This was achieved by assuming that the signal recorded from the sample in line of sight, C_{out} , is correct. This means that a standard geometry is defined in which gas is only adsorbed from 92.4 % of the steradians available. Therefore, the measured value of C_{in} is incorrect, because the inert surface has a larger solid angle, 99 % of the steradians available, from which to receive flux. Our C_{in} value was corrected (after background subtraction) using equation 6.4

$$C_{in(corrected)} = \frac{92.4}{99} C_{in(measured)} \quad (6.4)$$

This gives the value which C_{in} would take if the inert surface had been in the same position as the sample. For future experiments this problem could be removed by the use of an inert surface which could be positioned in the same place as the sample.

AES-t adsorption experiments were performed using adsorption from iodine vapour which was allowed in to the chamber to a pressure of 5×10^{-8} Torr for a given period (usually either 150 or 300 s). This appears to be a high dose for each increment, but the ionisation gauge is 5.4 times as sensitive to iodine as it is to nitrogen [6.13]. This combined with the fact that the gauge was uncalibrated probably means that the “true” doses of iodine are much lower. The leak valve was then closed and the pressure fell to below 10^{-9} Torr almost immediately. The chamber was allowed to pump for a few minutes to recover, before the sample was then turned to face the RFA for LEED or AES analysis. These were generally performed in separate experiments, although the LEED pattern was checked occasionally during AES experiments to confirm reproducibility. AES spectra were recorded for the 67 eV aluminium LVV Auger and the 511 eV iodine MNN Auger. The exposure and analysis cycle was repeated until either the aluminium signal had fallen to zero or the iodine

signal had saturated. These experiments were carried out for sample temperatures of 103 and 308 K.

Variable temperature experiments were carried out following a saturation dose of 7200 s at 5×10^{-8} Torr with the sample at 103 K after liquid nitrogen cooling. The sample was heated slowly in 10 or 20 K steps. The temperature was raised to the required level, held approximately constant (± 5 K) for one to two minutes and then allowed to cool. LEED and AES analysis was performed once the temperature had fallen at least 100 K below the temperature for that increment if possible.

Both the AES-t experiments and the variable temperature experiments were repeated three times to ensure reproducibility.

LOSTPD experiments were performed for iodine exposures of 300, 600, 900 and 1200 seconds at an applied iodine pressure of 5×10^{-8} Torr. The apparatus and method of sample alignment was explained in section 3.5.2. The experiment is essentially a standard thermal desorption experiment, with the guarantee that all the species detected must have originated from the sample in a direct line of sight trajectory [6.12]. Due to low signal levels counting times were such that only two peaks could be recorded simultaneously. Counting times were 0.25 s for I_2^+ ($m/z = 254$) and AlI_1^+ ($m/z = 154$) and 0.5 s for AlI_3^+ ($m/z = 408$) and AlI_2^+ ($m/z = 281$). The I^+ peak at $m/z = 127$ was not used as the mass spectrometer filaments had become contaminated with iodine, therefore giving a constant large background signal. The heating ramp was provided using the e-beam heating for sample annealing. No equipment was available for keeping the temperature ramp constant, therefore initial heating was much more rapid than towards the end of the experiment. The choice of heating rate was further limited by the requirement to record data from 100 K to 800 K, as the computer used to record the data could only store a limited number of datapoints. This also affected the choice of counting times for each species. The current and voltage applied to the filaments and sample holders were chosen to meet the requirements discussed above, and provide a heating

rate that between 273 and 473 K (the temperature range of the important desorption peaks) was between approximately 2 and 6 Ks⁻¹.

6.4 Results

Figures 6.1 to 6.4 contain the results of the various experiments performed using the LOSSP technique. Figure 6.1, shows the I₂⁺ and AlI⁺ signals recorded versus time for the inert surface, with the sample out of the line of sight position for a sequence in which the iodine gas pressure in the chamber was initially zero, raised to 4 x 10⁻⁷ Torr and then reduced again to zero. Upon introduction of iodine into the chamber, the I₂⁺ signal rose from its background level of 5 ± 1 Hz, to 101 ± 2 Hz. After correction using equation 6.4, this becomes C_{in} = 90 ± 2 Hz. On removal of the iodine vapour, the I₂⁺ signal returned to its background level. During this sequence, the AlI⁺ peak remained at its background level of ≈ 10 Hz.

Figure 6.2, shows the results of repeating the same sequence of pressure changes described above, but with the sample in its line of sight position at a temperature of 103 K. Neither the I₂⁺ or the AlI⁺ peak showed a measurable change as a result of the iodine pressure changes. Using the background corrected value for C_{out} of 0.2 ± 0.8 Hz, and the C_{in} value of 90 ± 2 Hz, then applying equation 6.3, gives the sticking probability of iodine on the cold aluminium surface as 0.98 ± 0.02. It is assumed that the iodine is forming physisorbed multilayers, so therefore the sticking probability is also the sticking probability for iodine on solid iodine at 103 K.

The same sequence of iodine pressure changes was used to measure the I₂⁺ and AlI⁺ peaks, with the sample in the line of sight position again, however, the sample temperature was held at 300 K. The results are shown in Figure 6.3. On the introduction of iodine vapour to the chamber there is an initial period before a steady state situation is achieved. The I₂⁺ signal is reduced compared to that from the inert surface, to approximately half its previous value, such that C_{out} = 58 ± 6 Hz. This represents the fact that some, but not all of the

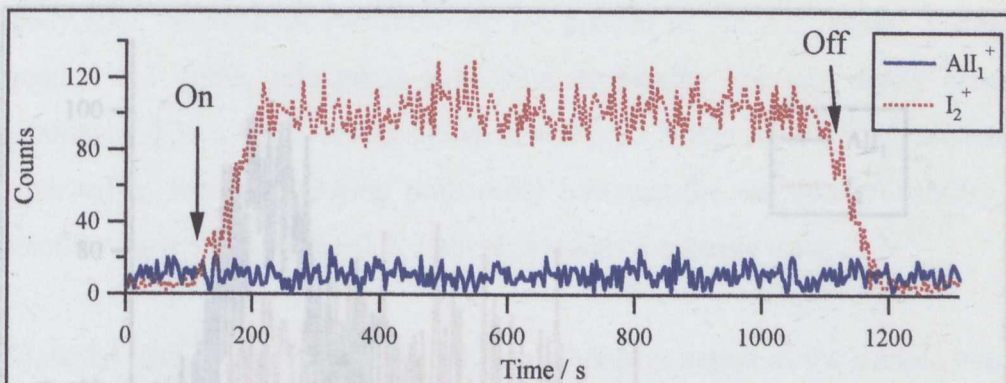


Figure 6.1 : LOSSP data for inert surface

Iodine flux at 4×10^{-7} Torr On/Off indicated by arrows on plot.

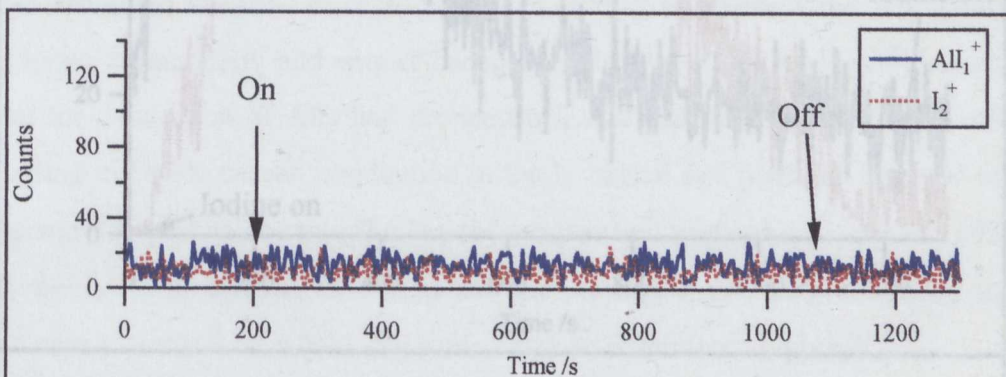


Figure 6.2 : LOSSP data for sample at 103 K

Iodine flux at 4×10^{-7} Torr On/Off indicated by arrows on plot.

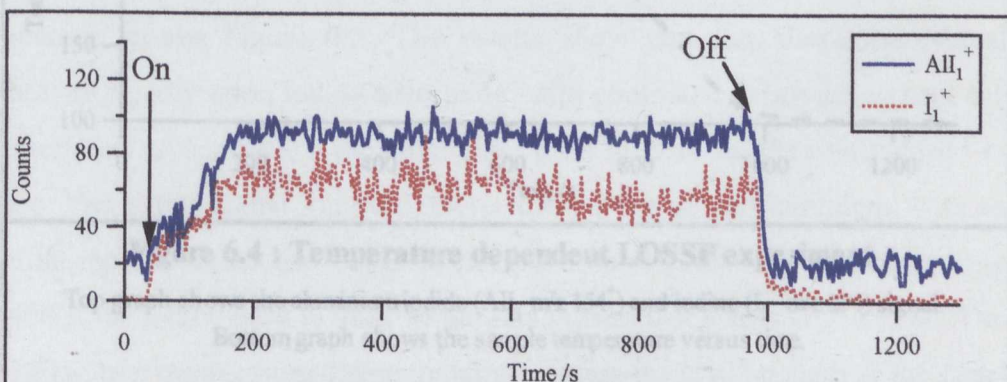


Figure 6.3 : LOSSP data for sample at 300 K

Iodine flux at 4×10^{-7} Torr On/Off indicated by arrows on plot.

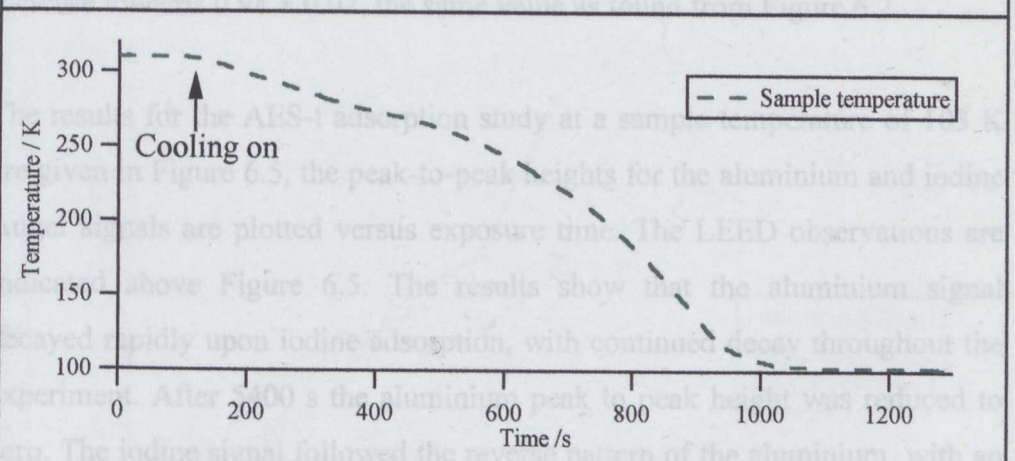
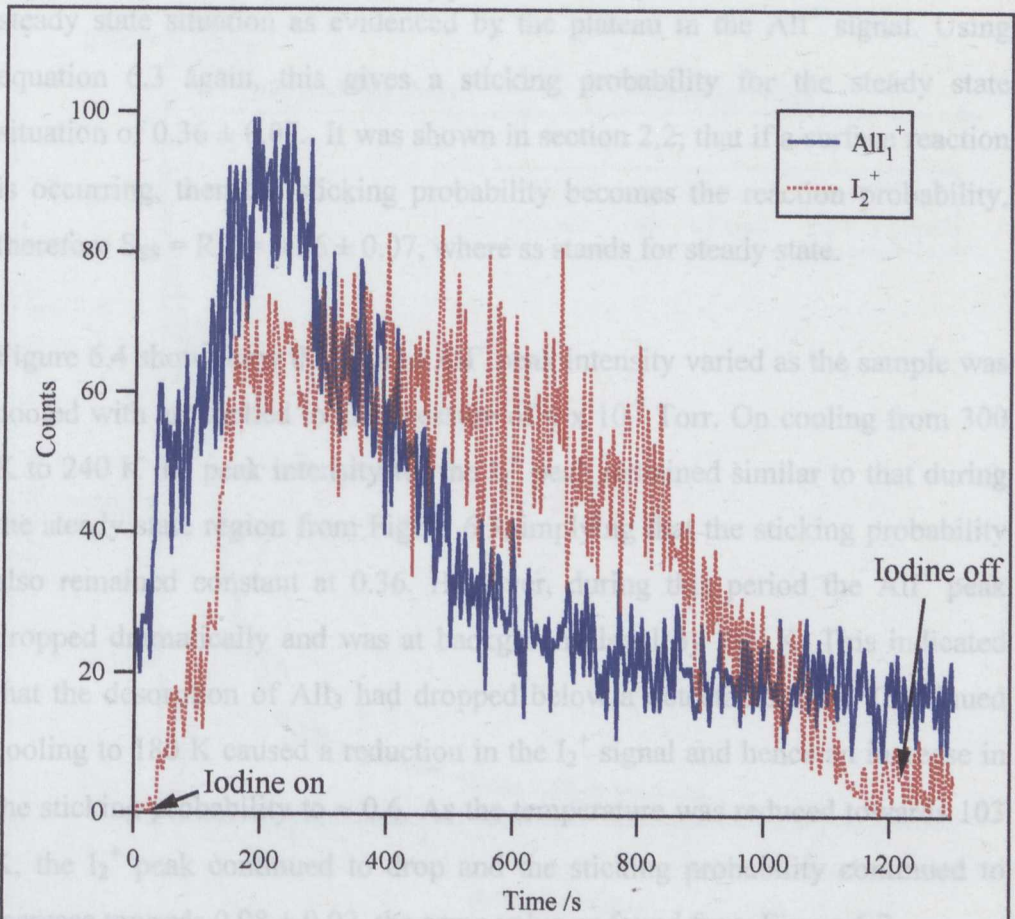


Figure 6.4 : Temperature dependent LOSSP experiment

Top graph shows the aluminium iodide (AlI_1 m/z 154⁺) and iodine (I_2^+ m/z 254) signal.

Bottom graph shows the sample temperature versus time.

iodine is sticking to the surface. The presence of an AlI^+ signal indicates that a surface etching reaction is occurring. The etching reaction also reaches a steady state situation as evidenced by the plateau in the AlI^+ signal. Using equation 6.3 again, this gives a sticking probability for the steady state situation of 0.36 ± 0.07 . It was shown in section 2.2, that if a surface reaction is occurring, then the sticking probability becomes the reaction probability, therefore $S_{\text{SS}} = R_{\text{SS}} = 0.36 \pm 0.07$, where ss stands for steady state.

Figure 6.4 shows how the I_2^+ and AlI^+ peak intensity varied as the sample was cooled with an applied iodine pressure of 4×10^{-7} Torr. On cooling from 300 K to 240 K the peak intensity for the I_2^+ peak remained similar to that during the steady state region from Figure 6.3, implying that the sticking probability also remained constant at 0.36. However, during this period the AlI^+ peak dropped dramatically and was at background level by 240 K. This indicated that the desorption of AlI_3 had dropped below a detectable level. Continued cooling to 180 K caused a reduction in the I_2^+ signal and hence an increase in the sticking probability to ≈ 0.6 . As the temperature was reduced towards 103 K, the I_2^+ peak continued to drop and the sticking probability continued to increase towards 0.98 ± 0.02 , the same value as found from Figure 6.2.

The results for the AES-t adsorption study at a sample temperature of 103 K are given in Figure 6.5, the peak-to-peak heights for the aluminium and iodine Auger signals are plotted versus exposure time. The LEED observations are indicated above Figure 6.5. The results show that the aluminium signal decayed rapidly upon iodine adsorption, with continued decay throughout the experiment. After 5400 s the aluminium peak to peak height was reduced to zero. The iodine signal followed the reverse pattern of the aluminium, with an initial rapid increase that began to decline around 1200 s. By approximately 2400 s the iodine peak to peak height had saturated at a value of ~ 1200 . The LEED observations were distinctly uninteresting, the (1x1) pattern of the clean surface (see Figure 6.7a) was seen to gradually fade with increasing iodine exposure. By 3000 s no LEED spots were visible. Figure 6.5 also shows a plot of the ratio of the iodine to aluminium peak-to-peak heights during adsorption.

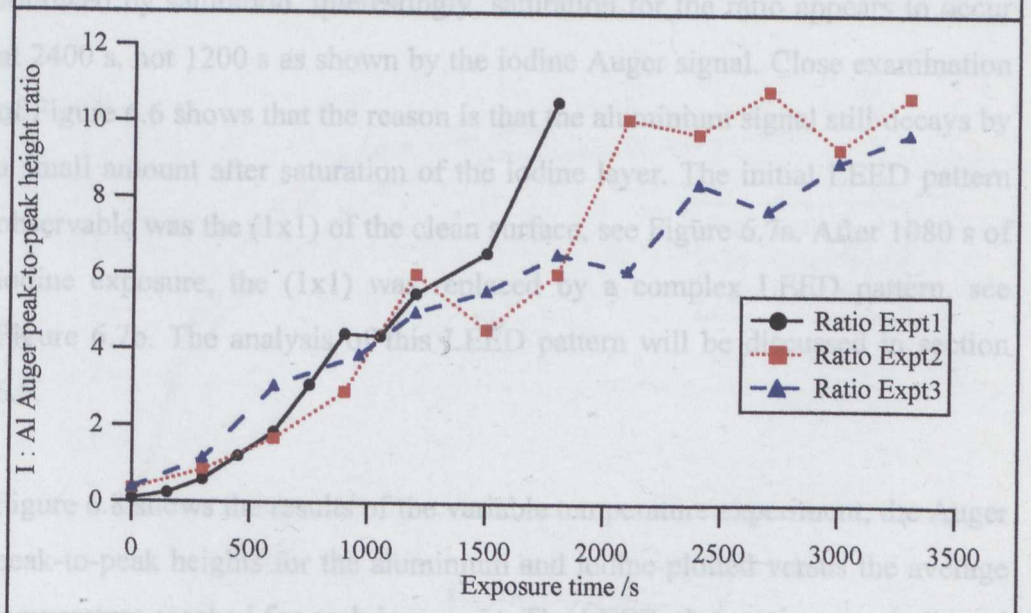
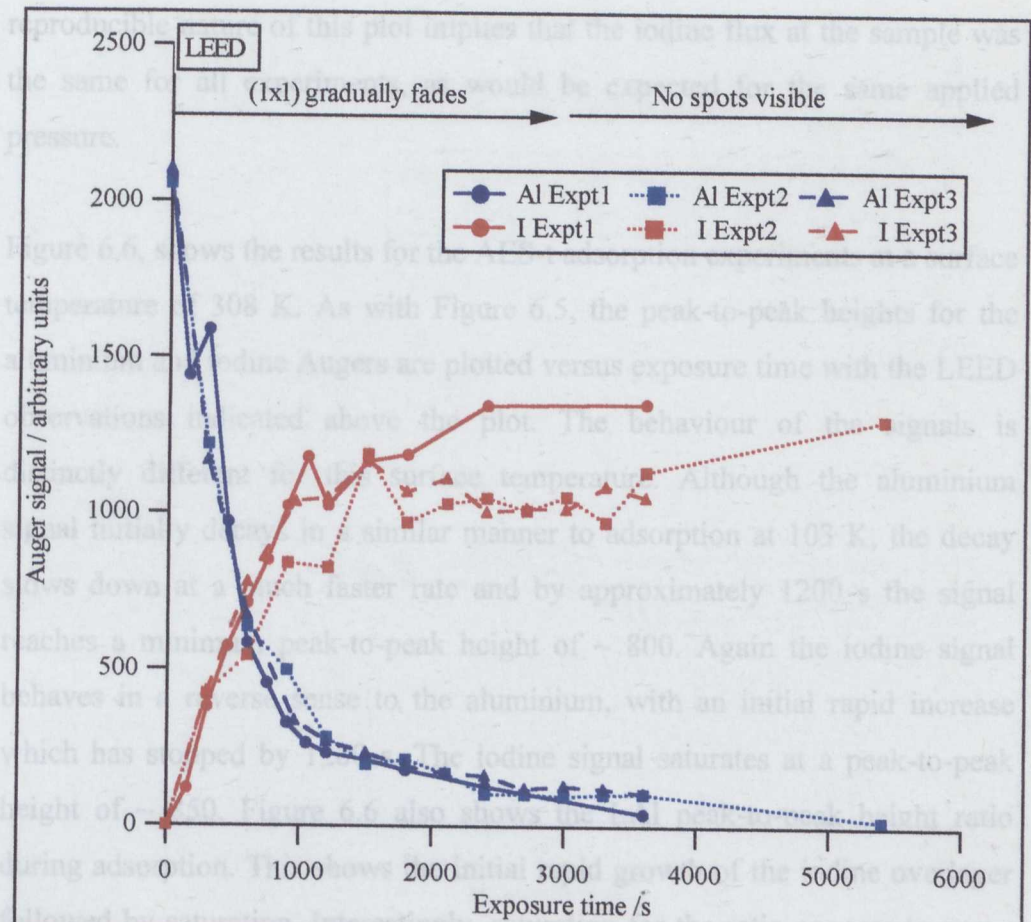


Figure 6.5 : AES-t plot for Iodine adsorption at 103 K, at 5×10^{-8} Torr
 Top graph shows Auger peak-to-peak heights versus exposure time.
 Bottom graph shows iodine:aluminium Auger peak-to-peak height ratio versus exposure time.
 LEED observations are indicated above the plots.

The later points become more erratic as the iodine signal becomes larger and the aluminium signal approaches zero and the errors become greater. The reproducible nature of this plot implies that the iodine flux at the sample was the same for all experiments, as would be expected for the same applied pressure.

Figure 6.6, shows the results for the AES-t adsorption experiments at a surface temperature of 308 K. As with Figure 6.5, the peak-to-peak heights for the aluminium and iodine Augers are plotted versus exposure time with the LEED observations indicated above the plot. The behaviour of the signals is distinctly different for this surface temperature. Although the aluminium signal initially decays in a similar manner to adsorption at 103 K, the decay slows down at a much faster rate and by approximately 1200 s the signal reaches a minimum peak-to-peak height of ~ 800 . Again the iodine signal behaves in a reverse sense to the aluminium, with an initial rapid increase which has stopped by 1200 s. The iodine signal saturates at a peak-to-peak height of ~ 850 . Figure 6.6 also shows the I:Al peak-to-peak height ratio during adsorption. This shows the initial rapid growth of the iodine overlayer followed by saturation. Interestingly, saturation for the ratio appears to occur at 2400 s, not 1200 s as shown by the iodine Auger signal. Close examination of Figure 6.6 shows that the reason is that the aluminium signal still decays by a small amount after saturation of the iodine layer. The initial LEED pattern observable was the (1x1) of the clean surface, see Figure 6.7a. After 1080 s of iodine exposure, the (1x1) was replaced by a complex LEED pattern, see Figure 6.7b. The analysis of this LEED pattern will be discussed in section 6.5.

Figure 6.8 shows the results of the variable temperature experiment, the Auger peak-to-peak heights for the aluminium and iodine plotted versus the average temperature reached for each increment. The LEED observations are indicated above the plot. Figure 6.8 shows three main regions where the behaviour of the iodine and aluminium Auger peak-to-peak heights are different. On initial heating there is a drop in the peak-to-peak height of the iodine signal from

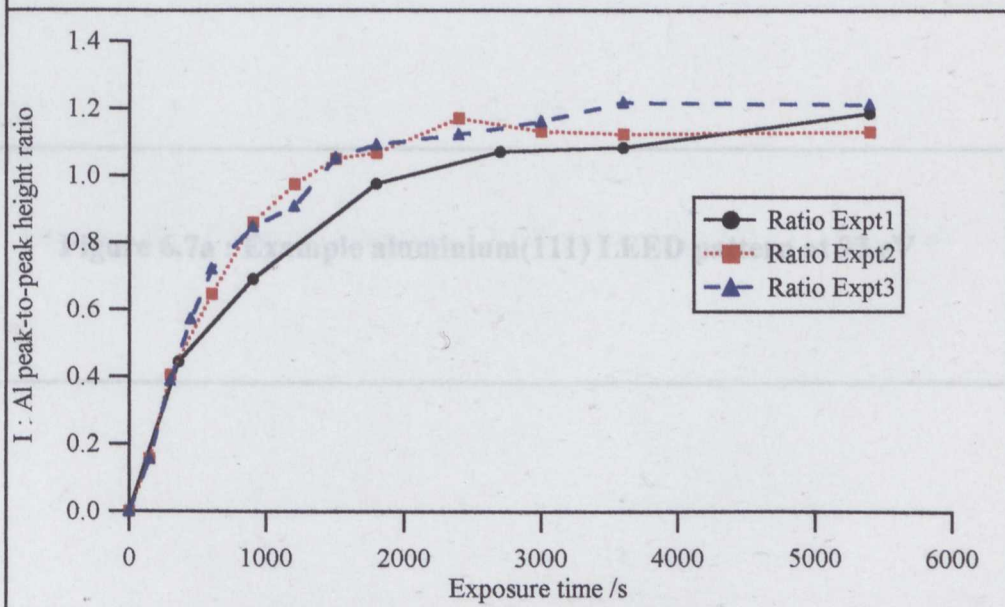
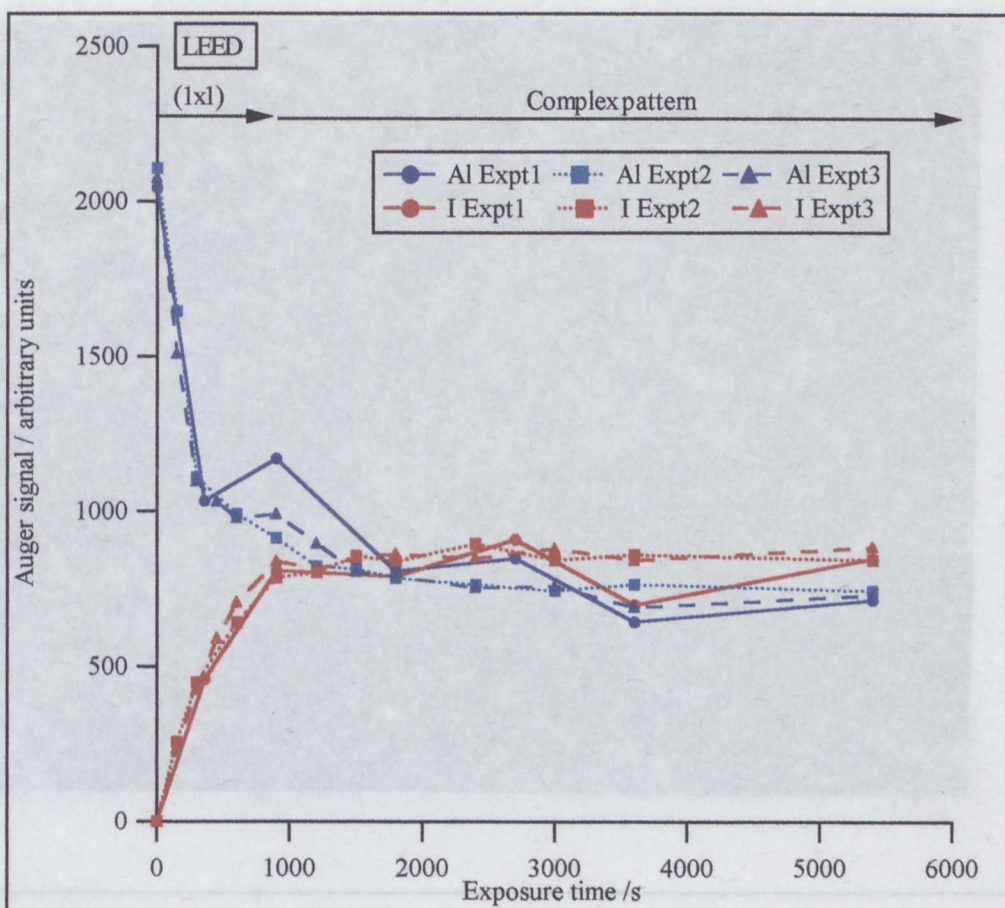


Figure 6.6 : AES-t plot for Iodine adsorption at 308 K at 5×10^{-8} Torr

Top graph shows Auger peak-to-peak heights versus exposure time.
 Bottom graph shows iodine:aluminium Auger peak-to-peak height ratio versus exposure time.
 LEED observations are indicated above the plots.



Figure 6.7a : Example aluminium(111) LEED pattern at 93 eV

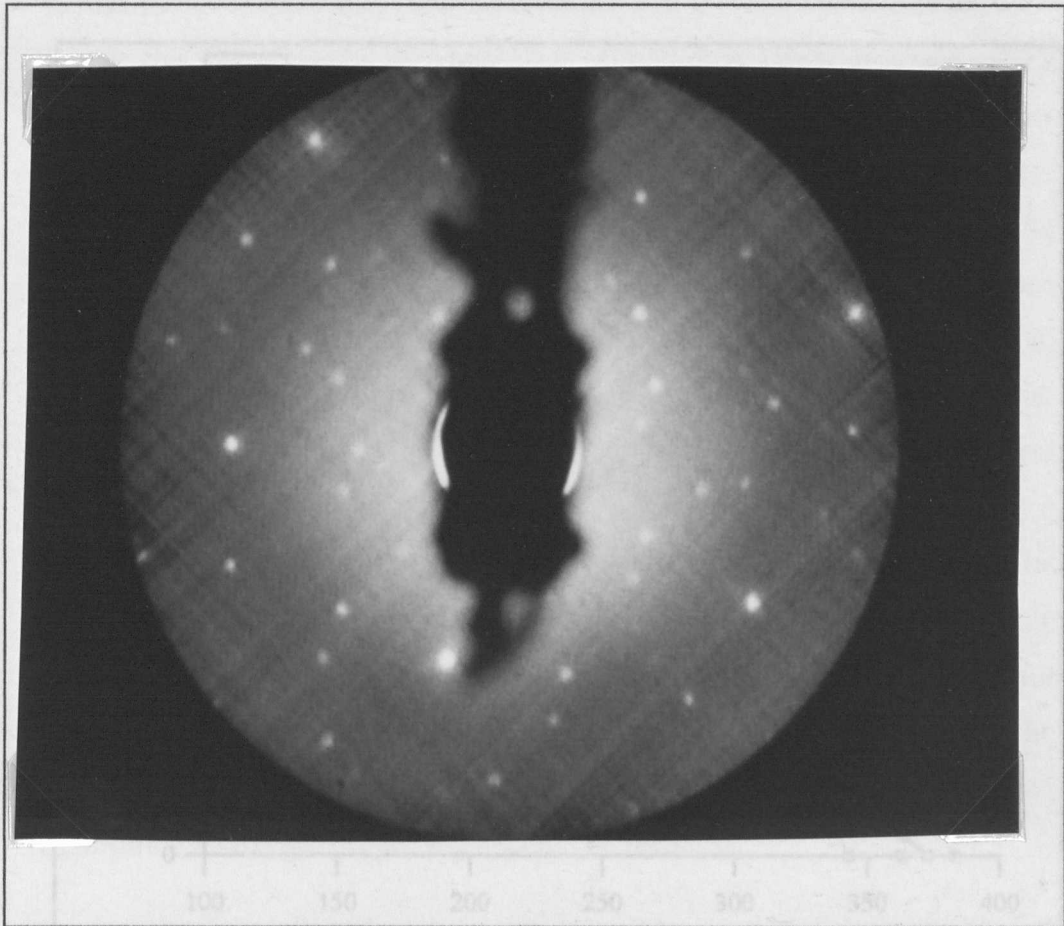


Figure 6.7b : Example Complex LEED pattern for I/Al(111) at 60 eV

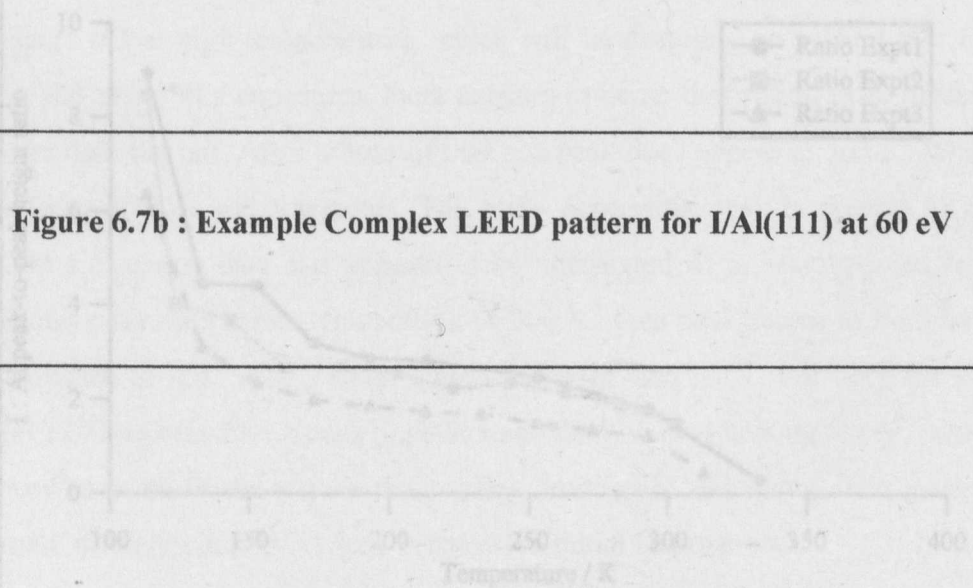


Figure 6.8 : Variable temperature experiment following adsorption at 103 K.

Top graph shows Auger peak-to-peak heights versus temperature. Bottom graph shows the iodine/aluminum Auger peak-to-peak height ratio versus temperature. LEED observations are shown above the plots.

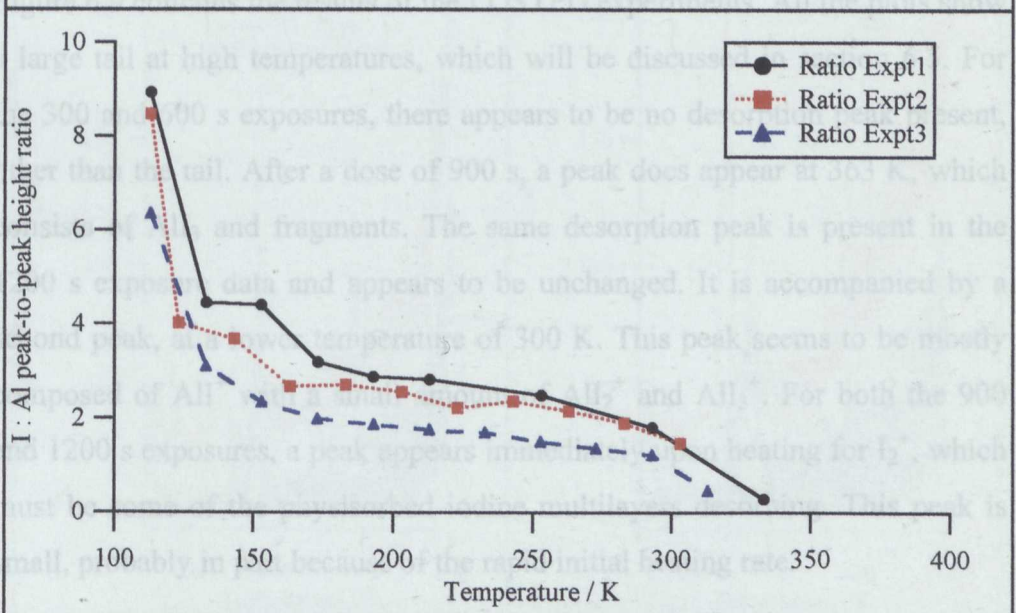
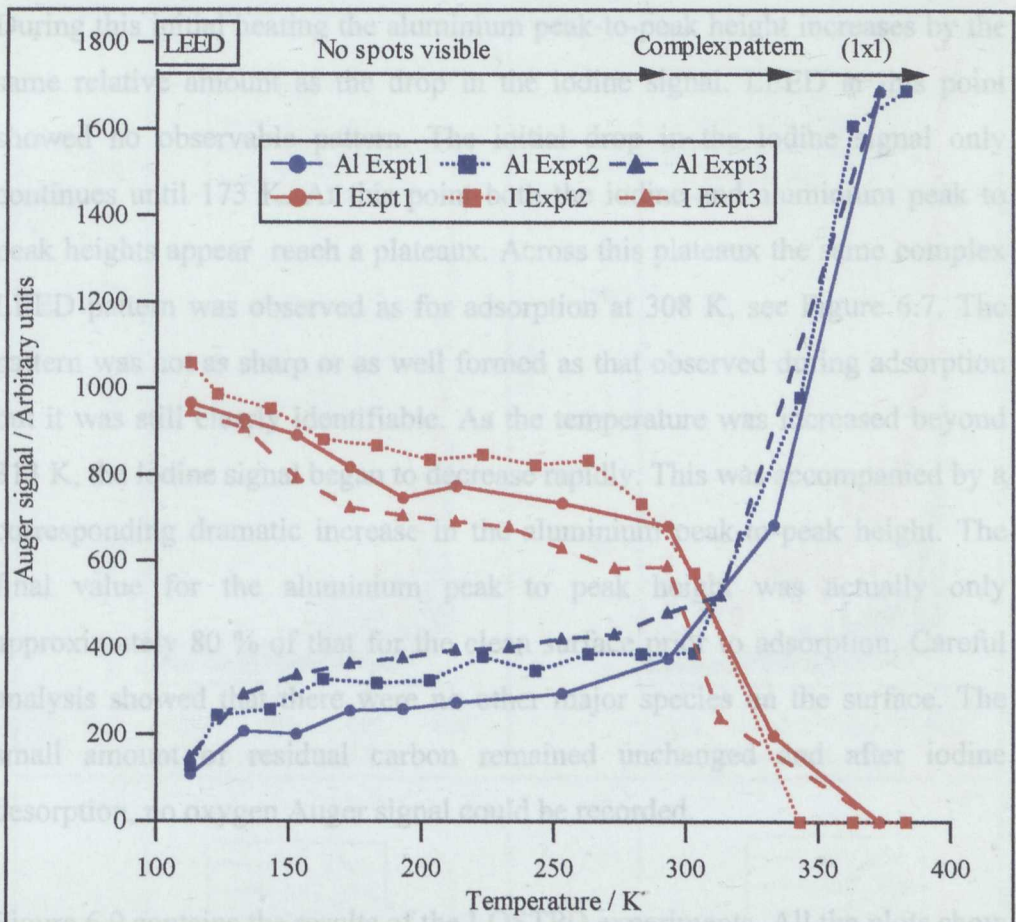


Figure 6.8 : Variable temperature experiment following adsorption at 103 K

Top graph shows Auger peak-to-peak heights versus temperature. Bottom graph shows the iodine:aluminium Auger peak-to-peak height ratio versus temperature. LEED observations are shown above the plots.

1100 down to 800. These values are very similar to the peak-to-peak heights for saturation of the iodine peak for adsorption at 103 and 308 K respectively. During this initial heating the aluminium peak-to-peak height increases by the same relative amount as the drop in the iodine signal. LEED at this point showed no observable pattern. The initial drop in the iodine signal only continues until 173 K. At this point both the iodine and aluminium peak to peak heights appear reach a plateau. Across this plateau the same complex LEED pattern was observed as for adsorption at 308 K, see Figure 6.7. The pattern was not as sharp or as well formed as that observed during adsorption but it was still clearly identifiable. As the temperature was increased beyond 313 K, the iodine signal began to decrease rapidly. This was accompanied by a corresponding dramatic increase in the aluminium peak-to-peak height. The final value for the aluminium peak to peak height was actually only approximately 80 % of that for the clean surface prior to adsorption. Careful analysis showed that there were no other major species on the surface. The small amount of residual carbon remained unchanged and after iodine desorption, no oxygen Auger signal could be recorded.

Figure 6.9 contains the results of the LOSTPD experiments. All the plots show a large tail at high temperatures, which will be discussed in section 6.5. For the 300 and 600 s exposures, there appears to be no desorption peak present, other than the tail. After a dose of 900 s, a peak does appear at 363 K, which consists of AlI_3 and fragments. The same desorption peak is present in the 1200 s exposure data and appears to be unchanged. It is accompanied by a second peak, at a lower temperature of 300 K. This peak seems to be mostly composed of AlI^+ with a small amount of AlI_2^+ and AlI_3^+ . For both the 900 and 1200 s exposures, a peak appears immediately upon heating for I_2^+ , which must be some of the physisorbed iodine multilayers desorbing. This peak is small, probably in part because of the rapid initial heating rate.

6.5 Discussion

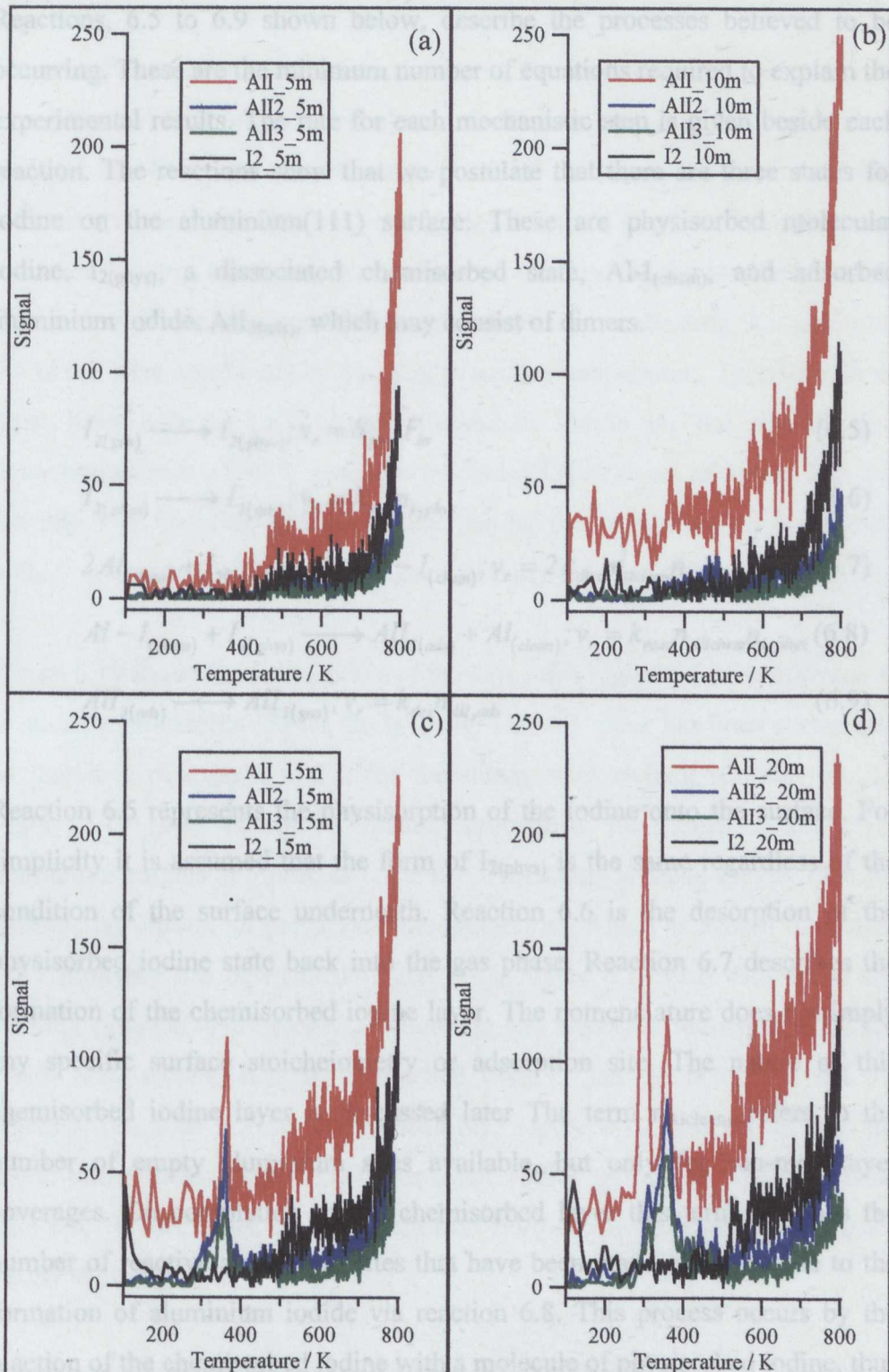
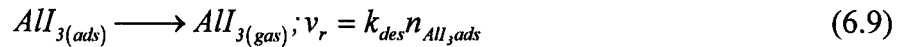
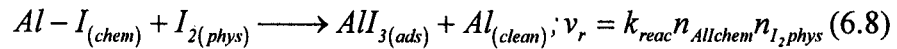
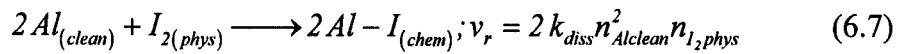


Figure 6.9 : LOSTPD data

Figures show TPD for AlI₁₋₃ ($m/z = 154, 281$ and 408) and I₂ ($m/z = 254$) for exposures of (a) 300 s (b) 600 s (c) 900 s and (d) 1200 s at 5×10^{-8} Torr.

6.5 Discussion

Reactions, 6.5 to 6.9 shown below, describe the processes believed to be occurring. These are the minimum number of equations required to explain the experimental results. The rate for each mechanistic step is given beside each reaction. The reactions show that we postulate that there are three states for iodine on the aluminium(111) surface. These are physisorbed molecular iodine, $I_{2(\text{phys})}$, a dissociated chemisorbed state, $Al-I_{(\text{chem})}$, and adsorbed aluminium iodide, $AlI_{3(\text{ads})}$, which may consist of dimers.



Reaction 6.5 represents the physisorption of the iodine onto the surface. For simplicity it is assumed that the form of $I_{2(\text{phys})}$ is the same regardless of the condition of the surface underneath. Reaction 6.6 is the desorption of the physisorbed iodine state back into the gas phase. Reaction 6.7 describes the formation of the chemisorbed iodine layer. The nomenclature does not imply any specific surface stoichiometry or adsorption site. The nature of this chemisorbed iodine layer is discussed later. The term $n_{Al_{\text{clean}}}$, refers to the number of empty aluminium sites available, but only for sub-monolayer coverages. On completion of the chemisorbed layer this term becomes the number of reactive aluminium sites that have been made available due to the formation of aluminium iodide via reaction 6.8. This process occurs by the reaction of the chemisorbed iodine with a molecule of physisorbed iodine, thus producing a molecule of adsorbed aluminium iodide and a new reactive aluminium site from the next layer down. The desorption of the aluminium

iodide produced by reaction 6.8 is described by reaction 6.9, this process is very rapid due to the large vapour pressure of aluminium iodide [6.13].

These reactions enable the interpretation of the results from the temperature dependent LOSSP experiment shown in Figure 6.4. As the temperature dropped to 240 K, the rate of emission of AlI^+ also dropped and eventually became unmeasurable. The rate of equation 6.9 must therefore have followed the same pattern. However, the reaction probability for the incoming iodine flux remained constant over this temperature range, indicating that reactions 6.5 to 6.8 were unaffected by the drop in surface temperature. Therefore, there must have been a build up of aluminium iodide on the surface. For temperatures below 240 K, reactions 6.6 and 6.8 slow down and stop. This has the effect of reducing and eventually halting the production of aluminium iodide on the surface. Solid iodine consequently build up on the surface.

Figure 6.10 shows the initial 600 s of the data from Figure 6.3 after conversion to sticking probability (S) for the I_2^+ peak. The AlI^+ peak has been normalised so that it is equivalent to 1.0 for the steady state etching reaction ($G_{1,\text{out}}$). Figure 6.10 gives the initial sticking probability for iodine on the clean aluminium surface at 300 K as 0.8 ± 0.1 . This value is much greater than for chlorine adsorption on polycrystalline aluminium, which as shown in section 6.1.1 probably lies between 0.01 and 0.12. Figure 6.10 also shows that the sticking probability decreases as coverage and exposure increases, until the steady state etching reaction is reached when S has fallen to 0.36 ± 0.07 , where it becomes the reaction probability. Figure 6.10 also shows that the initial rate of desorption for the aluminium iodide product is slightly greater than zero. It then rises until it reaches the normalised value of 1.0 during the steady state region.

In the initial reaction of iodine with the clean surface, only reactions 6.5, 6.6 and 6.7 need to be considered, as the concentrations of $\text{Al-I}_{(\text{chem})}$ and $\text{AlI}_{3(\text{ads})}$ are zero at this point.

Applying the steady state approximation to reactions 6.5, 6.6 and 6.7 with $I_2(\text{phys})$ as a reactive intermediate gives equation 6.10.

$$\frac{dI_2(\text{phys})}{dt} = 0 = S_{\text{phys}} F_{I_2} - k_{\text{des}} n_{I_2(\text{phys})} - 2k_{\text{des}} n_{I_2(\text{chem})}^2 n_{I_2(\text{phys})} \quad (6.10)$$

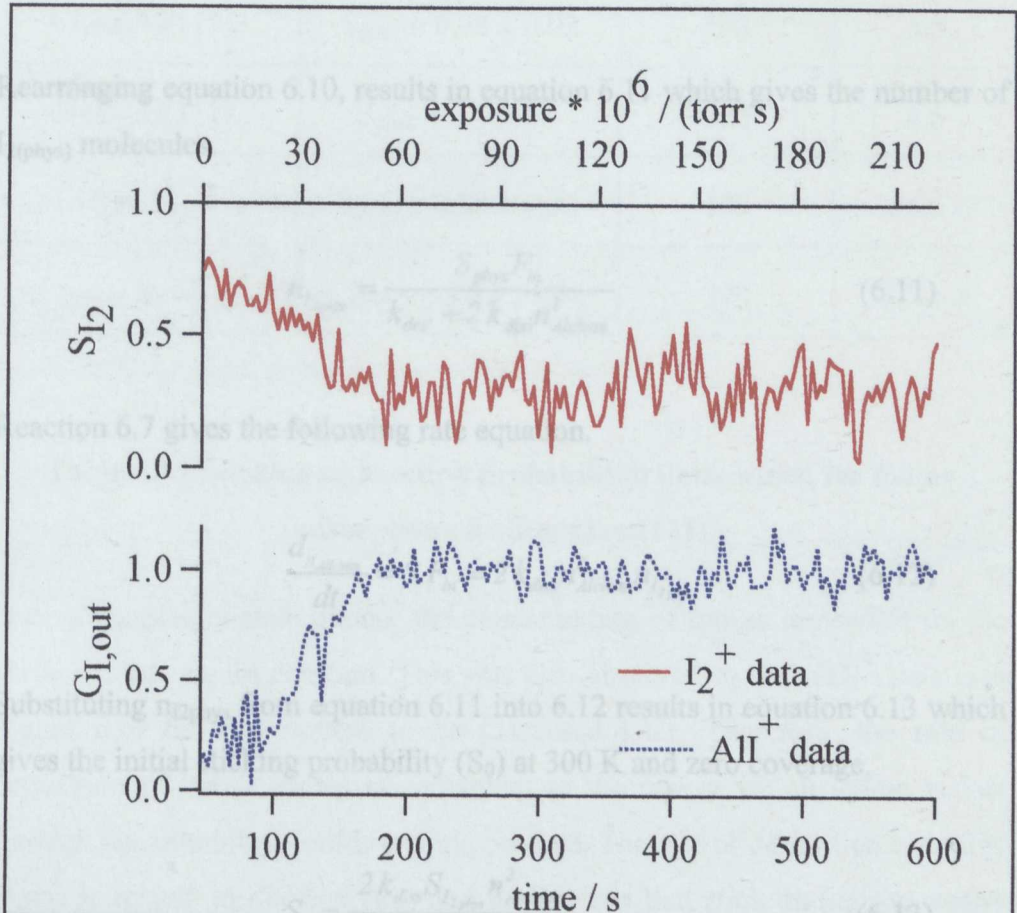


Figure 6.10 : Conversion of Figure 6.3

Graph shows the results from Figure 6.3 replotted as the sticking probability for iodine, and the normalised signal for AlI₃ desorption (G_{I,out}).

As the rate constant for desorption from the physisorbed state, k_{des} , is the concentration of reactive aluminium sites on the surface and k_{des} is the desorption rate constant for iodine in the physisorbed state from reaction 6.6. S_0 was determined earlier from Figure 6.10, as 0.8 ± 0.1 . Substituting this value into equation 6.13 implies that S_{phys} must be greater than 0.8 for adsorption into the physisorbed state at 300 K. Figure 6.2 gave the value for $S_{I_2(\text{phys})}$ at 103 K as 0.98 ± 0.02 , therefore it is probable that $S_{I_2(\text{phys})}$ has the same value at 300 K. Table 6.1 summarises all the sticking and reaction probabilities that have been determined from these experiments.

Applying the steady state approximation to reactions 6.5, 6.6 and 6.7 with $I_{2(\text{phys})}$ as a reactive intermediate gives equation 6.10.

$$\frac{dn_{I_2(\text{phys})}}{dt} = 0 = S_{\text{phys}} F_{\text{in}} - k_{\text{des}'} n_{I_2(\text{phys})} - 2 k_{\text{diss}} n_{\text{Alclean}}^2 n_{I_2(\text{phys})} \quad (6.10)$$

Rearranging equation 6.10, results in equation 6.11 which gives the number of $I_{2(\text{phys})}$ molecules.

$$n_{I_2(\text{phys})} = \frac{S_{\text{phys}} F_{\text{in}}}{k_{\text{des}'} + 2 k_{\text{diss}} n_{\text{Alclean}}^2} \quad (6.11)$$

Reaction 6.7 gives the following rate equation.

$$\frac{dn_{\text{Alchem}}}{dt} = S F_{\text{in}} = 2 k_{\text{diss}} n_{\text{Alclean}}^2 n_{I_2(\text{phys})} \quad (6.12)$$

Substituting $n_{I_2(\text{phys})}$ from equation 6.11 into 6.12 results in equation 6.13 which gives the initial sticking probability (S_0) at 300 K and zero coverage.

$$S_0 = \frac{2 k_{\text{diss}} S_{I_2(\text{phys})} n_{\text{Alclean}}^2}{k_{\text{des}'} + 2 k_{\text{diss}} n_{\text{Alclean}}^2} \quad (6.13)$$

k_{diss} is the rate constant for reaction 6.7, S_{phys} is the sticking probability for iodine adsorbing into the physisorbed state, n_{Alclean} is the concentration of reactive aluminium sites on the surface and $k_{\text{des}'}$ is the desorption rate constant for iodine in the physisorbed state from reaction 6.6. S_0 was determined earlier from Figure 6.10, as 0.8 ± 0.1 . Substituting this value into equation 6.13 implies that S_{phys} must be greater than 0.8 for adsorption into the physisorbed state at 300 K. Figure 6.2 gave the value for $S_{I_2(\text{phys})}$ at 103 K as 0.98 ± 0.02 , therefore it is probable that $S_{I_2(\text{phys})}$ has the same value at 300 K. Table 6.1 summarises all the sticking and reaction probabilities that have been determined from these experiments.

Surface	Sticking or reaction probability (S or R)	Temperature / K	Reaction(s)
Clean Al(111)	$S_0 = 0.8 \pm 0.1$	300	6.5-6.7
Clean Al(111)	$S_{\text{phys}} = 0.98 \pm 0.02$	103	6.5
Clean Al(111)	$S_{\text{phys}} > 0.8 \pm 0.1$	300	6.5
Solid I ₂	$S_{\text{phys}} = 0.98 \pm 0.02$	103	6.5
Al-I _(chem) & AlI _{3(ads)}	$R_{\text{SS}} = 0.36 \pm 0.07$	300	6.5-6.9

Table 6.1 : Sticking or reaction probabilities determined for iodine adsorption on aluminium(111)

During the steady state period, the concentration of iodine molecules on the surface must remain constant. This was also observed in the AES-t data (see Figure 6.6) for this system to be discussed later. Therefore, the rate of deposition of iodine atoms is equivalent to the rate at which iodine is lost through the aluminium iodide etching product. The rate of deposition of iodine atoms is related to the flux (F_{in}) and the amount that stick during the steady state situation (S_{ss}) using equation 6.14. The factor of two accounts for the presence of two iodine atoms in a molecule of iodine gas.

$$\frac{dn_I}{dt} = 2 S_{\text{ss}} F_{\text{in}} (\text{iodine atoms } m^{-2}) \quad (6.14)$$

The rate of iodine atom loss from the surface is directly related to the flux of aluminium iodide product.

The rate of loss of aluminium iodide must also be in mass balance with the amount being produced by reaction 6.8 in order to maintain the constant iodine atom coverage, therefore

$$-\frac{dn_I}{dt} = 3 F_{AlI_3, out} = 3 \frac{dn_{AlI_3 ads}}{dt} = 2 R_{ss} F_{in} G_{I, out} \quad (6.15)$$

$G_{I, out}$ is 1.0 for the steady state reaction, as defined earlier. The factor of three accounts for the presence of three iodine atoms in each aluminium iodide molecule. Equation 6.15 allows the flux of aluminium iodide to be described in terms of the experimentally determined quantity, $G_{I, out}$.

Before the steady state etching begins, equations 6.14 and 6.15 are still valid, but because $S > S_{ss}$, and $G_{I, out} < 1.0$, the result is a build up of chemisorbed iodine on the surface during the initial 200 s of adsorption. Using equations 6.14 and 6.15, then the total concentration of iodine on the surface after a time t ($[I_{surf}]$) is therefore given by equation 6.16.

$$[I_{surf}] = 2 \int_0^t S F_{in} dt - 2 \int_0^t R_{ss} F_{in} G_{I, out} dt \quad (\text{iodine atoms m}^{-2}) \quad (6.16)$$

The first term describes the amount of iodine adsorbed from the incident iodine flux, and the second term describes the total amount lost through the desorption of aluminium iodide. Equation 6.16 can be simplified to give equation 6.17.

$$[I_{surf}] = 2 F_{in} \int_0^t S - R_{ss} G_{I, out} dt \quad (6.17)$$

The function $S - R_{ss} G_{I, out}$ and the integral are plotted in Figure 6.11. R_{ss} was 0.36, as determined experimentally, F_{in} was calculated using the ionisation gauge pressure allowing for a relative sensitivity factor of 5.4 for iodine compared to nitrogen, giving $F_{in} = 9.4 \times 10^{16}$ molecules m^{-2} . There is a

possible source of error here as the ionisation gauge had not been calibrated against a standard gauge, resulting in up to a 50 % error in the pressure reading. Figure 6.11 shows that the equilibrium iodine surface coverage is $\approx 9 \times 10^{18}$ atoms m^{-2} . If this is compared with the surface density of aluminium atoms for the (111) surface, 1.41×10^{19} atoms m^{-2} , then the surface coverage of iodine is calculated as ≈ 0.6 monolayers. This surface coverage includes both the chemisorbed iodine, and the adsorbed aluminium iodide. It is suggested however, that the adsorbed aluminium iodide only comprises a minor surface component compared to chemisorbed iodine. This is because the aluminium iodide desorption ceases almost simultaneously with the removal of the incident iodine flux, as shown in Figure 6.3. This implies only a small quantity of aluminium iodide on the surface for equilibrium conditions at 290 K.

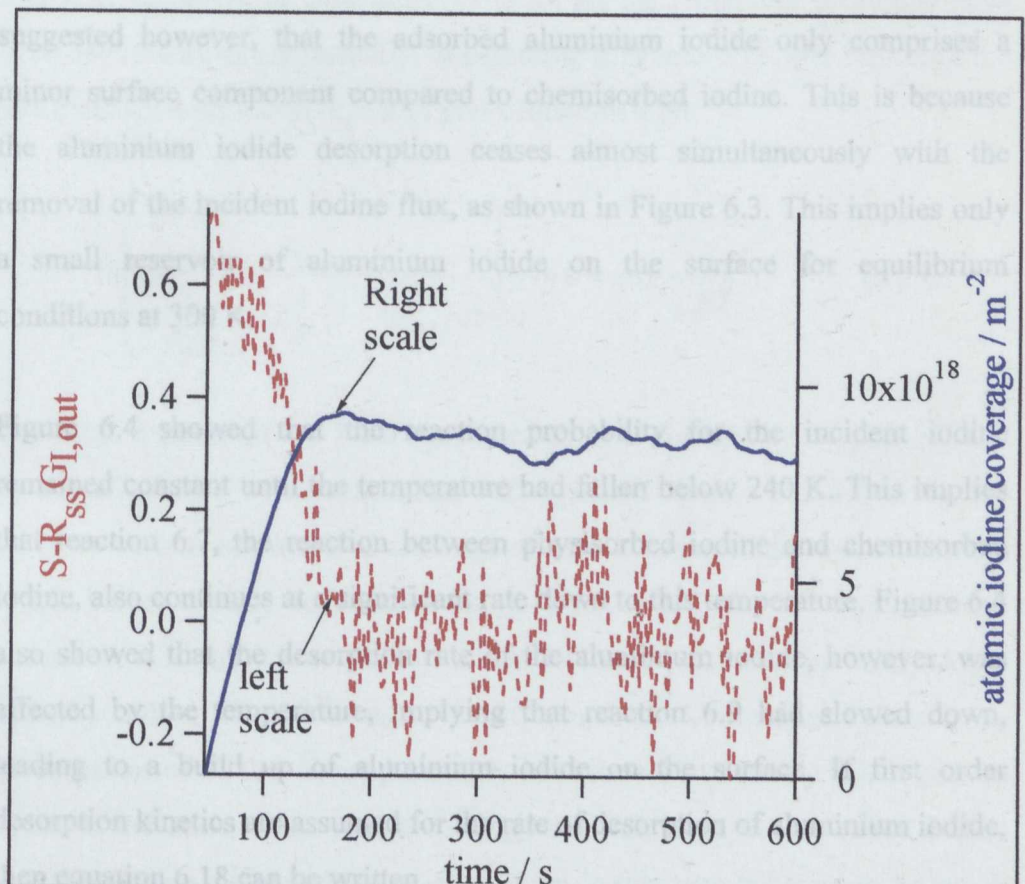


Figure 6.11 : Determination of atomic iodine coverage as a function of time

Plot shows the quantity $S-R_{ss} G_{I,out}$ (dotted line) and the value of equation 6.17 (full line), which gives the atomic iodine coverage as a function of time.

Equation 6.18 gives the rate of desorption of aluminium iodide, where k is the rate constant for the reaction. Equation 6.18 is essentially identical to equation 6.15, but with $G_{I,out} < 1.0$. The surface coverage of aluminium iodide in molecules per metre squared is given by the integral of equation 6.18 with respect to time, with the addition of n_0 , the concentration of aluminium iodide

possible source of error here as the ionisation gauge had not been calibrated against a standard gauge, resulting in up to a 50 % error in the pressure reading. Figure 6.11 shows that the equilibrium iodine surface coverage is $\approx 9 \times 10^{18}$ atoms m^{-2} . If this is compared with the surface density of aluminium atoms for the (111) surface, 1.41×10^{19} atoms m^{-2} , then the surface coverage of iodine is calculated as ≈ 0.6 monolayers. This surface coverage includes both the chemisorbed iodine, and the adsorbed aluminium iodide. It is suggested however, that the adsorbed aluminium iodide only comprises a minor surface component compared to chemisorbed iodine. This is because the aluminium iodide desorption ceases almost simultaneously with the removal of the incident iodine flux, as shown in Figure 6.3. This implies only a small reservoir of aluminium iodide on the surface for equilibrium conditions at 300 K.

Figure 6.4 showed that the reaction probability for the incident iodine remained constant until the temperature had fallen below 240 K. This implies that reaction 6.7, the reaction between physisorbed iodine and chemisorbed iodine, also continues at a significant rate down to this temperature. Figure 6.4 also showed that the desorption rate of the aluminium iodide, however, was affected by the temperature, implying that reaction 6.9 had slowed down, leading to a build up of aluminium iodide on the surface. If first order desorption kinetics are assumed for the rate of desorption of aluminium iodide, then equation 6.18 can be written.

$$rate = k n_{Al_3(ads)} = k_{des} \frac{2}{3} F_{in} R_{ss} G_{I,out} \text{ molecules } m^{-2} s^{-1} \quad (6.18)$$

Equation 6.18 gives the rate of desorption of aluminium iodide, where k is the rate constant for the reaction. Equation 6.18 is essentially identical to equation 6.15, but with $G_{I,out} < 1.0$. The surface coverage of aluminium iodide in molecules per metre squared is given by the integral of equation 6.18 with respect to time, with the addition of n_0 , the concentration of aluminium iodide

(in units of iodine atoms m^{-2}) already present on the surface prior to reaching steady state conditions. This is shown by equation 6.19.

$$n_{\text{Al}_3(\text{ads})} = \frac{I}{3} \left(n_0 + 2 F_{\text{in}} R_{\text{ss}} \int_0^t (1 - G_{I,\text{out}}) dt \right) \quad (6.19)$$

The only unknown in equation 6.19 is n_0 , all the remaining quantities have been determined experimentally. Substituting 6.19 into 6.18, and replacing the rate constant with $\nu \exp(-E_a / RT)$ gives equation 6.20.

$$\ln \left(\frac{G_{I,\text{out}}}{\frac{n_0}{2 F_{\text{in}} R_{\text{ss}}} + 2 \int_0^t (1 - G_{I,\text{out}}) dt} \right) = \ln C = \ln \nu - \frac{E_a}{RT} \quad (6.20)$$

The large expression has been simplified to $\ln C$ for brevity. A plot of $\ln C$ versus $1/T$ should be a straight line with gradient of $-E_a / RT$. However, the value of n_0 is unknown. If a coverage of zero is assumed for the aluminium iodide before cooling began, then the $\ln C$ versus $1/T$ plot has a pronounced curvature. It is possible to achieve a straight line for this plot by using values of n_0 , such that, $1.4 \times 10^{18} < n_0 < 9 \times 10^{18}$ atoms m^{-2} . Using these values for n_0 gives values of E_a that lie in the range, $57 > E_a > 39$ kJ mol^{-1} . The higher n_0 figure is the same as the iodine coverage for saturation. It was stated earlier that the surface concentration of aluminium iodide was believed to be much lower than the iodine coverage. Therefore, the lower n_0 is considered to be the more realistic value, giving E_a as 57 kJ mol^{-1} , see Figure 6.12. This value compares very well with half the entropy of sublimation for Al_2I_6 at 58.15 kJ mol^{-1} , which adds extra support to the analysis [6.13].

The LOSSP data above shows that iodine physisorbs at 103 K producing multilayers. The AES-t experiment performed at this temperature (see Figure 6.5) produced results that are consistent with that conclusion. The total exposure in the AES-t experiment, is less compared to that in the LOSSP experiment for the same sample temperature. Therefore, all the iodine incident

upon the surface during the AES-t experiment is assumed to have stuck, as in the LOSSP experiment. No ordered structure could have been formed as evidenced by the absence of a LEED pattern. The shape of the AES-t plot in Figure 6.5, is difficult to determine precisely. The plot appears to contain distinct linear regions separated by breaks in the gradient for the aluminium,

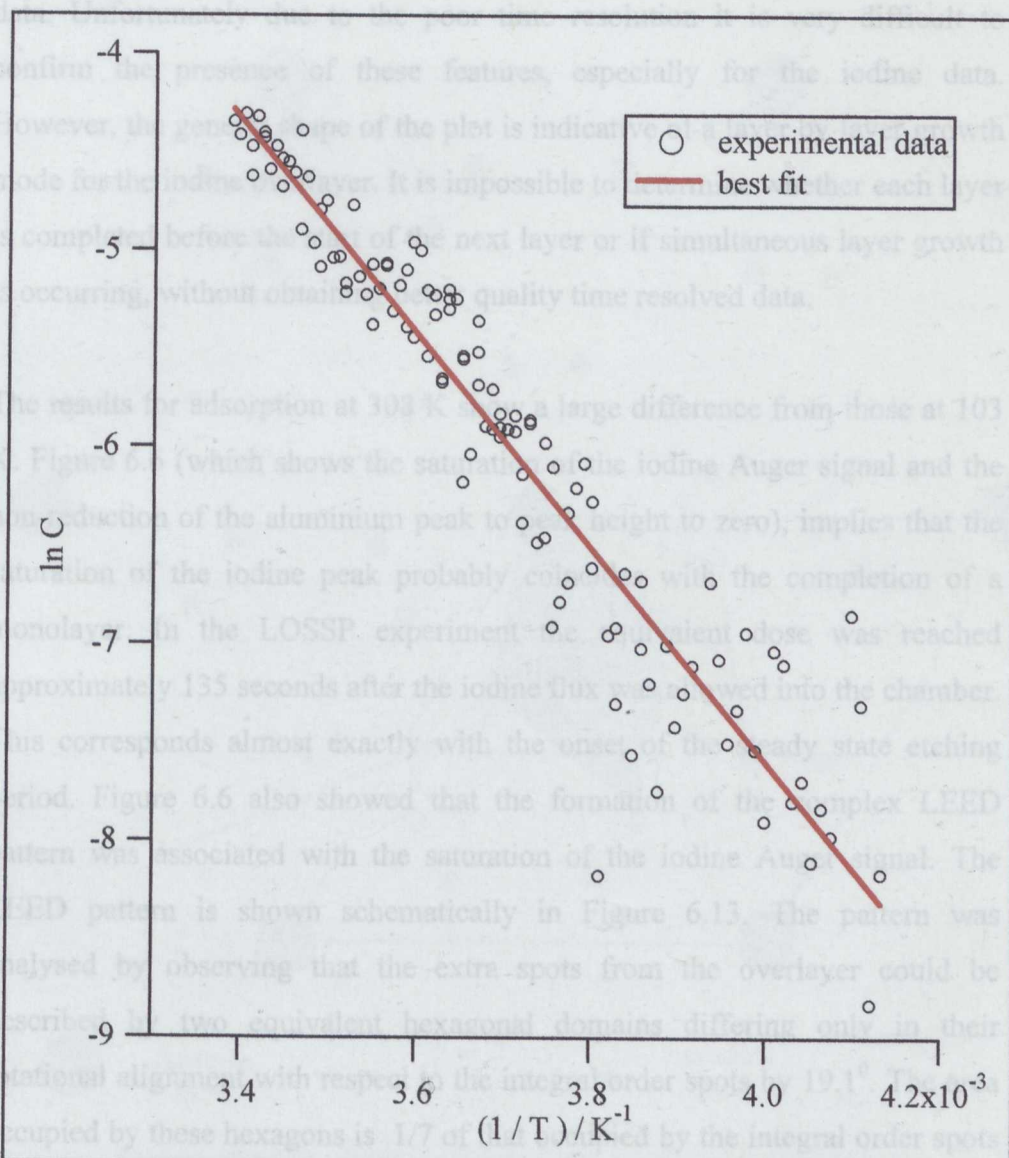


Figure 6.12 : Plot of $\ln C$ versus $1/T$
 Plot uses an n_0 value of 1.4×10^{18} iodine atoms m^{-2} , which gives an activation energy for desorption of $\sim 57 \text{ kJmol}^{-1}$.

community, since they represent a difficult challenge for structural determination techniques because of the large size of the real space unit mesh. Systems which show this symmetry include, I/Pt(111) [6.14-6.16], S/Cu(111) [6.17], S/Pd(111) [6.18], and P/Ru(111) [6.19]. Of these systems the

upon the surface during the AES-t experiment is assumed to have stuck, as in the LOSSP experiment. No ordered structure could have been formed as evidenced by the absence of a LEED pattern. The shape of the AES-t plot in Figure 6.5, is difficult to determine precisely. The plot appears to contain distinct linear regions separated by breaks in the gradient for the aluminium, data. Unfortunately due to the poor time resolution it is very difficult to confirm the presence of these features, especially for the iodine data. However, the general shape of the plot is indicative of a layer by layer growth mode for the iodine overlayer. It is impossible to determine whether each layer is completed before the start of the next layer or if simultaneous layer growth is occurring, without obtaining better quality time resolved data.

The results for adsorption at 308 K show a large difference from those at 103 K. Figure 6.6 (which shows the saturation of the iodine Auger signal and the non-reduction of the aluminium peak to peak height to zero), implies that the saturation of the iodine peak probably coincides with the completion of a monolayer. In the LOSSP experiment the equivalent dose was reached approximately 135 seconds after the iodine flux was allowed into the chamber. This corresponds almost exactly with the onset of the steady state etching period. Figure 6.6 also showed that the formation of the complex LEED pattern was associated with the saturation of the iodine Auger signal. The LEED pattern is shown schematically in Figure 6.13. The pattern was analysed by observing that the extra spots from the overlayer could be described by two equivalent hexagonal domains differing only in their rotational alignment with respect to the integral order spots by 19.1° . The area occupied by these hexagons is $1/7$ of that occupied by the integral order spots (see Figure 6.13). Therefore, the LEED pattern is a $(\sqrt{7} \times \sqrt{7})R19.1^\circ$ (generally abbreviated to $\sqrt{7}$ for the rest of this thesis). Surface structures which generate this LEED pattern have recently been of great interest to the surface science community, since they represent a difficult challenge for structural determination techniques because of the large size of the real space unit mesh. Systems which show this symmetry include, I/Pt(111) [6.14-6.16], S/Cu(111) [6.17], S/Pd(111) [6.18], and P/Rh(111) [6.19]. Of these systems the

"simplest" overlayer structure is the 1×1 surface, where the $\sqrt{7}$ structure is formed at a surface coverage of $3/7$, with the surface mesh containing three iodine atoms. The structure has been studied by a combination of LEED, AES, TPD, ADAM and STM [6.14-6.16], and have shown that the iodine is

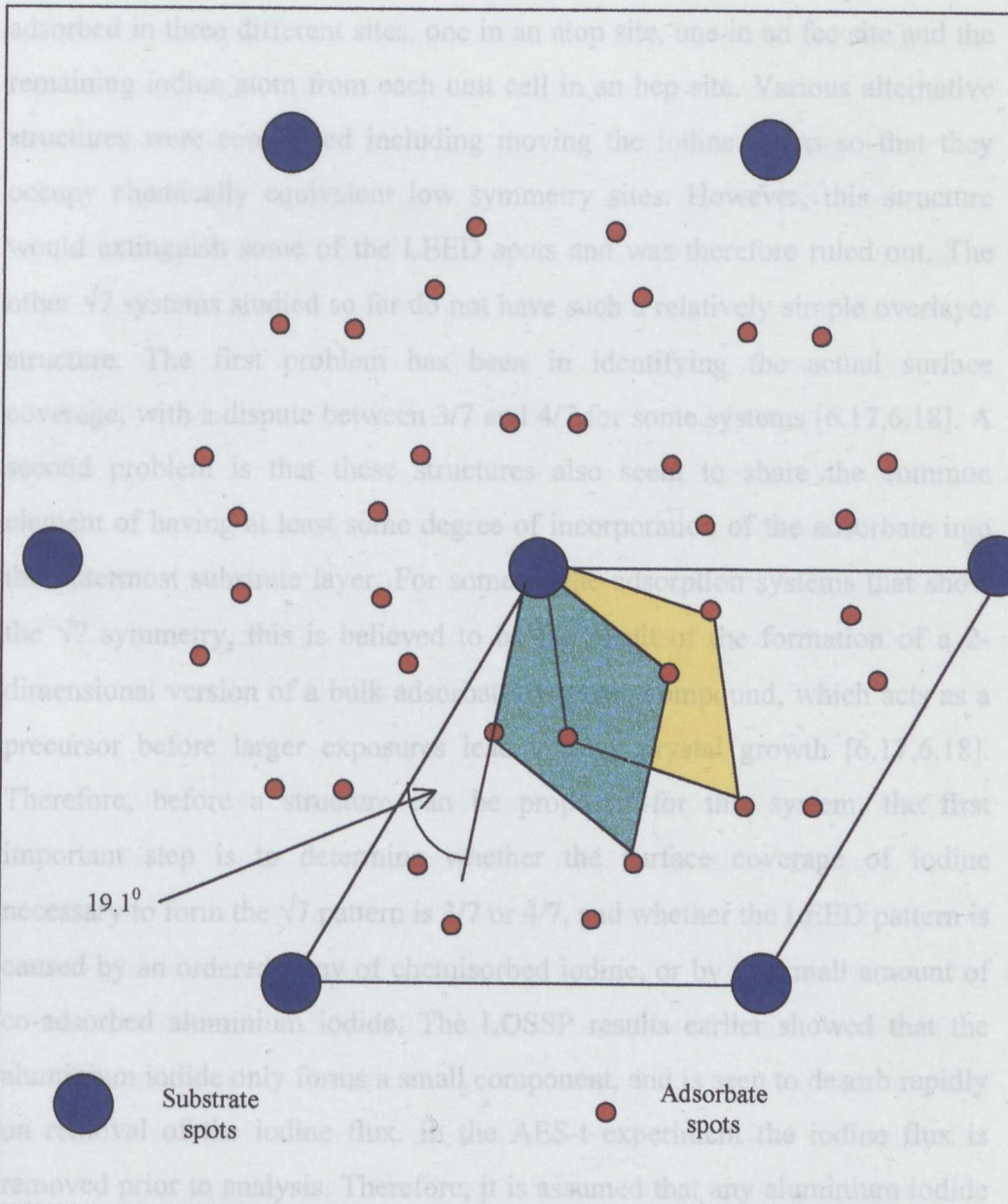


Figure : 6.13 Schematic diagram of complex LEED pattern

Figure shows the substrate spots as blue circles, with the adsorbate induced spots as red circles. The two domains of the complex pattern are shown by the shaded areas.

“simplest” overlayer structure is the I/Pt(111) surface, where the $\sqrt{7}$ structure is formed at a surface coverage of $3/7$, with the surface mesh containing three iodine atoms. The structure has been studied by a combination of LEED, AES, TPD, ADAM and STM [6.14-6.16], and have shown that the iodine is adsorbed in three different sites, one in an atop site, one in an fcc site and the remaining iodine atom from each unit cell in an hcp site. Various alternative structures were considered including moving the iodine atoms so that they occupy chemically equivalent low symmetry sites. However, this structure would extinguish some of the LEED spots and was therefore ruled out. The other $\sqrt{7}$ systems studied so far do not have such a relatively simple overlayer structure. The first problem has been in identifying the actual surface coverage, with a dispute between $3/7$ and $4/7$ for some systems [6.17,6.18]. A second problem is that these structures also seem to share the common element of having at least some degree of incorporation of the adsorbate into the outermost substrate layer. For some of the adsorption systems that show the $\sqrt{7}$ symmetry, this is believed to be the result of the formation of a 2-dimensional version of a bulk adsorbate-substrate compound, which acts as a precursor before larger exposures lead to bulk crystal growth [6.17,6.18]. Therefore, before a structure can be proposed for this system, the first important step is to determine whether the surface coverage of iodine necessary to form the $\sqrt{7}$ pattern is $3/7$ or $4/7$, and whether the LEED pattern is caused by an ordered array of chemisorbed iodine, or by the small amount of co-adsorbed aluminium iodide. The LOSSP results earlier showed that the aluminium iodide only forms a small component, and is seen to desorb rapidly on removal of the iodine flux. In the AES-t experiment the iodine flux is removed prior to analysis. Therefore, it is assumed that any aluminium iodide produced on the surface will have already desorbed. Therefore, the LEED pattern must be the result of an ordered layer of chemisorbed iodine. In order to decide if the surface coverage is $3/7$ or $4/7$, two methods have been used. Figure 6.14 shows how a close packed layer of iodine, in the same structural arrangement as for I/Pt(111) [6.14-6.16], produces a structure, that cannot contain more than a coverage of $3/7$. The other method relies on using the LOSSP results, these showed that the saturation coverage of iodine was $9 \times$

10^{18} iodine atoms m^{-2} or ~ 0.6 ML (the error in the LOSSP data is large, with possible values from $4 \rightarrow 18 \times 10^{18}$). The $3/7$ and $4/7$ coverages that correspond to the $\sqrt{7}$ structures above are equivalent to 0.43 and 0.57 ML respectively. The LOSSP results showed that a percentage of the iodine on the surface during equilibrium etching conditions was associated with aluminium iodide. During the AES-t experiment aluminium iodide could and probably was formed on the surface. However, prior to analysis the iodine vapour was removed from the chamber, therefore due to its high vapour pressure the aluminium iodide would have probably have desorbed rapidly as discussed above, thus reducing the equilibrium iodine surface coverage. If the surface coverage was only $3/7$ then the concentration of iodine atoms would be $1.41 \times 10^{19} \times 3/7$ which gives 6×10^{18} iodine atoms m^{-2} . The LOSSP data gave an equilibrium value of 9×10^{18} iodine atoms m^{-2} , the difference between these two values must be due to the aluminium iodide that has formed during the experiment. This leaves 3×10^{18} iodine atoms m^{-2} which corresponds to 1×10^{18} aluminium iodide molecules m^{-2} , which is an almost exact match to that determined from the LOSSP data discussed earlier.

The discussion above means that any structure proposed for the $\sqrt{7}$ pattern must contain 3 atoms per unit cell. The simplest possible structure is that which matches the iodine/platinum(111) system as shown in Figure 6.14, with a close packed layer of chemisorbed iodine forming a $\sqrt{7}$ overlayer (the iodine is drawn as having a radius of 2.2 \AA , then same as its Van der Waals radius). No data collected here enables a complete structure determination for this system. However, the structure proposed in Figure 6.14 does not contradict any of the results presented. However, it was shown in section 6.1 that there was some evidence for sub-surface site occupation for chlorine adsorption on aluminium. This has also been suggested as a possible mechanism for the formation of Al_2Cl_6 during etching of aluminium by chlorine [6.20]. It is probable here that Al_2I_6 dimers are formed during the experiments described in this chapter, however it was not possible to detect them. So it can only be concluded that the structure shown in Figure 6.14 is entirely possible, but that

sub-surface site occupation probably accompanied by some reconstruction or rearrangement of the substrate surface cannot be ruled out.

The variable temperature experimental data shown in Figure 6.4 suggested four main regions. The nature of each of these regions is discussed below.

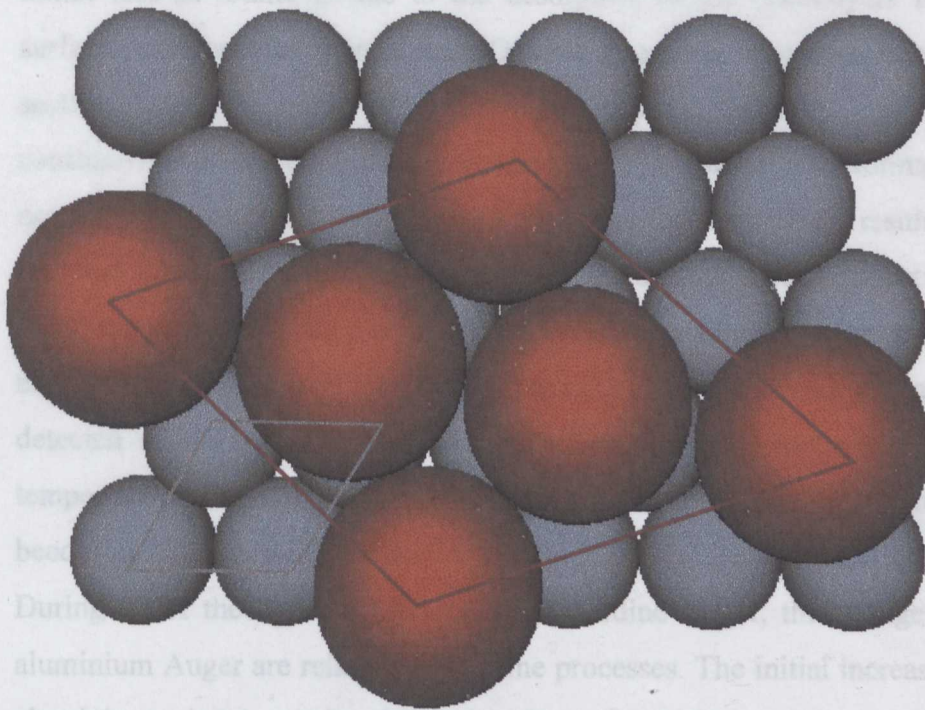


Figure 6.14 : Proposed structure for Al(111)-($\sqrt{7}\times\sqrt{7}$)R19.1⁰

Diagram shows aluminum atoms as grey, and iodine as red. Only one domain of the ($\sqrt{7}\times\sqrt{7}$)R19.1⁰ iodine lattice is shown (red line). The iodine is shown to adsorb in mixed sites, with 1 atom per unit cell in each of the atop, fcc and hcp hollow. The iodine atoms are shown with a radius of 2.2 Å. The unit cell of the substrate (grey line) and iodine lattice (red line) are highlighted on the figure.

It was noted in section 6.4 that the aluminium Auger peak-to-peak height recorded at the end of a variable temperature experiment was only approximately 80% of the clean surface value. This can be explained again by the etching reaction. It is probable that the etching reaction does not uniformly remove aluminium from the surface, leaving it disordered. Because of the relatively short mean free path for aluminium Auger electrons due to their low energy (67-eV) the disordered surface must cause a reduction in signal after the etching process has occurred. Confirmation for the disordered state of the

sub-surface site occupation probably accompanied by some reconstruction or rearrangement of the aluminium surface cannot be ruled out.

The variable temperature experiment data shown in Figure 6.8 contained four main regions. The nature of each of these is relatively easy to interpret. The initial loss in iodine is due to the desorption of the multilayers from the surface, this was also seen in the LOSTPD data to be discussed later in this section. The next phase with the iodine signal remaining approximately constant is because the reactions leading to aluminium iodide formation are not thermally activated until ~ 240 K as shown by the LOSSP results. Once the temperature reaches 240 K then reaction 6.8 becomes active and aluminium iodide production starts. This removes iodine from the Auger data either because aluminium iodide is formed as crystallites which cannot be detected easily [6.21] or that the aluminium iodide is desorbing. As the temperature increases it is the desorption of the aluminium iodide that becomes the dominant process in the reduction of the iodine Auger signal. During all of the above behaviour for the iodine Auger, the changes in the aluminium Auger are related to the same processes. The initial increase in the aluminium signal results from the desorption of the iodine multilayers allowing the aluminium Auger electrons to escape and be detected. The plateau corresponds to the static situation before the etching reactions start. Once these become thermally activated the aluminium peak-to-peak height begins to increase slowly at first and then quickens with the increased rate of aluminium iodide formation and desorption.

It was noted in section 6.4 that the aluminium Auger peak-to-peak height recorded at the end of a variable temperature experiment was only approximately 80 % of the clean surface value. This can be explained again by the etching reaction. It is probable that the etching reaction does not uniformly remove aluminium from the surface, leaving it disordered. Because of the relatively short mean free path for aluminium Auger electrons due to their low energy (67 eV) the disordered surface must cause a reduction in signal after the etching process has occurred. Confirmation for the disordered state of the

surface comes from the LEED observations which showed that (1x1) LEED pattern following a variable temperature experiment was much less well formed than for the clean surface.

The LOSTPD data shown in Figure 6.9 shows one consistent dominant feature, which is a large rise in the signal from all four species at the higher end of the temperature range. Close examination for the data, in particular that of the 300s exposure (Figure 6.9a) shows that all signals are at background levels (except for any desorption peaks) prior to approximately 500 K. At this point there is a step increase in the I_2^+ signal which is matched by the signal from all the other species. However, if the desorption peaks for the 900 and 1200 s exposure times are examined it is clear that the AlI_n^+ peaks are independent of the I_2^+ signal. If this is combined with the variable temperature experiments which show that iodine is removed from the surface after 300 K, it is clear that at temperatures above 500 K, iodine must be desorbing from the sample holder and filaments, resulting in thermal etching of the aluminium surface and leading to the large increases in the AlI_n^+ peaks.

The absence of any desorption peak for the 300 and 600 s exposure data, suggests that the iodine is probably being removed from the surface as atomic iodine, rather than as aluminium iodide etch products. Unfortunately, as stated in section 6.3, it was not possible to record the I^+ peak at m/z 127, due to contamination of the mass spectrometer filaments, so it was not possible to confirm this. This does seem a reasonable explanation as the formation of AlI_3 as described by reaction 6.8 requires the combination of physisorbed iodine with chemisorbed iodine. However, for the low exposures the concentration of chemisorbed iodine will be low, and there should not be any physisorbed iodine left to react and hence form aluminium iodide, by the time that temperatures are reached in the LOSTPD experiment where the etching reactions are thermally activated. This goes against the LOSSP results which showed aluminium iodide formation even for low coverages, the difference is assumed to be caused by the different experimental conditions, with the

LOSSP experiment carried out under a constant iodine overpressure, and the LOSTPD data after a single dose.

For the higher exposure data, which is past the point of monolayer formation, the desorption peak at 363 K, does not seem to change with the increased exposure from 900 to 1200 s. This suggests that this peak is due to the desorption of a fixed amount of iodine from the surface. The most likely source is the chemisorbed iodine that forms the $\sqrt{7}$ LEED pattern. It is suggested that as the coverage is higher than for the 300 and 600 s data, instead of desorbing as atomic iodine, the iodine reacts directly with the surface at this higher temperature to produce AlI_3 . The 363 K desorption peak appears at the same time as the iodine Auger signal is seen to disappear (see Figure 6.8) and the disappearance of the $\sqrt{7}$ LEED pattern, adding weight to this conclusion. The lower temperature desorption peak at 300 K must be associated with the etching reaction seen during the LOSSP experiment, with the remaining physisorbed iodine reacting with the chemisorbed iodine layer to produce AlI_3 . This process must result in the removal of all physisorbed iodine, and a saturated iodine monolayer. The data appears to show that AlI_1 is the major product from this desorption peak. However, it is believed that this could be due to experimental error. As described in section 6.3, it was necessary to record the peaks in separate experiments and to use different counting times. It is possible errors in the heating rate, and exposures were such that the relative amount of AlI_n^+ collected were not the same in every experiment. Combined with the differing counting times this means it is possible that the data for the AlI_n^+ peaks, could be misleading. Attempts were made to repeat the data presented, however experimental difficulties made this impossible. Comparison with the Al-Cl results of Janssen et al [4.7] discussed earlier (see section 6.1.1), adds further weight to the assumption that the lower desorption peak is the result of AlI_3 desorption and not AlI , because AlCl was not seen as a major product until much higher temperatures and only after AlCl_3 formation had stopped.

The LOSTPD data could in theory be fitted to provide detailed kinetic information, however because of the limited data and the noise levels, it was decided that this process would not provide any significant or reliable results so it has not been carried out.

6.6 Summary

This chapter presented a new and novel methodology by which sticking & reaction probabilities can be determined. The technique relies on the use of a randomised incident flux and the detection of a reflected “beam” using a liquid nitrogen cooled shroud to provide a line of sight between the sample and the mass spectrometer. This new technique has been termed Line Of Sight Sticking Probability or LOSSP. The technique was used to study the etching of an aluminium(111) surface by iodine vapour. An initial sticking probability on the clean surface at 300 K was determined as 0.8 ± 0.1 , this increased to 0.98 ± 0.02 for the clean surface at 103 K. The reaction probability for the formation of aluminium iodide (AlI_3 or Al_2I_6) was found to be 0.36 ± 0.07 at 300 K. Temperature dependent LOSSP measurements were used to determine the equilibrium iodine surface coverage as 1.4×10^{18} iodine atoms m^{-2} . This was then used to calculate the activation energy for desorption of AlI_3 as 57 kJmol^{-1} .

AES, LEED and TPD data was also presented for this system. This confirmed the results from the LOSSP data which suggested the formation of physisorbed multilayers of iodine at 103 K. For adsorption at 308 K a $(\sqrt{7} \times \sqrt{7})\text{R}19.1^0$ LEED pattern was seen to form at the completion of the monolayer as adjudged by AES. The structure was assumed to consist of a close packed layer of chemisorbed iodine. No firm conclusions could be drawn about the structure, although a simple close packed layer of iodine does form a $(\sqrt{7} \times \sqrt{7})\text{R}19.1^0$ structure, the possibility of sub-surface adsorption accompanied by reconstruction of the aluminium surface was considered. The coverage of the iodine $\sqrt{7}$ structure was considered to be $3/7$ of a monolayer. Variable temperature and LOSTPD data confirmed the presence and temperature dependence of the etching reactions.

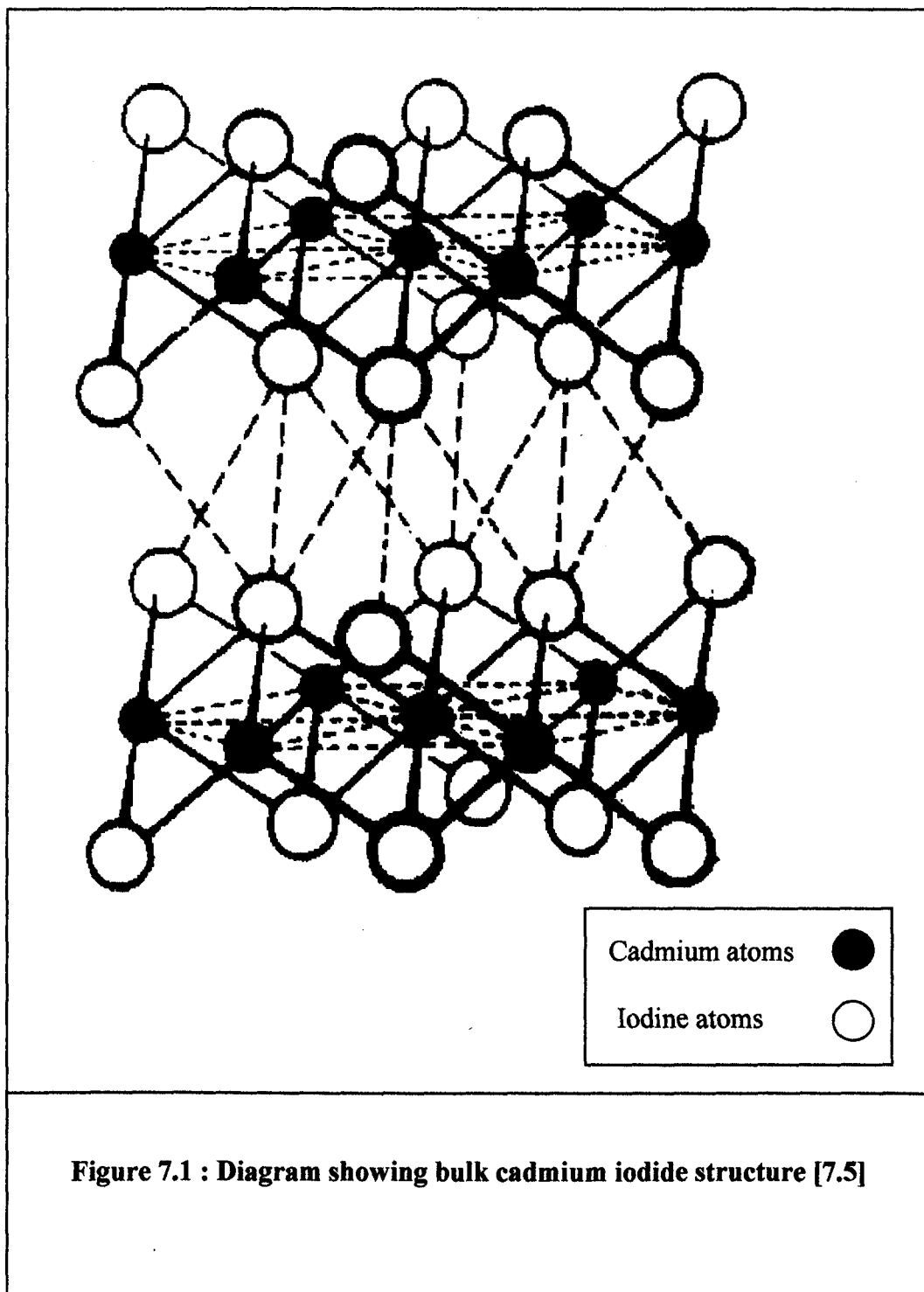
Chapter 7 : Growth and reaction of Cadmium Iodide (CdI₂) on Aluminium(111)

7.0 Introduction

This chapter presents a study of cadmium iodide surface chemistry on an aluminium(111) surface and forms part of a continued investigation into the surface chemistry of transition metal di-halides. The systems studied so far include CdI₂ / InSb(001) [7.1], CdI₂ / Cu(111) [7.2], CdBr₂ / Cu(111) [7.3], CdBr₂ / InSb(001) [7.3] and PbI₂ / InSb(001) [7.4].

The transition metal di-halides that the group has studied, are those which have the “sandwich layer” structure type, as illustrated in Figure 7.1. This structure consists of two hexagonal-close packed layers of halogen ions, with the metal ions in the interstices between the halogen layers. These layers then stack together to form the completed “sandwich” structure.

The interest in these materials arises from the different bonding types that occur within the bulk structure. The “sandwich layers” have strong intralayer chemical bonding, but bonding between layers is only of weak Van der Waals type forces. These materials therefore present an intriguing case when adsorbed on a metal surface, because, the strong intralayer bonding will try and maintain the integrity of the sandwich layer, whilst bonding to the substrate will try to disrupt it and might overcome the weaker interlayer forces.



7.1 Relevant Studies

This section details two studies of the surface chemistry of transition metal dihalides, which are the most relevant to the results to be presented in this chapter.

7.1.1 Indium Antimonide(001)-Cadmium Iodide

Mowbray et al [7.1] studied the adsorption of cadmium iodide on an InSb(001) surface, in the first reported study of the adsorption of a transition-metal dihalide. For adsorption at room temperature, AES-t plots indicated that the cadmium iodide was adsorbing onto the surface, in a layer-by-layer growth mode. The cadmium (376 eV) and iodine Auger (511 eV) peak-to-peak height ratio was reported as 1.38:1. As adsorption progressed the (4x1) LEED pattern of the clean reconstructed surface was replaced in turn by a p(2x1), a (1x1) with blurred spots, and a low background pattern with two hexagons superimposed, with one rotated at $\sim 7^\circ$ to the other. The conclusion was that cadmium iodide was growing epitaxially upon the InSb(001) surface with the basal plane of the cadmium iodide lattice parallel to the InSb(001) surface. By rotating the cadmium iodide mesh by 7.46° and contracting the lattice by 1.5%, there is alignment between the substrate and adsorbate meshes every two substrate unit meshes. Thereby, row matching occurs which, lowers the interfacial energy.

Heating the adsorbed multilayers formed by adsorption at room temperature caused a rapid drop in the cadmium and iodine Auger signals by $\sim 50\%$ at temperatures between 393 and 413 K. Further step drops in the intensity of these signals were seen at higher temperatures, until the cadmium and iodine Auger peak-to-peak heights fell below the detection limit at 493 K. Each drop in the cadmium and iodine signals was matched by a simultaneous increase in the indium and antimony signal. Additionally, each step in the variable

temperature plot coincided with a change in the observed LEED pattern. The starting point was the two hexagons, followed by a p(2x1), a (1x1)-CdI, and a (1x1) clean surface pattern.

The (1x1)-CdI structure exhibited a cadmium to iodine Auger peak-to-peak height ratio of 2:1 compared to the 1.38:1 during epitaxial growth. A model for this structure was proposed which consisted of a (1x1) array of iodine atoms with a stoichiometric amount of cadmium (0.5 monolayers) randomly distributed in the 4-fold octahedral sites above the iodine layer.

7.1.2 Copper(111)-Cadmium Iodide

Ithnin et al [7.2] also studied the surface chemistry of cadmium iodide, this time on a metal surface, copper(111). Adsorption at 308 K, was studied using both LEED and AES. LEED showed the appearance of a $(\sqrt{3}\times\sqrt{3})R30^\circ$ pattern very quickly. After 660 s, this pattern became sharp with a low background. Further adsorption caused a gradual deterioration of the adsorbate spots, with the background slowly increasing. Large exposures caused complete loss of all but the innermost diffraction spots, whilst retaining the $(\sqrt{3}\times\sqrt{3})R30^\circ$ pattern. AES-t data indicated that layer-by-layer growth was occurring. This was probably not true Frank van der Merwe growth, but probably consisted of several incomplete layers growing simultaneously without crystallite growth. The ratio of the cadmium to iodine Auger peak-to-peak heights was initially 1:1.4, but this decreased to 1:1.1 after 2000 s, where it remained constant. The constant value of the ratio showed that the cadmium iodide was deposited in a fixed ratio, assumed to be the stoichiometric ratio of 1:2, i.e. CdI₂. A variable temperature experiment was carried out, this showed multilayer desorption at temperatures between 380 – 410 K. However, as the temperature was increased the Cd:I peak-to-peak height ratio did not remain constant. Between 300 and 380 K, the ratio was 1:1.3, approximately the same as seen during adsorption. But, for temperatures between 380 and 410 K, the ratio increased to 1:2.6,

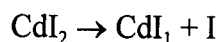
indicating a stoichiometry of CdI_1 at 410 K. This surface also exhibited a $(\sqrt{3}\times\sqrt{3})\text{R}30^\circ$ LEED pattern. Above 410 K, the cadmium signal fell below the detectable limit and was assumed to have desorbed. At 410 K the iodine coverage had dropped to a value which remained constant even after annealing to temperatures greater than 650 K. This surface showed a $(\sqrt{3}\times\sqrt{3})\text{R}30^\circ$ LEED pattern and it was therefore deemed to be the copper(111)- $(\sqrt{3}\times\sqrt{3})\text{R}30^\circ$ -iodine structure, with a coverage of 1/3 of a monolayer.

The initial $(\sqrt{3}\times\sqrt{3})\text{R}30^\circ$ pattern, was assigned as being the result of the epitaxial growth of cadmium iodide on the copper (111) surface with its basal plane along the copper $\sqrt{3}$ direction. This is because there was only a 4 % difference between the cadmium iodide lattice parameters and the copper $\sqrt{3}$ distance.

For an iodine coverage of 0.33 ML, with an associated cadmium coverage of 0.16 ML, the $(\sqrt{3}\times\sqrt{3})\text{R}30^\circ$ structure originated from the iodine atoms, with the cadmium located in an unspecified position (see chapter 5). For a higher iodine coverage of 0.66 ML, the structure would have been expected to consist of a complete sandwich layer of cadmium iodide, however this structure was not considered to have formed. Higher coverages produced multilayer cadmium iodide, presumably with the bulk CdI_2 structure. The CdI_1 surface seen during the variable temperature experiment, was determined to contain 0.33 ML of iodine, and 0.33 ML of cadmium. The cadmium atoms were assumed to be located between the $(\sqrt{3}\times\sqrt{3})\text{R}30^\circ$ iodine layer and the copper surface. It was suggested that as the temperature at which the CdI_1 forms during the variable temperature experiment is only ~ 130 K higher than the adsorption temperature, that any rearrangement processes operating there might also operate during adsorption. Therefore, it was proposed that the initial structure formed is a $(\sqrt{3}\times\sqrt{3})\text{R}30^\circ - \frac{1}{2}(\text{CdI}_2)$ surface, consisting of 0.33 ML of iodine in a $(\sqrt{3}\times\sqrt{3})\text{R}30^\circ$ arrangement, with 0.16 ML cadmium randomly located in the

three fold hollows below the iodine layer (see chapter 5 for a study of this structure).

The CdI₁ structure implies loss of iodine from the surface. The iodine was concluded to be liberated by the following reaction.



Where it was considered to diffuse to the copper surface, react and form three-dimensional crystallites of copper iodide, hence contributing only a small amount to the iodine Auger signal.

7.2 Experimental methods

The UHV chamber used to obtain these results was discussed in this chapter was described in section 3.3. Note however, the sample holder used was slightly different from that described in section 3.3.1 and only allowed the sample temperature to reach a minimum of 143 K, compared to 103 K for the experiments described in chapter 6. Cadmium iodide (CdI₂) was produced using the solid-state source described in section 3.4, operated at a temperature of 523 K. It should be noted that a different pellet of CdI₂ & AgI was used to perform these experiments than the one used to obtain the results in chapters 4 and 5. The aluminium (111) crystal used was the same one used for the iodine adsorption experiments presented in chapter 6. The preparation of the crystal was described in section 3.1.1.

AES and LEED experiments were carried out during adsorption. Cadmium iodide was deposited onto the clean aluminium surface which was either liquid nitrogen cooled to 143 K, or at room temperature, 308 K. The sample was turned to face the source, with the baffle open for periods of 900 s at 143 K or 1800 s at 308 K, the baffle was then closed, and the sample rotated to face the

RFA for analysis. Three Auger transitions were followed, the 67 eV aluminium, 376 eV cadmium and the 511 eV iodine peaks.

Variable temperature experiments were carried out following adsorption. The sample was heated to the required temperature, held for ~ 90 s and then allowed to cool. AES and LEED data were then recorded, before the sample was heated to progressively higher temperatures. AES data was again recorded for the aluminium, cadmium and iodine Augers, at 67, 376 and 511 eV respectively.

Unlike the experiments described in chapter 6, TPD experiments were performed in the more usual manner without the liquid nitrogen shroud. The experiments were conducted in a different experimental chamber to the one used to obtain the LEED and AES results. A different cadmium iodide source also had to be used for the TPD experiments compared to the LEED/AES experiments. Therefore, comparative exposures for the TPD compared to the LEED/AES results are unknown. An older mass spectrometer was used to perform the TPD experiments, allowing only the cadmium and aluminium mono-iodide (AlI_1^+) peaks to be recorded. The AlI_2^+ and AlI_3^+ peaks were of too high a mass, and as for the results in chapter 6, the iodine (I^+) peak at m/z 127 was not used due to filament contamination.

7.3 Results

The angle-integrated AES data for adsorption at 143 K versus exposure time is shown in Figure 7.2. It can be seen that the aluminium signal exhibited an approximately exponential decay, with no signal being detectable after 9000 s. The cadmium and iodine Auger peak-to-peak heights showed a continuous increase throughout the experiment, with a slight tail off towards the end. Figure 7.2 also shows the cadmium to iodine Auger peak-to-peak height ratio, which remained approximately constant throughout the experiment at $\sim 1.25:1$.

LEED observations during the adsorption are indicated above Figure 7.2. The (1×1) of the clean surface faded rapidly and became invisible after 5400 s, with no further diffraction spots seen. However, between 900 and 5400 s, it was possible to see very faint signs of a complex LEED pattern, believed to be the $(\sqrt{7} \times \sqrt{7})R19.1^\circ$ seen for iodine adsorption on aluminium (111) described in chapter 6.

Adsorption at room temperature (308 K) produced different results. The angle integrated peak-to-peak AES data recorded is plotted against exposure time in Figure 7.3. As for adsorption at 143 K, the aluminium Auger peak-to-peak height showed an exponential decay, however, the rate of decay was much slower, with the signal not having decayed to zero even by 10800 s. The iodine Auger however showed a striking difference to its behaviour at 143 K. Initially, a similar rise was seen compared to the 143 K adsorption experiment. However, at 3600 s the iodine Auger signal saturated and remained constant for the remainder of the adsorption. The cadmium signal seemingly behaved in a similar way to the experiment at 143 K, however, close examination of the peak-to-peak heights shows that they were actually much higher for a given exposure time. In fact, after 9000 s the cadmium peak-to-peak height for adsorption at 308 K was $\sim 50\%$ higher than for the equivalent exposure time for adsorption at 143 K. The Cd:I peak-to-peak height ratio during adsorption

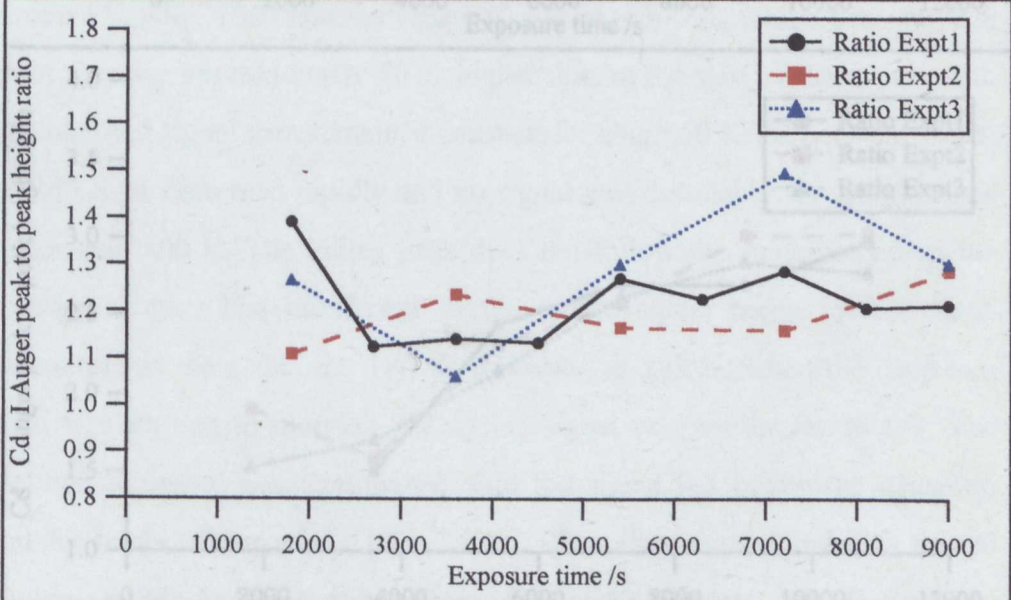
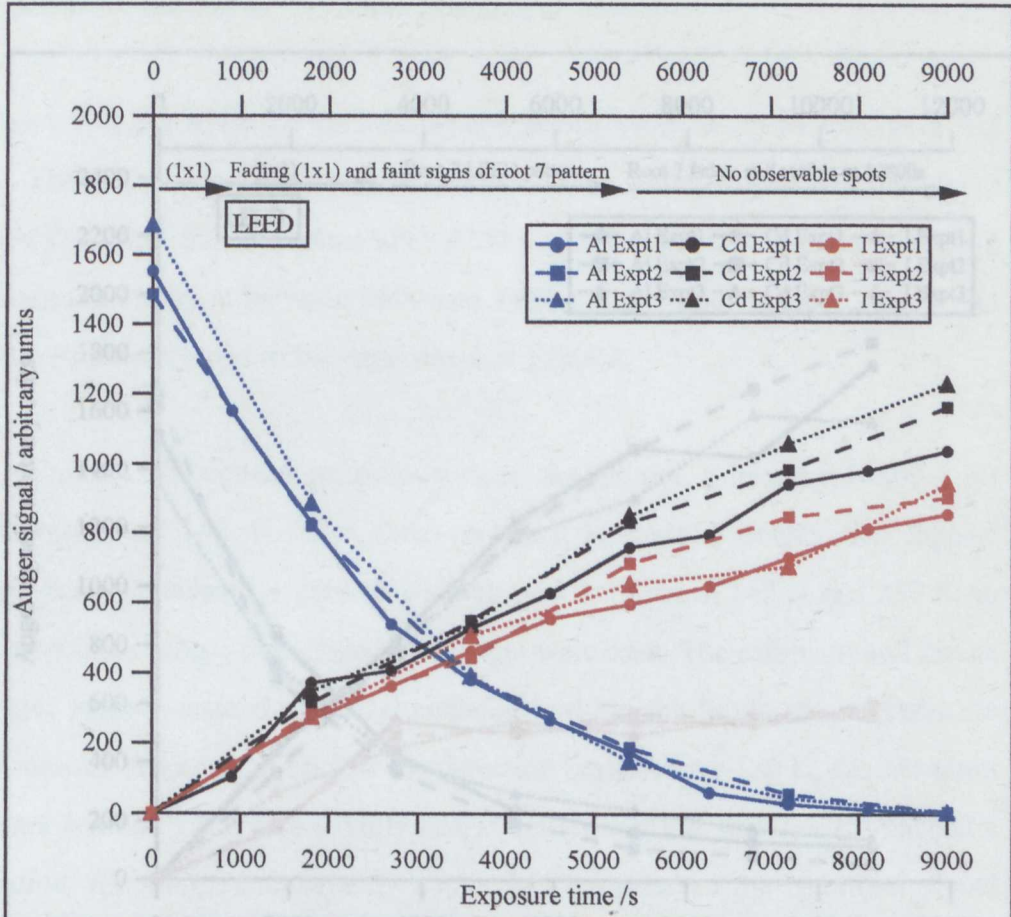


Figure 7.2 : AES-t plot for CdI₂ adsorption at 143 K

Top graph shows Auger peak-to-peak heights versus exposure time.
 Bottom graph shows cadmium:iodine Auger peak-to-peak height ratio versus exposure time.

is also included in Figure 7.3 It showed a continuous rise throughout the experiment, starting at $\sim 1.5:1$ and finishing at $\sim 3.0:1$.

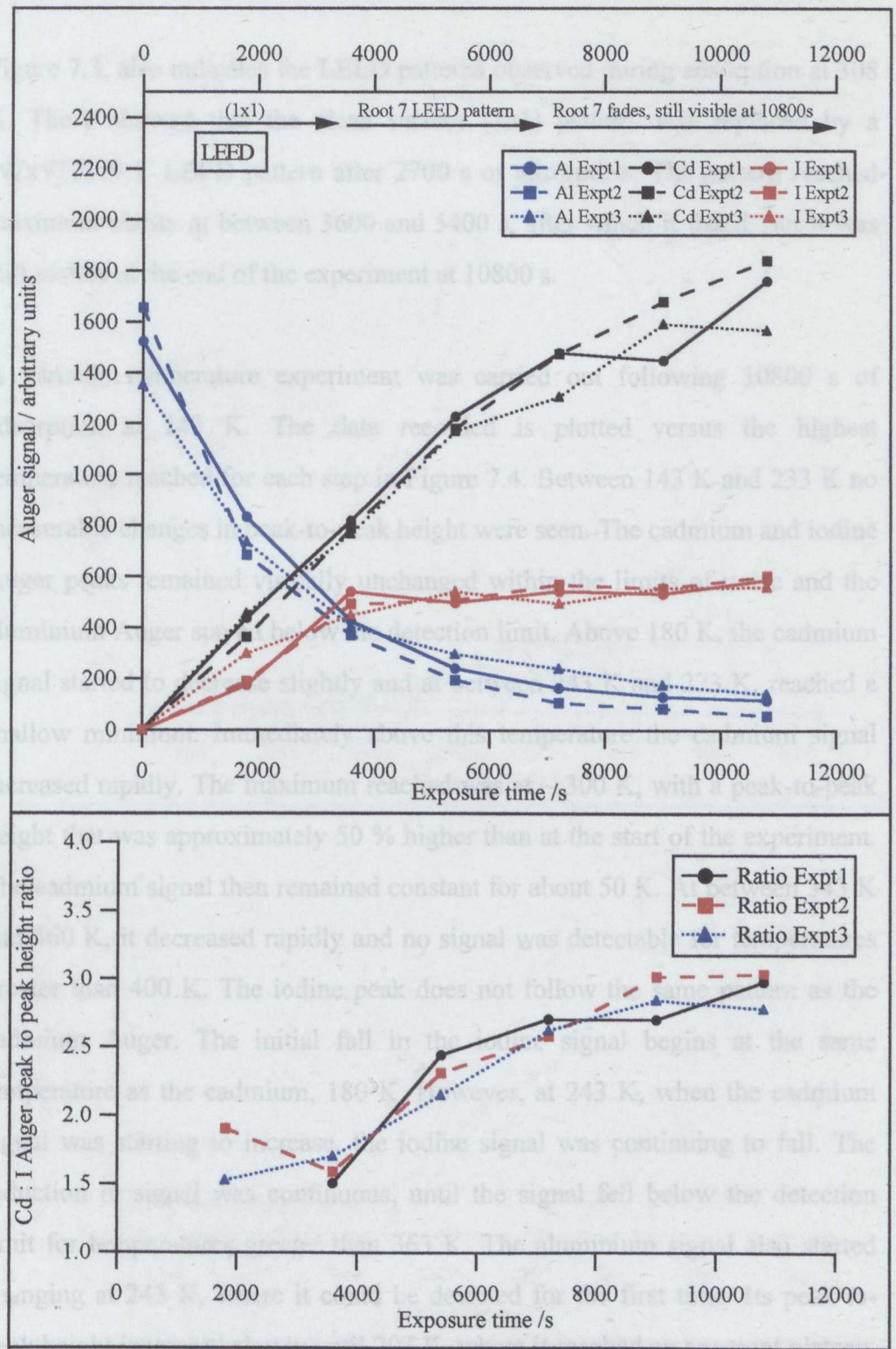


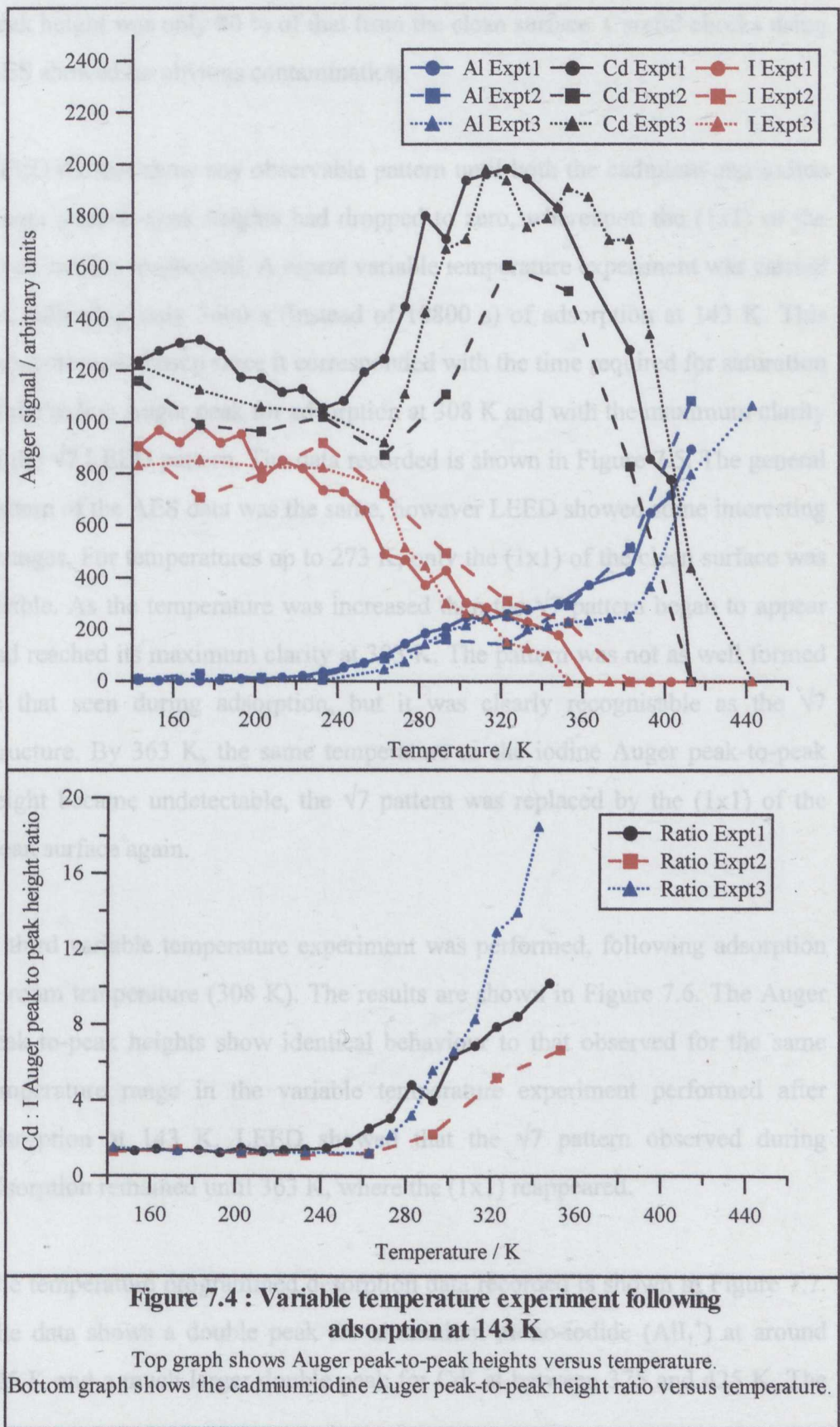
Figure 7.3 : AES-t plot for CdI_2 adsorption on Al(111) at 308 K

Top graph shows Auger peak-to-peak heights versus exposure time.
 Bottom graph shows cadmium:iodine Auger peak-to-peak height ratio versus exposure time.

is also indicated on Figure 7.3 It showed a continuous rise throughout the experiment, starting at ~1.5:1 and finishing at ~3.0:1.

Figure 7.3, also indicates the LEED patterns observed during adsorption at 308 K. These showed that the clean surface (1x1) pattern, was replaced by a $(\sqrt{7}\times\sqrt{7})R19.1^0$ LEED pattern after 2700 s of adsorption. The pattern reached maximum clarity at between 3600 and 5400 s, after which it faded, but it was still visible at the end of the experiment at 10800 s.

A variable temperature experiment was carried out following 10800 s of adsorption at 143 K. The data recorded is plotted versus the highest temperature reached for each step in Figure 7.4. Between 143 K and 233 K no measurable changes in peak-to-peak height were seen. The cadmium and iodine Auger peaks remained virtually unchanged within the limits of noise and the aluminium Auger stayed below the detection limit. Above 180 K, the cadmium signal started to decrease slightly and at between 243 K and 273 K, reached a shallow minimum. Immediately above this temperature the cadmium signal increased rapidly. The maximum reached was at ~ 300 K, with a peak-to-peak height that was approximately 50 % higher than at the start of the experiment. The cadmium signal then remained constant for about 50 K. At between 343 K and 360 K, it decreased rapidly and no signal was detectable for temperatures greater than 400 K. The iodine peak does not follow the same pattern as the cadmium Auger. The initial fall in the iodine signal begins at the same temperature as the cadmium, 180 K. However, at 243 K, when the cadmium signal was starting to increase, the iodine signal was continuing to fall. The reduction in signal was continuous, until the signal fell below the detection limit for temperatures greater than 363 K. The aluminium signal also started changing at 243 K, where it could be detected for the first time. Its peak-to-peak height increased slowly until 293 K, where it reached an apparent plateau. This coincided with the plateau at the top of the temperature dependent cadmium signal. After the disappearance of the iodine signal at 363 K, the



aluminium signal began to increase rapidly, However, its peak-to-peak height did not return to the same level as for the clean surface, prior to adsorption. The peak height was only 80 % of that from the clean surface. Careful checks using AES showed no obvious contamination.

LEED did not show any observable pattern until both the cadmium and iodine Auger peak-to-peak heights had dropped to zero, whereupon the (1x1) of the clean surface reappeared. A repeat variable temperature experiment was carried out following only 3600 s (instead of 10800 s) of adsorption at 143 K. This exposure was chosen since it corresponded with the time required for saturation of the iodine Auger peak for adsorption at 308 K and with the maximum clarity of the $\sqrt{7}$ LEED pattern. The data recorded is shown in Figure 7.5. The general pattern of the AES data was the same, however LEED showed some interesting changes. For temperatures up to 273 K, only the (1x1) of the clean surface was visible. As the temperature was increased then the $\sqrt{7}$ pattern began to appear and reached its maximum clarity at 303 K. The pattern was not as well formed as that seen during adsorption, but it was clearly recognisable as the $\sqrt{7}$ structure. By 363 K, the same temperature as the iodine Auger peak-to-peak height became undetectable, the $\sqrt{7}$ pattern was replaced by the (1x1) of the clean surface again.

A third variable temperature experiment was performed, following adsorption at room temperature (308 K). The results are shown in Figure 7.6. The Auger peak-to-peak heights show identical behaviour to that observed for the same temperature range in the variable temperature experiment performed after adsorption at 143 K. LEED showed that the $\sqrt{7}$ pattern observed during adsorption remained until 363 K, where the (1x1) reappeared.

The temperature programmed desorption data recorded is shown in Figure 7.7. The data shows a double peak for aluminium mono-iodide (AlI_1^+) at around 325 K and a much larger double peak for Cd^+ at between 375 and 425 K. The

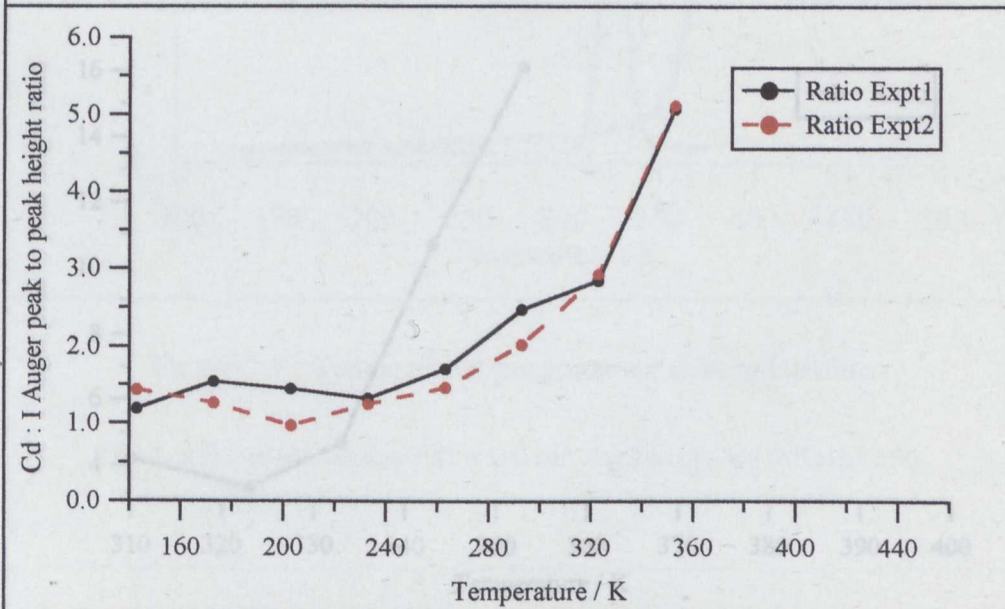
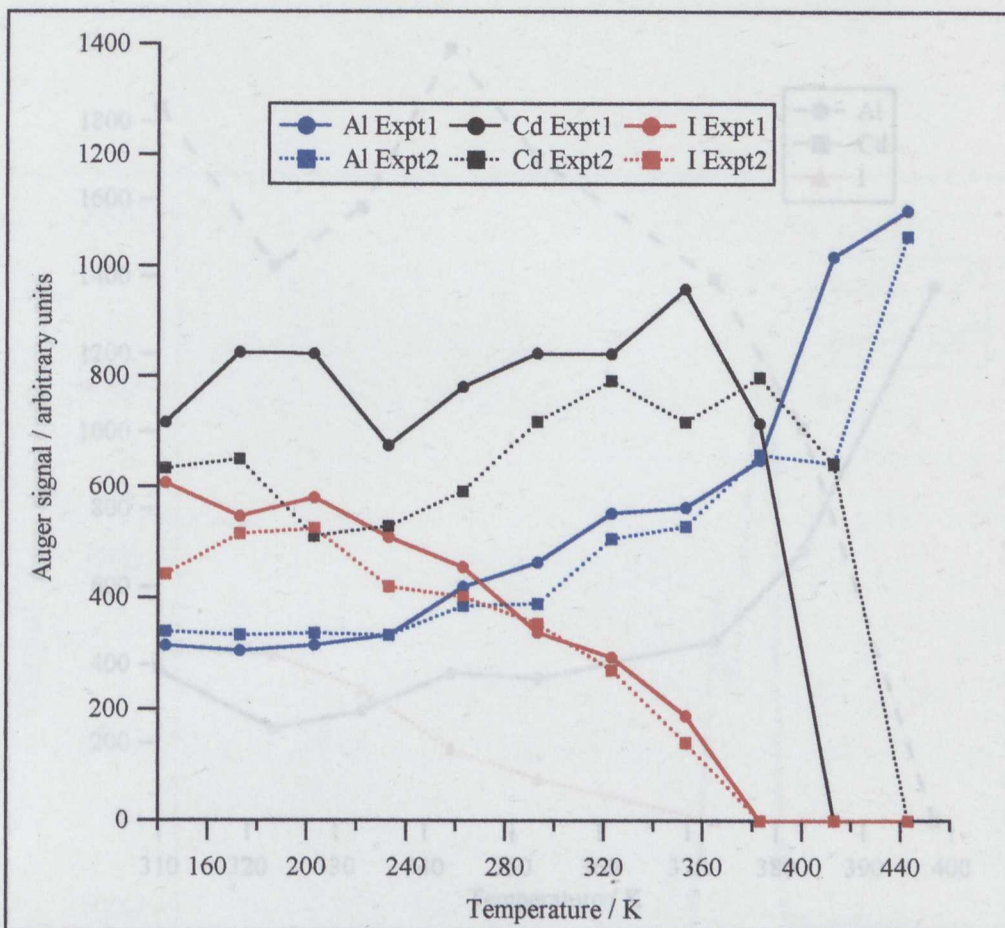


Figure 7.5 : Variable temperature experiment following 3600 s exposure at 143 K

Top graph shows Auger peak-to-peak heights versus temperature. Bottom graph shows cadmium : iodine Auger peak-to-peak height ratio versus temperature .

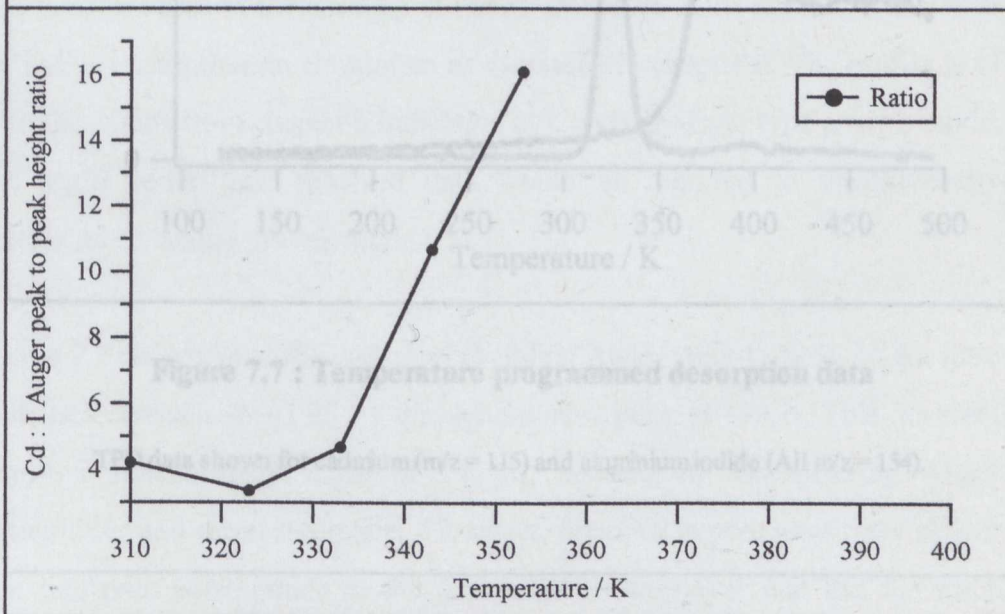
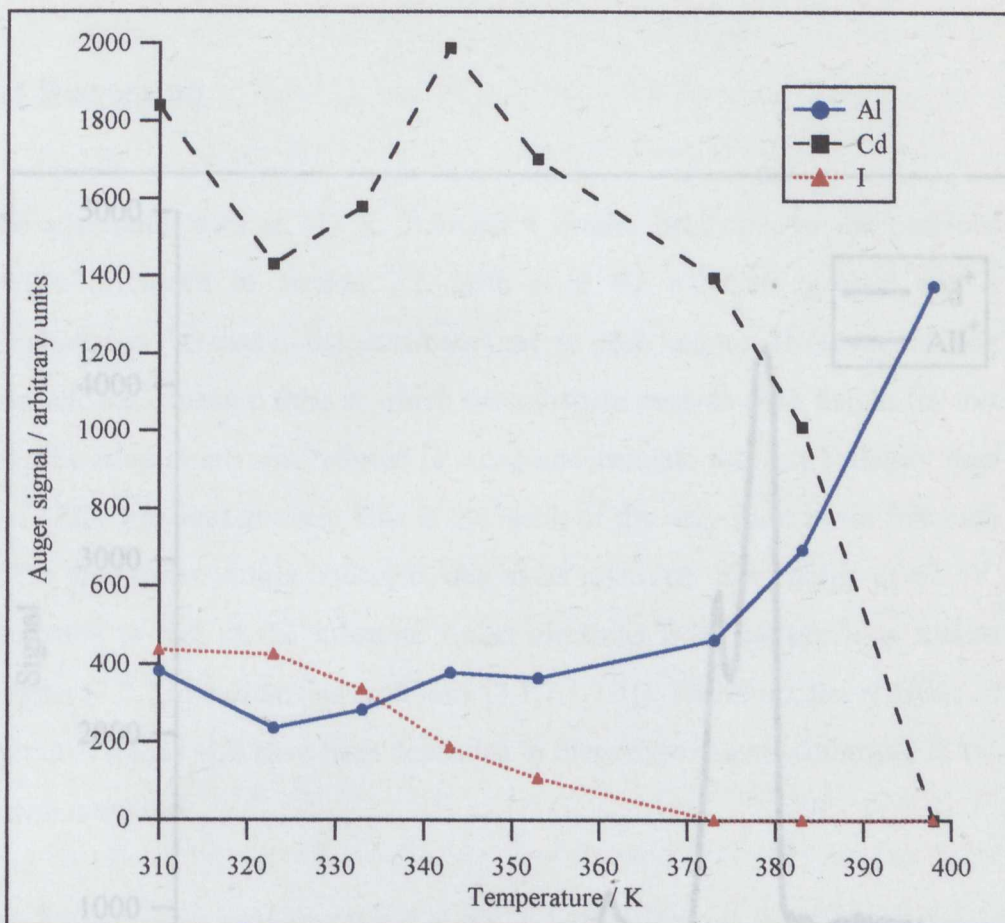


Figure 7.6 : Variable temperature experiment following adsorption at 308 K

Top graph shows Auger peak-to-peak heights versus temperature.
 Bottom graph shows the cadmium:iodine Auger peak-to-peak height ratio versus temperature.

cadmium desorption peak is followed by a plateau and the signal does not return to zero.

7.4 Discussion

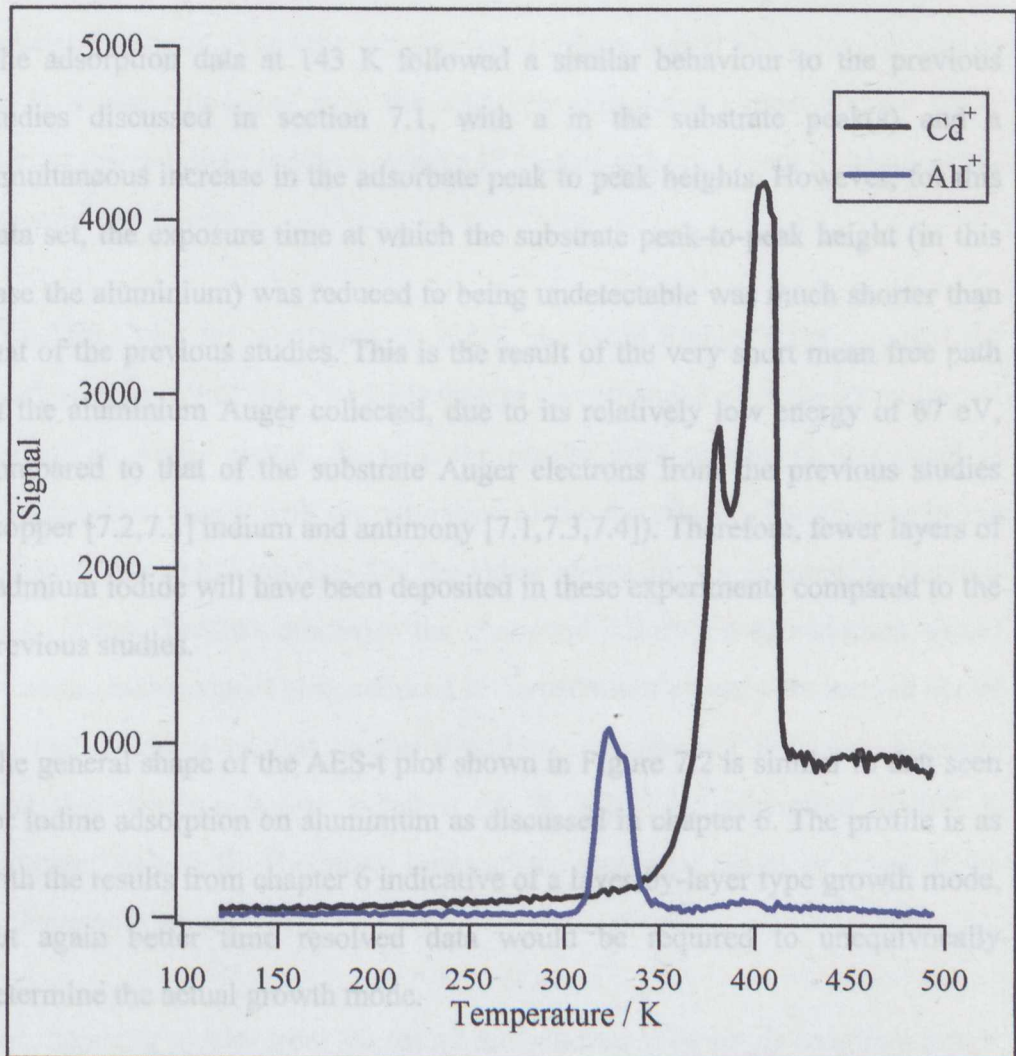


Figure 7.7 : Temperature programmed desorption data

TPD data shown for cadmium ($m/z = 115$) and aluminium iodide (All $m/z = 154$).

cadmium desorption peak is followed by a plateau and the signal does not return to zero.

7.4 Discussion

The adsorption data at 143 K followed a similar behaviour to the previous studies discussed in section 7.1, with a in the substrate peak(s) and a simultaneous increase in the adsorbate peak to peak heights. However, for this data set, the exposure time at which the substrate peak-to-peak height (in this case the aluminium) was reduced to being undetectable was much shorter than that of the previous studies. This is the result of the very short mean free path of the aluminium Auger collected, due to its relatively low energy of 67 eV, compared to that of the substrate Auger electrons from the previous studies (copper [7.2,7.3] indium and antimony [7.1,7.3,7.4]). Therefore, fewer layers of cadmium iodide will have been deposited in these experiments compared to the previous studies.

The general shape of the AES-t plot shown in Figure 7.2 is similar to that seen for iodine adsorption on aluminium as discussed in chapter 6. The profile is as with the results from chapter 6 indicative of a layer-by-layer type growth mode, but again better time resolved data would be required to unequivocally determine the actual growth mode.

Figure 7.2 showed that the cadmium to iodine Auger peak-to-peak height ratio remained constant at $\sim 1.25 : 1$ throughout adsorption at 143 K. This does not imply a stoichiometric ratio of $\text{Cd}_{1.25}\text{I}_1$, because of the differing Auger sensitivities and mean free paths. However, previous experiments have shown that this ratio corresponds to the growth of an overlayer that has the same stoichiometric ratio as bulk cadmium iodide, i.e. CdI_2 [7.1-4]. The absence of a LEED pattern shows that the cadmium iodide growth must have been disordered. However, for adsorption at 308 K, the complex $\sqrt{7}$ LEED pattern

was seen, indicating the formation of an ordered overlayer. The assumption is that the $\sqrt{7}$ pattern is the result of the formation of the same chemisorbed iodine structure seen for molecular iodine adsorption on aluminium (see Chapter 6). For this structure to have formed, the cadmium iodide molecules must have decomposed on the surface either during or after adsorption. Given the reactive nature of aluminium and the fact that for cadmium iodide adsorption on copper (111) it was noted that even the relatively unreactive copper surface could disrupt the cadmium iodide overlayer [7.2], this does not seem to be an unfair assumption to make.

The AES-t plot for adsorption at 308 K shown in Figure 7.3 shows that the maximum clarity of the $\sqrt{7}$ LEED pattern corresponded with the saturation of the iodine Auger signal. As with the results from chapter 6, this point is assumed to coincide with the saturation of the monolayer. The plateau in the iodine Auger signal suggests that the iodine atoms are not appreciably covered by cadmium, because otherwise the continued adsorption of cadmium would cause the iodine signal to be reduced if the cadmium atoms were located above the iodine. However, this creates a problem, because for the same exposure time the cadmium Auger signal is 50 % larger for adsorption at 308 K compared to 143 K. Therefore, how can the cadmium signal be larger if the iodine atoms are above it?

The incoming species from the source are believed to be single cadmium iodide molecules, although this could not be proven conclusively using the experimental apparatus. Gas phase studies of cadmium iodide have shown it to be molecular with a linear structure [7.6]. During adsorption therefore, there are linear cadmium iodide molecules reaching the surface. For adsorption at 143 K, it is suggested that the I-Cd-I species adsorb vertically on the surface, with the cadmium atoms being sandwiched between the iodine atoms. The overlayer does not obviously form an ordered structure as evidenced by the lack of any LEED pattern. The very faint signs of the $\sqrt{7}$ pattern are most likely

explained either by an incomplete freezing out of the surface decomposition reaction or to electron beam induced damage during analysis. Either of these could prevent the formation of an ordered overlayer.

As stated above, it is believed that the cadmium atoms are sandwiched between the iodide atoms for adsorption at 143 K. Therefore, as the cadmium Auger electrons at 376 eV have a much shorter mean free path than the iodine Auger electrons at 511 eV, the result is that the cadmium Auger signal is reduced as it passes through either iodine atoms or more cadmium iodide layers. For adsorption at 308 K there must have been a structural change to move the cadmium atoms to locations where the cadmium Auger electrons can more readily escape and hence produce the 50 % larger signal recorded. It is known that the structure does indeed change because of the appearance of the $\sqrt{7}$ LEED pattern for adsorption at 308 K. It was stated earlier (see section 7.1) that for cadmium iodide adsorption on InSb(001) [7.1] a (1x1) surface phase was formed which consisted of a close packed iodine overlayer with the cadmium atoms randomly located in the 4-fold octahedral sites above the iodine layer. The important point about this structure is that it was chosen to explain an increase in the cadmium to iodine Auger peak to peak height ratio. This rose from a value of 1.38:1 to 2:1. The increase in the cadmium to iodine peak-to-peak height ratio seen in these experiments is very similar to this. Therefore, it is suggested that for adsorption at 308 K the surface consists of the a $\sqrt{7}$ iodine overlayer, with the cadmium atoms presumed to be randomly located. This is for the same reason as with the $\text{Cu}(111)-(\sqrt{3}\times\sqrt{3})R30^\circ-\frac{1}{2}(\text{CdI}_2)$ structure discussed in chapter 5, which is that if there were organised then the LEED pattern would have been different, due to the changed unit mesh. If the chemisorbed iodine structure is as described in chapter 6, with the iodine radius 2.2 Å, then the cadmium atoms must be located above the iodine layer. However, if the iodine radius is 1.34 Å, as for iodine in the $(\sqrt{3}\times\sqrt{3})R30^\circ-\frac{1}{2}(\text{CdI}_2)$ structure discussed in chapter 5, then it will still be most likely that the

cadmium is located above the iodine because even with this smaller iodine radius, the space available for the cadmium would be negligible.

If the cadmium atoms are located above the iodine, it contradicts the hypothesis stated earlier that the iodine atoms are above the cadmium atoms, due to the plateau in the iodine Auger signal. This can be resolved by the differences in the mean free paths of the respective Augers again. The iodine Auger electron at 511 eV has a longer mean free path than the cadmium Auger, therefore the signal from the iodine is not retarded significantly by the cadmium atoms above it. Further evidence for the cadmium atoms being located above the ordered iodine overlayer comes from the fading of the $\sqrt{7}$ LEED pattern for higher exposures at 308 K.

Figure 7.3 shows that the cadmium continued to build up on the surface even after saturation of the iodine Auger. An obvious question is to ask what happens to the excess iodine? The assumption is that similar etching processes of aluminium by iodine must be occurring here as were studied in chapter 6. Instead of physisorbed iodine being the reservoir for etching, here it must be the iodine liberated after cadmium iodide decomposition. Therefore, any iodine remaining following saturation of the monolayer is used in the formation of aluminium iodide etch products, which either desorb or form crystallites with a small Auger footprint [7.7].

Although the exposures for the TPD data cannot be quantified, the data still provides useful information. The AlI^+ signal ($m/z = 154$) produces a double desorption peak as shown in Figure 7.7. This peak appears at a higher temperature than the reduction in iodine Auger signal from the variable temperature experiments (see Figures 7.4-7.6). The assumption is that the first peak (lower temperature) corresponds to desorption of the aluminium iodide crystallites formed by the etching reaction on the surface, which therefore lowered the iodine signal in the Auger data. The second peak (higher

temperature) is assumed to be caused by the iodine from the $\sqrt{7}$ structure reacting with the surface producing more aluminium iodide which then desorbs. This agrees with both the disappearance of the $\sqrt{7}$ LEED pattern during the variable temperature experiment and the loss of any detectable iodine Auger signal. This is a similar hypothesis put forward to explain the LOSTPD results for pure iodine adsorption on aluminium (111) presented in chapter 6. The only difference between the two sets of results is the separation between the two AlI^+ desorption peaks. Whether this is due to the difference in the apparatus used or if it is due to the co-adsorbed cadmium in this study is uncertain. As the LOSTPD apparatus was not used, species desorbing from elsewhere as well as the aluminium sample could be detected. Whilst this was not a problem for the AlI^+ TPD data because the only aluminium in the chamber was the sample, for the cadmium data, it is possible for cadmium to have desorbed from anywhere within the chamber. The low temperature peak in the cadmium TPD data is believed to be the cadmium desorbing from the aluminium sample. However, the second peak is thought to have originated from the copper sample holder. The study of cadmium iodide adsorption on copper (111) showed that desorption started at around this temperature range. It is considered that this is also the cause of the long tail that follows the two desorption peaks. This would also explain the small bump in the AlI^+ TPD data, which is probably caused by any iodide atoms encountering the surface causing spontaneous etching, as with the iodine LOSTPD data described in chapter 6.

Before discussing the variable temperature data it is useful to recap and summarise what has been concluded so far from the data discussed. For adsorption at 308 K the $\sqrt{7}$ iodine structure forms at 3600 seconds of adsorption, therefore giving 1 layer of iodine (see Figure 7.8a). As the cadmium iodide has cracked immediately upon adsorption, then at 3600 s there must be a $\frac{1}{2}$ layer of cadmium, located above the iodine as determined earlier (see Figure 7.8b). For adsorption at 143 K, the cadmium iodide is adsorbed

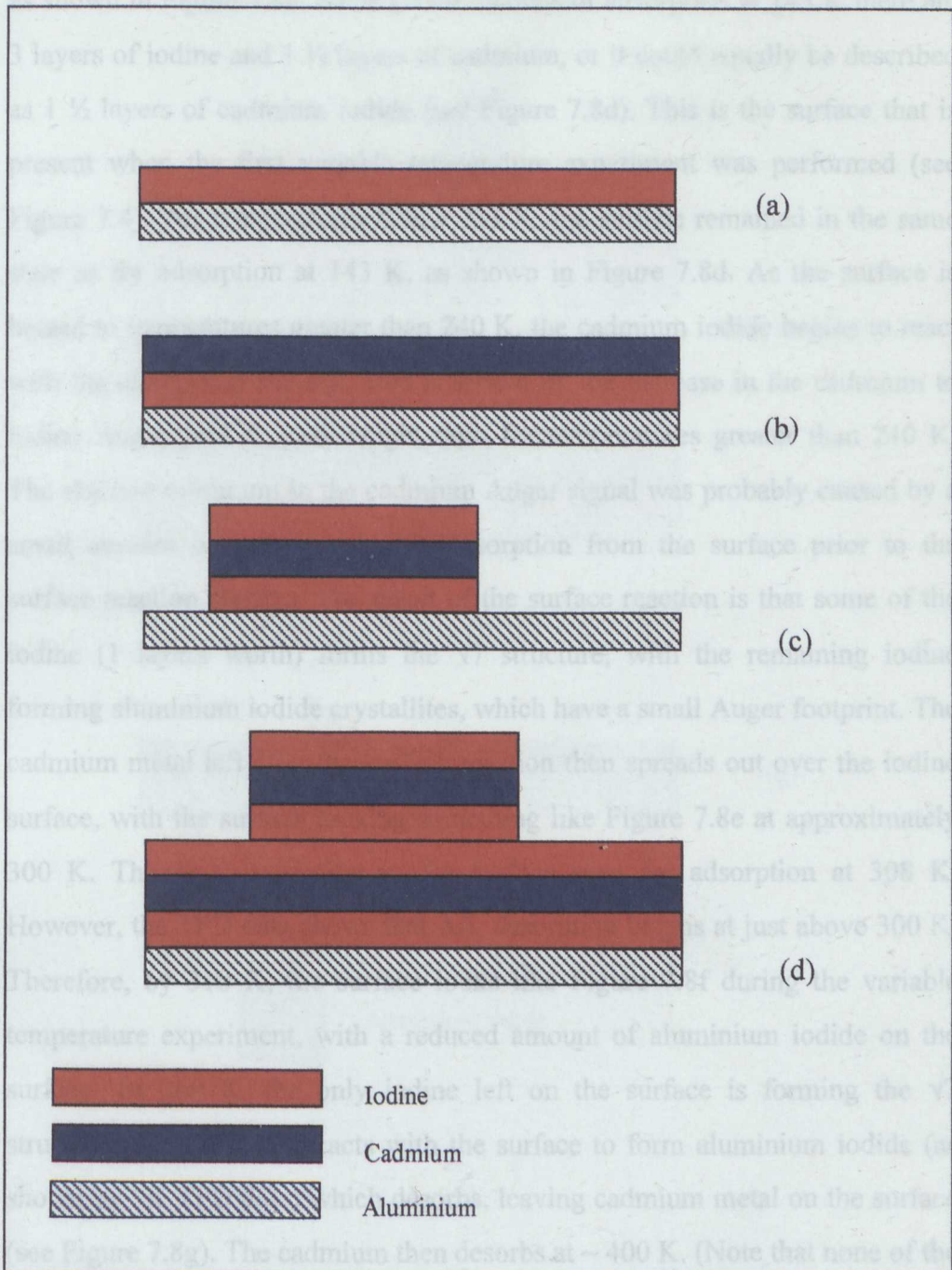


Figure 7.8a-d : Diagrams illustrating surface at various stages of the experiment

The conditions where each structure appears are discussed in the text.

intact as linear I-Cd-I molecules. Therefore, at 3600 s the surface is $\frac{1}{2}$ covered as shown in Figure 7.8c. After 11000 seconds of adsorption at 143 K there are 3 layers of iodine and $1\frac{1}{2}$ layers of cadmium, or it could equally be described as $1\frac{1}{2}$ layers of cadmium iodide (see Figure 7.8d). This is the surface that is present when the first variable temperature experiment was performed (see Figure 7.4). For temperatures below 233 K, the surface remained in the same state as for adsorption at 143 K, as shown in Figure 7.8d. As the surface is heated to temperatures greater than 240 K, the cadmium iodide begins to react with the aluminium surface. This is shown by the increase in the cadmium to iodine Auger peak-to-peak height ratio for temperatures greater than 240 K. The shallow minimum in the cadmium Auger signal was probably caused by a small amount of cadmium iodide desorption from the surface prior to the surface reaction starting. The result of the surface reaction is that some of the iodine (1 layers worth) forms the $\sqrt{7}$ structure, with the remaining iodine forming aluminium iodide crystallites, which have a small Auger footprint. The cadmium metal left after the surface reaction then spreads out over the iodine surface, with the surface looking something like Figure 7.8e at approximately 300 K. This is very similar to the surface seen for adsorption at 308 K. However, the TPD data shows that AlI_3 desorption begins at just above 300 K. Therefore, by 310 K, the surface looks like Figure 7.8f during the variable temperature experiment, with a reduced amount of aluminium iodide on the surface. At 360 K, the only iodine left on the surface is forming the $\sqrt{7}$ structure, this then also reacts with the surface to form aluminium iodide (as shown by the TPD data) which desorbs, leaving cadmium metal on the surface (see Figure 7.8g). The cadmium then desorbs at ~ 400 K. (Note that none of the surfaces illustrated in Figure 7.9 are exact representations of the surface, they are purely to aid in understanding the text and the details of the processes occurring.)

The results showed that the aluminium peak-to-peak height did not return to its clean surface value following desorption of all the adsorbate. The same

phenomenon was observed by the LEED results from chapter 6. It is assumed

that the etching process has not yet removed aluminium from the

surface, leaving it relatively smooth. The relatively short mean free path for

aluminium-Auger electrons (at 138 eV) the disordered

observations which showed that (1x1) LEED pattern following a variable

temperature experiment was much less well formed than for the clean surface.

As suggested by the LEED results, the experiment carried

out following room temperature adsorption (Figure 7.6) does not show any

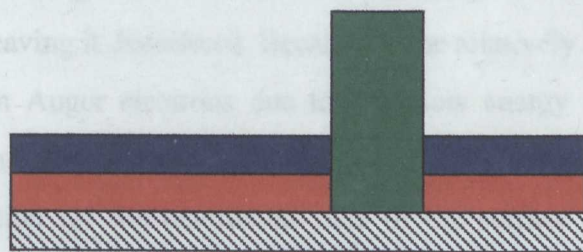
differing behaviour from the variable temperature experiment following

adsorption at 143 K. This provides further evidence that during the variable

temperature experiment the surface structure had indeed changed from the

structure observed with adsorption at 143 K and seen for adsorption at

108 K.



(e)



(f)



(g)

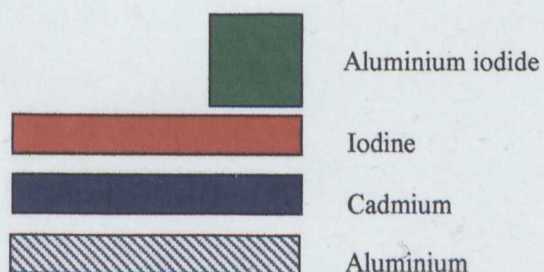


Figure 7.8e-g : Diagrams illustrating surface at various stages of the experiment

The conditions where each structure appears are discussed in the text.

phenomenon was observed for the I/Al results from chapter 6. It is assumed that a similar process is occurring, due to the etching reactions. It is probable that the etching reaction does not uniformly remove aluminium from the surface, leaving it disordered. Because of the relatively short mean free path for aluminium Auger electrons due to their low energy (67 eV) the disordered surface must cause a reduction in signal after the etching process has occurred. Confirmation for the disordered state of the surface comes from the LEED observations which showed that (1x1) LEED pattern following a variable temperature experiment was much less well formed than for the clean surface.

As suggested in the results section the variable temperature experiment carried out following room temperature adsorption (Figure 7.6) does not show any differing behaviour from the variable temperature experiment following adsorption at 143 K. This provides further evidence that during the variable temperature experiment from 143 K, the surface does indeed change from the structure associated with adsorption at 143 K into that seen for adsorption at 308 K.

7.5 Summary

Adsorption of cadmium iodide (CdI_2) at 143 K on aluminium (111) results in disordered multilayer growth of linear I-Cd-I units on the surface. Adsorption at 308 K produces an ordered $(\sqrt{7} \times \sqrt{7})R19.1^\circ$ iodine overlayer (see chapter 6) with cadmium atoms randomly located in sites above this overlayer. A variable temperature experiment performed after adsorption at 143 K causes the surface structure to change at around 273 K from that associated with adsorption at 143 K into that for adsorption at 308 K. Iodine is removed from the surface in the form of aluminium iodide, which is complete by 363 K. Similar etching processes are assumed compared to the results described in chapter 6. Cadmium desorbs from the surface by 398 K.

References

Chapter 2 : Theory

- [2.1] D.P. Woodruff & T.A. Delchar, *Modern techniques of surface science – second edition*, Cambridge University Press, Cambridge (1994)
- [2.2] M. Prutton, *Introduction to surface physics*, Oxford Science Publications, Oxford (1994)
- [2.3] *Surface analysis*, edited by J.C. Vickerman, Wiley, Chichester (1997)
- [2.4] P. Auger, *J. Phys. Radium* **6**, 205 (1925)
- [2.5] L.E. Davies, N.C. MacDonald, P.W. Palmberg, G.E. Riach & R.E. Weber, *Handbook of Auger Electron Spectroscopy, 2nd ed.*, Perkin Elmer Corp., Phys. Electronics Division, Eden Prairie, Minn./USA (1976)
- [2.6] D. Briggs & M.P. Seah, *Practical surface analysis. Volume 1 : Auger and X-ray photoelectron spectroscopy*, Wiley (1990)
- [2.7] C. Argile & G.E. Rhead, *Surf. Sci. Rep.*, **10**, 277, (1989)
- [2.8] B.W. Batterman & H Cole, *Rev. Mod. Phys* **36**, 681 (1964)
- [2.9] J. Zegenhagen, *Surf. Sci. Rep.*, **18**, 199 (1993)
- [2.10] R.W. James, *The optical principles of the diffraction of X-rays*, Bell, London (1962)
- [2.11] D.P. Woodruff, D.L. Seymour, C.F. McConville, C.E. Riley, M.D. Crapper, N.P. Prince & R.G. Jones, *Phys. Rev. Lett*, **58**, 1460 (1987)
- [2.12] D.P. Woodruff, B.C.C. Cowie & A.R.H.F. Ettema, *J. Phys. Condens. Matt.*, **6**, 10633 (1994)
- [2.13] D.P. Woodruff, *Prog. In Surf. Sci.*, **57**, 1, (1998)

Chapter 3 : Experimental Methods

- [3.1] L.E. Davies, N.C. MacDonald, P.W. Palmberg, G.E. Riach & R.E. Weber, *Handbook of Auger Electron Spectroscopy, 2nd ed.*, Perkin Elmer Corp., Phys. Electronics Division, Eden Prairie, Minn./USA (1976)
- [3.2] D.T. Quinto & W.D. Robertson, *Surf. Sci.*, **27**, 645, (1971)
- [3.3] R. Ithnin, *PhD Thesis University of Nottingham*, (1998)
- [3.4] A.A. MacDowell, D. Norman & J.B. West, *Rev. Sci. Instrum.*, **57**, 2667, (1986)
- [3.5] A.A. MacDowell, D. Norman, J.B. West & R.G. Jones, *Nuc. Instrum. & Meth. In Phys. Res.*, **A246**, 131, (1986)
- [3.6] W. Walter, *PhD Thesis University of Nottingham*, (1991)
- [3.7] A. Mowbray & R.G. Jones, *J. Vac. Sci. Technol A*, **7**, 3373, (1989)
- [3.8] *CRC Handbook of Chemistry and Physics 78th Ed.*, Edited by D.R. Lide, CRC Press, (1997)

Chapter 4 : Non-dipole photoemission and Normal Incidence

X-Ray Standing Wave Experiments : Copper(111)-($\sqrt{3}\times\sqrt{3}$)R30⁰-Iodine

- [4.1] R. Ithnin, *PhD Thesis University of Nottingham*, (1998)
- [4.2] G. Jackson, *PhD Thesis University of Warwick*, (1999)
- [4.3] R.G. Jones, N.E. Abrams, G.J. Jackson, N.A. Booth, M.T. Butterfield, B.C.C. Cowie, D.P. Woodruff & M.D. Crapper, *Surf. Sci.*, **414**, 396, (1998)
- [4.4] G. Scragg, M. Kerkar, A.R.H.F. Ettema, D.P. Woodruff, B.C.C. Cowie, A. Daïmellah, S. Turton & R.G. Jones, *Surf. Sci.*, **328**, L533, (1995)
- [4.5] M. Sugiyama & S. Maeyama, *Phys. Rev. B*, **57**, 7079, (1998)
- [4.6] D.P. Woodruff & T.A. Delchar, *Modern techniques of surface science – second edition*, Cambridge University Press, Cambridge (1994)
- [4.7] S. Hufner, *Photoelectron spectroscopy*, Springer-Verlag, Berlin, (1995)

- [4.8] K. Wille, *Rep. Progr. Phys.*, **54**, 1069, (1991)
- [4.9] R. Ithnin & R.G. Jones, *J. Phys. Condens. Matter*, **8**, 3285, (1996)
- [4.10] I.A. Vartanyants & J. Zegenhgen, *Il Nuovo Cimento*, **19D**, 617, (1997)
- [4.11] L.E. Berman & M.J. Bedzyk, *Phys. Rev. Lett.*, **63**, 1172, (1989)
- [4.12] O. Hemmers, O. Glans, D.L. Hansen, H. Wang, S.B. Whitfield, D.W. Lindle, R. Wehlitz, J.C. Levin, I.A. Sellin, & R.C.C. Perera, *Synctron Radiation News*, **9**, 40, (1996)
- [4.13] J.W. Cooper, *Phys. Rev. A.*, **42**, 6942, (1990)
- [4.14] B. Krassig, M. Jung, D.S. Gemell, E.P. Kanter, T. LeBrun, S.H. Southworth & L. Young, *Phys. Rev. Lett.*, **75**, 4736, (1996)
- [4.15] M. Jung, B. Krassig, D.S. Gemell, E.P. Kanter, T. LeBrun, S.H. Southworth & L. Young, *Phys. Rev. A*, **54**, 2127, (1997)
- [4.16] J.W. Cooper, *Phys. Rev. A*, **47**, 1841, (1993)
- [4.17] R.G. Jones, *Prog. Surf. Sci.*, **27**, 25, (1988)
- [4.18] P.H. Citrin, P. Eisenberger & R.C Hewitt, *Phys. Rev. Lett.*, **45**, 1948, (1980)
- [4.19] P.H. Citrin, P. Eisenberger & R.C Hewitt, *Surf. Sci.*, **89**, 28, (1979)
- [4.20] F. Forstmann, W. Berndt & P. Buttner, *Phys. Rev. Lett.*, **30**, 17, (1973)
- [4.21] M. Maglietta, E. Zanazzi, U. Bardi, D. Sondericker, F. Jona & P.M. Marcus, *Surf. Sci.*, **123**, 141, (1982)
- [4.22] M.F. Kadoodwaala, A.A. Davis, G. Scragg, B.C.C. Cowie, M. Kerkar, D.P. Woodruff & R.G. Jones, *Surf. Sci.*, **324**, 122, (1995)

Chapter 5 : A NIXSW Study of Copper(111)-($\sqrt{3}$ - $\sqrt{3}$)-R30⁰- $\frac{1}{2}$ (CdI₂)

- [5.1] R. Ithnin & R.G. Jones, *J. Phys. Condens. Matter*, **8**, 3285, (1996)
- [5.2] G. Jackson, *PhD Thesis University of Warwick*, (1999)
- [5.3] *CRC Handbook of Chemistry and Physics 78th Ed.*, Edited by D.R. Lide, CRC Press, (1997)

- [5.4] D.P. Woodruff, *Prog. In Surf. Sci.*, **57**, 1, (1998)
- [5.5] <http://www.povray.org>
- [5.6] R. Ithnin, *PhD Thesis University of Nottingham*, (1998)

Chapter 6 : Iodine Etching of Aluminium(111)

- [6.1] R.G. Jones, *Prog. Surf. Sci.*, **27**, 25, (1988)
- [6.2] J.R. Anderson & M.S.J. Gani, *J. Phys. Chem. Solids*, **23**, 1087, (1962)
- [6.3] T. Smith, *Surf. Sci.*, **32**, 527, (1972)
- [6.4] V.M. Bermudez & A.S. Glass, *J. Vac. Sci. Technol A*, **7**, 1961, (1986)
- [6.5] D.W. Hess & R.H. Bruce, in *Dry etching for microelectronics edited by R.A. Powell*, North-Holland, Amsterdam, (1984)
- [6.6] D.A. Danner & D.W. Hess, *J. Appl. Phys.*, **59**, 940, (1986)
- [6.7] R.J.A.A. Janssen, A.W. Kolfshoten & G.N.A. van Veen, *Appl. Phys. Lett.*, **52**, 98, (1988)
- [6.8] M. Hara, K. Domen, M. Kato, T. Onishi & H. Nozoye, *J. Phys. Chem.*, **96**, 2637, (1992)
- [6.9] H.E. Simmons, *Org. Reactions*, **20**, 1, (1973)
- [6.10] D.A. King & M.G. Wells, *Surf. Sci.*, **29**, 217, (1972)
- [6.11] R.G. Jones & S. Turton, *Surf. Sci.*, **377-379**, 719, (1997)
- [6.12] G. Cosma & R. David, *Surf. Sci. Rep.*, **5**, 145, (1985)
- [6.13] JANAF Thermochemical Tables, Part 1, 3rd edition, Am. Inst. Physics, (1986)
- [6.14] D.G. Frank, O.M.R. Chyan, T. Golden & A.T. Hubbard, *J. Phys. Chem.*, **97**, 3829, (1993)
- [6.15] S.K. Jo & J.M. White, *Surf. Sci.*, **261**, 111, (1992)
- [6.16] S.C. Chang, S.L. Yau, B.C. Schardt & M.J.J. Weaver, *J. Phys. Chem.*, **95**, 4787, (1991)

- [6.17] N.P. Prince, D.L. Seymour, M.J. Ashwin, C.F. McConville, D.P. Woodruff & R.G. Jones, *Surf. Sci.*, **230**, 13, (1990)
- [6.18] C.H. Patterson & R.M. Lambert, *Surf. Sci.*, **187**, 339, (1987)
- [6.19] W. Liu, K.C. Wong & K.A.R. Mitchell, *Surf. Sci.*, **372**, 312, (1997)
- [6.20] H.F. Winters, *J. Vac. Sci. Technol B.*, **3**, 9, (1985)
- [6.21] C. Argile & G.E. Rhead, *Surf. Sci. Rep.*, **10**, 277, (1989)

Chapter 5 : Growth and reaction of cadmium iodide on Aluminium(111)

- [7.1] A.P. Mowbray & R.G. Jones, *Appl. Surf. Sci.*, **48,49**, 27, (1992)
- [7.2] R. Ithnin & R.G. Jones, *J. Phys. Condens. Matter*, **8**, 3285, (1996)
- [7.3] R. Ithnin, *PhD Thesis University of Nottingham*, (1998)
- [7.4] A.A. Davis & R.G. Jones, *Surf. Sci.*, **310**, 73, (1994)
- [7.5] R.W.G. Wyckoff, *Crystal Structures vol 1*, Wiley, New York, (1963)
- [7.6] A. Loewenschuss, A. Ron & O. Schnepp, *J. Chem. Phys.*, **50**, 2502, (1969)
- [7.7] C. Argile & G.E. Rhead, *Surf. Sci. Rep.*, **10**, 277, (1989)

Appendix

Fortran program to calculate coherent position and coherent fraction for mixed adsorption sites

```
program calc
c Percentage in hcp sites
    real*8 pchcp(101)
c Percentage in fcc sites
    real*8 pcfcc(101)
c Calculated coherent position
    real*8 cptheory(101)
c Calculated coherent fraction
    real*8 cftheory(101)
    character*32 file
1000 format(a32)
c input
    write(6,*)'Input coherent fraction to reduce components by'
    read(5,*) cfe
    write(6,*)'Input file name for results'
    read(5,1000) file
    open(unit=11,file=file,access='sequential',status='new')
c radius of Argand diagram
    rad=1.0d0
c angle for pure fcc vector
    fcca=0.95d0
c angle for pure hcp vector
    hcpa=240.96d0
    do 10,i=1,100
        a=float(i-1.0d0)
```

```

pchcp(i)=a/100.0d0
pcfcc(i)=(100.0d0-a)/100.0d0

```

c length of fcc vector

```
dfcc=cfe*pcfcc(i)*rad
```

c length of hcp vector

```
dhcp=cfe*pchcp(i)*rad
```

c x co-ordinate for end of hcp vector

```
x1=-((sind(270.0d0-hcpa))*dhcp)
```

c y co-ordinate for end of hcp vector

```
y1=-((cosd(270.0d0-hcpa))*dhcp)
```

c x co-ordinate for end of fcc vector

```
x2=(cosd(fcca))*dfcc
```

c y co-ordinate for end of fcc vector

```
y2=(sind(fcca))*dfcc
```

c x co-ordinate for end of resultant vector

```
x3=x1+x2
```

c y co-ordinate for end of resultant vector

```
y3=y1+y2
```

c calculation of theoretical coherent fraction

```
cftheory(i)=(sqrt((x3*x3)+(y3*y3)))/rad
```

c the following if else loops calculate the coherent position according to which
c sector of the argand diagram the resultant vector occupies

```
if (i.eq.1) then
```

```
write(6,*)x3,y3
```

```
endif
```

```
if (y3.gt.0.0d0) then
```

```
theta=atand(y3/x3)
```

```

        cptheory(i)=theta/360.0d0
    else if (y3.lt.0.0d0.and.x3.gt.0.0d0) then
        theta=atand(y3/x3)
        cptheory(i)=(360.0d0+theta)/360.0d0
    else if (y3.lt.0.0d0.and.x3.lt.0.0d0) then
        theta=atand(y3/x3)
        cptheory(i)=(180.0d0+theta)/360.0d0
    else if (x3.eq.0.0d0) then
        cptheory(i)=0.75
    endif

```

c loop to output results

```

10 continue
do 20, i=1,101
    pcfcc(i)=pcfcc(i)*100.0d0
    pchcp(i)=pchcp(i)*100.0d0
write(11,*) pcfcc(i), pchcp(i), cptheory(i), cftheory(i)
20 continue
end

```

Publications

Non-dipole photoemission effects in X-Ray standing wavefield determination of surface structure.

C.J. Fisher, R.Ithnin, R.G. Jones, G.J. Jackson, D.P. Woodruff & B.C.C. Cowie
Journal of Physics Condensed Matter, **10**, L623, (1998)

Reaction and sticking probabilities using line of sight techniques : Iodine on Al(111)

R.G. Jones & C.J. Fisher
Surface Science, **424**, 127, (1999)